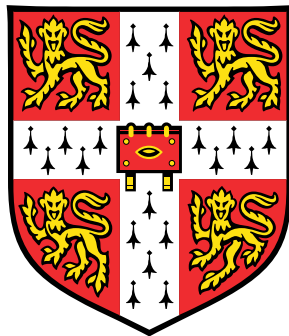


# **A moving mesh method for non-isothermal multiphase flows**



**Zekang Cheng**

Department of Engineering  
University of Cambridge

This dissertation is submitted for the degree of  
*Doctor of Philosophy*

Queens' College

June 2018



## Declaration

I hereby declare that except where specific reference is made to the work of others, the contents of this dissertation are original and have not been submitted in whole or in part for consideration for any other degree or qualification in this, or any other university. This dissertation is my own work and contains nothing which is the outcome of work done in collaboration with others, except as specified in the text and Acknowledgements. This dissertation contains approximately 50,000 words including appendices, bibliography, footnotes, tables and equations, and contains 84 figures and 18 tables.

---

献给  
我的父母  
和  
我的大动

---

## Acknowledgements

The work presented in this thesis would have not been carried out without the help of many people, to whom I am profoundly grateful. First, and foremost, I would like to express my most sincere admiration and thanks to my supervisor, Dr. Jie Li, for his continuous support and guidance during my Ph.D. study, and for his patience, enthusiasm, and immense knowledge. He has generously shared his experience in research and in programming, which is of great benefit to me.

Many thanks to Shidi Yan for many stimulating discussions about numerical techniques, and many casual chats in the office. I would like to thank the BP Institute for the computational facilities and thank Patrick Welche and Dr. Chris Richardson for maintaining the IT infrastructure. I want to express my gratitude to the contributors to many open-source softwares, including, but not limiting to, Gnuplot, matplotlib, PYTHON and L<sup>A</sup>T<sub>E</sub>X. In addition, I sincerely appreciate the financial support from the the China Scholarship Council and the Cambridge Trust.

My life would have been very dull without the company of many friends, Zijian Guo, Yanting Jin, Soichiro Tottori, Haiyang Yun, Qian Sun, etc. A special thank to Adrien Lefauve for offering his help in proofreading parts of this thesis. I give my great appreciation to him and Andrew Williamson for the friendship in the past four years. Good luck to them both with their future life and career. I am also deeply grateful for the advice on career development received from Zhong Zheng, Zhidong Fu, Zhe Wang, Xiaolei Chen, and Runze Tang.

Furthermore, I would like to thank my ex-housemates, Michael Hope, Georgia Vann and Lissa Eyre. Living with them has enormously improved my oral English.

I would like to thank my parents and other family members for their endless love, support and encouragement. Last, but certainly not least, I owe my greatest gratitude to my girlfriend Jingyi Wan, who always overwhelms me with love, for bringing joys to me every day and for cheering me up when I feel depressed. I am very fortunate to have her in my life, and there is nothing that is more precious to me. With the woman I love, I feel more confident facing the future full of uncertainties.



## Abstract

In this thesis, a numerical method is developed for simulating non-isothermal multiphase flows, which are important in many technical applications such as crystal growth and welding. The method is based on the arbitrary Lagrangian Eulerian method of Li (2013). The interface is represented explicitly by mesh lines, and is tracked by an adaptive moving unstructured mesh. The  $P2 - P1d$  finite element method (FEM) is used for discretisation and the incompressible Navier-Stokes equations are solved by the *uzawa* method.

Firstly, a thorough study is presented on the method's capability in numerically representing the force balance condition on the interface. An inaccurate representation of this condition induces the non-physical spurious currents, which degrade the simulation accuracy especially when the viscous damping is weak (small *Ohnesorge* number,  $Oh$ ). For the example of a circular/spherical droplet, the interfacial tension and the associated pressure jump are exactly balanced numerically and thus the static Laplace solution exists in our method. The stability of this solution is examined numerically. The amplitude of the dimensionless spurious currents is found to be around  $10^{-15}$  for  $Oh \geq 10^{-3}$ . Another benchmark test is the axisymmetric oscillation of a freesurface droplet/bubble. The simulation results are in good agreement with the analytical solution for  $Oh = 10^{-3}$ . This is by far the first successful simulation of droplet/bubble oscillation with such weak viscous damping and it demonstrates the ability of our method in simulating flows with strong capillary forces.

Secondly, a numerical treatment of interface topology changes is incorporated into our method for studying problems with interface breakup. Thanks to the adaptive mesh generator, the thin region between the interface boundary and another boundary consists of one layer of elements. The interface topology change is performed once the minimum distance between the two boundaries falls below a pre-set scale  $l_{breakup}$ . The numerical implementation is verified through two different examples: dripping faucet and droplet coalescence. Remarkably good agreement has been obtained with the experimental results. The simulation of the low  $Oh$  dripping problem shows both the accuracy and robustness of our method. The simulation of droplet coalescence demonstrates the great advantage of our method in solving problems with a large disparity in length scales.

Finally, an FEM solver for temperature is developed and the non-isothermal effects are included in our method for the purpose of simulating non-isothermal multiphase flows. The modified method is validated to be accurate through three benchmark examples: natural convection in a cavity, thermocapillary convection of two layers, and droplet migration subject to a temperature gradient. Our method is then applied to investigate the liquid bridge breakup with thermocapillary effect. The non-isothermal liquid bridge breakup in the viscous and inertial regimes are studied. It has been found that the inertial regime breakup exhibits different pinchoff shapes as the *Capillary* number increases, and that the viscous regime breakup is accelerated by the thermocapillary motion.

# Contents

<b>Acknowledgement</b>	<b>v</b>
<b>Abstract</b>	<b>vii</b>
<b>Contents</b>	<b>ix</b>
<b>List of Figures</b>	<b>xiii</b>
<b>List of Tables</b>	<b>xvii</b>
<b>1 Introduction</b>	<b>1</b>
1.1 Background . . . . .	1
1.2 Overview of thermocapillary flow . . . . .	3
1.3 Overview of interface-tracking methods . . . . .	8
1.4 Thesis outline . . . . .	14
<b>2 Mesh generator</b>	<b>17</b>
2.1 Moving mesh and local re-arrangement . . . . .	17
2.2 Adaptive mesh principles . . . . .	20
<b>3 Basics of finite element method</b>	<b>27</b>
3.1 Theory of FEM . . . . .	27
3.1.1 Weak formulation . . . . .	28
3.1.2 Galerkin finite element method . . . . .	29
3.2 Practical implementation . . . . .	32
3.3 An FEM Poisson solver . . . . .	36

## CONTENTS

---

<b>4</b>	<b>FEM for multiphase flows</b>	<b>41</b>
4.1	Mathematical formulations for multiphase flows . . . . .	42
4.2	Numerical procedures . . . . .	45
4.2.1	Weak formulation . . . . .	45
4.2.2	Spatial and temporal discretisation . . . . .	47
4.2.3	Solution steps . . . . .	51
4.2.4	ALE method and approximation of material derivatives . .	52
4.2.5	Numerical evaluation of interfacial tension . . . . .	55
4.3	Laplace solution for a circular/spherical droplet . . . . .	56
4.3.1	Existence of a static solution . . . . .	57
4.3.2	Numerical experiment of spurious current . . . . .	59
4.4	Benchmark test: drop/bubble oscillation . . . . .	65
<b>5</b>	<b>Multiphase flow with interface topology changes</b>	<b>71</b>
5.1	Interface split/re-connection algorithms . . . . .	72
5.2	Dripping faucet . . . . .	76
5.2.1	Numerical set-up for dripping . . . . .	77
5.2.2	Equilibrium shape of a pendant droplet . . . . .	79
5.2.3	Simulation results of dripping faucet . . . . .	85
5.3	Droplet head-on collision . . . . .	90
5.3.1	Modelling the inter-drop gas film . . . . .	92
5.3.2	Simulation results . . . . .	94
5.3.3	Discussion on droplet collision . . . . .	98
5.3.3.1	Rarefied effects and van der Waals forces . . . . .	98
5.3.3.2	Compressibility of the inter-droplet gas . . . . .	102
5.3.3.3	Comparison with interface non-conforming methods	103
<b>6</b>	<b>FEM applied to non-isothermal multiphase flows</b>	<b>107</b>
6.1	Mathematical formulation for thermocapillary flow . . . . .	107
6.2	Numerical implementation . . . . .	110
6.2.1	An FEM solver for temperature equation . . . . .	111
6.2.2	Coupling the temperature solver with the NS solver . . . .	112
6.3	Validation tests . . . . .	113
6.3.1	Natural convection in a square cavity . . . . .	113

6.3.2	Thermocapillary convection of two superimposed fluids . . .	119
6.3.3	Thermocapillary migration of a spherical droplet . . . . .	124
6.3.3.1	Solution for a limiting case: $Re, Ma, Ca \ll 1.0$ . . .	125
6.3.3.2	Solution for finite $Re, Ma$ and $Ca$ . . . . .	127
6.4	Liquid bridge with thermocapillarity . . . . .	130
6.4.1	Configuration and numerical set-up . . . . .	132
6.4.2	Mesh convergence . . . . .	134
6.4.3	Isothermal simulation: effect of $Oh$ . . . . .	134
6.4.4	Non-isothermal simulation: effect of $Ca$ . . . . .	136
6.4.5	Conclusion . . . . .	143
<b>7</b>	<b>Conclusions and future works</b>	<b>145</b>
<b>A</b>	<b>Numerical implementation of FEM</b>	<b>151</b>
A.1	Mesh data structure . . . . .	151
A.2	Storage for a sparse matrix . . . . .	153
A.3	Hammer integration formulas . . . . .	155
<b>B</b>	<b>The force balance on the interface</b>	<b>159</b>
<b>C</b>	<b>Weak formulation in axisymmetric geometry</b>	<b>163</b>
<b>D</b>	<b>Computing information</b>	<b>165</b>
	<b>Bibliography</b>	<b>167</b>

## CONTENTS

---

# List of Figures

1.1	Illustration of thermal driven Marangoni effect . . . . .	2
1.2	A Sketch of the cohesive forces for molecules on the surface and within the bulk fluid by De Gennes et al. (2004). . . . .	3
1.3	Temperature dependence of surface tension of water in contact with air . . . . .	4
1.4	A thin liquid layer heated from below . . . . .	5
1.5	Sketches of the velocity profile for (a) linear-flow and (b) return-flow basic state. . . . .	6
1.6	Illustration of the floating zone method in Kawamura et al. (2012)	7
1.7	Schematics of different interface-tracking methods . . . . .	10
1.8	Example of spurious currents . . . . .	12
2.1	Example of mesh moving and smoothing . . . . .	19
2.2	Schematics of three basic local remesh operations . . . . .	19
2.3	Procedures of mesh generation from the simplest configuration . .	22
2.4	Relation between number of vertices and mesh size scale $\alpha$ . . . .	24
2.5	Example of a one-layered triangles between two boundaries . . . .	25
3.1	Example of domain $\Omega$ and two types of boundaries $\partial\Omega_N$ and $\partial\Omega_D$	28
3.2	Finite element triangulation in domain $\Omega$ . . . . .	30
3.3	Example of approximation functions . . . . .	30
3.4	Examples of $P1$ and $P2$ elements . . . . .	32
3.5	Examples of $P1$ basis functions . . . . .	33
3.6	Examples of $P2$ basis functions . . . . .	34
3.7	Transformation of a reference triangle to an arbitrary triangle . .	34

## LIST OF FIGURES

---

3.8	$P1$ and $P2$ reference triangles in $s - t$ plane . . . . .	35
3.9	Numerical solution to the Poisson equation and corresponding mesh	37
3.10	Maximum relative error plotted against $l_{max}$ . . . . .	38
4.1	Schematics of two immiscible fluids separated by an interface . . .	42
4.2	Example of a piece of triangulation near the interface . . . . .	48
4.3	Taylor-Hood element . . . . .	48
4.4	Schematic of method of characteristics . . . . .	53
4.5	A piece of interface represented by mesh lines . . . . .	55
4.6	Triangulation near a circular interface which separates $\Omega_1$ and $\Omega_2$	58
4.7	Temporal evolution of maximum $Ca$ at different $Oh$ . . . . .	61
4.8	Temporal evolution of maximum $Ca$ for different meshes at $Oh = 10^{-3}$ . . . . .	64
4.9	Temporal evolution of the second mode of deformation of a bubble set in a liquid initially at rest. . . . .	68
4.10	Comparisons of droplet/bubble oscillation with analytical solution	69
5.1	Examples of interface topology changes . . . . .	71
5.2	Schematic of interface break-up in Quan and Schmidt (2007) . . .	73
5.3	Mesh topology change sequence in an example of jet breakup . . .	74
5.4	Two initial configuration for dripping simulation . . . . .	78
5.5	Example of the mesh used in two-phase simulation . . . . .	79
5.6	Schematic of a pendant droplet . . . . .	80
5.7	Relation between $p_b$ and $V$ in pendant droplet . . . . .	81
5.8	The equilibrium shape of a pendant droplet of different volume $V$	82
5.9	The relative error of $L$ plotted against $l_{interface}$ and $t$ . . . . .	83
5.10	Illustration of spurious current in the pendant droplet simulation .	84
5.11	Simulated results compared to experiment of Peregrine et al. (1990)	85
5.12	Interface shape and a close-up of the neck region before pinchoff in dripping simulation . . . . .	87
5.13	Evolution of the bottom node with the pendant drop volume $V$ .	88
5.14	Comparisons between two-phase and free-surface simulations . . .	89
5.15	Illustration of spurious currents in dripping simulation . . . . .	90
5.16	Schematic of the head-on collision of two droplets of the same size	92



## LIST OF FIGURES

---

5.17 Example of triangulation in the thin gas film . . . . .	93
5.18 Simulated result of the head-on collision of binary tetradecane droplet with $D = 214.4$ $\mu\text{m}$ in atmospheric air at $We = 2.25$ and the computational mesh. . . . .	95
5.19 Example of two droplet collision with a bounce outcome . . . . .	98
5.20 Temporal evolution of the dimensionless minimum thickness $h/D$ of gas film in between the two droplets . . . . .	99
5.21 Temporal evolution of the interface shape near the second thickness minimum . . . . .	101
5.22 Temporal evolution of the maximum relative pressure in the droplet collision simulation. . . . .	102
5.23 Comparison between conforming and non-conforming method . . . . .	104
5.24 Temporal evolution of the minimum thickness of the inter-drop gas film in the $We = 0.2$ tetradecane droplet collision with the size of $D = 240$ $\mu\text{m}$ . . . . .	105
6.1 Configuration of natural convection in a square cavity of side $L$ and the computational mesh. . . . .	114
6.2 The temporal evolution of the relative error $\tilde{u}_{max}$ compared to the benchmark value. . . . .	116
6.3 Steady temperature field in the natural convection simulation . . . . .	117
6.4 Steady velocity solution in the natural convection simulation . . . . .	118
6.5 The configuration of two superimposed layers . . . . .	120
6.6 Comparison of simulated temperature contour (in blue dashed isothermal line) to analytical solution (in red solid isothermal lines). . . . .	122
6.7 Comparison of simulated velocity field (in blue arrows) to analytical solution (in red arrows) . . . . .	123
6.8 Configuration of migration of a spherical droplet . . . . .	124
6.9 Numerical results at small $Ma, Re, Ca$ with different mesh resolution . . . . .	127
6.10 The temporal evolution of the droplet migration velocity . . . . .	128
6.11 The temperature field around the droplet in case of $Ma = 1.0, 10.0$ and $100.0$ when $tU/R = 20.0$ . . . . .	129

## LIST OF FIGURES

---

6.12	The temporal evolution of migration velocity at $Re = 1.0$ , $Ma = 100.0$ and $Ca = 0.1$ , from 3D LBM and our axisymmetric simulation with different mesh resolutions and mesh domains. . . . .	130
6.13	Experimental pictures from the non-isothermal liquid bridge break-up experiment by Ueno et al. (2012) . . . . .	131
6.14	Configuration (a) and mesh (b) for our study of liquid bridge. . .	132
6.15	Mesh convergence study for liquid bridge simulation . . . . .	134
6.16	Interface evolution in two isothermal break-up regimes . . . . .	135
6.17	Break-up shape and instant for $Oh = 0.01$ and varied values of $Ca$ . 137	
6.18	Temporal evolution of the interface shape and the thermal field in the simulation with $Oh = 0.01$ , $Ca = 0.05$ and $Pr = 5$ . . . . .	138
6.19	Temporal evolution of the interface shape and the thermal field in the simulation with $Oh = 0.01$ , $Ca = 0.2$ and $Pr = 5$ . . . . .	139
6.20	Velocity field ( $t = 2.0$ ) for $Oh = 0.01$ , $Ca = 0.0$ (blue) and $0.2$ (red).140	
6.21	Break-up interface shapes in non-isothermal simulation ( $Oh = 1.0$ ) 141	
6.22	Volume ratio between the upper and lower fractions of the liquid bridge $R_V$ (a) and time to pinchoff (b) are plotted against $Ca$ . . .	141
6.23	Velocity field at $t = 20.0$ from $Oh = 1.0$ and $Ca = 0.0, 0.2$ : . . . .	142
6.24	Temporal evolution of the temperature field inside the liquid bridge from the non-isothermal simulation with $Oh = 1.0$ and $Ca = 0.2$ . 143	
A.1	Direct formulas for Hammer integration over a reference triangle (part 1). The image is from Dhatt et al. (2012). . . . .	156
A.2	Direct formulas for Hammer integration over a reference triangle (part 2). The image is from Dhatt et al. (2012). . . . .	157
B.1	Schematics of the force balance on the interface . . . . .	160

# List of Tables

2.1	Mesh scale $\alpha$ and the corresponding mesh vertices number . . . . .	23
3.1	Performance of $P2$ finite element Poisson solver . . . . .	38
4.1	Error in velocity after one time step for the inviscid static drop . . . . .	60
4.2	Maximum $Ca$ and maximum CFL number at $T = 100$ for simulation of a circular/spherical droplet with different $Oh$ and the corresponding mesh information . . . . .	63
4.3	The initial value solution of an oscillating drop/bubble . . . . .	66
5.1	Dimensionless numbers in the simulation of a dripping faucet . . . . .	78
5.2	Relative error of $L$ to the analytical solution for $V = 0.629$ . . . . .	83
5.3	Physical parameters used in the simulation . . . . .	96
6.1	Comparison with benchmark solution in De Vahl Davis (1983) . . . . .	116
6.2	Maximum relative error of temperature compared to the analytical solution . . . . .	121
6.3	Numerical results for different mesh resolutions . . . . .	126
6.4	Size of the satellite droplet and time to breakup in isothermal simulations with different values of $Oh$ . . . . .	136
A.1	LISTOFNODES[NUMBEROFNODES] . . . . .	152
A.2	LISTOFTRIANGLES[NUMBEROFTRIANGLES] . . . . .	152
A.3	LISTOFEDGES[NUMBEROFEDGES] . . . . .	152
A.4	CSR representation of matrix (A.1). . . . .	155
D.1	CPU information . . . . .	165

**LIST OF TABLES**

---

D.2 Computing time . . . . . 166

# Chapter 1

## Introduction

### 1.1 Background

Multiphase flow consists of two or more immiscible components, such as air/water and oil/water. It is a subject rich with fascinating physics; it is also ubiquitous in many technical applications and in the natural world, examples including ink-jet printing, cavitation, the formation of rain drops, spray, and atomization. The key element of multiphase flow is the presence of an interface separating different phases. Many physical properties, for example density and viscosity, are discontinuous across the interface. The interface also possesses localised properties, the most prominent of which is the interfacial tension  $\sigma$ . It represents the magnitude of force per unit length normal to a cut in the interface (Davis, 1987), and it results in the discontinuity of the stress tensor on the interface. Furthermore, owing to the fact that the interface is a moving boundary, the evolution of the interface is coupled with the velocity field and pressure, and all of these must be determined simultaneously (Davis, 2002).

In non-isothermal multiphase flows, not only does the heat transfer have to be considered, but also the temperature dependence of important fluid properties. As a result, the fluid density and the interfacial tension vary spatially and temporally. If gravity is taken into consideration, the density variation leads to buoyancy forces. The variation of interfacial tension results in shear stresses that act on the interface and induce flow motion along the interface. In general, the interfacial tension decreases with increasing temperature. Figure 1.1 illustrates the

# 1. INTRODUCTION

---

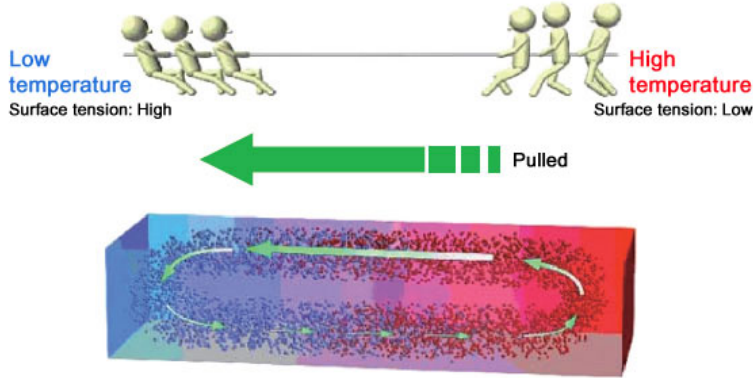


Figure 1.1: Thermal-driven Marangoni forces induce interfacial flow towards the cold side (larger interfacial tension). Due to mass conservation, fluid in the bulk moves towards the warm end. The image is taken from <http://iss.jaxa.jp/en/kiboexp/theme/first/marangoni/>

effect of non-uniform interfacial tension in a slot. As interfacial tension is larger in regions where the temperature is lower, fluid on the interface is pulled from the warmer region towards the cooler region. Due to mass conservation, the bulk fluid moves towards the warmer side. This effect is known as the Marangoni effect (Scriven and Sternling, 1960), which can also be triggered by other mechanisms, such as surface active molecules (surfactants), electric and magnetic fields. The thermal driven Marangoni flow is the main focus of this thesis and is typically referred to as *thermocapillary flow*.

Both the buoyancy and thermocapillary effects are present in non-isothermal multiphase flows on earth, with the thermocapillary flow often overshadowed by the buoyancy driven flow. However, for small geometry and microgravity environments, the thermocapillary flow usually dominates. For example, it plays an important role in technical processes including thin film rupture in heat transfer devices, the propagation of flames over liquid fuels, the texturing of surfaces in magnetic storage devices, the behaviour of welding pools, and crystal growth in semiconductor materials (Schatz and Neitzel, 2001). Recently it has also been applied to manipulate droplet motion in microfluidic devices (Darhuber and Troian, 2005).

This thesis is motivated by the importance of thermocapillary flow in countless industrial applications. For the in-depth understanding of thermocapillary flow, we develop a numerical method for simulating non-isothermal multiphase flows. This method is based on the existing method for isothermal multiphase flows. Non-isothermal effects are incorporated and the modifications are validated. The modified method is then applied to study the effect of thermocapillary motion in the breakup of liquid bridge. Before introducing our method, we first review the literature for previous research on thermocapillary flow, and then provide an overview on numerical methods for multiphase flows.

## 1.2 Overview of thermocapillary flow

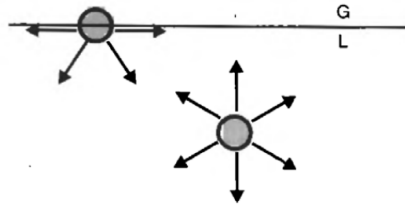


Figure 1.2: A Sketch of the cohesive forces for molecules on the surface and within the bulk fluid by De Gennes et al. (2004).

First, we would like to give a brief introduction to the physical origin of the surface tension  $\sigma$ . As shown in Figure 1.2, the molecule in the midst of the fluid is exposed to cohesive forces (as visualised by arrows) from all its neighbours in all directions, resulting in zero net force. In contrast, the molecule on the surface loses half its cohesive interactions, and is in an unfavourable energy state. If the cohesion energy per molecule is  $U$  inside the bulk, a molecule sitting at the interface finds itself short of roughly  $U/2$ . The surface tension is a direct measure of the energy shortfall, defined as the amount of energy required to increase the surface area by one unit. The interfacial tension between two immiscible fluids can be defined likewise. Since the fluctuations of the interface thickness are of the order of a mere Ångström, in fluid mechanics under the continuum

## 1. INTRODUCTION

---

assumption, the interface is usually modelled as a moving boundary with zero thickness. The interfacial tension then has the mechanical definition stated in the previous section.

Cohesive forces decrease with an increase of molecular thermal activity, e.g. an increase in the system temperature. A higher temperature corresponds to lower energy shortfall on the interface, and thus a lower surface tension. Eötvös (1886) came up with the Eötvös rule:

$$\sigma = \frac{k(T_c - T)}{V^{2/3}} \quad (1.1)$$

where  $V$  is the molar volume,  $T_c$  is the critical temperature and  $k$  the Eötvös constant. Later a nonlinear relation was proposed (Guggenheim, 1945). However, for simplicity it is conventional to adopt the linear relationship in studying thermocapillary flow. As shown in Figure 1.3, though the interfacial tension of water in contact with air does not depend on temperature strictly linearly, a linear relationship is a good approximation.

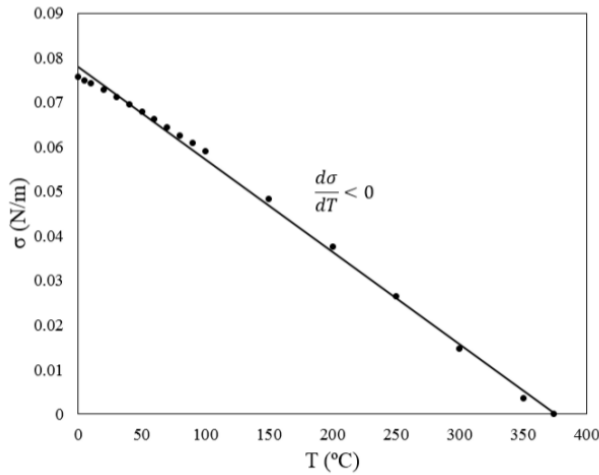


Figure 1.3: The interfacial tension between air and water decreases with an increasing temperature. This relationship can be approximated as a linear one. This image is from Karbalaei et al. (2016).



## 1.2 Overview of thermocapillary flow

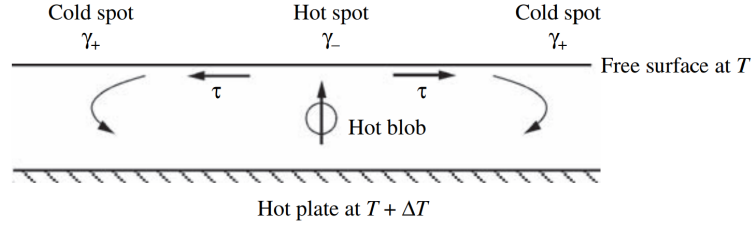


Figure 1.4: Fluid motion is induced in a thin liquid layer by temperature gradient perpendicular to the interface. This image is from Charru (2011).

Early studies on thermocapillary flow focus on the instabilities triggered by temperature inhomogeneity. According to whether the imposed temperature gradient is perpendicular or parallel to the interface, Davis (1987) classified these instabilities into (1) Marangoni instability (perpendicular) and (2) hydrothermal instability (parallel).

An example of the Marangoni instability, a thin liquid layer heated from below, is illustrated in Figure 1.4. Assuming a disturbance creates a hot spot on the interface, there is a net surface traction away from the hot spot, and as the fluid is viscous, fluid near the hot spot is dragged away. Thus an upflow beneath the hot spot is created due to mass conservation. The rising fluid coming from the warm end can maintain the heat excess at the hot spot given that the temperature gradient is large enough. The resulted convection, called the Marangoni-Bénard convection, was first observed by Bénard (1901). The dimensionless Marangoni number (to be defined later) is used to characterise the strength of the thermocapillary motion. Pearson (1958) conducted the first linear stability analysis on this problem and found the critical  $Ma$  number for the onset of the steady convection with different heating condition on the bottom boundary. In his paper, the interface was considered non-deformable and gravity was neglected. Following his work, two-layer system (Scriven and Sternling, 1960), buoyancy (Smith, 1966), and interface deformation (Davis, 1983; Davis and Homay, 1980) were taken into consideration. The post-instability behaviour was examined by nonlinear analysis (Clout and Lebon, 1984; Scanlon and Segel, 1967; Vanhook et al., 1997).

When a temperature gradient is imposed parallel to the interface, the cor-

## 1. INTRODUCTION

---

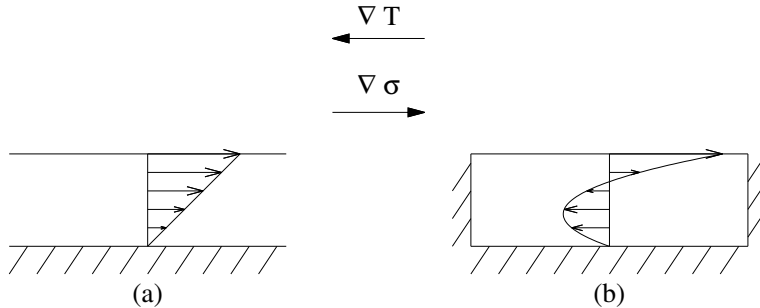


Figure 1.5: Sketches of the velocity profile for (a) linear-flow and (b) return-flow basic state.

responding surface tension gradient is created and tangential forces are induced along the interface. Smith and Davis (1983a,b) considered a two-dimensional thin liquid layer. Two basic states were obtained, the linear-flow of an infinite horizontal layer and the return-flow for a layer confined at both ends, as illustrated in Figure 1.5. Assuming a flat interface, two instabilities associated with the two basic states were identified: (1) the hydrothermal instability which grows in the form of propagation of waves; (2) the previously discussed Marangoni instability induced by the basic state in which temperature is higher at the bottom. With the interface deformation involved, a surface-wave instability was found. Subsequent investigations on such instabilities have been extended to the axisymmetric configuration such as a liquid bridge or a capillary jet. A liquid bridge is a liquid column held between two coaxial solid disks, and a capillary jet is a liquid column of infinite length. Xu and Davis (1983, 1984, 1985) revealed the appearance of hydrothermal wave in the two configurations.

The liquid bridge is a configuration simplified from the floating zone crystal growth process. Figure 1.6 illustrates schematically the full floating zone process and the half-zone liquid bridge configuration. The unprocessed materials pass through the ring heater, melts, and re-solidifies into a single crystal. As most impurities are more soluble in the melt than the crystal, the molten zone carries the impurities away with it, and the purity of the single crystal is significantly improved. The quality of the formed crystal highly depends on the homogeneity of the local temperature field and is affected by the thermocapillary motion.

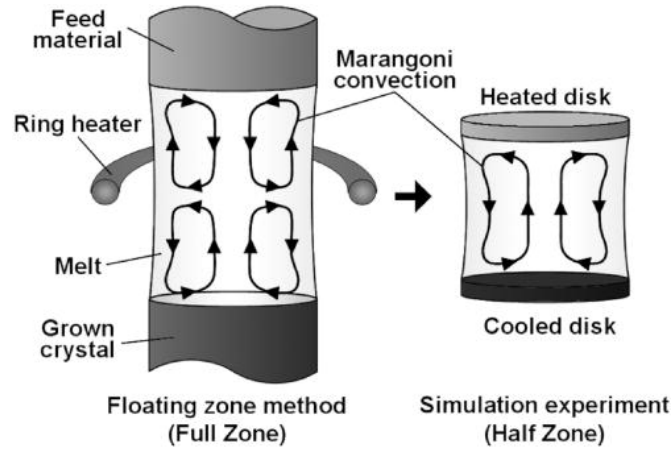


Figure 1.6: Illustration of the floating zone crystal growth process and the simplified half zone configuration (Kawamura et al., 2012). The indicated flow is induced by the interfacial tension gradient on the melt/gas interface.

The thermal-driven convective flow promotes the non-uniform dopant distribution and crystal striations, both of which degrade crystal quality (Anilkumar et al., 1993; Eyer and Leiste, 1985). Due to its application in crystal growth, the non-isothermal liquid bridge has been extensively investigated with the focus on the transition to the oscillatory convection state. A number of non-axisymmetric instabilities have been identified through linear stability analysis and numerical simulation (Kuhlmann and Rath, 1993; Rupp et al., 1989; Wanschura et al., 1995), and microgravity experiment were performed in space to exclude the influence of gravitational effect (Nakamura et al., 1998). For more details on analytical and experimental investigations of thermocapillary instabilities, the reader is referred to the reviews by Davis (1987) and Schatz and Neitzel (2001).

Thermocapillary instabilities are detrimental in the example of crystal growth, but they can be beneficial in some other applications. For instance, the interfacial tension gradient along the interface due to temperature variation can be used for controlled break-up of liquid jet or sheet. Nahas and Panton (1990) used a modulated laser to induce periodic temperature perturbation on the interface of a long cylindrical liquid thread and found that the onset of the classic Rayleigh-Plateau instability was delayed. Dijkstra and Steen (1991) studied the stabilising effect

## 1. INTRODUCTION

---

of thermocapillarity on the breakup of an annular film. Mashayek and Ashgriz (1995) conducted numerical investigation to study the competition between thermocapillary breakup and capillary breakup. A series of theoretical investigations on thermal-induced rupture of liquid sheet have been carried out by Bowen and Tilley (2012, 2013); Tilley and Bowen (2005). There are some more applied examples. For instance, Furlani and Hanchak (2011) proposed a design of an ink-jet printer with a heater at the nozzle such that a periodic temperature fluctuations is induced along jet interface; De Saint Vincent et al. (2015) applied a laser beam to destabilise liquid thread in a confined microchannel for the developing of a microfluidic flow focusing device.

A new contribution of this thesis is the investigation on the role played by the thermocapillary effect in the breakup of a liquid bridge. As explained before, this configuration is of great importance in the floating zone method, and its breakup also occurs in some applications such as welding. Furthermore, previous investigations on interface breakup with thermocapillary effect focused on a long thread subject to a periodic temperature variation. We expect that the effect of thermocapillary motion may be different in the breakup of a liquid bridge, as the liquid bridge is confined and the imposed temperature variation is linear.

### 1.3 Overview of interface-tracking methods

Numerical methods are important tools for investigating multiphase flows. The interface, the key feature of multiphase flows, causes considerable difficulties in numerical simulations. As it is constantly moving, the location of the interface is not known a priori and has to be determined as part of the solution. On the other hand, some physical phenomena at/across the interface are so important that the interface actively influences and sometimes dominates the bulk flow. The interface and the bulk flow are tightly coupled and a numerical method for multiphase flows has to address the three issues: (1). how to represent the interface? (2). how to describe the evolution of the interface? and (3). how to deal with the boundary conditions on the interface as well as the discontinuous physical properties?

### 1.3 Overview of interface-tracking methods

---

Various numerical methods have been developed to tackle the three issues. Depending on the relation between the interface and the computational mesh, we classify these methods into two categories: (1) the interface-conforming method where the interface is represented by lines of the mesh system; and (2) the non-conforming method where the interface intersects with mesh lines. The method presented in this thesis falls into the first category (Li, 2013), and some popular methods including front-tracking method, Volume of Fluid (VOF) method, Level-Set (LS) method and phase-field method (Ding et al., 2007; Scardovelli and Zaleski, 1999; Sussman et al., 1994; Tryggvason et al., 2001) belong to the second category. Those methods are illustrated schematically in Figure 1.7: (a) shows the interface-conforming method where the interface (red solid line) separates two phases drawn in blue and green respectively, while (b) and (c) shows two types of non-conforming methods: front-tracking and volume-tracking (or front-capture). In the schematic diagram for non-conforming method, the interface drawn in red line does not align with mesh lines drawn in blue.

The distinct difference between front-tracking and volume-tracking methods is that the interface is explicitly represented by a series of lines connecting marker points (black dots in Figure 1.7(b)) in front-tracking, while in volume-tracking such as VOF, LS and phase-field, the interface is implicitly captured through a marker function. The marker function in VOF and phase-field method is the volume fraction of one phase in each cell, and that in LS method is the level-set function representing the signed distance from the interface. Due to the implicit nature of volume-tracking method, evaluation of some geometric quantities such as interface curvature is not as straightforward as in front-tracking method. The principal advantage of implicit representation is that volume-tracking method can easily deal with severe deformations of the interface and is capable of handling interface topology changes automatically (Lafaurie et al., 1994; Zaleski et al., 1995). Some excellent multiphase simulations of atomization which involve large amount of interface topology changes were performed with volume-tracking methods (see the examples of VOF in (Chen et al., 2013) and LS in (Desjardins et al., 2008)).

In the interface-conforming method, the interface always coincides with lines of the mesh system and each cell (or element in finite element terminology) contains only one type of fluid, as shown in Figure 1.7(a). The computational mesh

## 1. INTRODUCTION

---

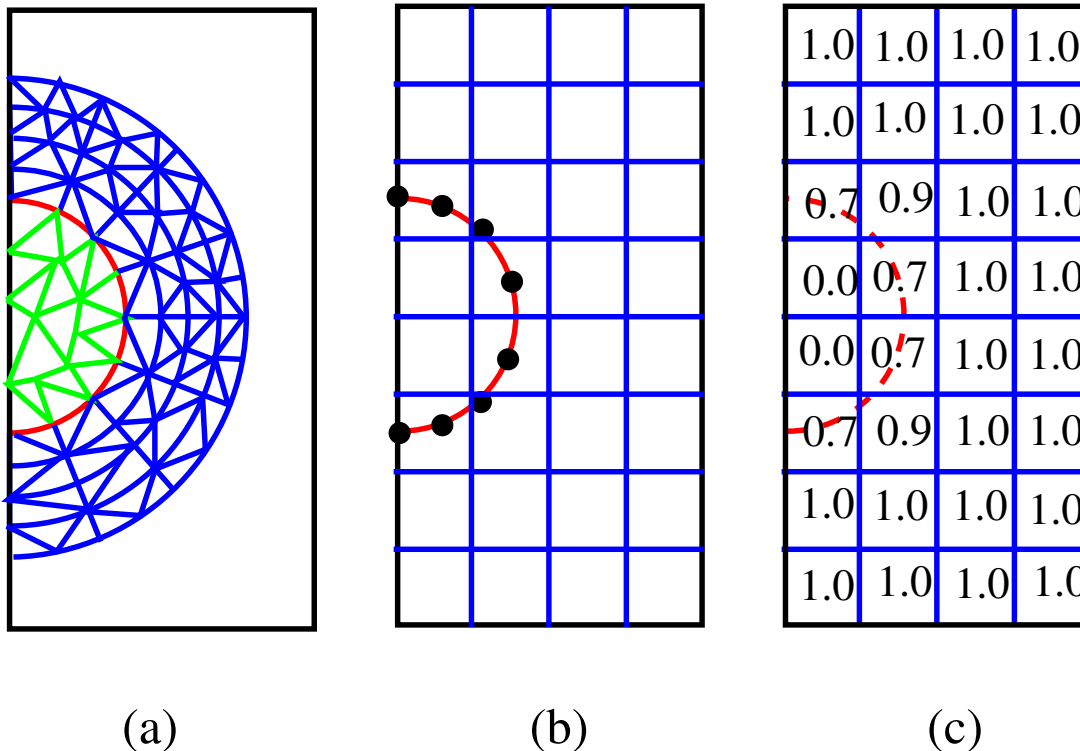


Figure 1.7: Schematics of different interface-tracking methods: (a) an interface-conforming method using an unstructured mesh; (b) a front-track method where the interface nodes are drawn in black dots; (c) a front-capture/volume-tracking method. The interface are all in red. The red solid line in (a) and (b) indicates that the interface is explicitly tracked, while the red dashed line in (c) indicates that the interface is implicitly captured through a marker function.

is updated constantly to follow the evolution of the interface. A robust mesh algorithm is required to maintain this interface-conforming mesh system (Bejanov et al., 2008; Li, 2013; Quan and Schmidt, 2007). The use of unstructured mesh enhances the flexibility for generating high-quality meshes. Note that the mesh in non-conforming methods can also be adaptive, for instance, the VOF solver Gerris (Popinet, 2003) and the phase-field method with adaptive meshing (Yue et al., 2006). Similar to front-tracking, the explicit representation of the interface requires explicit treatment of interface topology changes. Extra efforts are required on mesh manipulation to split and re-connect the interface (Cristini et al.,

### 1.3 Overview of interface-tracking methods

---

2001; Quan et al., 2009).

Although the practical implementation is technically difficult, the interface-conforming method possesses tremendous advantages in dealing with physics taking place at/across the interface. Firstly, as each cell/element of the mesh contains only one type of fluid, fluid properties like density and viscosity are well defined in each cell. The discontinuity of fluid properties across the interface is then resolved exactly. By contrast, in non-conforming methods, fluid properties are not clearly defined in cells intersected by the interface and have to be approximated. When the ratio of fluid properties is very large, this approximation is highly inaccurate. This will not cause a problem under most circumstances. However accurate representation of fluid properties is crucial in some cases. For example in the lubrication flow within the air film between two colliding droplets, the usual averaging operation leads to a gross over-estimation of the viscosity and hence of the lubrication force. As a consequence, the non-conforming method might predict a wrong outcome of droplet collision (Li, 2016). Secondly, thanks to the explicit representation of the interface, geometrical quantities such as the unit normal vector and curvature are calculated directly similar to front-tracking method. Finally, the force balance condition on the interface can be incorporated naturally into finite volume or finite element formulations in conforming methods (Li, 2013; Li et al., 2005). The numerical discretization is simply an evaluation of a boundary integral and can be calculated accurately. In contrast, the numerical implementation of the force balance condition is not as straightforward in the non-conforming method. The interfacial tension is often modelled by the Continuum Surface Force (CSF) method (Brackbill et al., 1992) in which the interfacial tension is interpreted as a continuous effect across the interface rather than as a boundary condition.

A frequently encountered issue in multiphase flow simulation is the spurious currents, which are mainly induced by the inaccuracy in the numerical implementation of the force balance condition on the interface. The numerical imbalance on the interface keeps feeding energy into the system and can not be damped by viscous and/or numerical dissipation in some cases where the interfacial tension is dominantly strong. Consequently, the numerical simulation may stop prematurely. The non-physical velocities are best illustrated with the example of a

## 1. INTRODUCTION

---

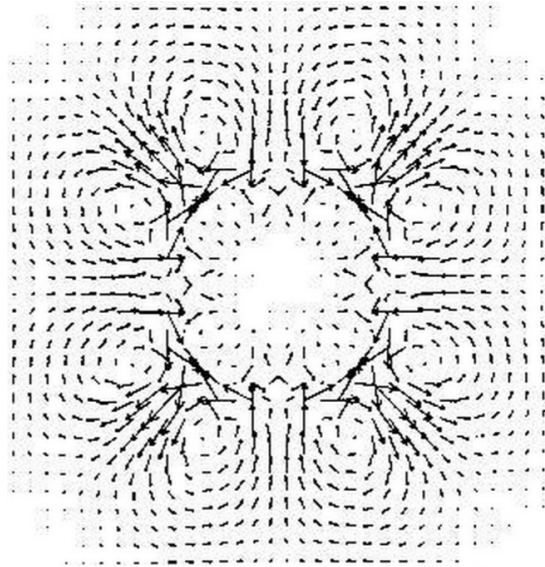


Figure 1.8: Spurious currents around a circular bubble in a VOF simulation. The image is from Popinet and Zaleski (1999)

circular/spherical droplet in equilibrium without external forcing. They appear as vortices near the droplet interface as illustrated in Figure 1.8 and can not be reduced with spatial refinement. As a result, the static Laplace solution which is seemingly trivial can not be obtained numerically. Popinet and Zaleski (1999) made a correction on the pressure gradient calculation by taking account of the pressure jump across the interface in a front-tracking method. The modified method achieved very accurate results and the spurious current was reduced in the Laplace drop test. Another remarkable work in reducing spurious current was carried out by Renardy and Renardy (2002). Aiming to achieve the discrete balance between the interfacial tension and the pressure jump, they dedicated great efforts on improving the flow solver, curvature estimation and the approximation of the interface shape. The spurious currents were effectively reduced in their improved VOF method. The key to these successes in reducing spurious currents is to obtain the discrete balance between the interfacial force and the associated pressure jump. A series of work have recently been carried out with the aim to recover such balance numerically (Abadie et al., 2015; Francois et al., 2006; Herrmann, 2008; Popinet, 2009). The recent progress of interface non-conforming



### 1.3 Overview of interface-tracking methods

---

methods on surface tension modelling was summarised by Popinet (2018). To the best of our knowledge, there are few in-depth studies of spurious currents for the interface-conforming methods.

Although a number of numerical methods for multiphase flows have been developed and well validated, there are many multiphase flow problems still challenging to solve. One such challenge is the flow within the inter-droplet gas film during the head-on collision of two droplets. Experimental observations have exhibited the important role this gas film plays in determining whether the outcome of head-on collision is bounce or coalescence (Qian and Law, 1997). During the entire course of coalescence of droplet with radius  $\sim 100 \mu\text{m}$ , the flow within the gas film experiences a wide range of flow regimes, from continuum lubrication flow, to rarefied flow, and to intermolecular flow where the van der Waals force dominates and the rupture of the gas film takes place. This requires the numerical method not only include modelling of the rarefied gas effects and van der Waals force, but also to resolve all length scales involved, spanning a range from larger than the droplet size ( $> 10^{-4}$  m) to length scale where intermolecular forces prevail ( $\sim 10^{-8}$  m). It is not yet feasible to capture all length scales in an non-conforming method even with excessive mesh refinement. The automatic handling of interface topology change may lead to a false predict of the collision outcome or collision instant. In a few attempts using VOF and LS, whether and when droplet coalescence takes place were determined artificially by an empirical parameter or model (Kwakkel et al., 2013; Pan et al., 2008). The numerical study of Li (2016) using interface-conforming method successfully simulated this problem without introducing any adjustable parameters. Lack of numerical treatment for interface topology changes, only droplet collision with a bounce outcome was simulated. However the fact that their method accurately resolves 6 orders of magnitude of length scales with no artificial parameters demonstrates the robustness of their method and the advantage of interface-conforming method in this problem.

The numerical method in this thesis is an interface-conforming method. It is based on the method developed through a series of publications by Étienne et al. (2006) and Li (2013, 2016). The mesh lines conforms the interface all the time, and an adaptive mesh generator is employed to satisfy this condition. The

## 1. INTRODUCTION

---

popular Taylor-Hood  $P2 - P1$  element is used for finite element discretization. The conventional approach that the pressure is continuous all over the domain ( $P1 - C0$ ) is sufficient for single-phase flow or free-surface flow as in Étienne et al. (2006), but not for multiphase flows due to the pressure jump on the interface. Li (2013) introduced a new element space for pressure discretization, called the  $P1d$  element space, such that the pressure has one value in the bulk fluid, double values on the interface and triple value on triple junction points where three interfaces intersect. This novel element space has been validated in three-phase simulations and has been applied to the simulation of binary droplet collisions with a bounce outcome. We further verify the capability of the method in accurately representing the force balance condition on the interface in this thesis.

The aim of this thesis is first to develop an accurate numerical method for simulating two-dimensional/axisymmetric non-isothermal multiphase flows, and then to apply the method to study the break-up of liquid bridge with the thermocapillary effect. For this purpose, we require a robust treatment of interface topology changes and an accurate numerical implementation of thermocapillary flow. The numerical development will be detailed in later chapters.

### 1.4 Thesis outline

The remainder of this thesis is structured into six chapters:

In Chapter 2, the adaptive mesh generator is introduced. It is the foundation of our numerical method. This mesh generator developed by Li (2013) is designed to produce a high-quality unstructured mesh specifically for multiphase flows. It enables us to generate mesh according to the need and provides us with full control of the mesh.

In Chapter 3 we present the basics of finite element methods (FEM) through the example of a Poisson solver. Both theoretical aspect and practical implementation of FEM are detailed. This chapter ends with the evaluation of the accuracy of an FEM Poisson solver.

Chapter 4 illustrates the numerical procedures in developing an FEM solver for the incompressible Navier-Stokes (NS) equations. The finite element formula-

tion and discretisation are presented in detail. The discretised NS equations are solved with the *uzawa* method (Glowinski and Le Tallec, 1989) on an adaptive moving mesh. The interfacial tension is treated as a boundary integral. We prove that our method achieves the discrete force balance on the interface on the circular/spherical interface. The accuracy of our method is then examined through two benchmark examples: the static Laplace solution of a spherical/circular droplet and the axisymmetric oscillation of a droplet/bubble.

In Chapter 5 we develop an algorithm to split and re-connect the interface. Using the adaptive mesh generator, we incorporate this algorithm seamlessly into the finite element code. Two completely different examples involving interface topology changes are used to validate our numerical implementation: droplet formation from a faucet and coalescence in binary droplet collision. The accuracy of our numerical method and the robustness of our adaptive mesh generator are also tested in this chapter.

Chapter 6 is dedicated to non-isothermal multiphase flows. An FEM solver for temperature is added into the existing NS solver and our method is extended to include thermal-driven buoyancy force and thermocapillarity. The modifications are validated using three benchmark tests: natural convection in a square cavity, thermocapillary convection in two layers, and droplet migration subject to a vertical temperature gradient. The method is then applied to study the effect of thermocapillary flow on the break-up of a liquid bridge.

Chapter 7 concludes the thesis with main findings and potential future work.

## 1. INTRODUCTION

---

# Chapter 2

## Mesh generator

The interface is the key factor in numerical simulation of multiphase flows. In interface-conforming method such as ours, the interface always coincides with boundaries of elements. The mesh is required to be constantly adjusted to follow the interface evolution. Hence, maintaining a valid and high-quality mesh is the cornerstone for the success of our numerical method.

There are many excellent mesh generator available, such as BAMG (Hecht, 1998), GRUMMP (Ollivier-Gooch, 2010), Gmsh (Geuzaine and Remacle, 2009) and Triangles (Shewchuk, 1996). These mesh softwares allow the prescription of boundary position, but not the vertices on the boundaries. This could lead to a problem for multiphase flow: the vertices on the interface boundary are not the same for both sides. In order to have full control over the computational mesh, our in-house adaptive mesh generator has been developed by Li (2013). In this chapter, the mesh generator is detailed: we start with operations performed on the mesh and in the second part, the principles for mesh manipulation are presented.

### 2.1 Moving mesh and local re-arrangement

In an interface-conforming method, the mesh is adapted to the interface at each time step. Two strategies are possible to realise this, either completely remeshing occasionally or locally re-arranging constantly. The former seems more computationally efficient, but its shortcoming is that too many interpolations

## 2. MESH GENERATOR

---

would take place at one instance. This will lead to a slightly large deviation from the pre-interpolation velocity field. Therefore the accuracy of the numerical method is undermined. To avoid this, we choose to constantly re-arrange the mesh such that a moderate number of remesh operations occur at each instance.

We employ an unstructured mesh in our method. The difference from a structured one is the irregular connectivity between elements. This leads to high space inefficiency as the connectivity information between elements is stored explicitly. However, unstructured meshes are more flexible and can fit complicated boundaries, making the treatment of boundary conditions very simple and accurate. The triangular element is chosen in our method since it is the simplest element.

The vertex on the interface moves with its actual velocity while most interior vertices stay fixed. As the interface evolves, the new positions of interface vertices are computed in a Lagrangian manner:

$$\mathbf{x}^{n+1} = \mathbf{x}^n + \mathbf{u}^n(\mathbf{x}^n)\Delta t, \quad (2.1)$$

in which  $\mathbf{x}$  and  $\mathbf{u}$  denote position and velocity of a vertex,  $\Delta t$  is the time step and the superscript represents time level of  $\mathbf{u}$  and  $\mathbf{x}$ . An example of interface mesh movement is shown in Figure 2.1(a) where the interface nodes are drawn in red and their tracks are in green.

After the interface is updated, triangulation near the interface becomes distorted, as illustrated in Figure 2.1(b). To improve this, we re-locate interior nodes via Laplacian smoothing. This technique adjusts the location of a vertex  $\mathbf{q}$  to the arithmetic mean of its adjacent vertices:

$$\mathbf{q} = \frac{1}{N} \sum_{i=1}^N \mathbf{p}_i, \quad (2.2)$$

in which  $\mathbf{p}_i$  is the coordinate of the  $i$ -th adjacent vertex of  $\mathbf{q}$  and  $N$  is the number of adjacent nodes of vertex  $\mathbf{q}$ . This smoothing technique is applied vertex by vertex, and in practice, we repeat this process 10 times in one smoothing step. The Laplacian smoothing can avoid the occurrences of acute triangles and produce a high-quality mesh as shown in Figure 2.1(c).

## 2.1 Moving mesh and local re-arrangement

---

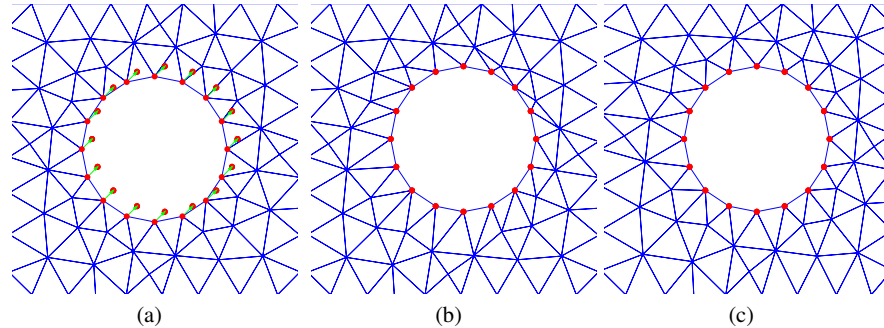


Figure 2.1: Examples of mesh moving and smoothing: the mesh is drawn as blue solid lines and the interface nodes are drawn as red circular nodes: (a) the interface nodes move to their new position in a Lagrangian manner with green arrows representing their tracks; (b) the interface has been updated while some triangles near the interface become distorted; (c) the quality of the triangulation is improved through smoothing.

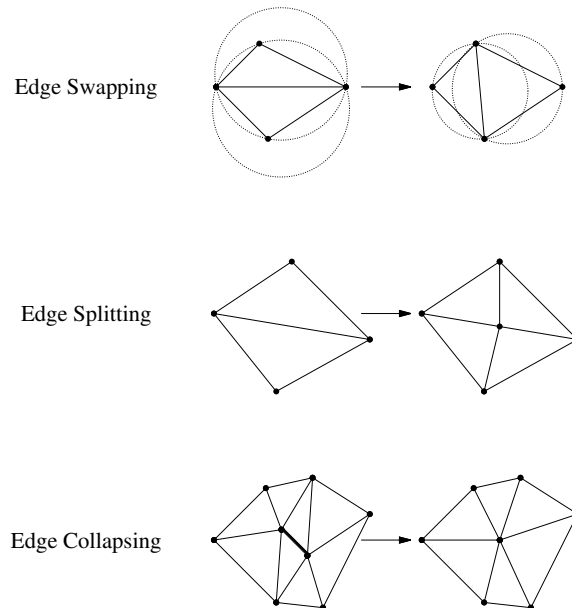


Figure 2.2: Schematics of three basic local remesh operations: edge swapping (top), edge splitting (middle) and edge collapsing (bottom). In the collapsing sketch, the collapsed edge is drawn as a thick solid line.

## 2. MESH GENERATOR

---

Apart from smoothing, three other operations are available to improve mesh quality, namely edge swapping/splitting/collapsing. These are local mesh arrangement and involve changes in the mesh topology. The schematics of the three operations are drawn in Figure 2.2.

Edges not on the interface are swapped based on the *Delaunay condition* (Bern and Plassmann, 1999) to avoid sliver triangles. If a vertex lies within the circumcircle (dotted lines in the top panel of Figure 2.2) of another triangle, the common edge of the two triangles is then swapped to another position. To preserve a valid interface definition, edge swapping is not performed on interface edges.

Edge splitting/collapsing are used to refine/coarsen the mesh as shown in the middle and bottom panel in Figure 2.2. To keep the interface topology, we do not perform edge collapsing on edges which connect two separate interfaces. When an edge on the interface is split into two, the new position of the new vertex is calculated by a local spline algorithm (Dritschel, 1988) in order to preserve the smoothness of the interface.

To determine whether edge splitting/collapsing should proceed, a quantitative description of mesh quality is necessary, which is presented in the next section.

### 2.2 Adaptive mesh principles

Our numerical method is designed for multiphase flows where the surface tension plays an important role. Thus we must resolve areas near interface with sufficiently fine mesh when generating computational mesh. Meanwhile, regions which are far away from the interface are less demanding in mesh resolution. Applying a coarser mesh in these regions can significantly reduce the overall computing costs. In this section, we introduce rules that our mesh generator must follow to meet the above requirements.

Like many previous authors (Freitag and Ollivier-Gooch, 1997; Yue et al., 2006; Zheng et al., 2005), we introduce a local characteristic length scale  $l_s$  as the desirable mesh size at each vertex of the mesh. On the interfaces,  $l_s$  at a vertex



## 2.2 Adaptive mesh principles

---

$\mathbf{q}$  is defined to be proportional to the inverse of the local interface curvature  $\kappa$ :

$$l_s(\mathbf{q}) = \frac{\alpha}{\kappa(\mathbf{q})}, \quad (2.3)$$

in which  $\alpha$  is the mesh scale, a constant controlling the mesh quality on the interface. This formulation ensures a decent mesh resolution at high-curvature regions near the interface, where the surface tension force is strong. The evaluation of  $\kappa(\mathbf{q})$  is explained later. To guarantee that a flat interface can still be resolved by a sufficient number of points, we set a maximum  $l_{interface}$  for nodes on the interface. Then  $l_s$  for vertex  $\mathbf{q}$  on the interface is rewritten as:

$$l_s(\mathbf{q}) = \min\left(\frac{\alpha}{\kappa(\mathbf{q})}, l_{interface}\right). \quad (2.4)$$

We can set  $l_s$  flexibly on other boundaries according to need in a similar manner, for instance a curved wall boundary or inlet/outlet boundaries.

To control the mesh between two interfaces or other types of boundaries, the distance  $l_d$  between vertices on two different boundaries is taken into consideration:

$$l_s(\mathbf{q}) = \min(l_s, \beta l_d(\mathbf{q})), \quad (2.5)$$

where  $\beta$  is a constant,  $l_s$  is from equation (2.4) and  $l_d(\mathbf{q})$  is the minimum distance from vertex  $\mathbf{q}$  on the interface to all vertices  $\mathbf{p}$  on another interface or boundary.

The length scale function is then extended to all vertices: for a given vertex  $\mathbf{q}$  in the mesh,  $l_s(\mathbf{q})$  must satisfy:

$$l_s(\mathbf{q}) \leq l_s(\mathbf{p}) + G|\mathbf{q} - \mathbf{p}|, \quad (2.6)$$

in which  $G$  is a constant, called the mesh size gradient and  $|\mathbf{q} - \mathbf{p}|$  is the distance between the two vertices. This formulation allows mesh size to grow exponentially with distance from the interface so that the total number of vertices is reduced. A fast marching algorithm (Sethian, 2001) is used to realise this condition starting from vertices with the smallest length scale, normally interface vertices with high curvature.

To prevent mesh from becoming over-refined or under-refined,  $l_s$  is restrained by the global maximum and minimum mesh size:

$$l_{min} \leq l_s \leq l_{max}. \quad (2.7)$$

## 2. MESH GENERATOR

---

With  $l_s$  defined for every vertices in the computational domain, the desired length scale of an edge is taken as the average  $l_s$  of its two vertices. We require that the actual length  $l$  of an edge satisfy the condition:

$$r_{min} \leq \frac{l}{l_{s,edge}} \leq r_{max}, \quad (2.8)$$

where the  $r_{max}$  and  $r_{min}$  are the maximum and minimum ratios allowed: edge collapsing (*or* splitting) is performed when the ratio is smaller than  $r_{min}$  (*or* greater than  $r_{max}$ ). In practice, it is found that  $r_{min} = 1.0$  and  $r_{max} = 2.8$  work well to produce mesh with minimum angle  $\geq 20^\circ$ , except probably triangles in thin gaps between two interfaces.

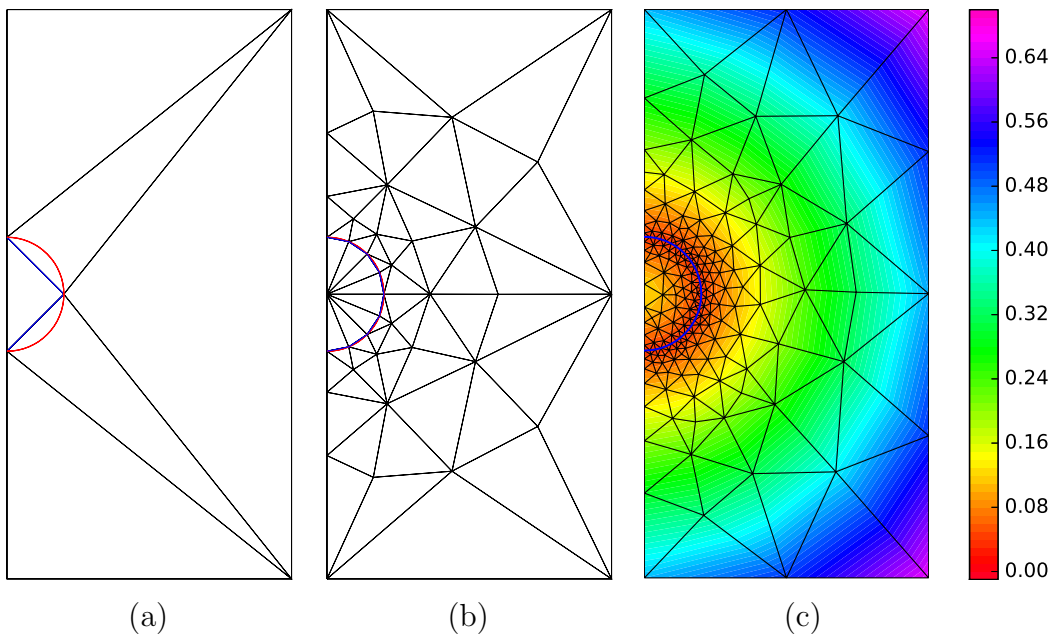


Figure 2.3: The aimed interface is a circle depicted in red solid line while the interface edges are drawn in blue solid line: (a) shows the initial mesh; (b) is the mesh after several refinement steps; (c) illustrates the final mesh and the contour of the mesh size density  $l_s$ .

With these rules, it is sufficient to generate a desired mesh for a given configuration. Figure 2.3 illustrates an example of mesh generation from the simplest configuration for a circular interface of radius 1 within a rectangular box of size

## 2.2 Adaptive mesh principles

---

$5 \times 10$ . In this example,  $\alpha = 0.05$  and  $G = 0.2$ . Initially, the interface only consists of two edges (blue solid lines in Figure 2.3(a)), while the expected circular interface is drawn in red solid lines. We first determine  $l_s$  on interface vertices using equation (2.4) and then determine  $l_s$  on interior vertices using equation (2.6). The mesh is then refined through edge swapping/splitting/collapsing. The interface is refined by more edges, for example 8 edges in Figure 2.3(b). This process does not stop until the desired mesh is achieved as shown in Figure 2.3(c).

By varying  $\alpha$  we can obtain meshes with different resolutions. We take the above mesh with a circular interface for example. The number of interface edges  $N_{interface}$  and the total number of vertices  $N_{total}$  are documented in Table 2.1, together with the corresponding mesh scale  $\alpha$  and mesh size gradient  $G$ . As shown in the table,  $N_{interface}$  is generally proportional to the inverse of  $\alpha$ . We plot  $N_{total}$  against  $1/\alpha$  in Figure 2.4, with  $G$  fixed at 0.2. The total number of vertices is found to increase linearly with the inverse of  $\alpha$ : the data from the table drawn as circular point almost all fall onto the dotted line representing  $1.6/\alpha$ .

Table 2.1: Mesh scale  $\alpha$  and the corresponding mesh vertices number

$\alpha$	$G$	$N_{interface}$	$N_{total}$
0.1	0.2	16	114
0.05	0.0	32	3417
0.05	0.1	32	381
0.05	0.2	32	207
0.025	0.2	64	381
0.0125	0.2	128	764
0.00625	0.2	256	1521

The mesh size gradient  $G$  enables us to simulate a large domain at a relatively smaller computing costs. When  $G = 0$ , the mesh is almost uniform everywhere within the computational domain. As shown in Table 2.1, increasing  $G$  from 0 to 0.1 reduces the total number of vertices significantly by nearly 90% while the interface is still resolved by 32 edges. A mesh with a relatively larger  $G$  is coarse everywhere except in regions near the interface. Practically the choice of  $G$  is

## 2. MESH GENERATOR

---

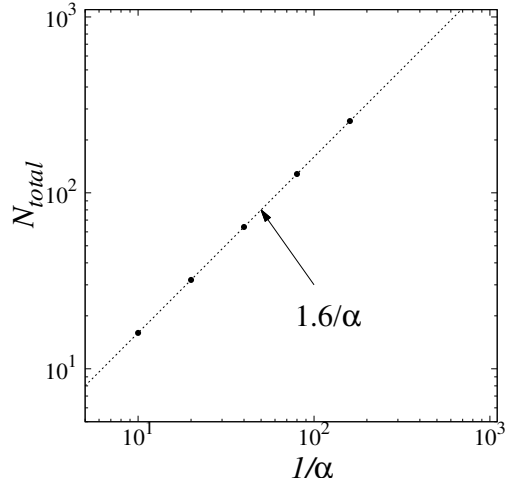


Figure 2.4: Data in Table 2.1 is drawn in black circular point with mesh size gradient  $G$  kept at 0.2. The dotted line is  $1.6/\alpha$  and the data point are almost all on the dotted line.

between 0.15 and 0.25 such that the computing costs are reduced without loss in simulation fidelity.

The constant  $\beta$  in equation (2.5) is an important mesh parameter especially when two boundaries get very close. For instance, Figure 2.5 shows the computational mesh used in a simulation of the head-on collision of two droplets with equal size. Due to symmetry, only half of the domain is simulated. The bottom boundary is the symmetry boundary while the red solid line represents the interface. One distinctive feature of this mesh is that there are only one layer of triangles (see the close-up in Figure 2.5) to model the thin gas film between the two boundaries. In this example, the distance  $d$  between the two boundaries are used to control the desired length scale  $l_s$  through equation (2.5). Since the interface is very flat (small curvature), curvature on the interface has little influence on  $l_s$  according to equation (2.4). If  $\beta$  is chosen to be a number large enough, for instance  $\beta = 1/2$ , according to equation (2.8), edges shorter than  $r_{min}l_s = \beta d > 1/2d$  are collapsed. Hence there will be no edge shorter than  $d$  between the two boundaries and we manage to achieve only one layer of triangles in the gap of two boundaries.

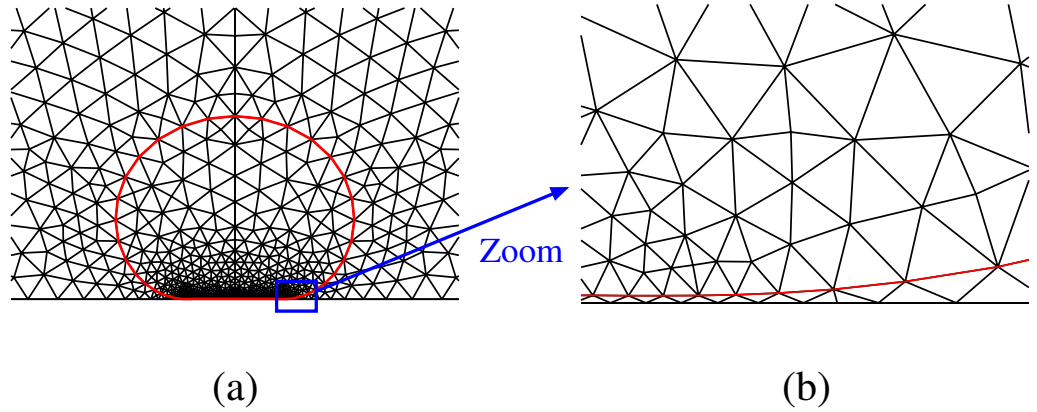


Figure 2.5: Example of a single-layer triangles between two boundaries: (a) shows the mesh of a colliding droplet above the symmetry plane. The red solid line represents the air-droplet interface, and the black solid lines the computational mesh. (b) is the close-up of the mesh in a region within the lubrication layer where triangles are small within the gap.

In our simulation, we frequently use  $\beta = 2$  and then only edges of length larger than  $r_{max}\beta d = 5.8d$  are split, resulting in very slim triangles in the gap regions. The thin gap regions between interfaces are in general lubrication layers (Zhang and Law, 2011), where the velocity profile is parabolic and can be resolved exactly by second-order polynomial (in our method, velocity is quadratic in the element). Hence the use of one layer of slim triangles can avoid over-fined mesh and significantly enhance the efficiency of the method.

Another advantage of keeping a single layer of triangles between the two interfaces is that it make topology changes of the interface easier to implement. How the mesh generator handles interface topology change is discussed in Chapter 5.

## 2. MESH GENERATOR

---

# Chapter 3

## Basics of finite element method

The governing equations for fluid flow and heat transfer are a set of partial differential equations (PDEs). In most cases, it is not possible to find an analytical solution to these PDEs. This is particularly so for nonlinear PDEs on an irregular domain with complicated source terms and boundary conditions, as commonly seen in engineering applications. If the solution cannot be obtained in closed form, we approximate the solution with numerical techniques. The finite element method (FEM) is a flexible and powerful technique to find numerical solutions to PDEs. It is based on the weak formulation of PDEs. To obtain the weak formulation, we multiply a test function on both sides of a PDE and integrate it over the whole domain. The weak formulation can be transformed into algebraic equations through finite element discretisation and then solved numerically. In this chapter, we illustrate the basics of FEM through an example: the numerical solution of a Poisson equation. We start with the theory of FEM, then move on to the practical implementation and conclude this chapter with a numerical test of Poisson solver.

### 3.1 Theory of FEM

We consider a Poisson equation:

$$-\nabla \cdot (k\nabla u) = f \quad \text{in } \Omega, \quad (3.1)$$

### 3. BASICS OF FINITE ELEMENT METHOD

---

with boundary conditions:

$$u = g \quad \text{on} \quad \partial\Omega_D, \quad (3.2a)$$

$$\partial u / \partial n = h \quad \text{on} \quad \partial\Omega_N, \quad (3.2b)$$

in which  $u, f, k, g$  and  $h$  are scalar functions,  $\Omega$  is a bounded open domain,  $\partial\Omega_D$  is the Dirichlet boundary, and  $\partial\Omega_N$  is a Newman boundary, as illustrated in Figure 3.1. Note that  $\partial\Omega_N = \partial\Omega \setminus \partial\Omega_D$ .

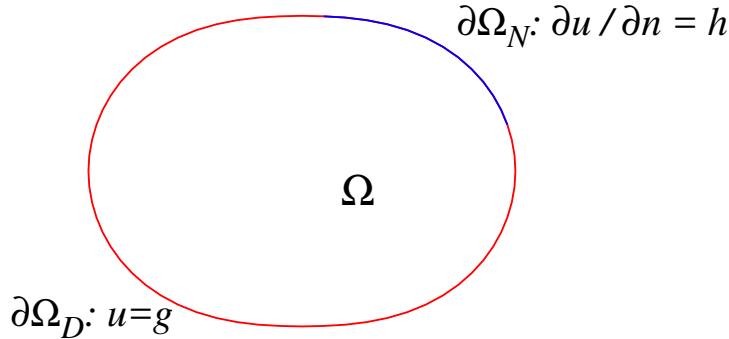


Figure 3.1: Example of domain  $\Omega$  and two types of boundaries  $\partial\Omega_N$  (drawn in blue) and  $\partial\Omega_D$  (drawn in red).

#### 3.1.1 Weak formulation

We first multiply equation (3.1) with a test function  $v$  and then integrate it over  $\Omega$ :

$$\int_{\Omega} -\nabla \cdot (k\nabla u) v d\Omega = \int_{\Omega} DV D\Omega. \quad (3.3)$$

Next, we use the product rule on the left hand side:

$$\int_{\Omega} (-\nabla \cdot (kv\nabla u) + k\nabla u \cdot \nabla v) d\Omega = \int_{\Omega} f v d\Omega. \quad (3.4)$$

By applying the divergence theorem onto the first term in the left hand side of equation (3.4), we obtain:

$$\int_{\partial\Omega} -kv \frac{\partial u}{\partial n} dl + \int_{\Omega} k\nabla u \cdot \nabla v d\Omega = \int_{\Omega} f v d\Omega. \quad (3.5)$$



The boundary integral in the above equation (3.5) can be split into:

$$- \int_{\partial\Omega_D} kv \frac{\partial u}{\partial n} dl - \int_{\partial\Omega_N} kv \frac{\partial u}{\partial n} dl. \quad (3.6)$$

The test functions are chosen so that  $v$  is zero on Dirichlet boundaries, and thus the first term of the above equation vanishes. While on the Neumann boundary,  $\partial\Omega_N$ ,  $\partial u/\partial n = h$  according to equation (3.2b). To summarise, the weak formulation has the form below:

$$\int_{\Omega} k \nabla u \cdot \nabla v d\Omega = \int_{\Omega} f v d\Omega + \int_{\partial\Omega_N} k h v dl. \quad (3.7)$$

Equation (3.1) suggests that the solution  $u$  should be twice differentiable, while equation (3.7) only involves the first derivative of  $u$ . For this reason, equation (3.7) is called as the weak form of the original PDE. The arbitrariness of the test function is essential in the weak form. If the weak formulation holds for all test functions from a sufficiently large set, then equation (3.1) must hold. For more mathematical theories about the weak formulation, the reader is referred to Gockenbach (2006).

### 3.1.2 Galerkin finite element method

FEM is generalised from the classical variational and weighted-residual methods (Reddy and Gartling, 2010). These methods are based on the idea that the solution  $u$  can be represented as a linear combination of unknown parameters  $c_i$  and appropriately selected functions  $\phi_i$  in the entire domain. The function  $\phi_i$ , called the approximation functions, are selected to satisfy the boundary conditions. The parameters  $c_i$  are determined such that the PDE holds, often in a weighted-integral sense, e.g. the weak formulation holds. The shortcoming is that  $\phi_i$  can be difficult to construct due to the complex boundary conditions and geometry in real-world problems.

The basic idea of FEM is to view the domain as a collection of “simple sub-domains”, or called *finite elements*. In this way, it is possible to construct the approximation function for arbitrary boundary conditions. In our method, triangular elements are used. Figure 3.2 shows an example of triangulation in domain  $\Omega$ .

### 3. BASICS OF FINITE ELEMENT METHOD

---

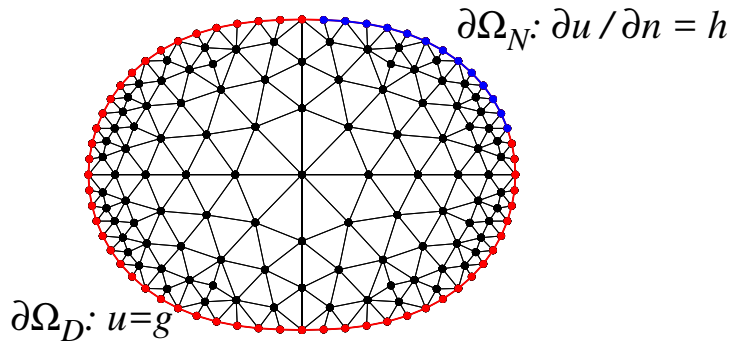


Figure 3.2: Finite element triangulation of domain  $\Omega$ .

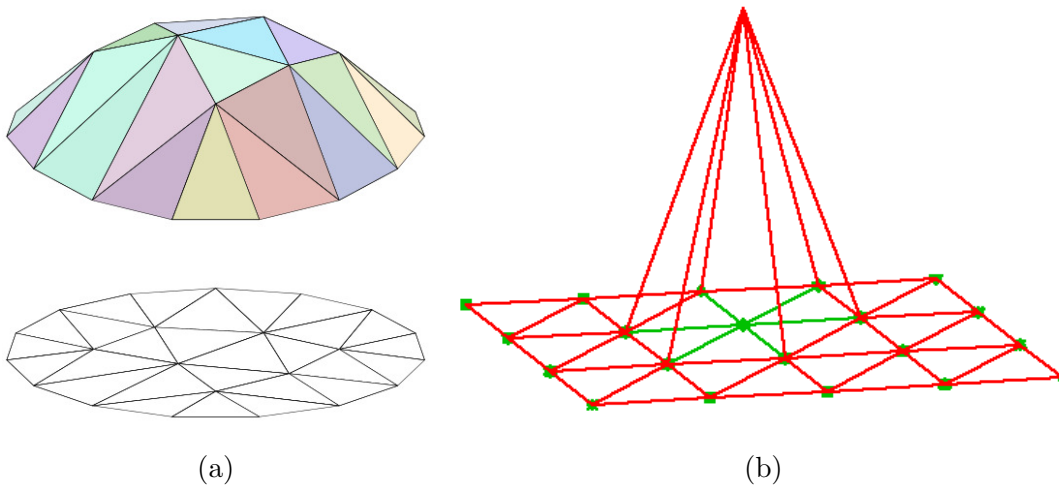


Figure 3.3: (a) A piecewise linear approximation. This image is from [https://en.wikipedia.org/wiki/Finite\\_element\\_method](https://en.wikipedia.org/wiki/Finite_element_method); (b) A “tent-like” basis function  $\phi_i$ . This image is from [http://hplgit.github.io/INF5620/doc/notes/fem-sphinx/main\\_fem.html](http://hplgit.github.io/INF5620/doc/notes/fem-sphinx/main_fem.html).

In each element, the solution to the weak formulation is approximated by low-degree polynomials. The simplest of them are functions which are piecewise linear and continuous as shown in Figure 3.3(a). If  $\mathbf{x}_i$ ,  $i = 1, \dots, N$ , are nodes of the triangulation, then a “tent-like” basis function  $\phi_i$  can be defined associated with it. As drawn in Figure 3.3(b),  $\phi_i$  is linear in elements containing  $\mathbf{x}_i$  and

vanishes outside these elements. Hence  $\phi_i$  satisfies the below condition:

$$\phi_i(x_j, y_j) = \delta_{ij} = \begin{cases} 1 & i = j \\ 0 & i \neq j \end{cases}. \quad (3.8)$$

The solution  $u$  is approximated as:

$$u \approx \sum_{i=1}^N u_i \phi_i(x, y), \quad (3.9)$$

in which  $N$  is the total number of nodes and  $u_i$  is the approximate solution at node  $i$ .

In the Galerkin finite element method, we choose the test function  $\phi_j$ ,  $j = 1, \dots, N$ , the same as the basis functions. The weak formulation equation (3.7) is turned into:

$$\sum_{i=1}^N A_{ij} u_i = \sum_{i=1}^N M_{ij} f_i + g_j, \quad (3.10)$$

where

$$A_{ij} = \int_{\Omega} k \nabla \phi_j \cdot \nabla \phi_i d\Omega, \quad M_{ij} = \int_{\Omega} \phi_j \phi_i d\Omega, \quad g_j = \int_{\partial\Omega_N} k \phi_j h dl. \quad (3.11)$$

By varying  $j$  from 1 to  $N$  (but excluding  $N_D$  Dirichlet boundary nodes), we obtain a system of  $N_u$  ( $N_u$  is the number of unknown values and  $N_u + N_D = N$ ) algebraic equations, written in matrix form:

$$\mathbf{A}\mathbf{u} = \mathbf{M}\mathbf{f} + \mathbf{g}. \quad (3.12)$$

The matrix  $\mathbf{A}$  is called the stiffness matrix,  $\mathbf{M}$  is called the mass matrix and their dimensions are both  $N_u \times N_u$ . The vector  $\mathbf{u} = (u_1, u_2, \dots, u_N)^T$  is the solution vector and  $\mathbf{f} = (f_1, f_2, \dots, f_N)^T$  is the load vector. Note that matrix  $\mathbf{A}$  and  $\mathbf{M}$  are both sparse, as  $A_{ij}$  and  $M_{ij}$  are only non-zero when the node  $j$  is adjacent to node  $i$ . The  $j$ -th element of vector  $\mathbf{g}$  is only non-zero when node  $j$  is located on the Neumann boundary. We rearrange the order of elements in vector  $\mathbf{u}$  such that the unknown values are listed first, followed by the known values at Dirichlet boundary nodes:  $\mathbf{u} = (\mathbf{u}_u^T \ \mathbf{u}_D^T)^T$  in which the dimensions of  $\mathbf{u}_u$  and  $\mathbf{u}_D$  are  $N_u \times 1$  and  $N_D \times 1$  in respect. Correspondingly, we rearrange the

### 3. BASICS OF FINITE ELEMENT METHOD

---

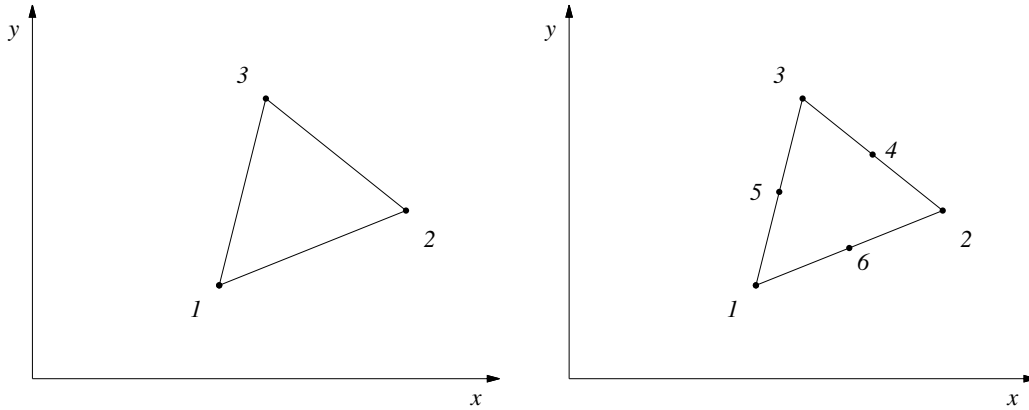
matrix  $\mathbf{A} = (\mathbf{A}_{uu} \ \mathbf{A}_{uD})$  where the dimensions of  $\mathbf{A}_{uu}$  and  $\mathbf{A}_{uD}$  are  $N_u \times N_u$  and  $N_u \times N_D$ , respectively. Equation (3.12) becomes:

$$(\mathbf{A}_{uu} \ \mathbf{A}_{uD}) \begin{pmatrix} \mathbf{u}_u \\ \mathbf{u}_D \end{pmatrix} = \mathbf{A}_{uu}\mathbf{u}_u + \mathbf{A}_{uD}\mathbf{u}_D = \mathbf{M}\mathbf{f} + \mathbf{g}. \quad (3.13)$$

Moving the term  $\mathbf{A}_{uD}\mathbf{u}_D$  to the right hand side, we eventually obtain  $\mathbf{A}_{uu}\mathbf{u}_u = \mathbf{M}\mathbf{f} + \mathbf{g} - \mathbf{A}_{uD}\mathbf{u}_D$ , a system of  $N_u$  linear equations with  $N_u$  unknown values to be determined.

## 3.2 Practical implementation

Having introduced the theory of FEM, we now present how FEM is implemented numerically in our method. One important part of the implementation is to find the basis functions for a triangular element before assembling related matrices and vectors.



(a)  $P1$  basis functions are defined on three vertices  
 (b)  $P2$  basis functions are defined on three vertices and three edge midpoints

Figure 3.4: Examples of  $P1$  and  $P2$  elements

$P1$  and  $P2$  basis functions are used in our method and the corresponding elements are called  $P1$  and  $P2$  element, as shown in Figure 3.4. They both satisfy equation (3.8), vanishing at all nodes except the one they are associated with.

## 3.2 Practical implementation

The difference is that the  $P1$  basis function is linear within the element, while the  $P2$  basis function is quadratic. The  $P1$  basis functions are defined on three vertices, as illustrated in Figure 3.4(a). The  $P2$  basis functions are associated with three vertices and three edge midpoints, as shown in Figure 3.4(b).

The  $P1$  finite element method uses the simplest linear functions of the form:  $\phi = a + bx + cy$  as basis functions. The shapes of the basis functions are shown in Figure 3.5. The  $P2$  basis functions are quadratic in the element, with the form  $\psi = a + bx + cy + dxy + ex^2 + fy^2$ . The shape of  $P2$  basis function  $\psi_1$  and  $\psi_4$  are illustrated in Figure 3.6.

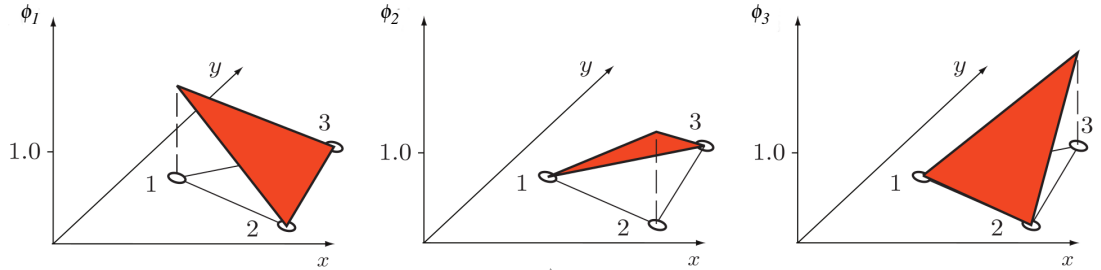


Figure 3.5:  $P1$  functions are linear in the element. The shape of  $P1$  functions in a triangular element is shaded ( $\phi_1$ ,  $\phi_2$  and  $\phi_3$  from left to right). This figure and the below figure are modified from the image from the 3D7 lecture note by Li and Wells at CUED (Cambridge University Engineering Department).

In the real computations, the triangular elements are of arbitrary shape and have different positions. To tackle this, a widely used strategy is employed to transform all triangles on 2D  $x - y$  plane from a reference triangle with vertices  $(0, 0)$ ,  $(0, 1)$  and  $(1, 0)$  on 2D  $s - t$  plane, as depicted in Figure 3.7. For simplicity, we only consider triangular elements with straight edges. This transformation is an affine transformation ( $\mathbf{J}$  represents the affine mapping matrix):

$$\begin{pmatrix} x \\ y \end{pmatrix} = \begin{pmatrix} x_0 \\ y_0 \end{pmatrix} + \mathbf{J} \begin{pmatrix} s \\ t \end{pmatrix}, \quad (3.14a)$$

$$\mathbf{J} = \begin{pmatrix} \frac{\partial x}{\partial s} & \frac{\partial x}{\partial t} \\ \frac{\partial y}{\partial s} & \frac{\partial y}{\partial t} \end{pmatrix} = \begin{pmatrix} x_1 - x_0 & x_2 - x_0 \\ y_1 - y_0 & y_2 - y_0 \end{pmatrix}. \quad (3.14b)$$

### 3. BASICS OF FINITE ELEMENT METHOD

---

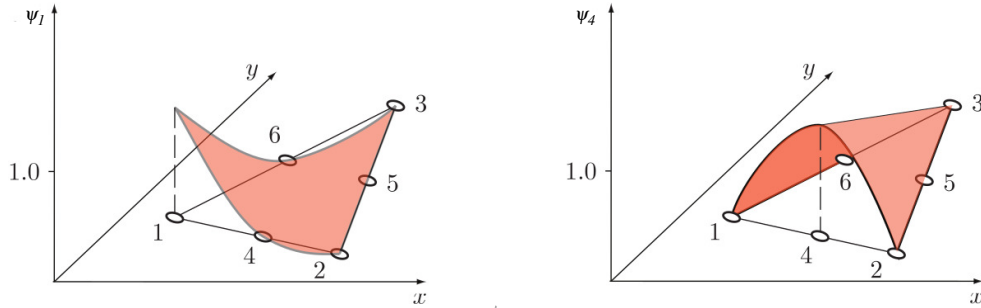


Figure 3.6:  $P_2$  functions are quadratic in the element. The shape of  $P_2$  basis functions defined on a vertex node 1 (in the left panel) and an edge midpoint node 4 (in the right panel) are shaded.

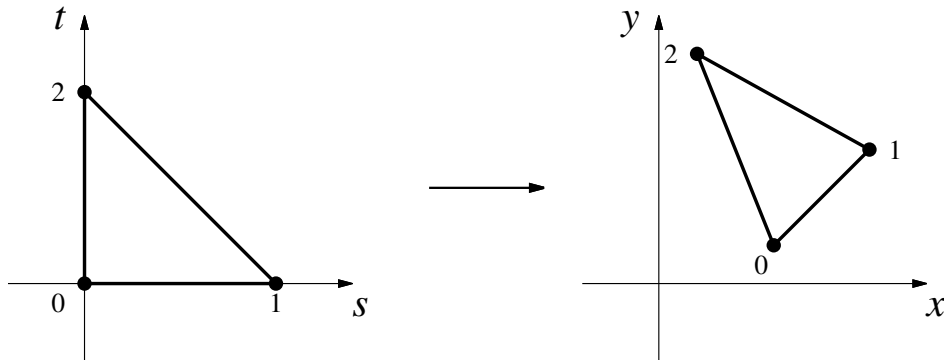


Figure 3.7: Transformation of a reference triangle to an arbitrary triangle

The  $P_1$  basis functions  $\varphi_i(s, t)$  for each node defined in the  $P_1$  reference triangle in Figure 3.8(a) are:

$$\varphi_0(s, t) = 1 - s - t, \quad (3.15a)$$

$$\varphi_1(s, t) = s, \quad (3.15b)$$

$$\varphi_2(s, t) = t, \quad (3.15c)$$

and their gradients are:

$$\nabla\varphi_0 = (-1, -1)^T, \quad (3.16a)$$

$$\nabla\varphi_1 = (1, 0)^T, \quad (3.16b)$$

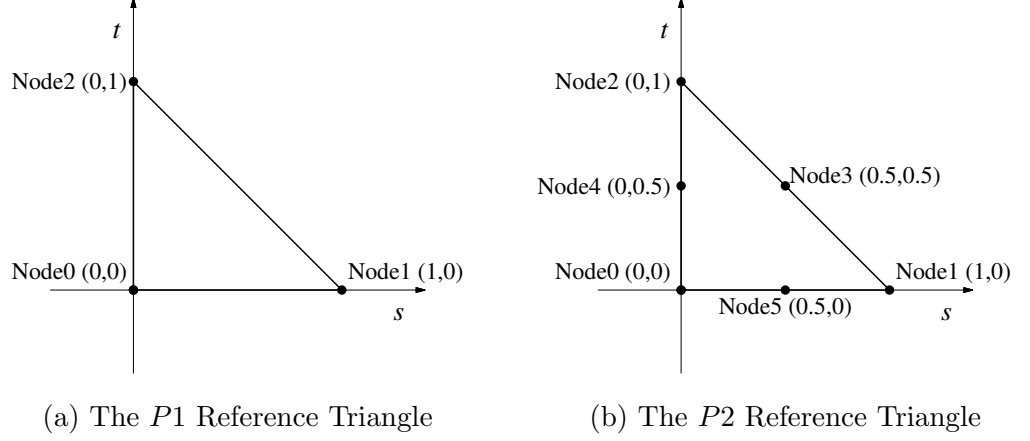


Figure 3.8:  $P_1$  and  $P_2$  reference triangles in  $s - t$  plane

$$\nabla\varphi_2 = (0, 1)^T. \quad (3.16c)$$

The  $P_2$  basis function  $\varphi_i(s, t)$  for each node defined in the  $P_2$  reference triangle in Figure 3.8(b) are:

$$\varphi_0(s, t) = (1 - s - t)(1 - 2s - 2t), \quad (3.17a)$$

$$\varphi_1(s, t) = s(2s - 1), \quad (3.17b)$$

$$\varphi_2(s, t) = t(2t - 1), \quad (3.17c)$$

$$\varphi_3(s, t) = 4st, \quad (3.17d)$$

$$\varphi_4(s, t) = 4t(1 - s - t), \quad (3.17e)$$

$$\varphi_5(s, t) = 4s(1 - s - t), \quad (3.17f)$$

and their gradients are:

$$\nabla\varphi_0 = (-3 + 4s + 4t, -3 + 4s + 4t)^T, \quad (3.18a)$$

$$\nabla\varphi_1 = (-1 + 4s, 0)^T, \quad (3.18b)$$

$$\nabla\varphi_2 = (0, -1 + 4t)^T, \quad (3.18c)$$

$$\nabla\varphi_3 = (4t, 4s)^T, \quad (3.18d)$$

$$\nabla\varphi_4 = (-4t, 4 - 4s - 8t)^T, \quad (3.18e)$$

$$\nabla\varphi_5 = (4 - 8s - 4t, -4s)^T. \quad (3.18f)$$

### 3. BASICS OF FINITE ELEMENT METHOD

---

With known basis functions, we can calculate the integrals  $\int_{\Omega} \nabla \varphi_i \cdot \nabla \varphi_j d\Omega$  and assemble the stiffness matrix or other forms of integrals for other matrices according to the need. By applying the inverse mapping matrix,  $\partial \phi_i / \partial x$ ,  $\partial \phi_i / \partial y$  can be calculated using the chain rule:

$$\nabla \phi_i = \begin{pmatrix} \frac{\partial \phi_i}{\partial x} \\ \frac{\partial \phi_i}{\partial y} \end{pmatrix} = \begin{pmatrix} \frac{\partial s}{\partial x} & \frac{\partial t}{\partial x} \\ \frac{\partial s}{\partial y} & \frac{\partial t}{\partial y} \end{pmatrix} \begin{pmatrix} \frac{\partial \varphi_i}{\partial s} \\ \frac{\partial \varphi_i}{\partial t} \end{pmatrix} = \mathbf{J}^{-\mathbf{T}} \cdot \nabla \varphi_i. \quad (3.19)$$

in which

$$\mathbf{J}^{-\mathbf{T}} = \frac{1}{\det(\mathbf{J})} \begin{pmatrix} y_2 - y_0 & y_0 - y_1 \\ x_0 - x_2 & x_1 - x_0 \end{pmatrix}. \quad (3.20)$$

The integrals over an arbitrary triangle in  $x - y$  plane are computed as:

$$\int_{\Omega} \nabla \phi_i \cdot \nabla \phi_j dx dy = \int_{\Omega_R} (\mathbf{J}^{-\mathbf{T}} \nabla \varphi_i) \cdot (\mathbf{J}^{-\mathbf{T}} \nabla \varphi_j) \det(\mathbf{J}) ds dt, \quad (3.21)$$

in which  $\Omega_R$  is the referenced triangle on  $s - t$  plane. The use of reference triangle simplifies the calculation of integrals over an arbitrary triangle. The integration over a reference triangle is numerically calculated by Hammer integration formulas, as listed in Appendix A.3.

More details regarding how FEM is implemented into our code are attached in Appendix A.

### 3.3 An FEM Poisson solver

In this section, we consider a Poisson equation in two-dimensional ring domain ( $x = r \cos \theta$ ,  $y = r \sin \theta$ ):

$$\nabla^2 u = \frac{1}{r} \frac{\partial}{\partial r} \left( r \frac{\partial u}{\partial r} \right) + \frac{1}{r^2} \frac{\partial^2 u}{\partial \theta^2} = 1, \quad 1 < r < 2, \quad (3.22a)$$

$$u|_{r=1} = 1 + \cos^2 \theta, \quad (3.22b)$$

$$u|_{r=2} = 1 + \sin^2 \theta. \quad (3.22c)$$

The analytical solution is:

$$u(r, \theta) = \frac{1}{2} + \frac{r^2}{4} + \frac{3}{4} \left( 1 - \frac{\ln r}{\ln 2} \right) - \frac{1}{6} \left( r^2 - \frac{4}{r^2} \right) \cos 2\theta. \quad (3.23)$$



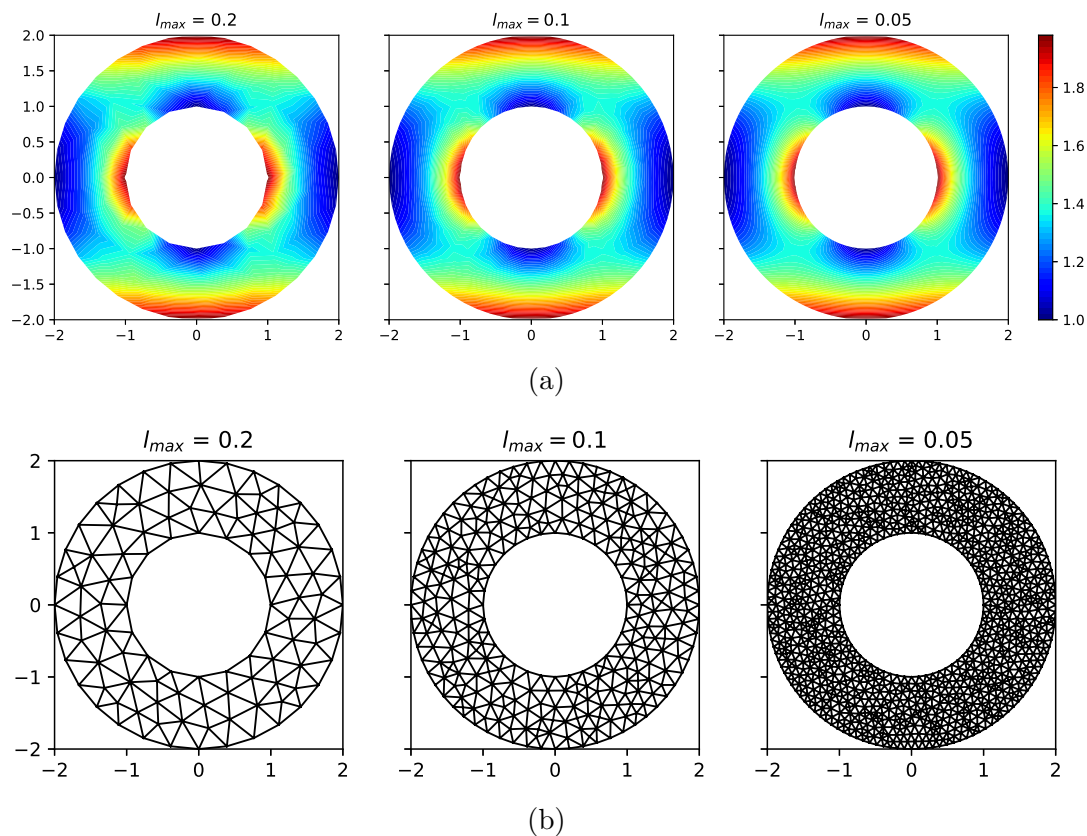


Figure 3.9: Results from left to right are from simulation with  $l_{max} = 0.2, 0.1$  and  $0.05$  respectively. (a) shows the temperature contour and (b) shows the corresponding computational mesh.

We have implemented a  $P2$  finite element Poisson solver for this problem. The ring domain is discretised using a mesh with a uniform mesh size density ( $G = 0$ ,  $l_s = l_{max}$ ), but the mesh is not necessarily uniform. We vary  $l_{max}$  for different mesh resolution. The numerical solution for  $u$  is plotted in Figure 3.9(a), and the corresponding computational meshes are shown in Figure 3.9(b). The contour plot becomes smoother with a finer mesh (smaller  $l_{max}$ ).

We document the maximum relative error compared to the analytical solution of  $u$  in Table 3.1 and plot it against  $l_{max}$  in Figure 3.10. From the plot, we can clearly see that the maximum relative error converges to zero with a decreasing  $l_{max}$  and the data points almost all fall on the line  $0.35l_{max}^2$ . This indicates that

### 3. BASICS OF FINITE ELEMENT METHOD

---

Table 3.1: Performance of  $P2$  finite element Poisson solver

$l_{max}$	total number of vertices	maximum relative error (%)
0.2	106	1.048
0.1	310	0.313
0.05	1192	0.086
0.025	4541	0.026

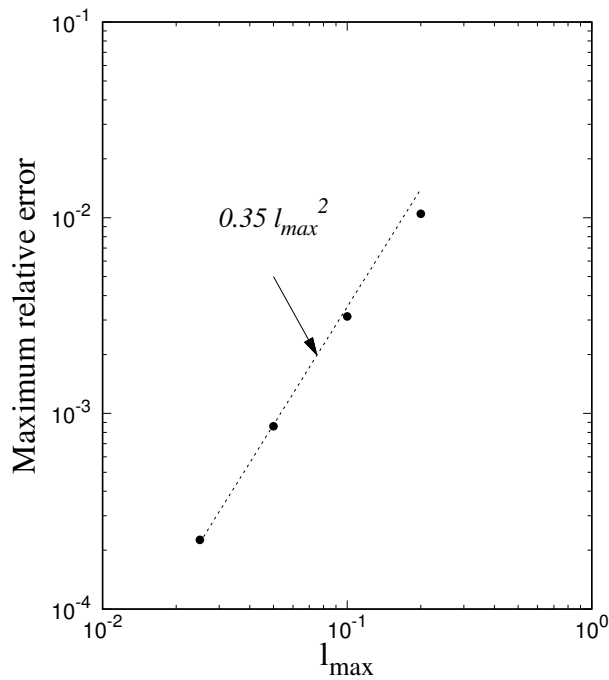


Figure 3.10: The maximum relative error of the numerical solution is plotted as circular dots and the dashed line represents  $0.35l_{max}^2$ .

the  $P2$  finite element method converges to the analytical solution at a convergence rate of 2. This can be explained by the fact that  $P2$  basis functions are quadratic in each element, and we expect the error to be almost zero if the analytical solution can be exactly represented by second-order polynomial.

In this problem, the boundary is curved, and the isoparametric  $P2$  curved finite element method has a better performance<sup>1</sup>. Since the midpoints are put on

---

<sup>1</sup> We initially intended to implement an isoparametric  $P2/P1d$  finite element method

the curved boundary, the boundary condition is better represented numerically.

---

for solving Navier-Stokes equations with the interface tracked by piecewise curved segments. Later it is found that a lot of additional work were required as described in the last paragraph in Section 4.2.5, We have evaluated the performance of an isoparametric P2 finite element solver for Poisson equation in our earlier work (Section 4.4 in <https://github.com/cz295/Thesis/blob/master/FYR.pdf>)

### 3. BASICS OF FINITE ELEMENT METHOD

---

# Chapter 4

## FEM for multiphase flows

FEM has been introduced from its theoretical and practical aspects in the previous chapter. In this chapter we demonstrate how FEM is applied to solve multiphase flows on an adaptive moving mesh. The difference between multiphase flows from single-phase flows is the presence of the interface separating two immiscible fluids. To resolve multiphase flows, not only do we need to determine the flow in two phases simultaneously, but also to track the moving interface, and to impose the boundary conditions correctly. In our method, the interface is explicitly represented by lines of the mesh system and the mesh is adapted to follow the interface motion. The boundary conditions on the interface can be naturally embedded in the weak formulation of the Navier-Stokes equation. Hence, FEM based on the weak formulation has the tremendous advantage in handling the interface boundary conditions.

We start this chapter with the mathematical formulations of multiphase flows. Then the numerical procedures are illustrated step by step, including the finite element discretization, Navier-Stokes solver, the arbitrary Lagrangian Eulerian (ALE) method, and the numerical treatment of interfacial tension. We prove that our method achieves the static Laplace solution of a circular/spherical droplet. The numerical stability of this solution is further examined. At the end of this chapter, the accuracy and robustness of our method is validated with a more rigorous example: the axisymmetric droplet/bubble oscillation.

## 4.1 Mathematical formulations for multiphase flows

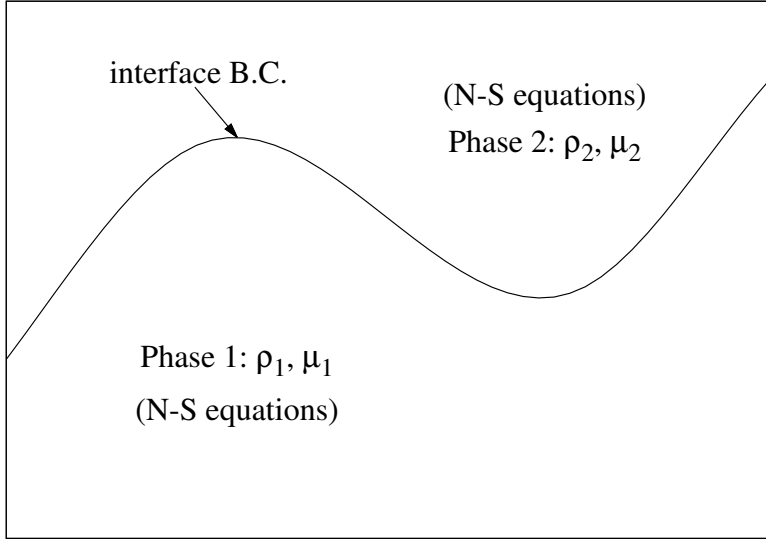


Figure 4.1: Flow in the bulk fluid is determined by solving the Navier-Stokes equations with boundary conditions on the interface matching simultaneously.

We consider two immiscible incompressible Newtonian fluids with density  $\rho_i$  and viscosity  $\mu_i$  ( $i = 1, 2$ ). The density ratio and viscosity ratio are denoted as  $\eta$  and  $\lambda$ :

$$\eta = \frac{\rho_2}{\rho_1}, \quad (4.1a)$$

$$\lambda = \frac{\mu_2}{\mu_1}. \quad (4.1b)$$

As illustrated in Figure 4.1, the two fluids are separated by an interface whose location, shape and evolution are to be determined. Flow in the bulk fluid is governed by the incompressible Navier-Stokes equations. The vector form of the continuity equation reads:

$$\nabla \cdot \mathbf{u} = 0, \quad (4.2)$$

## 4.1 Mathematical formulations for multiphase flows

---

and the momentum equation reads:

$$\rho_i \frac{d\mathbf{u}}{dt} = \nabla \mathbf{T} + \mathbf{f}, \quad (4.3)$$

where we use  $\mathbf{f}$  for body force and  $\mathbf{T}$  for the stress tensor:

$$\mathbf{T} = -p\mathbf{I} + \mu_i (\nabla \mathbf{u} + \nabla \mathbf{u}^T). \quad (4.4)$$

In the above equations,  $d(\cdot)/dt$  is the material derivative:

$$\frac{d}{dt}(\cdot) = \frac{\partial}{\partial t}(\cdot) + (\mathbf{u} \cdot \nabla)(\cdot). \quad (4.5)$$

The density and viscosity is discontinuous across the interface, while the velocity is continuous across the interface. The most important boundary condition on the interface is the force balance between interfacial tension and stress from both sides of the interface. Since the interface is massless, a singularity will appear without this condition. This condition is written as follows:

$$[\mathbf{T} \cdot \mathbf{n}]_{-}^{+} = \sigma \kappa \mathbf{n}, \quad (4.6)$$

where  $[\cdot]_{-}^{+}$  denotes the differences between both sides of the interface,  $\sigma$  is the surface tension coefficient,  $\kappa$  is the interface curvature, and  $\mathbf{n}$  is the unit normal vector on the interface. The derivation of this condition is attached in Appendix B. In this chapter we only consider uniform  $\sigma$ . This formulation is also applicable to free-surface flow in which the ambient fluid is considered passive ( $\mathbf{T} = -p_0\mathbf{I}$ , and we normally set  $p_0 = 0$ ).

Since our mesh generator produces mesh in two-dimension, we only consider two-dimensional or axisymmetric flow. The governing equations in the two-dimensional  $x - z$  plane reads:

$$\frac{\partial u}{\partial x} + \frac{\partial v}{\partial z} = 0, \quad (4.7a)$$

$$\rho_i \frac{du}{dt} = -\frac{\partial p}{\partial x} + \frac{\partial}{\partial x} \left( 2\mu_i \frac{\partial u}{\partial x} \right) + \frac{\partial}{\partial z} \left( \mu_i \left( \frac{\partial u}{\partial z} + \frac{\partial v}{\partial x} \right) \right) + f_x, \quad (4.7b)$$

$$\rho_i \frac{dv}{dt} = -\frac{\partial p}{\partial z} + \frac{\partial}{\partial x} \left( \mu_i \left( \frac{\partial u}{\partial z} + \frac{\partial v}{\partial x} \right) \right) + \frac{\partial}{\partial z} \left( 2\mu_i \frac{\partial v}{\partial z} \right) + f_z, \quad (4.7c)$$

#### 4. FEM FOR MULTIPHASE FLOWS

---

where  $u$  and  $v$  are horizontal and vertical component of the velocity, and  $f_x$  and  $f_z$  represent the body force in the horizontal and vertical direction, respectively.

The governing equations in the axisymmetric geometry ( $r - z$  plane) are listed below:

$$\frac{1}{r} \frac{\partial}{\partial r}(ru) + \frac{\partial v}{\partial z} = 0, \quad (4.8a)$$

$$\rho_i \frac{du}{dt} = -\frac{\partial p}{\partial r} + \frac{1}{r} \frac{\partial}{\partial r} \left( r 2\mu_i \frac{\partial u}{\partial r} \right) - \frac{2\mu_i u}{r^2} + \frac{\partial}{\partial z} \left( \mu_i \left( \frac{\partial u}{\partial z} + \frac{\partial v}{\partial r} \right) \right) + f_r, \quad (4.8b)$$

$$\rho_i \frac{dv}{dt} = -\frac{\partial p}{\partial z} + \frac{1}{r} \frac{\partial}{\partial r} \left( r \mu_i \left( \frac{\partial u}{\partial z} + \frac{\partial v}{\partial r} \right) \right) + \frac{\partial}{\partial z} \left( 2\mu_i \frac{\partial v}{\partial z} \right) + f_z, \quad (4.8c)$$

in which  $u$  and  $v$  represents the radial and axial velocity respectively, and  $f_r$  and  $f_z$  denote the body force in the radial and vertical direction, respectively.

To define a multiphase flow system, a group of dimensionless numbers are required apart from  $\eta$  and  $\lambda$  defined in equation (4.1). We characterise length and velocity with  $L$  and  $U$ , respectively. Gravity is also considered with  $g$  representing the gravitational acceleration. There are six physical variables ( $L$ ,  $U$ ,  $g$ ,  $\rho$ ,  $\mu$  and  $\sigma$ ) and three dimensions (time, length and mass). Hence three dimensionless numbers are needed. The commonly used numbers related to multiphase flows are, the *Reynolds* number, the *Weber* number and the *Froude* number, defined as below (Munson et al., 2014):

$$Re = \frac{\rho UL}{\mu} = \frac{UL}{\nu}, \quad We = \frac{\rho U^2 L}{\sigma}, \quad Fr = \frac{U}{\sqrt{gL}}. \quad (4.9)$$

The *Re* number measures the relative importance of the inertial effect with respect to the viscous stresses; the *We* number measures the relative magnitude between the inertial effect and the interfacial tension; the *Fr* number represents the measure of the inertial effect relative to the gravitational force. Some other dimensionless numbers are defined for convenient description of a particular problem. Other dimensionless numbers used in this thesis are presented below.

In the study of droplet formation from a nozzle, Ohnesorge (1936) defined the *Ohnesorge* number:

$$Oh = \frac{\mu}{\sqrt{\rho\sigma L}} = \frac{\sqrt{We}}{Re}, \quad (4.10)$$



which reflect the relative magnitudes of inertial, viscous and capillary effects. McKinley and Renardy (2011) pointed out that the  $Oh$  number can also be understood as a ratio between two time scales important in capillary jet breakup, the Rayleigh timescale for breakup of an inviscid fluid jet and the viscocapillary time scale characterising the thinning of a viscous thread. In the numerical study of the static Laplace solution of a circular droplet, the  $Oh$  number was interpreted by Popinet (2018) as the ratio of the capillary oscillating time scale and the viscous dissipation time scale. In the above examples,  $L$  is chosen as the diameter of the nozzle/jet/droplet.

The *Capillary* number is widely used in flows with droplet/bubble and flow of thin films, defined as follows:

$$Ca = \frac{\mu U}{\sigma} = \frac{We}{Re}, \quad (4.11)$$

which represents a measure of the viscous force relative to the interfacial tension. In general, a small value of  $Ca$  corresponds to weaker deformation of the interface. For example, the droplet shape is nearly spherical provided that the  $Ca$  number is sufficiently small (Stone, 1994).

In the investigation on measuring the surface tension of liquid, Bond (1935) defined a dimensionless number, later known as the *Bond* number

$$Bo = \frac{\rho g L^2}{\sigma} = \frac{We}{Fr^2}, \quad (4.12)$$

to measure the relative importance of the gravitational force to the capillary force. It is a crucial dimensionless number in deciding the shape of a pendant or sessile droplet (Middleman, 1995).

## 4.2 Numerical procedures

### 4.2.1 Weak formulation

The first step is to obtain the weak formulation of the governing equations. In this section, we consider the governing equations in 2D geometry. The weak formulation in axisymmetric geometry can be obtained similarly, as provided in

#### 4. FEM FOR MULTIPHASE FLOWS

---

Appendix C. The difference is that  $\int_{\Omega} d\Omega$  corresponds to  $\int_{\Omega} dx dz$  in 2D geometry and  $\int_{\Omega} r dr dz$  in axisymmetric geometry, respectively.

We multiply a test function  $\psi$  on both side of equation (4.7a) to obtain the weak form of the continuity equation:

$$\int_{\Omega} \left( \frac{\partial u}{\partial x} + \frac{\partial v}{\partial z} \right) \psi dx dz = 0. \quad (4.13)$$

The momentum equation (4.7b, 4.7c) are multiplied by  $\phi$  on both sides and integrated by parts. The subscript  $i$  is dropped for convenience. We obtain:

$$\begin{aligned} & \int_{\Omega} \left( \rho \phi \frac{du}{dt} + 2\mu \frac{\partial \phi}{\partial x} \frac{\partial u}{\partial x} + \mu \frac{\partial \phi}{\partial z} \frac{\partial u}{\partial z} + \mu \frac{\partial \phi}{\partial z} \frac{\partial v}{\partial x} - p \frac{\partial \phi}{\partial x} \right) dx dz \\ &= \int_{\partial \Omega} \phi \left[ \left( -p + 2\mu \frac{\partial u}{\partial x} \right) n_x + \mu \left( \frac{\partial u}{\partial z} + \frac{\partial v}{\partial x} \right) n_z \right] dl + \int_{\Omega} f_x \phi dx dz, \end{aligned} \quad (4.14a)$$

$$\begin{aligned} & \int_{\Omega} \left( \rho \phi \frac{dv}{dt} + \mu \frac{\partial \phi}{\partial x} \frac{\partial u}{\partial z} + \mu \frac{\partial \phi}{\partial x} \frac{\partial v}{\partial x} + 2\mu \frac{\partial \phi}{\partial z} \frac{\partial v}{\partial z} - p \frac{\partial \phi}{\partial z} \right) dx dz \\ &= \int_{\partial \Omega} \phi \left[ \mu \left( \frac{\partial u}{\partial z} + \frac{\partial v}{\partial x} \right) n_x + \left( -p + 2\mu \frac{\partial v}{\partial z} \right) n_z \right] dl + \int_{\Omega} f_z \phi dx dz. \end{aligned} \quad (4.14b)$$

In the above equations,  $n_x$  and  $n_z$  denote the horizontal and vertical components of the normal vector on the boundary  $\partial \Omega$ . Dirichlet boundary conditions for velocity can be implemented easily by choosing  $\phi$  suitably such that it vanishes on the related Dirichlet boundary. Note that the Dirichlet boundary for  $u$  and  $v$  may differ. For example, the up-and-down symmetry boundary is a Dirichlet boundary for  $v$  ( $v = 0$ ), but not for  $u$ . In most cases, the interface is the only Neumann boundary we consider, and equation (4.14) is then written as:

$$\begin{aligned} & \int_{\Omega} \left( \rho \phi \frac{du}{dt} + 2\mu \frac{\partial \phi}{\partial x} \frac{\partial u}{\partial x} + \mu \frac{\partial \phi}{\partial z} \frac{\partial u}{\partial z} + \mu \frac{\partial \phi}{\partial z} \frac{\partial v}{\partial x} - p \frac{\partial \phi}{\partial x} \right) dx dz \\ &= \int_{\Gamma} \phi \left[ \left( -p + 2\mu \frac{\partial u}{\partial x} \right) n_x + \mu \left( \frac{\partial u}{\partial z} + \frac{\partial v}{\partial x} \right) n_z \right]_{-}^{+} dl + \int_{\Omega} f_x \phi dx dz, \end{aligned} \quad (4.15a)$$

$$\begin{aligned} & \int_{\Omega} \left( \rho \phi \frac{dv}{dt} + \mu \frac{\partial \phi}{\partial x} \frac{\partial u}{\partial z} + \mu \frac{\partial \phi}{\partial x} \frac{\partial v}{\partial x} + 2\mu \frac{\partial \phi}{\partial z} \frac{\partial v}{\partial z} - p \frac{\partial \phi}{\partial z} \right) dx dz \\ &= \int_{\Gamma} \phi \left[ \mu \left( \frac{\partial u}{\partial z} + \frac{\partial v}{\partial x} \right) n_x + \left( -p + 2\mu \frac{\partial v}{\partial z} \right) n_z \right]_{-}^{+} dl + \int_{\Omega} f_z \phi dx dz, \end{aligned} \quad (4.15b)$$

where the interface is denoted as  $\Gamma$ . By applying the force balance condition, equation (4.6), the following equations are obtained:

$$\begin{aligned} \int_{\Omega} \left( \rho\phi \frac{du}{dt} + 2\mu \frac{\partial\phi}{\partial x} \frac{\partial u}{\partial x} + \mu \frac{\partial\phi}{\partial z} \frac{\partial u}{\partial z} + \mu \frac{\partial\phi}{\partial z} \frac{\partial v}{\partial x} - p \frac{\partial\phi}{\partial x} \right) dx dz \\ = \int_{\Gamma} \phi \sigma \kappa n_x dl + \int_{\Omega} f_x \phi dx dz, \end{aligned} \quad (4.16a)$$

$$\begin{aligned} \int_{\Omega} \left( \rho\phi \frac{dv}{dt} + \mu \frac{\partial\phi}{\partial x} \frac{\partial u}{\partial z} + \mu \frac{\partial\phi}{\partial x} \frac{\partial v}{\partial x} + 2\mu \frac{\partial\phi}{\partial z} \frac{\partial v}{\partial z} - p \frac{\partial\phi}{\partial z} \right) dx dz \\ = \int_{\Gamma} \phi \sigma \kappa n_z dl + \int_{\Omega} f_z \phi dx dz. \end{aligned} \quad (4.16b)$$

The finite element discretisation for the above equations is presented in the following section.

### 4.2.2 Spatial and temporal discretisation

The whole computational domain is discretised with a triangulation  $T_h$  in which the interface is represented by mesh lines. A piece of triangulation in the interfacial region is drawn in Figure 4.2. The interface drawn in red divides the computational domain into two parts, each of which consists of only one phase. This triangulation is generated by our adaptive mesh generator described in Chapter 2.

A semi-implicit method is used for the temporal discretisation. We first update the location of the interface in a Lagrangian manner as previously explained using Figure 2.1(a). Then the triangulation is updated from  $T_h^n$  to  $T_h^{n+1}$  through smoothing and local mesh arrangement (the superscript  $n$  and  $n+1$  denote the time level). The weak forms of the incompressible Navier-Stokes equation are then solved implicitly at time level  $n+1$  on the updated triangulation. When we swap/split/collapse an edge, physical quantities at the new nodes are obtained through local interpolation.

Pressure and velocity are approximated with a Taylor-Hood element, as shown in Figure 4.3. In each element, the velocity is approximated by  $P2$  basis functions and is continuous over the entire domain. Within the element, velocity is obtained by local interpolation with its value on 6 nodes (3 vertices and edge midpoints,

## 4. FEM FOR MULTIPHASE FLOWS

---

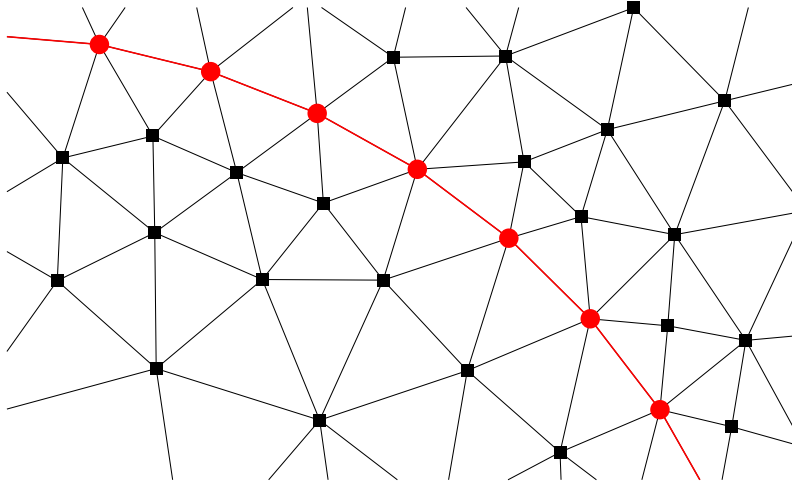


Figure 4.2: The red solid line represents the interface and the black solid lines form the triangulation. Pressure nodes on the interface (drawn as red circular nodes) have two values while in the interior pressure nodes (drawn as black square nodes) have one value.

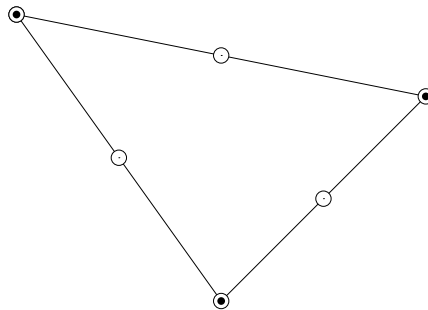


Figure 4.3: In a Taylor-Hood element, the pressure are defined on three vertices (●) while the velocity nodes (○) are three vertices and edge midpoints.

denoted as  $\circ$  in Figure 4.3). This finite element space is called  $P2 - C0$ . Pressure is approximated by its values on 3 vertices (denoted as  $\bullet$  in Figure 4.3) and thus is linear in each element. The conventional continuous finite element space ( $P1 - C0$ ) for pressure is adequate in the interior domain, but it is not able to address the pressure jump across the interface. Since a fully discontinuous

pressure space results in extra unnecessary computing costs over the interior domain, a pressure space ( $P1d - C0$ ) is introduced by Li (2013), in which the pressure has single value on interior nodes (square nodes in Figure 4.2) and double values on interfacial nodes (circular nodes in Figure 4.2). In practice,  $P2 - C0$  nodes are ordered as the list of vertices in the triangle followed by the list of edges;  $P1 - C0$  nodes are ordered as the list of vertices;  $P1d$  nodes are ordered as the list of vertices in phase 0, followed by the list of vertices in phase 1, such that vertices on the interface can be counted twice.

The velocity and pressure are approximated as follows:

$$u \approx \sum_{i=1}^{N_{P2}} u_i \phi_i, \quad v \approx \sum_{i=1}^{N_{P2}} v_i \phi_i, \quad p \approx \sum_{i=1}^{N_{P1d}} p_i \psi_i, \quad (4.17)$$

in which  $\phi_i$  is the  $P2$  basis function,  $\psi_i$  is the  $P1$  basis function,  $N_{P2}$  and  $N_{P1d}$  are numbers of  $P2$  and  $P1d$  nodes respectively, and  $u_i$  and  $v_i$  on Dirichlet boundaries are known values. Following the Galerkin finite element method,  $\psi_j$ ,  $j = 1, \dots, N_{P1d}$  are chosen as the test functions in the weak form of the continuity equation and  $\phi_j$ ,  $j = 1, \dots, N_{P2}$  are the test functions in the weak form of the momentum equation (see Reddy and Gartling (2010) for further details). We substitute equation (4.17) into the weak formulation, equation (4.13) and (4.16). Except the material derivatives, the discretised weak formulations written in a matrix-vector format are listed below:

$$\begin{bmatrix} \mathbf{M}^x & 0 & 0 \\ 0 & \mathbf{M}^z & 0 \\ 0 & 0 & 0 \end{bmatrix} \begin{bmatrix} d\mathbf{u}/dt \\ d\mathbf{v}/dt \\ \mathbf{p} \end{bmatrix} + \begin{bmatrix} \mathbf{K}^{xx} & \mathbf{K}^{xz} & \mathbf{B}^x \\ (\mathbf{K}^{xz})^T & \mathbf{K}^{zz} & \mathbf{B}^z \\ (\mathbf{B}^x)^T & (\mathbf{B}^z)^T & 0 \end{bmatrix} \begin{bmatrix} \mathbf{u} \\ \mathbf{v} \\ \mathbf{p} \end{bmatrix} = \begin{bmatrix} \mathbf{g}^x \\ \mathbf{g}^z \\ 0 \end{bmatrix} \quad (4.18)$$

in which

$$\mathbf{u} = (u_1, \dots, u_{N_{P2}})^T, \quad (4.19a)$$

$$\mathbf{v} = (v_1, \dots, v_{N_{P2}})^T, \quad (4.19b)$$

$$\mathbf{p} = (p_1, \dots, p_{N_{P1d}})^T, \quad (4.19c)$$

$$M_{ij}^{x,z} = \int_{\Omega} \rho \phi_i \phi_j dx dz, \quad (4.19d)$$

$$K_{ij}^{xx} = \int_{\Omega} \mu \left( 2 \frac{\partial \phi_i}{\partial x} \frac{\partial \phi_j}{\partial x} + \frac{\partial \phi_i}{\partial z} \frac{\partial \phi_j}{\partial z} \right) dx dz, \quad (4.19e)$$

#### 4. FEM FOR MULTIPHASE FLOWS

---

$$K_{ij}^{xz} = \int_{\Omega} \mu \frac{\partial \phi_i}{\partial z} \frac{\partial \phi_j}{\partial x} dx dz, \quad (4.19f)$$

$$K_{ij}^{zz} = \int_{\Omega} \mu \left( \frac{\partial \phi_i}{\partial x} \frac{\partial \phi_j}{\partial x} + 2 \frac{\partial \phi_i}{\partial z} \frac{\partial \phi_j}{\partial z} \right) dx dz, \quad (4.19g)$$

$$B_{ij}^x = - \int_{\Omega} \frac{\partial \phi_i}{\partial x} \psi_j dx dz, \quad (4.19h)$$

$$B_{ij}^z = - \int_{\Omega} \frac{\partial \phi_i}{\partial z} \psi_j dx dz. \quad (4.19i)$$

When calculating these values, we choose  $\rho$  and  $\mu$  according to which phase the element belongs to. The vectors in the right hand side are the source terms:

$$g_j^x = \int_{\Gamma} \phi_j \sigma \kappa n_x dl + \int_{\Omega} \phi_j f_x dx dz, \quad g_j^z = \int_{\Gamma} \phi_j \sigma \kappa n_y dl + \int_{\Omega} \phi_j f_z dx dz, \quad (4.20)$$

in which the first and second term represents the contribution from the interfacial tension and the body force respectively. The numerical evaluation of the interfacial tension source term is introduced in Section 4.2.5.

Equation (4.18) in a more compact form reads:

$$\mathbf{M} \frac{d\mathbf{U}}{dt} + \mathbf{K}\mathbf{U} + \mathbf{B}\mathbf{p} = \mathbf{g}, \quad (4.21a)$$

$$\mathbf{B}^T \mathbf{U} = \mathbf{0} \quad (4.21b)$$

in which the matrices are defined as below:

$$\mathbf{M} = \begin{pmatrix} \mathbf{M}^x & 0 \\ 0 & \mathbf{M}^z \end{pmatrix}, \quad \mathbf{K} = \begin{pmatrix} \mathbf{K}^{xx} & \mathbf{K}^{xz} \\ \mathbf{K}^{zx} & \mathbf{K}^{zz} \end{pmatrix}, \quad (4.22a)$$

$$\mathbf{B} = \begin{bmatrix} \mathbf{B}^x \\ \mathbf{B}^z \end{bmatrix}, \quad \mathbf{U} = \begin{bmatrix} \mathbf{u} \\ \mathbf{v} \end{bmatrix}, \quad \mathbf{g} = \begin{bmatrix} \mathbf{g}^x \\ \mathbf{g}^z \end{bmatrix}. \quad (4.22b)$$

and  $\mathbf{p}$  is unchanged. The matrix  $\mathbf{M}$  is the mass matrix,  $\mathbf{K}$  is the viscous matrix and  $\mathbf{B}$  is the constraint matrix constraining the velocity to be discretely divergence-free. It is known that the conventional  $P2 - C0/P1 - C0$  finite element space for velocity and pressure satisfies the condition for numerical stability (Gunzburger, 2012). Though it has not been proved that the new finite element space  $P2 - C0/P1d$  also satisfies this condition, our practice has shown that it works pretty well in various problems.

The discretised equations (4.21) are solved fully implicitly at time level  $n + 1$  on the triangulation  $T_h^{n+1}$ . The material derivative is discretised as follows:

$$\left(\frac{d\mathbf{U}}{dt}\right)^{n+1} \approx \frac{\mathbf{U}^{n+1} - \tilde{\mathbf{U}}^n}{\Delta t}, \quad (4.23)$$

where  $\Delta t$  is the time step. Equation (4.21) is thus expressed as:

$$\left(\frac{\mathbf{M}}{\Delta t} + \mathbf{K}\right) \mathbf{U}^{n+1} + \mathbf{B}\mathbf{p}^{n+1} = \frac{\mathbf{M}}{\Delta t} \tilde{\mathbf{U}}^n + \mathbf{g}, \quad (4.24a)$$

$$\mathbf{B}^T \mathbf{U}^{n+1} = \mathbf{0}. \quad (4.24b)$$

Bear in mind that  $\tilde{\mathbf{U}}^n$  is not the same as  $\mathbf{U}^n$ . For instance,  $(u_i^n, v_i^n)$  is the velocity of a fluid particle located at node  $\mathbf{x}_i^n$  at time level  $n$ . One time step later, this particle does not necessarily travel to node  $\mathbf{x}_i^{n+1}$  in the new triangulation  $T_h^{n+1}$ , unless it moves in a purely Lagrangian way as an interface node. To correctly approximate the material derivatives, we need to find the position  $\tilde{\mathbf{x}}_i^n$  at time level  $n$  of a fluid particle whose location is  $\mathbf{x}_i^{n+1}$  at time level  $n + 1$ . This position is called the characteristic foot at time level  $n$  of this fluid particle. Then the velocity at time level  $n$ ,  $(\tilde{u}_i^n, \tilde{v}_i^n)$ , can be calculated through local interpolation in the element within which  $\tilde{\mathbf{x}}_i^{n+1}$  is located. This procedure is detailed in Section 4.2.4.

### 4.2.3 Solution steps

The next step is to solve the discretised Navier-Stokes equations represented by equation (4.24). This is accomplished using an augmented Lagrangian technique with a Uzawa iterative algorithm as used in Étienne et al. (2006). The continuity equation (4.24b) is the constraint condition. We relax this constraint by adding  $\lambda$  amount of the divergence on the pressure vector as below:

$$\left(\frac{\mathbf{M}}{\Delta t} + \mathbf{K}\right) \mathbf{U}^{m+1} + \mathbf{B}\mathbf{p}^{m+1} = \frac{\mathbf{M}}{\Delta t} \tilde{\mathbf{U}}^n + \mathbf{g}, \quad (4.25a)$$

$$\mathbf{p}^{m+1} = \mathbf{p}^m + \lambda \mathbf{B}^T \mathbf{U}^{m+1}, \quad (4.25b)$$

in which  $m$  is the iteration time level. Then an area in which flow sinks has its pressure reduced to remove the sink to enforce continuity. Similarly an area

## 4. FEM FOR MULTIPHASE FLOWS

---

which acts as a source has its pressure increased. After calculating the value of  $\mathbf{p}^{m+1}$ , we substitute it into (4.25a) to obtain the value of  $\mathbf{U}^{m+1}$ . The iteration continues until  $\mathbf{p}^{m+1} = \mathbf{p}^m$ . The converged value of  $\mathbf{p}^{m+1}$  is the value of pressure of this iteration time level, and will be used for calculating the pressure at the next iteration step through iteration again. The iteration steps are written as:

$$\left(\frac{\mathbf{M}}{\Delta t} + \mathbf{K} + \lambda \mathbf{B}\mathbf{B}^T\right) \mathbf{U}^{m+1} = \frac{\mathbf{M}}{\Delta t} \tilde{\mathbf{U}}^n + \mathbf{g} - \mathbf{B}\mathbf{p}^m, \quad (4.26a)$$

$$\mathbf{p}^{m+1} = \mathbf{p}^m + \lambda \mathbf{B}^T \mathbf{U}^{m+1}. \quad (4.26b)$$

The constant  $\lambda$  and iteration time are carefully chosen such that the  $\mathbf{B}^T \mathbf{U}^{m+1}$  converges to a small value quickly. For Stokes flow where convective acceleration equals zero, the process of tracing backwards following the characteristics is not performed to remove the convective acceleration. The linear equations are solved with the SPOOLES (Sparse Object Oriented Linear Equation Solver, Ashcraft et al. (2002)).

### 4.2.4 ALE method and approximation of material derivatives

In our method, vertices on the interface move with the flow field. The motion of nodes on the interface are most conveniently understood from a Lagrangian point of view, e.g. moving with the flow, rather than from a fixed observer's Eulerian point of view. A purely Lagrangian method does not suit the fixed boundaries: the mesh close to the fixed boundaries will be sheared by the flow and consequently frequent remesh is required. The arbitrary Lagrangian Eulerian method (ALE) is thus adopted in our method which couples the advantages of the two methods. In each time step, we first update the location of the interface and then carry out remesh operations to improve the mesh quality. As a result, the triangulation may differ from the triangulation at the last time step. This brings a technical challenge in the approximation of material derivatives. We tackle this by a characteristic method under the ALE framework.

To describe the mesh movement, a mesh velocity  $\mathbf{a}$  is defined, which may locally differ from the material velocity  $\mathbf{u}$ . At the fixed boundary where  $\mathbf{a} = \mathbf{0}$ ,



the method is reduced to Eulerian method; at the moving boundary where  $\mathbf{a} = \mathbf{u}$ , such as the interface, a purely Lagrangian method is applied. The bulk region provides a smooth transition between the two. Node  $\mathbf{x}^n$  of the old triangulation  $T_h^n$  is moved to  $\mathbf{x}^{n+1} = \mathbf{x}^n + \mathbf{a}\Delta t$  in the new triangulation  $T_h^{n+1}$ . An example is sketched in Figure 4.4 where only the old triangulation is drawn. In the context of our ALE framework, the material derivative of a physical quantity  $f$  is then written as:

$$\frac{df}{dt} = \frac{\partial f}{\partial t} + (\mathbf{u} - \mathbf{a}) \cdot \nabla f, \quad (4.27)$$

and temporal discretisation of the above equation via a semi-implicit method is:

$$\left(\frac{df}{dt}\right)^{n+1} \approx \frac{f^{n+1} - \tilde{f}^n}{\Delta t}, \quad (4.28)$$

where  $\tilde{f}^n$  denotes the value of  $f$  at the characteristic foot  $\tilde{\mathbf{x}}^n$ . The characteristic foot  $\tilde{\mathbf{x}}^n$  is the location of a fluid particle at time level  $n$  whose location is  $\mathbf{x}^{n+1}$  at time level  $n + 1$ .

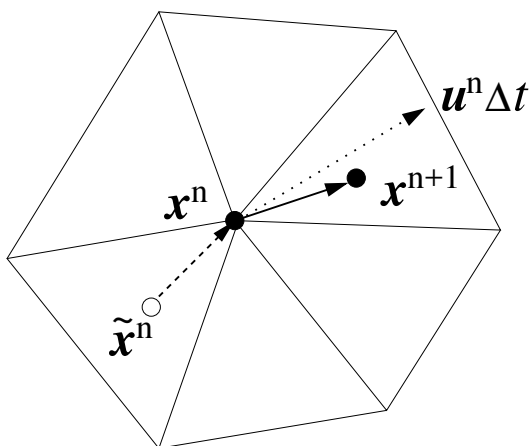


Figure 4.4: The new position of mesh node  $\mathbf{x}^{n+1}$  is connected to the old position  $\mathbf{x}^n$  via the vector  $\mathbf{a}\Delta t$  as represented by the arrow with solid line tail. The characteristic foot  $\tilde{\mathbf{x}}^n$  is connected to the old position via the vector  $(\mathbf{u} - \mathbf{a})\Delta t$ , which is drawn as an arrow with dashed-line tail. The arrow with dotted-line tail depicts the material trace during this time step of a fluid particle whose location at time level  $n$  is  $\mathbf{x}^n$ .

## 4. FEM FOR MULTIPHASE FLOWS

---

In a purely Lagrangian method, the characteristic foot is the mesh node itself, whereas in a purely Eulerian method, the characteristic foot is connected to the mesh node via a vector  $\mathbf{u}^n \Delta t$ . In the ALE framework, the characteristic foot is connected to the old mesh nodes via a vector  $(\mathbf{u} - \mathbf{a})\Delta t$ :

$$\begin{aligned}\tilde{\mathbf{x}}^n &= \mathbf{x}^{n+1} - \Delta t \cdot \mathbf{u}^n(\mathbf{x}^n) \\ &= \mathbf{x}^n - \Delta t \cdot (\mathbf{u}^n(\mathbf{x}^n) - \mathbf{a}^n(\mathbf{x}^n)),\end{aligned}\tag{4.29}$$

and this vector is drawn as the arrow with dashed-line tail in Figure 4.4.

Having identified  $\tilde{\mathbf{x}}$ , we can use local interpolation to calculate the velocity at  $\tilde{\mathbf{x}}$  and then correctly approximate the material derivatives. For simplicity and accuracy, we let the time step  $\Delta t$  be small enough to make sure that  $\tilde{\mathbf{x}}^n$  is located within a neighbouring triangle of mesh node  $\mathbf{x}^n$ . We identify the triangle where  $\tilde{\mathbf{x}}^n$  lies by looping all neighbouring triangles of  $\mathbf{x}^n$ . Having identified the triangle, we then calculate the barycentric coordinate  $(\lambda_0, \lambda_1, \lambda_2)$  of  $\tilde{\mathbf{x}}^n$  in this triangle:

$$\begin{cases} \lambda_0 + \lambda_1 + \lambda_2 = 1 \\ \lambda_0 x_0 + \lambda_1 x_1 + \lambda_2 x_2 = \tilde{x} \\ \lambda_0 z_0 + \lambda_1 z_1 + \lambda_2 z_2 = \tilde{z} \end{cases}$$

where  $(x_i, z_i)$ ,  $i = 0, 1, 2$  are the coordinates of vertices of this triangle.

Then  $\tilde{f}^n$  can be obtained through interpolation according to its approximate finite element space. If it is  $P1$  finite element space, the formulation of  $\tilde{f}^n$  is:

$$\tilde{f}^n = \sum_{i=0}^2 \lambda_i f_i^n,\tag{4.30}$$

where  $f_i$  is the value of  $f$  at vertex  $i$ .

If  $f$  is approximated by  $P2$  finite element space, the formulation is as below:

$$\tilde{f}^n = \sum_{i=0}^5 \phi_i f_i^n,\tag{4.31}$$

where the node  $i$  are defined as in a  $P2$  element illustrated in Figure 3.4(b) and  $\phi_i$  can be calculated using the barycentric coordinates:

$$\phi_0 = \lambda_0(2\lambda_0 - 1),\tag{4.32a}$$

$$\phi_1 = \lambda_1(2\lambda_1 - 1),\tag{4.32b}$$

$$\phi_2 = \lambda_2(2\lambda_2 - 1), \quad (4.32c)$$

$$\phi_3 = 4\lambda_1\lambda_2, \quad (4.32d)$$

$$\phi_4 = 4\lambda_2\lambda_0, \quad (4.32e)$$

$$\phi_5 = 4\lambda_0\lambda_1. \quad (4.32f)$$

### 4.2.5 Numerical evaluation of interfacial tension

As shown in the previous text, the interfacial tension enters the weak formulation as boundary integrals along the interface:

$$\int_{\Gamma} \sigma \kappa n_x \phi dl \quad \text{and} \quad \int_{\Gamma} \sigma \kappa n_z \phi dl, \quad (4.33)$$

in the horizontal and vertical direction respectively. In this section we present how we numerically evaluate these terms.

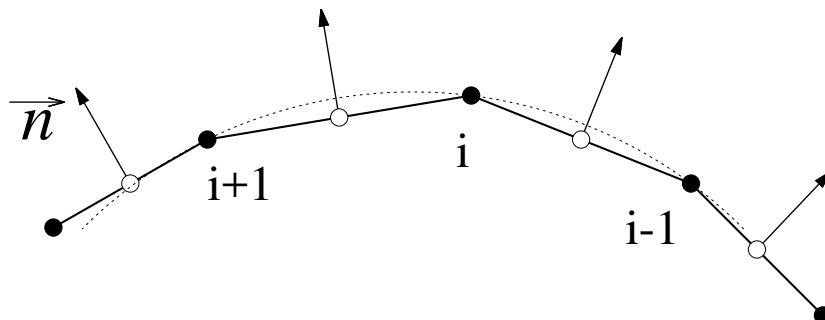


Figure 4.5: Vertex nodes and midpoint nodes are drawn in  $\bullet$  and  $\circ$  respectively and the unit normal vector of the interface edge is denoted by an arrow with solid-line tail. The dashed line is a local circle fitted onto nodes  $i$ ,  $i - 1$  and  $i + 1$ .

With the whole domain divided into triangulation, the interface is explicitly represented by a series of straight segments as illustrated in Figure 4.5. The boundary integrals in equation (4.33) are then numerically computed with Gaussian quadrature (Press et al., 1996). We use the unit normal and tangent vector of the interface edge directly in the calculation. Curvature at node  $i$  is calculated by fitting node  $i - 1$ ,  $i$  and  $i + 1$  with a local circle, which is depicted in dashed line in Figure 4.5 (Dritschel, 1988). Then we calculate the radius of this local

## 4. FEM FOR MULTIPHASE FLOWS

---

circle, denoted as  $R$ . In two-dimension, the curvature of node  $i$  is then  $-1/R$ . In the axi-symmetric case, another term is added<sup>1</sup>:

$$\kappa = -\frac{1}{R} - \frac{t_z}{r}, \quad (4.34)$$

where  $r$  and  $t_z$  are the radial coordinate and the vertical component of unit tangent vector at node  $i$  respectively. The value of  $t_z$  at node  $i$  is calculated as an average  $t_z$  of its two adjacent interface edges. Since curvatures are evaluated on vertex nodes,  $\kappa$  is considered linear on the interface edge.

As each interface segment has two vertices and one midpoint, the interface can also be approximated as a series of curved segments by the nonlinear isoparametric mapping. The author has worked on isoparametric mapping for a curved fixed boundary and has found that it indeed improves the accuracy as a result of better representation of boundary. The drawback is that the nonlinear mapping of the moving interface brings additional difficulties in interpolation and the tracking of the characteristic feet. The simpler treatment we adopt is capable of accurately calculating the interfacial tension source term, and the convergence test in later studies shows a convergence rate of 2.

### 4.3 Laplace solution for a circular/spherical droplet

The force balance condition on the interface is the most important boundary condition in multiphase flow simulations. An inaccurate representation of this condition can result in an imbalanced force which keeps disturbing the interface and generating tiny artifacts near the interface, the so-called spurious currents (Scardovelli and Zaleski, 1999). Provided that the viscous damping is sufficiently strong, the spurious currents might be suppressed or stay below a certain value. This problem becomes acute when we deal with common fluid like water, for which the interfacial tension force is often much stronger than the viscous damping. The ratio between viscous damping and capillarity is quantified by the dimensionless  $Oh$  number. For a water droplet of diameter  $D = 1.2$  mm,  $Oh = \mu/\sqrt{\rho\sigma D} \approx 10^{-3}$ . Hence, a method without an accurate implementation of the force balance condition can only be applied to a limited range of multiphase flows.

---

<sup>1</sup>See Appendix B for the formulation of curvature in axisymmetric geometry.

### 4.3 Laplace solution for a circular/spherical droplet

---

A typical example of spurious currents is a circular/spherical droplet under no external forcing. Theoretically the static Laplace solution exists: the fluid is at rest, and the interfacial tension is exactly balanced by the pressure jump across the interface. Some methods are not able to recover the force balance numerically and consequently spurious currents arise as vortices near the interface. Two influential works by Popinet and Zaleski (1999) and Renardy and Renardy (2002) effectively reduced spurious current in non-conforming methods (front-tracking and VOF). The key of their success was to modify the conventional methods such that the numerical balance is recovered.

In this section, we prove <sup>1</sup> that our method achieves the numerical equilibrium between the interfacial tension and the associated pressure jump. The static solution of a circular/spherical droplet exists in our method, and the numerical stability of the solution is further examined.

#### 4.3.1 Existence of a static solution

We consider a circular droplet with radius  $R$  initially at rest. The inner and outer fluids are marked as fluid 1 and 2, respectively (see the configuration in Figure 4.6). The interfacial tension is a constant  $\sigma$ . Without external forces, the theoretical solution is obtained by Laplace:  $u = v = 0$  and  $p_1 - p_2 = \sigma/R$ . The horizontal direction is taken as an example. The weak formulation of the momentum equation (4.16), is reduced to:

$$\int_{\Omega} \rho \phi \frac{du}{dt} d\Omega = \int_{\Omega} \frac{\partial \phi}{\partial x} p d\Omega + \int_{\Gamma} \sigma \kappa n_x \phi dl. \quad (4.35)$$

As long as the pressure term balances the surface tension source term, the static solution is obtained.

If the test function  $\phi$  is defined on an interior node, such as node  $i$  and  $k$  in Figure 4.6, pressure is a constant over the triangles containing the node. Taking node  $i$  as an example, we use  $\Omega_i$  to denote all the triangles containing it, illustrated as the shaded region around node  $i$  in Figure 4.6. As  $\phi_i$  vanishes

---

<sup>1</sup>This proof was communicated by Dr. Jie Li

#### 4. FEM FOR MULTIPHASE FLOWS

---

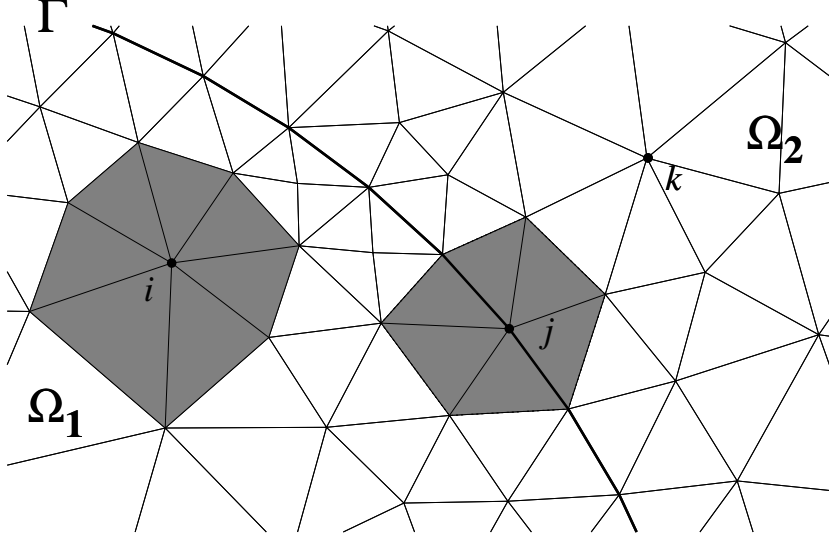


Figure 4.6: The interior and interface edges are depicted in thick and thin solid lines respectively. Node  $i$  is an interior node while node  $j$  an interface node. The shaded region represents triangles containing node  $i$  or  $j$ .

outside  $\Omega_i$ , including on the interface  $\Gamma$ , equation (4.35) turns into:

$$\int_{\Omega_i} \rho \phi_i \frac{du}{dt} d\Omega = p_1 \int_{\Omega_i} \frac{\partial(\phi_i)}{\partial x} d\Omega = p_1 \int_{\partial\Omega_i} \phi_i n_x dl = 0, \quad (4.36)$$

where the first equality is due to the fact that  $p = p_1$  in  $\Omega_i$ , and the last equality holds due to the fact that  $\phi_i$  vanishes on  $\partial\Omega_i$ .

If the test function  $\phi$  is defined on an interface node, node  $j$  in Figure 4.6 for example. Let  $\Omega_{j,1}$  and  $\Omega_{j,2}$  denote the triangles containing node  $j$  in  $\Omega_1$  and  $\Omega_2$ , respectively, and  $\Gamma_j$  be the piece of interface in  $\Omega_j$ . The radius of curvature on the interface is calculated by fitting a circle with three vertices. Since the initial shape is circular and the calculated curvature is a constant:  $\kappa = -1/R$ . In  $\Omega_j$ , the pressure is not a constant. But in our method, the pressure has two values on the interface and it is a constant in  $\Omega_{j,1}$  and  $\Omega_{j,2}$  respectively. As  $\phi_j$  vanishes outside  $\Omega_j$ , equation (4.35) thus turns into:

$$\int_{\Omega_j} \rho \phi_j \frac{du}{dt} d\Omega = p_1 \int_{\Omega_{j,1}} \frac{\partial\phi_j}{\partial x} d\Omega + p_2 \int_{\Omega_{j,2}} \frac{\partial\phi_j}{\partial x} d\Omega + \int_{\Gamma_j} \sigma \kappa n_x \phi_j dl$$

---

### 4.3 Laplace solution for a circular/spherical droplet

$$= p_1 \int_{\partial\Omega_{j,1}} \phi_j n_x dl + p_2 \int_{\partial\Omega_{j,2}} \phi_j n_x dl - \int_{\Gamma_j} \frac{\sigma}{R} n_x \phi_j dl. \quad (4.37)$$

The test function  $\phi_j$  vanishes on the boundary of  $\Omega_j$ , but not on the communal part of  $\partial\Omega_{j,1}$  and  $\partial\Omega_{j,2}$ , which is  $\Gamma_j$ . Hence, we obtain:

$$\int_{\Omega_i} \rho \phi_j \frac{du}{dt} d\Omega = (p_1 - p_2 - \frac{\sigma}{R}) \int_{\Gamma_j} \phi_j n_x dl = 0 \quad (4.38)$$

as  $n_x$  on  $\partial\Omega_{j,1}$  and  $\partial\Omega_{j,2}$  have the opposite sign.

Similar arguments can be applied to test functions defined on midpoint nodes and the weak formulation for the momentum equation in axisymmetric geometry. Therefore the interfacial tension source term is balanced by the pressure term discretely. Without external forcing, the static solution is obtained. In conclusion, we have proved the existence of the static Laplace solution for a circular/spherical droplet in our numerical method. This is accomplished thanks to the explicit representation of the interface and the  $P1d$  finite element space for pressure.

It is worthwhile to check whether this static solution is obtained numerically. As suggested in Xie et al. (2016), we only need to run an inviscid simulation for one time step to verify whether the static solution is obtained. We use the same parameter as in the literature and consider a circular/spherical droplet with radius  $R = 2$ , density  $\rho_0 = 1.0$  and interfacial tension  $\sigma = 73.0$ . The time step is set at  $\Delta t = 10^{-6}$ . The density of the ambient fluid is  $\rho_1$  and we vary the ratio in this experiment. The mesh parameters are  $G = 0.15$  and  $\alpha = 0.05$  (32 nodes on the interface). The error in velocity is presented in Table 4.1. The maximum velocity is approximately  $O(10^{-16})$  (machine accuracy) when the density ratio is not larger than  $10^3$ . The error in velocity is of the order of  $10^{-13}$  when the density ratio is  $10^5$ . We have not yet had an answer for this, but this will not be an issue as the density ratio is typically smaller than  $10^3$  in a two-phase system.

#### 4.3.2 Numerical experiment of spurious current

In the previous section, we have proved that our numerical method obtains the static Laplace solution for a circular/spherical droplet when no external forces are applied. The existence of the static Laplace solution in a numerical method

#### 4. FEM FOR MULTIPHASE FLOWS

---

Table 4.1: Error in velocity after one time step for the inviscid static drop

	$\rho_1/\rho_0$	maximum velocity
Circular droplet	1	$1.07 \times 10^{-17}$
	$10^3$	$6.91 \times 10^{-16}$
	$10^5$	$6.90 \times 10^{-14}$
Spherical droplet	1	$1.49 \times 10^{-17}$
	$10^3$	$1.87 \times 10^{-15}$
	$10^5$	$1.21 \times 10^{-13}$

shows that in theory the method recovers the balance on the interface numerically. Since the method is used mostly to study unsteady flows, it is also important to examine whether this force balance can be retained over a long period. For this purpose, we now investigate the numerical stability of the Laplace solution. This gives an insight on the capability of our method in retaining the force balance condition.

In literature, most researchers study a circular droplet for this numerical test. In our numerical experiment, a spherical droplet is also considered. The diameter of the droplet is set at  $D = 1.0$ . The density of the droplet is chosen as  $\rho = 1.0$  and the interfacial tension coefficient  $\sigma = 1.0$ . For simplicity the viscosity and density ratios of the inner and outer fluid are set to be 1.0. The viscosity  $\mu$  is varied for a desired  $Oh$  number,  $Oh = \mu/\sqrt{\rho\sigma D}$  which is the controlling dimensionless number in this problem. We can interpret it as the ratio between the capillary time scale  $\tau_\sigma = \sqrt{\rho D^3/\sigma}$  and the viscous damping time scale  $\tau_\mu = \rho D^2/\mu$ . Cases with small  $Oh$  numbers are associated with strong capillary effect and it is numerically challenging to simulate.

The initial velocity is set to be  $\mathbf{u} = \mathbf{0}$ . There is no need to set an initial value for pressure as it is deduced from the velocity for incompressible flow. Due to the symmetry condition, we only simulate half of the droplet. The droplet is centred at  $(0, 0)$  of a domain  $[0, 30] \times [-30, 30]$ . We vary mesh size scale  $\alpha$  in equation (2.4) for mesh with different resolutions. The mesh size gradient  $G$  from equation (2.6) is kept fixed at 0.1. In the numerical test, mesh size scale and time steps are chosen so that the computation is stable and converging. Numerical results



### 4.3 Laplace solution for a circular/spherical droplet

are presented in terms of the dimensionless time and the maximum velocity. The time is scaled by  $\tau_\sigma$ . The amplitude of the spurious current is characterised using the maximum velocity  $U_{max}$ . The accuracy of the method is measured by the dimensionless velocity, the *Capillary* number:

$$Ca = \frac{\mu U_{max}}{\sigma} \quad (4.39)$$

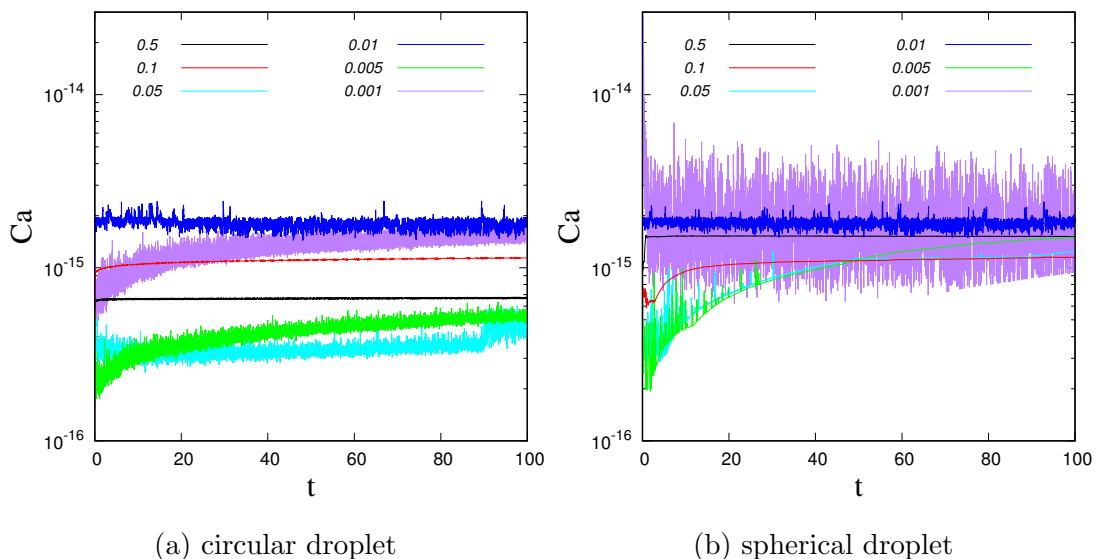


Figure 4.7: The numbers in legends indicates the  $Oh$  number. The left panel (a) is from simulations of a circular droplet, while the right panel (b) is from simulations of a spherical droplet. The computation is performed with maximum mesh size and time-steps so long that it is stable.

Figure 4.7 shows the temporal evolution of  $Ca$  with different  $Oh$  numbers in the simulations. The left panel is from two-dimensional simulations and the right panel shows results from axisymmetric simulations. We observe that for all cases,  $Ca$  starts at values of order  $10^{-15}$  or less. This is as expected since in theory the static solution exists in the framework of our method. For the duration of 100 dimensionless time,  $Ca$  in most cases remains of the same order. For the axisymmetric case with  $Oh = 5 \times 10^{-3}$ ,  $Ca$  starts at a low value and increases during the whole duration  $T = 100$ . One might question whether this

## 4. FEM FOR MULTIPHASE FLOWS

---

trend would continue and eventually lead to  $Ca$  deviating from the theoretical value. We carried out this case to  $T = 1000$  and found that  $Ca$  saturates around  $2 \times 10^{-15}$  from  $T = 320$ . These results show that our static solution is stable and the spurious current is due to machine error for  $Oh \geq 10^{-3}$ , for both two-dimensional and axisymmetric simulations.

We document the maximum  $Ca$  numbers at  $T = 100$  and the corresponding simulation information in Table 4.2. Smaller  $Oh$  number corresponds to weaker viscous damping and more capillary waves of high frequency persists<sup>1</sup>. To keep the simulation stable and convergent, a finer mesh is required for cases with smaller  $Oh$  numbers, as shown in Table 4.2. This fact is also reflected from the observation in Figure 4.7 that the evolution of  $Ca$  looks “noisier” in cases with small  $Oh$ . It is worthwhile to mention that our axisymmetric simulation also retains the force balance over a long period. The axisymmetric simulation is in general more difficult to deal with than two-dimensional simulation. For example, the time step in simulating a spherical droplet with  $Oh = 10^{-3}$  is one fifth of that in simulating a circular droplet with same  $Oh$ . This is owing to the fact that in the axisymmetric geometry, the curvature has a term which is proportional to  $1/r$ . Once an interface node is close to the axis (small  $r$ ), a tiny error in its location will cause inaccuracy in curvature evaluation, and hence, in the calculation of the interfacial tension source term. The successful simulation of a spherical droplet staying static at  $Oh = 10^{-3}$  demonstrates the high capability of our numerical treatment of interfacial tension.

Most methods with implicit representation of the interface do not know the numerical static solution a priori, and have to leave an approximate solution to converge to it. In contrast, we know the static solution from the beginning, and the solution is so accurate (up to some round-off error) that the above experiment is trivial for  $Oh \geq 10^{-3}$ . To further study the stability of this solution, we introduce an artificial sinusoidal disturbance to the initial circular shape of the droplet as:

$$R(\theta) = 0.5 + \epsilon/N \sum_{i=1}^N \sin(n\theta), \quad (4.40)$$

---

<sup>1</sup>Popinet (2009) points out that the damping coefficient of the capillary wave is proportional to  $\nu = \mu/\rho$ .

### 4.3 Laplace solution for a circular/spherical droplet

---

Table 4.2: Maximum  $Ca$  and maximum CFL number at  $T = 100$  for simulation of a circular/spherical droplet with different  $Oh$  and the corresponding mesh information

$Oh$	interface nodes	$\Delta t$	$Ca$	max CFL
Circular droplet				
0.5	8	0.02	$6.7 \times 10^{-16}$	$1.44 \times 10^{-16}$
0.1	16	0.01	$1.1 \times 10^{-15}$	$6.53 \times 10^{-16}$
0.05	32	0.005	$1.7 \times 10^{-15}$	$2.24 \times 10^{-15}$
0.01	32	0.002	$5.2 \times 10^{-16}$	$1.80 \times 10^{-15}$
0.005	64	0.001	$5.2 \times 10^{-16}$	$6.19 \times 10^{-15}$
0.001	256	0.00025	$1.6 \times 10^{-15}$	$9.52 \times 10^{-14}$
Spherical droplet				
0.5	16	0.02	$3.3 \times 10^{-15}$	$3.49 \times 10^{-16}$
0.1	16	0.01	$1.2 \times 10^{-15}$	$3.09 \times 10^{-16}$
0.05	32	0.005	$2.0 \times 10^{-15}$	$8.48 \times 10^{-16}$
0.01	32	0.002	$1.2 \times 10^{-15}$	$7.41 \times 10^{-16}$
0.005	64	0.001	$1.5 \times 10^{-15}$	$2.65 \times 10^{-15}$
0.001	256	0.00025	$1.7 \times 10^{-15}$	$7.09 \times 10^{-14}$

where  $N$  is the number of sinusoidal modes,  $\epsilon$  is the total amplitude of the disturbance and  $\theta$  is the argument of the interface point in the polar coordinate system. In this numerical test, we used  $N = 100$  and  $\epsilon = 10^{-6}$ . Here we consider the two-dimensional case with  $Oh = 10^{-3}$ .

For this case, we performed simulation using a quarter of a droplet and a half of a droplet. Initially we chose the quarter-droplet as the simulation is less time-consuming.

The temporal evolution of the maximum  $Ca$  is plotted in Figure 4.8. In simulation performed on coarse meshes (quarter-drop simulation with 8, 16, 32 interface nodes and half-drop simulation with 16, 32, 64, 128 interface nodes), the solution deviates from the static solution. Furthermore, the maximum  $Ca$  follows mainly exponential growth (the vertical axis is in log-scale in the two figures) in the initial stage, and saturates around  $10^{-4}$ , meaning that that the maximum

## 4. FEM FOR MULTIPHASE FLOWS

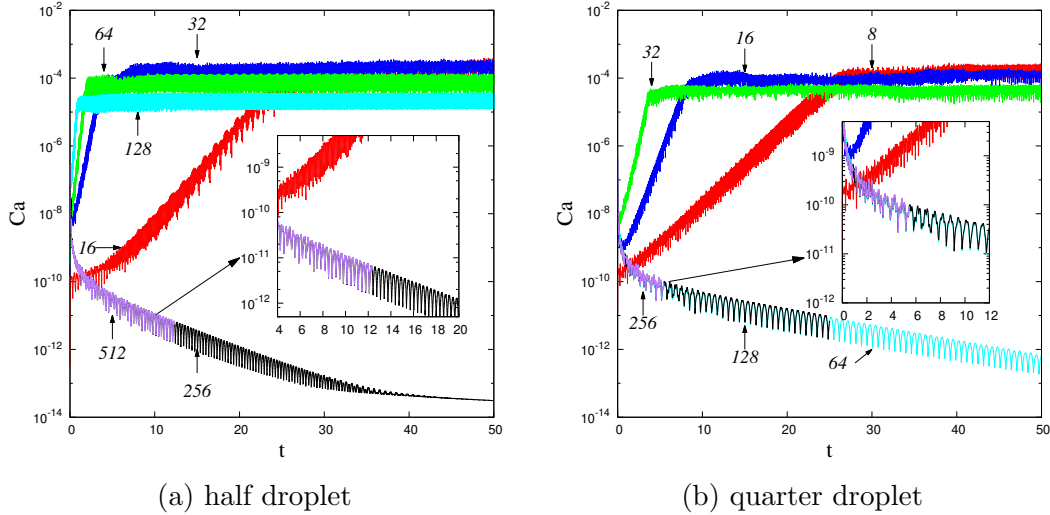


Figure 4.8: The results come from two-dimensional simulation of a slightly perturbed circular droplet. The numbers in the legends indicate the number of nodes on the interface. The left panel (a) is from simulation of a half of a droplet while the right panel (b) is from simulation of a quarter of a droplet.

velocity in the simulation is around 0.1. We notice that the coarser the mesh is, the later the simulation starts to deviate from the static solution. It is believed that this is the result of lack of more unstable modes of higher frequency on coarser meshes. Simulations on fine meshes all converge towards the theoretical static solution as  $t$  increases. As shown in the close-up in Figure 4.8, the temporal evolution of  $Ca$  in simulation with fine meshes agrees very well with each other.

Since the perturbation is symmetric to the horizontal axis, we can utilise the symmetry condition to use the quarter-drop configuration instead of half-drop one. The results turn out to be different from the comparison between simulations of half-droplet and quarter-droplet. There are two distinctions: (1) half-drop simulation with 128 interfacial nodes has the same interface resolution as quarter-drop simulation with 64 interfacial nodes, but the half-drop simulation does not converge to the static solution; (2) the oscillation amplitude of  $Ca$  vanishes in half-drop simulation while in contrast the quarter-drop simulation ends up with one mode and the oscillation amplitude is retained. It is reasonable to believe that the additional symmetry boundary in quarter-drop simulation has

an influence: one special oscillating mode might be promoted by this condition and thus the amplitude is retained.

## 4.4 Benchmark test: drop/bubble oscillation

In the numerical experiment of the Laplace solution, the motion of the interface is tiny as the interface is nearly kept circular/spherical. In this section, we consider the axisymmetric oscillation of a perturbed drop/bubble. In this example, the interface undergoes moderate deformation. The accuracy of our method is validated against the theoretical solution by Prosperetti (1980).

The drop/bubble is initially set at rest. The interface is perturbed as:

$$R(\theta) = R_0 + \epsilon_n P_n(\cos\theta), \quad 0 \leq \theta \leq \pi \quad (4.41)$$

in which  $R_0$  is the unperturbed radius,  $\epsilon_n$  is the amplitude of the initial perturbation of mode  $n$  and  $P_n$  is the Legendre polynomial of order  $n$ . Prosperetti (1980) obtained the solution for this initial value problems for a free-surface droplet/bubble. The Laplace transform of the oscillation amplitude  $a(t)$  is written as:

$$\tilde{a}(p) = \frac{1}{p} \left( a_0 + \frac{p\dot{a}_0 - \omega_n^2 a_0}{p^2 + 2b_0 p + \omega_n^2 + 2\beta b_0 p \tilde{Q}(p)} \right) \quad (4.42)$$

in which  $a_0$  is the initial amplitude,  $\dot{a}_0$  is the initial derivative of  $a(t)$ ,  $\omega_n$  is the angular frequency and  $b_0$  is the decaying rates. The expressions of  $\omega_n$ ,  $b_0$ ,  $\beta$  and  $\tilde{Q}(p)$  are different for an oscillating drop or bubble. They are listed in Table 4.3. Here  $\sigma$  is the interfacial tension,  $\nu = \mu/\rho$  is the kinematic viscosity, and  $I_n(q)$  and  $K_n(q)$  are modified Bessel function of the first and second kind, respectively. The analytical solution is numerically computed by a numerical Laplace inversion method (Durbin, 1974).

We first simulate the oscillation of a free-surface bubble. In the numerical experiment, the physical parameters are  $R_0 = 1$ ,  $\rho = 1.0$ ,  $\sigma = 1.0$ , and  $\mu = 0.01414$  ( $Oh = \mu/\sqrt{2R_0\rho\sigma} = 0.01$ ). Only perturbation of the second mode is considered and the initial perturbation is set to be  $\epsilon_2 = 0.01$ . The oscillating amplitude of the top node (corresponding to  $\theta = 0$ ) is plotted against time  $t$  in Figure 4.9. The simulated result (drawn as black circles) is compared to the

#### 4. FEM FOR MULTIPHASE FLOWS

---

Table 4.3: The initial value solution of an oscillating drop/bubble

	Drop	Bubble
$\omega_n^2$	$\frac{n(n-1)(n+2)\sigma}{\rho R_0^3}$	$\frac{(n+1)(n-1)(n+2)\sigma}{\rho R_0^3}$
$b_0$	$(n-1)(2n+1)\nu/R_0^2$	$(n+2)(2n+1)\nu/R_0^2$
$\beta$	$(n-1)(n+1)/(2n+1)$	$n(n+2)/(2n+1)$
$\tilde{Q}(p)$	$\frac{1}{1 - \frac{1}{2}\Gamma_n(R_0\sqrt{p/\nu})}$	$-\frac{1}{1 + \frac{1}{2}\Gamma_n(R_0\sqrt{p/\nu})}$
$\Gamma_n(q)$	$q \frac{I_{n+1/2}(q)}{I_{n+3/2}(q)}$	$q \frac{K_{n+1/2}(q)}{K_{n-1/2}(q)}$

analytical solution (draw as solid line) from the initial-value problem in Figure 4.9(a), and a good agreement is obtained. The mesh in our simulation has 854 vertices, 64 of which are on the interface ( $\alpha = 0.025$ ,  $G = 0.1$ ). Figure 4.9(b) is a close-up of the sixth crest illustrating two more numerical results. The black squares represent the simulated result using a coarser mesh with 592 vertices in total, 32 of which are on the interface ( $\alpha = 0.05$ ,  $G = 0.1$ ). A clear convergence towards the analytical solution is observed. The empty circles are obtained on a structured mesh of size  $128 \times 128$  ( $= 16384$ ) nodes (Li et al., 2005). The quality is similar to that of the unstructured mesh with 854 vertices. The relative difference at this crest is about 3% between our simulation and Prosperetti's theory. In the simulation using 854 vertices (the number of edges is 2331), the number of unknown values is approximately 6000<sup>1</sup>. At each time step, computing time spent on the numerical solver is approximately 0.46 s, and computing time spent on mesh manipulation is approximately 0.0036 s. Most ( $> 99\%$ ) of the computing time is spent on the linear solver, and if the total number of unknown values is reduced by a great amount, the computing cost can then be reduced significantly. By contrast, the total number of unknowns is approximately 32000 if the  $128 \times 128$  structured mesh is used. Hence, this numerical test not only validate both spatial and temporal accuracy of our method, but also demonstrate that less computing cost is required compared to structured mesh method.

---

<sup>1</sup>The velocity ( $u$ ,  $v$ ) is defined on both vertices and edge midpoints

#### 4.4 Benchmark test: drop/bubble oscillation

---

Compared to the study of the static Laplace solution, a finite size of perturbation is induced, resulting in relatively larger deformation of the interface. It is more likely to excite spurious currents. Hence it is much more challenging to obtain a stable and accurate solution, especially for cases with a small  $Oh$  number. We have to increase mesh nodes on the interface in order to keep the effects of spurious currents under control. In our next experiment, we consider the oscillation of a free-surface bubble and a free-surface droplet with  $Oh = 10^{-3}$ . The viscosity is set as  $\mu = 0.001414$  and the mesh used in this numerical experiment has 256 nodes on the interface. We only consider the initial perturbation of the second mode and record the oscillating amplitude of the top node. The simulated results are compared to the corresponding analytical initial-value solution in Figure 4.10. The top figure is the result from an oscillating droplet, and the bottom figure is the result from an oscillating bubble. We observe that the droplet oscillation decays much slower than bubble oscillation. Both simulations are in excellent agreement with the analytical solution.

Numerical simulation of oscillating droplet/bubble at  $Oh \sim 10^{-3}$  or smaller is very rare in the literature. To our knowledge, this is the first successful comparison to Prosperetti's theory at such a small  $Oh$  number, demonstrating that our method has great advantages in handling spurious currents.

#### 4. FEM FOR MULTIPHASE FLOWS

---

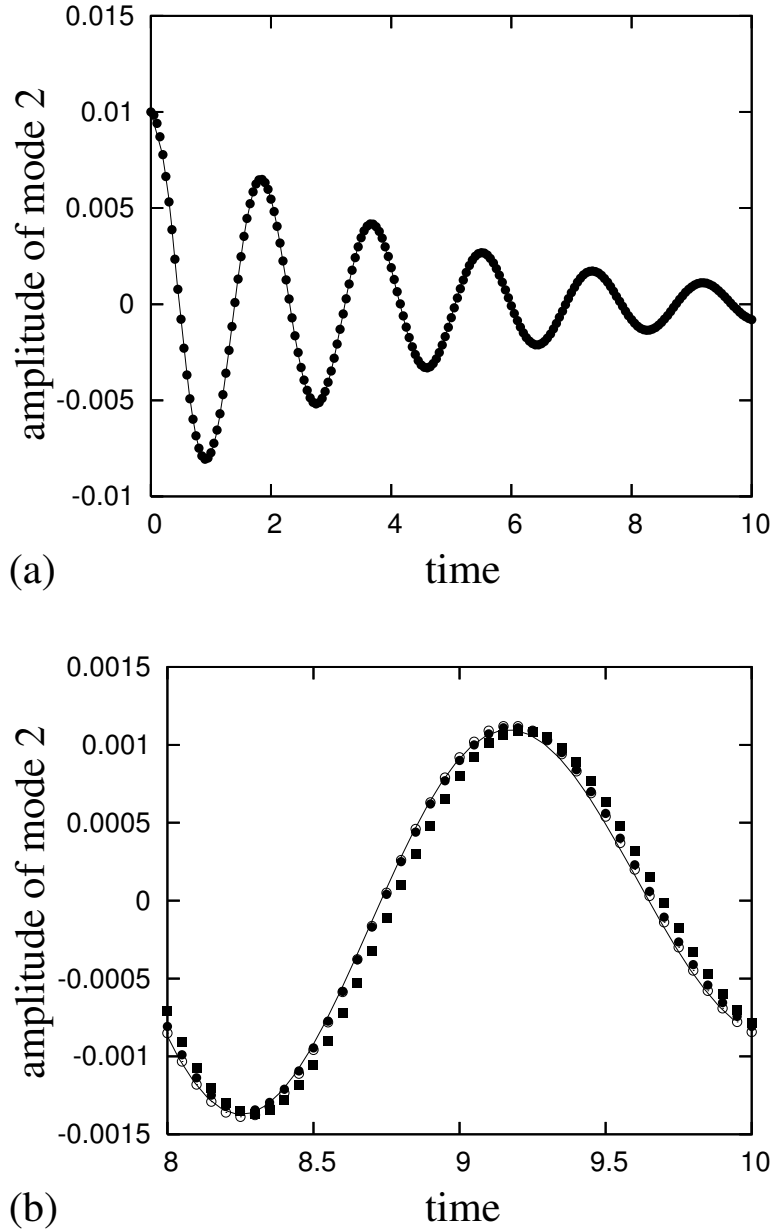


Figure 4.9: Temporal evolution of the second mode of deformation of a bubble set in a liquid initially at rest. (a) Our simulation uses a mesh with 854 vertices (the black circles). The theoretical curves are obtained from the exact solution to the initial-value problem (64 interface nodes, the black circles). (b) A close-up of (a) alongside with the results of a unstructured mesh with 592 vertices (32 interface nodes, the black squares) and structured mesh of size  $128 \times 128$  (the empty circles). The simulation using structured mesh is from Li et al. (2005).



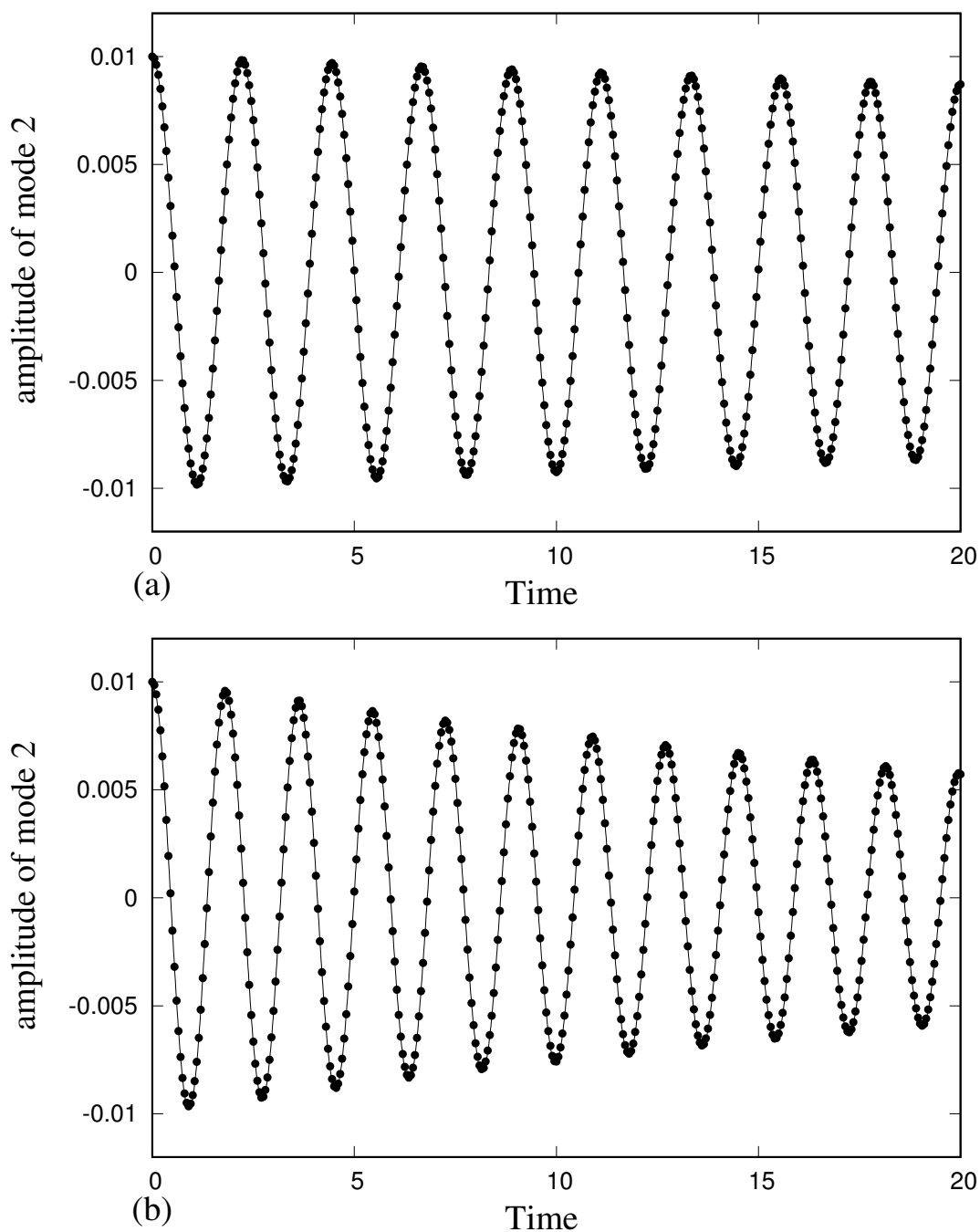


Figure 4.10: Comparisons between the analytical solution (in black solid lines) and the simulated results (in black circles) of an (a) oscillating droplet, and (b) oscillating bubble with  $Oh = 10^{-3}$ .

## 4. FEM FOR MULTIPHASE FLOWS

---

## Chapter 5

# Multiphase flow with interface topology changes

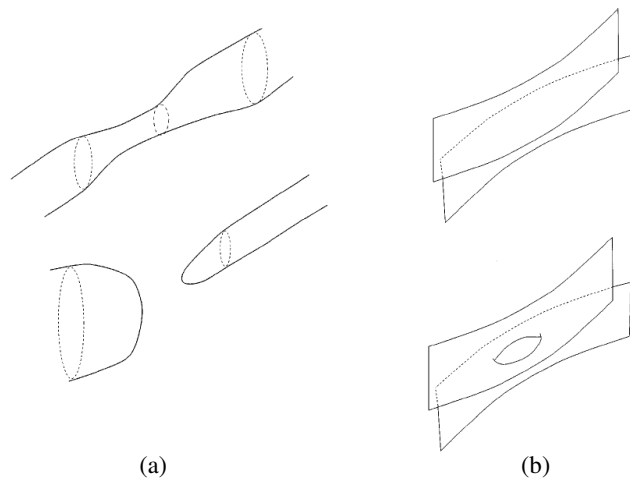


Figure 5.1: Two examples of interface topology changes are sketched: (a) liquid thread breakup; (b) thin film rupture. The two images are from Scardovelli and Zaleski (1999).

It is a common phenomenon that the interface undergoes topology changes in multiphase flows. For instance, a long liquid thread breaks up due to Rayleigh-Plateau instability, as illustrated in Figure 5.1(a), or the thin gas film between two droplets ruptures and then droplets coalesce together, as shown in Figure

## 5. MULTIPHASE FLOW WITH INTERFACE TOPOLOGY CHANGES

---

5.1(b). These topology changes not only lead to severe difficulties in theoretical analysis, but also in the practical implementation of numerical methods, which is the concern of this chapter.

In the first part of this chapter, we demonstrate how the adaptive mesh generator is used to tackle interface topology changes numerically. Then the numerical implementation is validated with two different problems: droplet formation from a faucet and the head-on collision of two droplets.

### 5.1 Interface split/re-connection algorithms

In methods where the interface is implicitly captured such as LS and VOF, the interface is constructed from the volume fraction (in VOF) or the LS function (in LS). Hence interface topology changes are dealt with automatically and effortlessly. Whereas this is not so in methods with an explicit representation of interface such as ours. An extra treatment is required to split and re-connect the interface: some old connections must be broken and some new connections must be established.

Assuming that all previous steps have been done correctly, a new issue arises because the newly established interface is in general not smooth enough, especially when the thin region consists of more than one layer of elements. For instance, the top right panel in Figure 5.2 illustrates the mesh after the interface was broken up in the 3D moving mesh method of Quan and Schmidt (2007). It is highly irregular, and without optimisation of the interface shape, severe numerical instabilities will be excited. Quan and Schmidt (2007) fitted the cut interface with a local sphere. The mesh after adjustment is drawn in the bottom right panel of Figure 5.2, which is much more smooth than before.

Unlike the approach working on the thin region consisting of multiple layers of elements, we would like to proceed topology changes on only one layer of elements. This configuration is achieved using our adaptive mesh generator, as explained in Section 2.2. The advantages of having a single layer of elements in the thin region are that: (a) it is sufficient to accurately describe the flow in the thin region; (b) the efforts spent on interface split, re-connection and smoothing are then minimised.

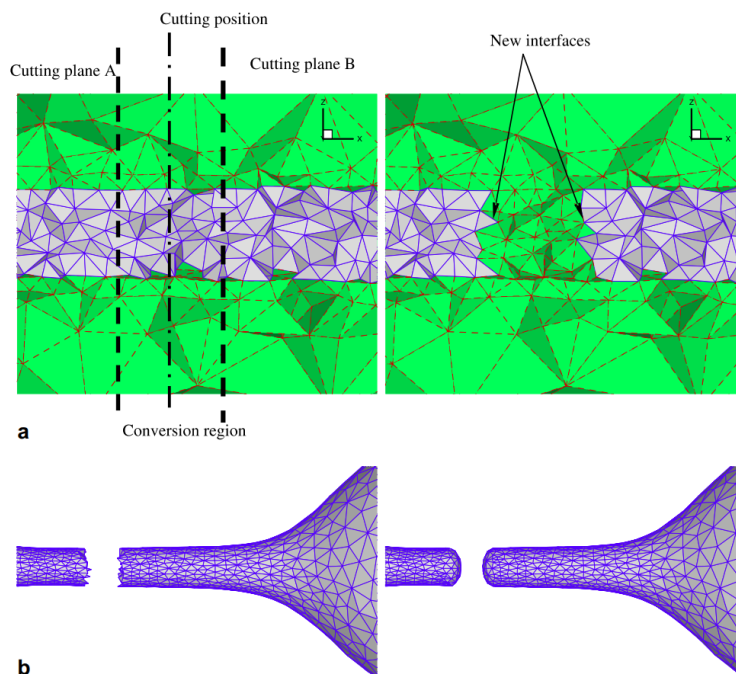


Figure 5.2: Quan and Schmidt (2007) cut the interface while the thin region consists of multiple layers of elements. The top two panels show the mesh near the interface before and after the interface breaks up, respectively. The bottom panels shows the mesh near the break-up point before and after conversion. The gas phase is shaded in green while the liquid shaded in grey.

Prior to topology changes of the interface, the length scales of the interface gaps become very small, for example, the thread before pinchoff of a capillary jet and the thin gas film before the coalescence of two droplets. Therefore the desired local interface mesh size  $l_s$  is mainly controlled by  $\beta l_d(\mathbf{q})$  in equation (2.5). With well-chosen values of  $\beta$  and  $\alpha$ , the thin region consists of only one layer of elements. We introduce a critical length scale  $l_{breakup}$ : when the minimum of a thread diameter or a film thickness is below  $l_{breakup}$ , the interface is to be broken up. The choice of this length scale is not universal and should be decided upon the simulated problem. In practice, we start with a few simulations using different  $l_{breakup}$  and then choose a scale which is small enough such that the global dynamics is not affected much.

## 5. MULTIPHASE FLOW WITH INTERFACE TOPOLOGY CHANGES

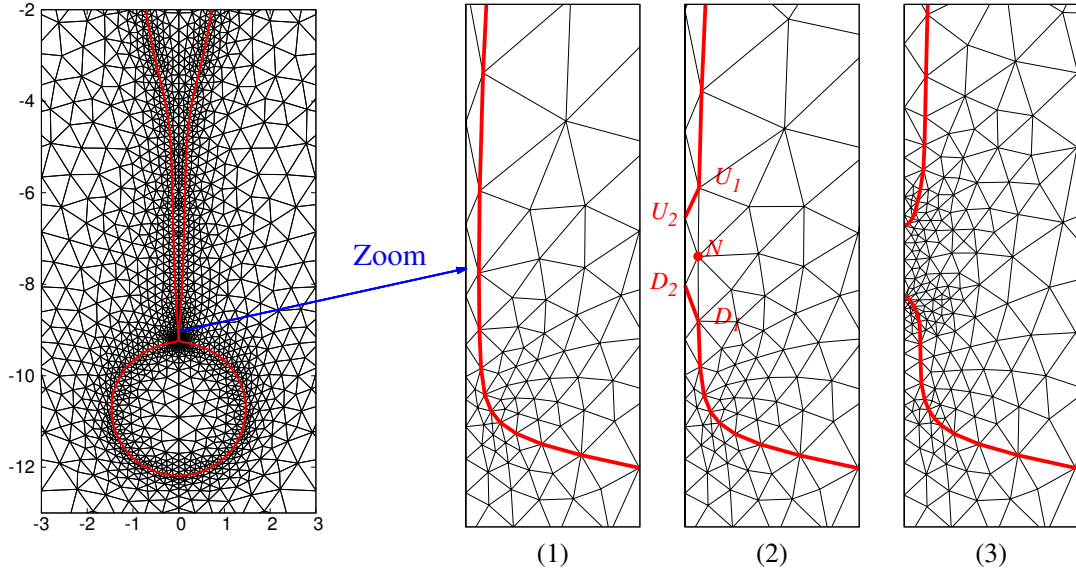


Figure 5.3: These figures are from a simulation of thread breakup. The interface is drawn in red thick solid line and the mesh lines are drawn in black. In the global view, the mesh is much denser near the break-up point compared to that in other regions. Due to symmetry, only half of the configuration is simulated. The close-up shows the sequence of mesh topology changes: (1) one layer of triangles in the thin regions; (2) interface reconnection at the instant of break-up; (3) remeshing after the topology change.

Figure 5.3 illustrates an example of the topology change procedure in the simulation of a thread breakup. In this example,  $\alpha = 0.1$ ,  $\beta = 1.0$  and  $l_{min} = 0.001$ . We only simulate half of the domain due to symmetry. Here we choose to break up the interface when the minimum thread radius is less than  $l_{breakup} = 0.01$ . Triangles between the interface and the symmetry boundary occupy only one layer as shown in Figure 5.3(1). The neck node on the interface is easily identified, as its distance to the symmetry boundary is a local minimum. It is denoted as node  $N$ , drawn as a circular dot in Figure 5.3(2). In practice, interface nodes are listed in an anti-clockwise order starting from the node where the interface intersects the symmetry boundary. Having identified the node  $N$ , we can then split the original list into two sublists: the one before the neck node, and the one after it. The status of the neck node is changed from an “interface” node to an “interior” node.

## 5.1 Interface split/re-connection algorithms

---

The next step is to find the nodes on the interface and on the symmetry boundary that are also adjacent to the neck node. These nodes are denoted as  $U_1$ ,  $D_1$ ,  $U_2$  and  $D_2$ , as in Figure 5.3(2). This can be done effortlessly as the information about which vertices are adjacent to the neck node is explicitly stored. Then we insert the two adjacent nodes on the symmetry boundary,  $U_2$  and  $D_2$ , into one of the interface sublists: node  $U_2$  is inserted into the sublist which starts from node  $U_1$ , and node  $D_2$  is inserted into the sublist which ends with node  $D_1$ . Then the status of nodes  $U_2$  and  $D_2$  are updated from “boundary” node to “interface” node. The status of the triangular elements  $\triangle U_1U_2N$ ,  $\triangle U_2D_2N$  and  $\triangle ND_2D_1$  is updated from the thread phase to the ambient phase. The status of edge  $D_1D_2$ ,  $U_1U_2$ ,  $NU_1$  and  $NU_2$  also need to be updated. Though up to this stage the triangulation remains the same, the interface has been split into two. The single-layer configuration of the thin regions has made this process straightforward and the computing costs are minimised. The topology change leaves a high-curvature tip region, where the interface mesh size is mainly controlled by  $\alpha/\kappa(\mathbf{q})$  in equation (2.4). The newly formed unsmooth interface is then refined by our adaptive mesh algorithm. The refined mesh is displayed in Figure 5.3(3). The topology changes of free-surfaces can be implemented in a similar way. The difference is that some triangles and edges are deleted rather than swapped to another phase.

The numerical implementation of interface topology changes violates the mass conservation. However, the influence can be kept small by choosing an appropriate length scale to control topology changes. For example, we consider the break-up of a perturbed liquid bridge held by two coaxial disks. The radius of the disk is  $R$  and the height of the liquid column is  $4R$ . We set the break-up length scale to be  $0.01R$ . When break-up takes place, liquid near the neck is removed from the liquid phase. Normally only three triangular element will be removed from the liquid phase. We estimate the mass loss of the liquid phase by approximating the removed liquid with a small liquid cylinder. The radius of the cylinder is approximately  $0.01R$  and the height is typically 3 to 5 times of the radius. The volume of the removed liquid is of the order of  $10^{-6}R^3$ , while the liquid volume is of the order of  $R^3$ . The mass loss of the bridge liquid is negligible.

## 5. MULTIPHASE FLOW WITH INTERFACE TOPOLOGY CHANGES

---

Note that the choice of this length scale depends on the simulated problems. The case of thread breakup is not very sensitive to the chosen value of this length as long as it is small enough. On the other hand, a mischosen one will lead to a wrong outcome in the simulation droplet coalescence (interface reconnection). Detailed examples are presented in the following sections.

### 5.2 Dripping faucet

The formation of droplets from a faucet is widely observed in everyday life. We often see that at the end of a tap a pendant drop forms and grows very slowly. Once the size of the pendant drop exceeds a certain limit, it then elongates, forms a neck in the middle, and eventually detaches from the faucet. The final breakup process is so rapid that the details can hardly be captured by the naked eye. This interface topology change is a critical phenomenon connected to a singularity of the nonlinear Navier-Stokes equation with interface (Eggers, 1997). It is a challenging issue to address for a numerical or analytical method. Peregrine et al. (1990) documented the shapes of a pendant droplet near the breakup instant using a high-speed camera. Their experiment involved a large disparity of time and length scales, including (1) the initial slow filling stage, of the order of seconds, (2) the formation of the neck and the transition to a columnar bridge, of the order of a millisecond, (3) the breakup of the interface and the generation of the droplet, of the order of  $100 \mu\text{s}$ , and (4) the recoil of the water thread involving capillary travelling waves. Their pictures have been well reproduced by a number of numerical studies including one-dimensional simulation (Eggers and Dupont, 1994; Fuchikami et al., 1999) and the VOF method (Gueyffier et al., 1999). Due to the weak viscous damping in the experiment ( $Oh \sim O(10^{-3})$ ), the slow filling stage is dominated by interfacial tension prone to spurious currents. Hence it is a good benchmark test for validating our implementation of interface topology change and both the accuracy and robustness of our method.



### 5.2.1 Numerical set-up for dripping

In the experiment of Peregrine et al. (1990), water is slowly dripped from the end of a glass capillary tube whose outer diameter  $D = 5.2$  mm. The initial shape and the inlet boundary condition are not explicitly mentioned except for the vague description “the drops were dripping as slowly as possible in order to minimise the initial motion in the pendant mass of water”. In our axisymmetric simulation, the initial interface is set either spherical or flat, drawn as dashed lines in Figure 5.4. As illustrated in the figure, a parabolic velocity profile is set at the inlet boundary:

$$u(r) = 0, \quad (5.1a)$$

$$v(r) = -V(4r^2 - D^2)/D^2, \quad (5.1b)$$

where  $V$  is the maximum velocity at the inlet, which is set at  $3.0 \times 10^{-3}$  m/s. Both free-surface and two-phase simulation are performed. For two-phase simulations at the outlet boundary we also set a parabolic velocity profile. The outlet velocity is determined according to the ratio between the inlet and outlet diameter such that the same volume of fluid is going in and out of the simulated domain.

In our simulation, the length is scaled by the inlet diameter  $D$ . The outlet diameter is 20 in two-phase simulation and the vertical distance between the nozzle and the outlet boundary is 20. We consider that the fluid flows through a tube before dripping out of the faucet. To ensure a good resolution within the inlet tube, a maximum length scale is set at the inlet boundary and the tube wall boundary ( $l_{inlet} = l_{tube} = 0.025$ ). A global maximum length scale  $l_{max}$  is set at 1.0 to ensure a decent mesh resolution at regions far from the interface. This treatment guarantees that the inlet and outlet boundary conditions are implemented correctly. Other mesh parameters are chosen as:  $\alpha = 0.01$ ,  $G = 0.2$  and  $l_{interface} = 0.01$ . An example of the two-phase mesh is shown in Figure 5.5. The mesh is almost uniform in regions far from the interface, and near the interface, mesh size grows with the increasing distance from the interface as illustrated in the close-up (b). The close-up (a) shows the mesh in the inlet tube where the inlet boundary and the tube wall are resolved with relatively finer mesh.

## 5. MULTIPHASE FLOW WITH INTERFACE TOPOLOGY CHANGES

---

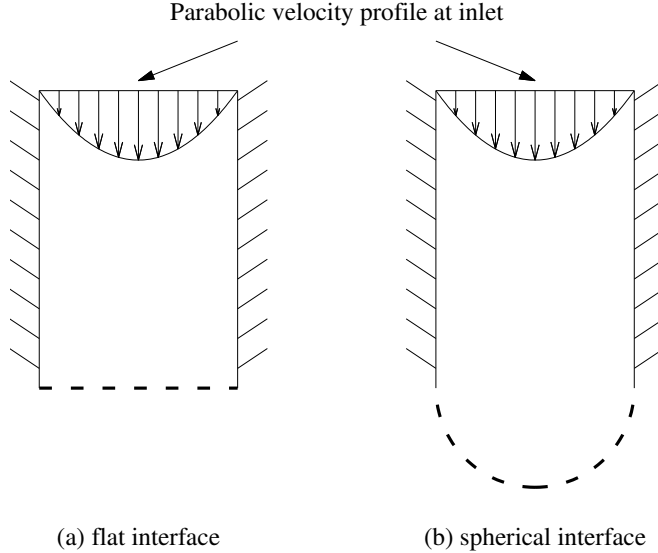


Figure 5.4: Our simulation starts from an initially (a) flat interface or (b) spherical interface. The interface is drawn as a dashed line. At the inlet boundary the velocity profile is set to be parabolic, and at the tube wall the no-slip boundary condition is applied.

Table 5.1: Dimensionless numbers in the simulation of a dripping faucet

$Oh = \mu_2/\sqrt{\rho_2\sigma D}$	$1.45 \times 10^{-3}$
$We = \rho_2 V^2 D/\sigma$	$6.50 \times 10^{-4}$
$Bo = \rho_2 g D^2/\sigma$	3.68
$\rho_2/\rho_1$	816.33
$\mu_2/\mu_1$	45.08

The dripping fluid is water ( $\rho = 10^3 \text{ kg/m}^3$ ,  $\mu = 8.9 \times 10^{-4} \text{ Pa}\cdot\text{s}$  and  $\sigma = 0.072 \text{ N}\cdot\text{m}^{-1}$ ). In the two-phase simulation, the ambient fluid is air. Relevant dimensionless parameters are listed in Table 5.1, where we use subscript 2 for the dripping fluid and 1 for the ambient fluid in the two-phase simulation. We only simulate half of the dripping configuration due to symmetry. In the interfacial tension calculation, the curvature at the fixed contact point with the faucet is obtained by fitting a circle onto the node and the two interfacial nodes which are close to it. This is not the most accurate approximation and spurious currents

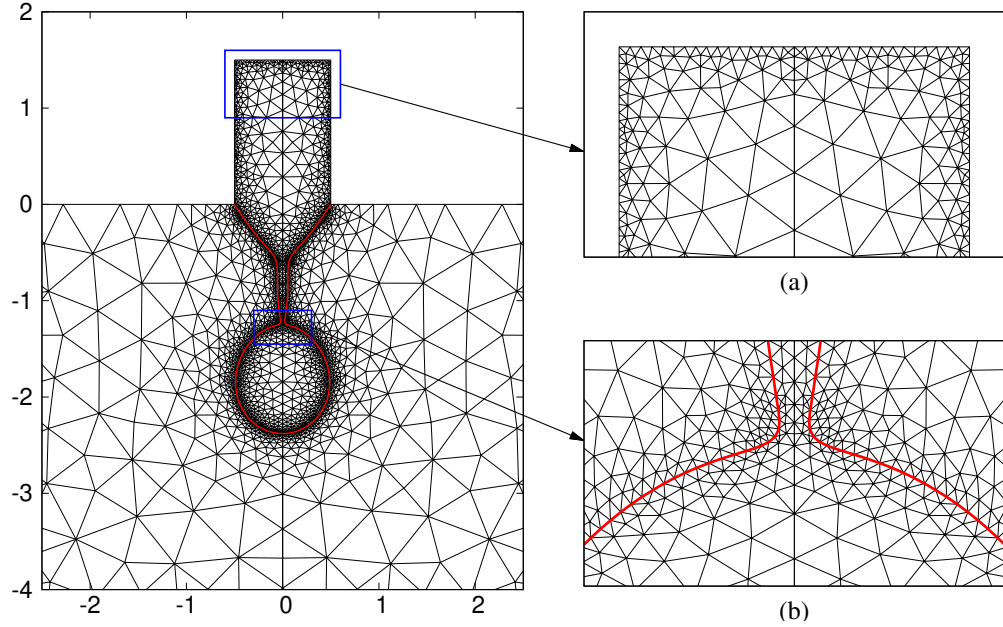


Figure 5.5: The interface is drawn in red solid line: (a) a close-up of the inlet boundary; (b) a close-up of the interface

are easily excited as the  $Oh$  number is around  $10^{-3}$ . We have not come up with a better way to approximate the curvature at the fixed contact point. In our practice, the spurious currents can be suppressed by a finer mesh.

### 5.2.2 Equilibrium shape of a pendant droplet

Before presenting the simulated results of dripping, we carry out a numerical experiment on the equilibrium shape of a pendant droplet. For a faucet of a sufficiently small diameter  $D$ , droplets with a volume  $V$  which is smaller than a threshold volume  $V_c$  can stay still. The static shape of such a pendant drop is determined by the balance between the gravitational and the surface tension forces. This problem is defined by the dimensionless *Bond* number  $Bo = \rho g D^2 / \sigma$  and the dimensionless volume  $V/D^3$ . For simplicity, we consider an axisymmetric pendant water droplet with a free-surface assuming the ambient pressure is 0.

As shown in Figure 5.6, we use  $s$  to denote the arc-length of the droplet interface starting from the axial axis. The interface is represented as  $(r(s), z(s))$

## 5. MULTIPHASE FLOW WITH INTERFACE TOPOLOGY CHANGES

---

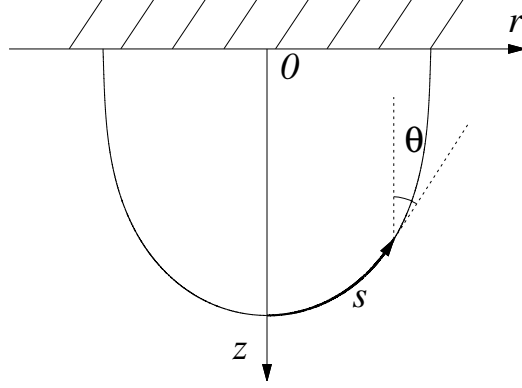


Figure 5.6: The pendant droplet is attached to the wall ( $z = 0$ ). The location of the contact point is  $r = D/2$ . We use a parametric representation  $(r(s), z(s))$  to describe the shape of the pendant droplet.

in the cylindrical coordinate. We denote the angle between the tangent of the interface and the axial axis as  $\theta$ . The four quantities  $r$ ,  $z$ ,  $s$  and  $\theta$  satisfy:

$$\frac{dr}{ds} = \sin \theta, \quad \frac{dz}{ds} = -\cos \theta. \quad (5.2)$$

According to Fuchikami et al. (1999), the force balance on the interface is:

$$P = \sigma \kappa = \sigma \left( -\frac{d\theta}{ds} + \frac{\cos \theta}{r} \right), \quad (5.3)$$

and the force balance in the pendant droplet is:

$$P = \rho g z, \quad (5.4)$$

where  $g$  denotes the gravitational acceleration. Combining the geometry relations in equation (5.2), we obtain a set of ODEs:

$$\begin{cases} \frac{dr}{ds} = \sin \theta, \\ \frac{dz}{ds} = -\cos \theta, \\ \frac{d\theta}{ds} = \frac{\cos \theta}{r} - \frac{\rho g z}{\sigma}. \end{cases} \quad (5.5)$$

The boundary condition at the bottom ( $s = 0$ ) is:

$$\begin{cases} r(0) = 0, \\ z(0) = p_b/(\rho g), \\ \theta(0) = \pi/2. \end{cases} \quad (5.6)$$

where  $p_b$  is the unknown pressure at the bottom of the drop and is used as a controlling parameter.

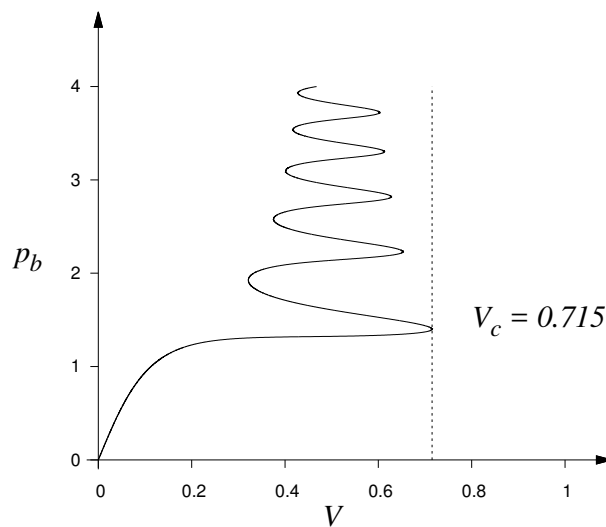


Figure 5.7: The dimensionless pressure at the bottom of the drop  $p_b$  (scaled by  $\rho g D$ ) is plotted as a function of the dimensionless volume  $V$  (scaled by  $D^3$ ) for a pendant water droplet hanging from a faucet with diameter  $D = 5.2\text{mm}$ .

We integrate equation (5.5) from  $r = 0$  to  $r = D/2$  with a fourth-order Runge-Kutta method. Then we can calculate its corresponding volume  $V = \int \pi r^2 dz$ . By varying  $p_b$ , we obtain a set of solutions of the static pendant droplet shape and  $p_b/(\rho g D)$  is plotted against the corresponding dimensionless volume in Figure 5.7. The threshold volume is found to be  $V_c = 0.715$  scaled by  $D^3$ . For a certain volume  $V < V_c$ , the pendant drop might have more than one equilibrium shape, however only the solutions of the branch from the origin to the first turning point in Figure 5.7 are stable static shapes (Padday and Pitt, 1973).

To obtain the static shape of a pendant droplet with our Navier-Stokes solver, we first start with a free-surface simulation of water slowly dripping from the

## 5. MULTIPHASE FLOW WITH INTERFACE TOPOLOGY CHANGES

---

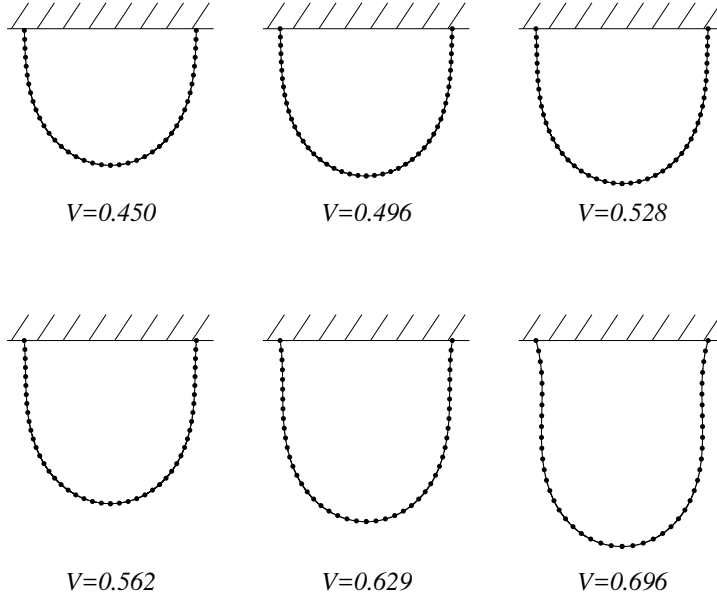


Figure 5.8: The pendant shape from the ODE solutions is drawn in solid lines while the simulation results are drawn in dots. The volume is scaled with  $D^3$ .

faucet. The interface is initially flat and once the volume of the pendant droplet reaches a certain value, the influx is switched off. As our interest is in the final static shape, the viscosity is then set at 1000 times the real viscosity so that the droplet shape converges faster<sup>1</sup>. Since the initial pendant droplet volume is zero and the volume influx is tiny in our simulation, we expect that the converged static solution corresponds to the stable equilibrium shape.

Figure 5.8 displays a comparison between the simulated results and the corresponding stable static solutions. The dots which represent the simulated pendant shape are superposed on the analytical shape drawn as solid lines. The good agreement with the analytical solution shows the high precision of our numerical method. Due to numerical error, the numerical solution deviates from the analytical solution. We perform a convergence study for  $V = 0.629$ . In the convergence study, we set a uniform mesh size density  $l_{interface}$  on the interface. In the analytical solution, the height of the pendant droplet  $L$  (scaled by  $D$ ) is 1.05218. The numerical height from a list of calculations is documented in Table 5.2 together

---

<sup>1</sup>

with corresponding values of  $l_{interface}$ , number of interface nodes  $N$ , and relative error. We plot the relative error of  $L$  against  $l_{interface}$  in Figure 5.9(a). Data from Table 5.2 is drawn as dots and we observe that the relative error converges to zero almost following  $0.4l_{interface}^2$ . This exhibits the second order convergence of our method.

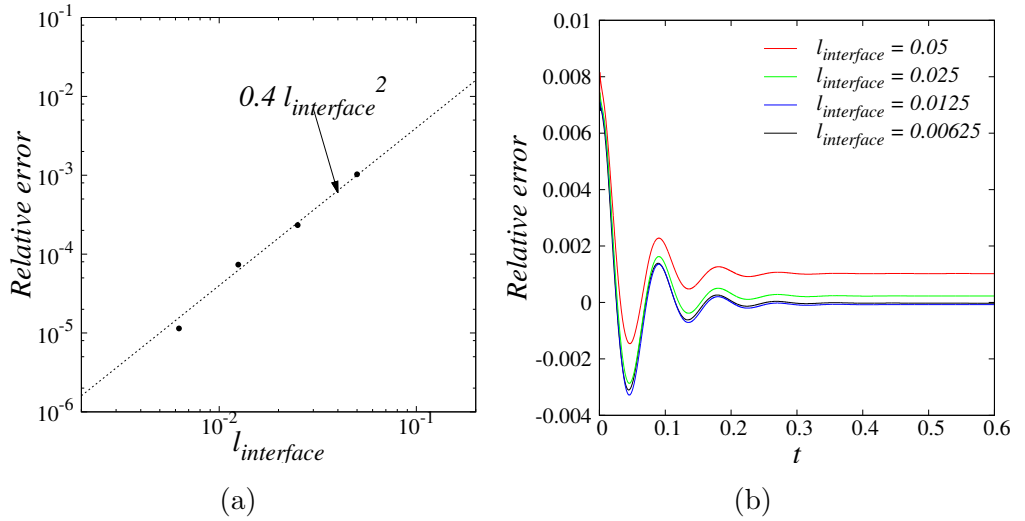


Figure 5.9: (a) The relative error of  $L$  to the analytical solution is plotted against mesh parameter  $l_{interface}$ . Data in Table 5.2 is drawn as dots which almost all fall onto the line  $0.4l_{interface}^2$ . (b) Temporal evolution of the relative error of  $L$  shows that  $L$  converges in every mesh.

Table 5.2: Relative error of  $L$  to the analytical solution for  $V = 0.629$

$l_{interface}$	$N$	$L$	Relative error (%)
0.05	30	1.05325	0.1
0.025	52	1.05242	0.02
0.0125	115	1.05210	0.007
0.00625	230	1.05216	0.001

We note that although  $L$  in each simulation converges as shown in Figure 5.9(b), the converged solution deviates from the static solution. This is due to the spurious current which is induced by the imperfect approximation of curvature

## 5. MULTIPHASE FLOW WITH INTERFACE TOPOLOGY CHANGES

---

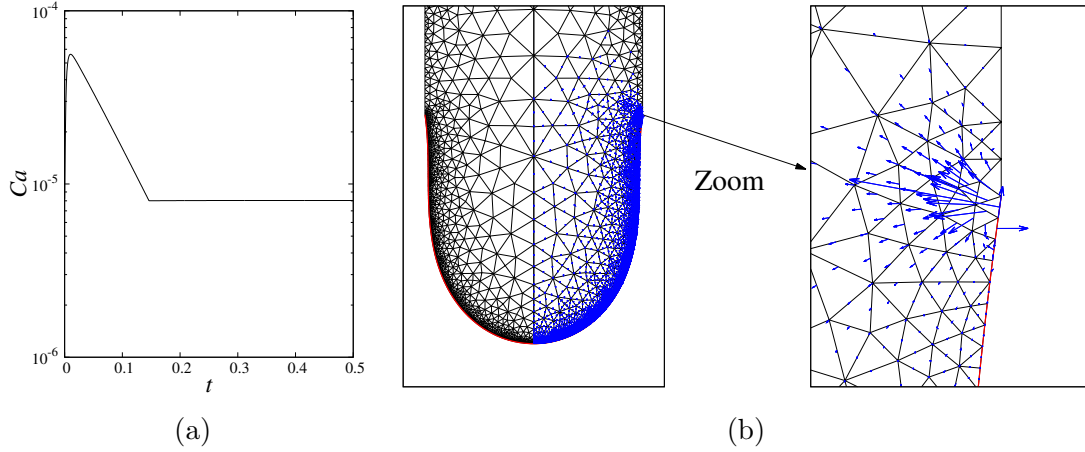


Figure 5.10: (a) illustrates the temporal evolution of  $Ca$  which converges at  $O(10^{-5})$ ; (b) shows the velocity field at  $t = 0.5$  and a close-up near the fixed contact point. The interface is drawn in red lines and the amplitude of the dimensionless velocity is amplified by  $10^4$  times.

at the fixed contact point. To show the effect of the spurious current, we conduct an experiment starting with the converged interface shape ( $l_{interface} = 0.00625$ ) and set the initial velocity at zero. The viscosity is still 1000 times that of the water viscosity. The temporal evolution of the maximum dimensionless velocity  $Ca = \mu U_{max}/\sigma$  is plotted in Figure 5.10(a). Theoretically  $Ca$  should converge to zero, however it saturates around  $10^{-5}$ . The velocity field is plotted in Figure 5.10(b) where the interface is drawn as red solid lines. The velocity is presented in a dimensionless number  $\mu U/\sigma$  and in the figure the amplitude of velocity is multiplied by  $10^4$  times so that the vectors are visible. The maximum velocity appears close to the fixed contact point as shown in the zoomed figure. It is believed that the inaccurate approximation for curvature at the fixed contact point accounts for the spurious currents, which can be reduced by refining the mesh nearby. In this example, we manage to reduce the influence of spurious currents on the pendant shape by using a strong viscous damping. However, we have not found an accurate and stable alternative to calculate the curvature at the fixed contact point.



## 5.2.3 Simulation results of dripping faucet

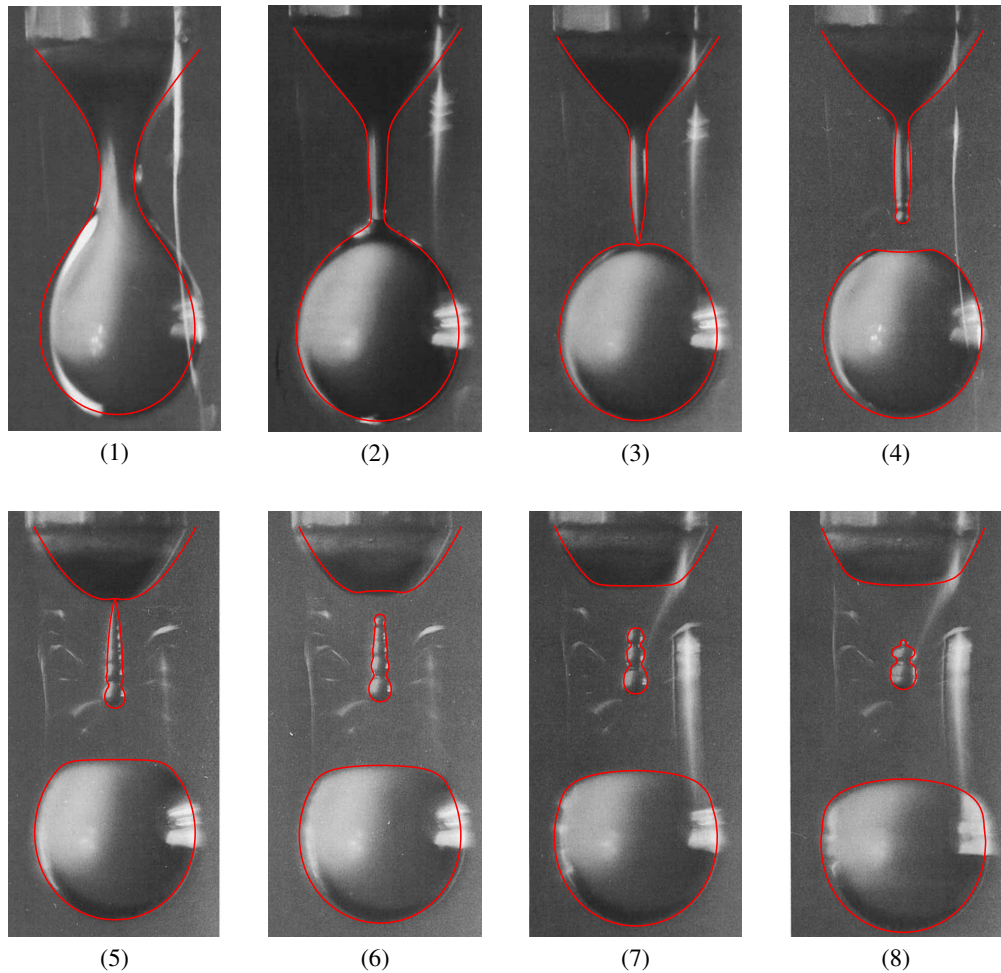


Figure 5.11: The simulation results are superposed on the photograph from the experiment. The interface shape (drawn in red solid line) from different stages are selected: (1-2) necking and the formation of the columnar bridge before the first breakup; (3) the instant after first breakup; (4) recoil of the dripping fluid; (5) the instant after the second breakup; (6-8) oscillation of the secondary droplet.

We now apply our numerical method to simulate the dripping experiment. In our simulation, the numerical parameter  $l_{breakup}$  is set to be 0.01 of the faucet diameter. Figure 5.11 superposes the interface shapes computed from our simu-

## 5. MULTIPHASE FLOW WITH INTERFACE TOPOLOGY CHANGES

---

lation (drawn as red solid lines) over the experimental photo in the experiment of Peregrine et al. (1990). The simulated results are from a two-phase simulation starting from an initially flat interface. Remarkably good agreement with the experimental results is achieved for all stages of the dripping process: (1) shows the initial stage of necking which exhibits an appreciable up-down symmetry; in (2) the necking has formed a columnar liquid bridge; (3) illustrates a sharp conic shape near the pinchoff point just after bifurcation; in (4) the strong interfacial tension after breakup rapidly accelerates the fluid in both water bodies, with the formation of a knob at the tip of the cone and a dimple at the top of the drop; (5) displays the propagation of the small-amplitude capillary waves, while a second bifurcation takes place with the formation of a secondary droplet; and (6-8) shows the interaction between the up and down capillary waves. Our simulation has captured three and four major waves on the droplet, including a minute detail, the tiny nodule at the top of the secondary droplet in (8). We notice that the experimental photograph is not exactly axisymmetric. For example, the pendant drop in the first photograph tilts clearly to the right. It is difficult to speculate what the reason is. It might be due to the some imperfections in the experimental apparatus, for instance, the experiment was not carried out on an anti-vibration table.

The driving force in thread breakup is the interfacial tension. The analytical solution (Eggers, 1997) reveals that the minimum neck diameter close to the breakup point decreases linearly with time. This process is entirely governed by continuum fluid mechanics. In our method, interface topology changes are performed manually. As long as the breakup length scale  $l_{breakup}$  is small enough, the numerical surgery does not disturb the global behaviour of the flow system by a large amount. In Figure 5.12, the interface shape near the breakup instant is shown when the minimum neck diameter reaches  $10^{-2}$ ,  $10^{-3}$  and  $10^{-4}$  of the faucet diameter. The interfaces overlay on each other very well except for near the breakup point, as shown in the close-up. Our concern in this problem is the evolution of the interface shape. Since computing costs increase rapidly with the decrease of  $l_{breakup}$  without obvious gain in accuracy, setting  $l_{breakup} = 0.01$  is adequate for this simulation. This figure also shows that the over-turning of the interface occurs before the breakup. When such over-turning takes place, the

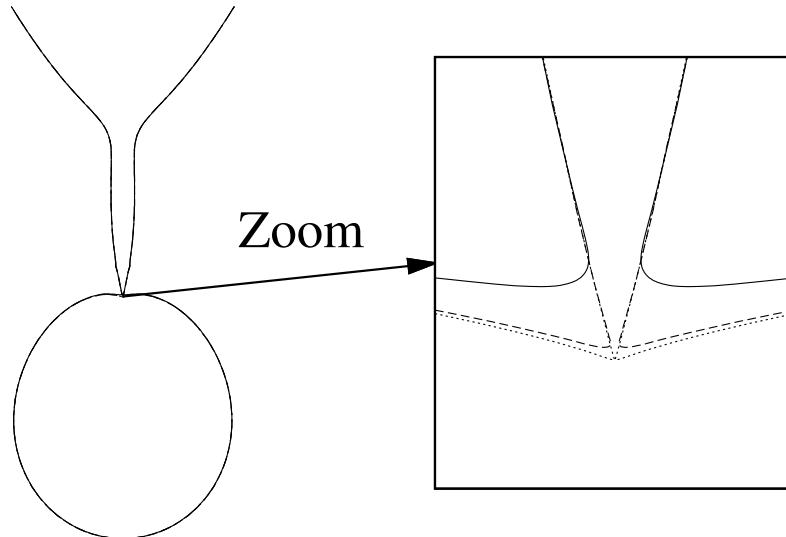


Figure 5.12: These interface shapes are from freesurface simulation when the neck diameter reaches 0.01 (solid line), 0.001 (dashed line) and 0.0001 (dotted line) of the faucet diameter.

one dimensional approximation is not applicable and numerical methods (Eggers and Dupont, 1994; Fuchikami et al., 1999) based on 1D theory were not able to capture this.

It is worthwhile to mention that the initial condition does not affect the final breakup shape much. We perform two simulations starting from a semi-spherical and a flat initial interface. The vertical coordinate  $z$  of the bottom point of the droplet is plotted against the volume  $V$  for both cases in Figure 5.13. Since the inflow volume flux is a constant and  $V$  grows linearly with time, this figure can also be interpreted as a temporal evolution of  $z$ . The semi-spherical interface is not an equilibrium shape. In this simulation, the evolution of  $z$  exhibits oscillations around the red solid line, which represents the evolution of  $z$  in the simulation starting from a flat interface. When both simulations enter the fast-necking stage, the discrepancy between the two is then substantially reduced.

We also compare the interface shapes at different dripping stages from two-phase and free-surface simulations starting from an initially flat interface, as shown in Figure 5.14. The differences between the two are negligible. The effect

## 5. MULTIPHASE FLOW WITH INTERFACE TOPOLOGY CHANGES

---

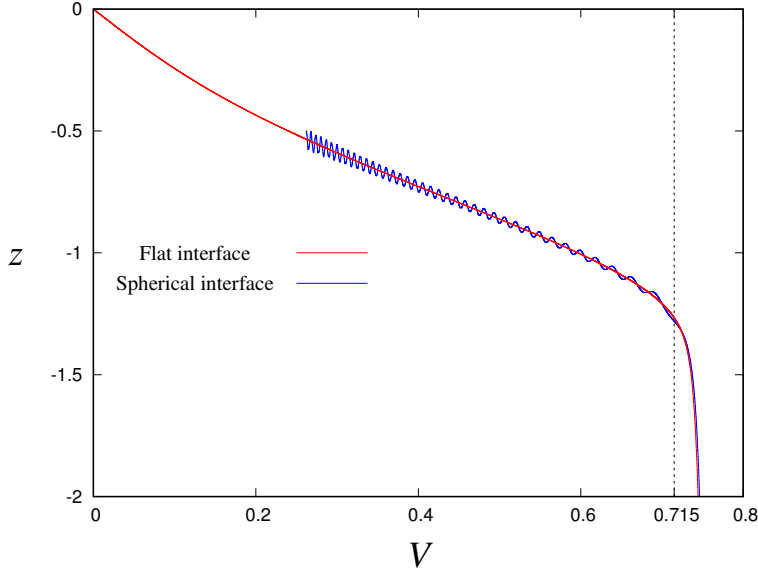


Figure 5.13: Results from simulation starting with a spherical and flat interface are drawn in blue and red lines respectively. The volume is scaled with  $D^3$ .

of ambient gas on the dripping simulation is tiny due to the large density ratio between the dripping fluid and the ambient fluid.

In this example, the  $Oh$  number is of the order of  $10^{-3}$ . Though the spurious current is tiny in the simulation of the static Laplace solution with  $Oh = 10^{-3}$ , it can become severe in the simulation of a dripping faucet. More factors could excite the spurious currents, including the interface advection, the oscillation due to the initial shape, and in particular the inaccurate approximation of curvature at the fixed contact point. One option to suppress spurious currents is to use a larger viscosity. We carry out a simulation with viscosity 10 times as large as that of the water ( $Oh \sim 10^{-2}$ ), with the results that the simulated interface shape near the instant of breakup agrees well with the experimental result even using a coarser mesh  $\alpha = 0.05$ . The final break-up is driven by interfacial tension, and this process is very fast once the volume grows beyond the critical value. Larger viscous damping makes the initial droplet-filling numerically more stable. Using the real parameters is thus more challenging numerically. In our practice, we reduce the effect of spurious currents by using a finer mesh. Figure 5.15 displays

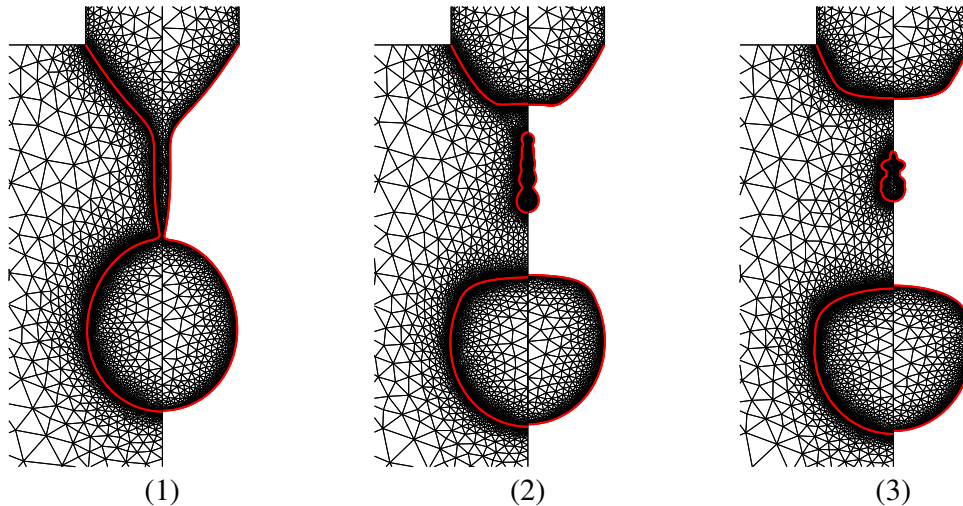


Figure 5.14: The left/right halves of each sub-figure are from free-surface/two-phase simulations, respectively. The interface is depicted in red solid lines. The same mesh parameters ( $\alpha$ ,  $\beta$  and  $G$ ) are applied.

the velocity field from two simulations starting from an initially flat interface. The interface is drawn in black solid line. The blue and red vector arrows represent the velocity from the simulation using a mesh with  $\alpha = l_{interface} = 0.02$  and  $\alpha = l_{interface} = 0.01$ , respectively. All other mesh parameters remain the same. It is evident that the amplitude of spurious currents is significantly reduced in the simulation with a finer mesh ( $\alpha = 0.01$ ), so that the velocity field represented by red vector arrows are much more smooth. Though spurious currents are very strong in the simulation with  $\alpha = 0.02$ , this simulation is still able to reach the final breakup stage. We notice that at the instant  $t = 3.0$ , the velocity field from the two simulations is similar. At this instant, the simulation enters the fast-necking stage, and a smaller time step is used which may contribute to the reduction of spurious currents.

The success in reproducing the experiment of Peregrine et al. (1990) numerically validates our implementation of interface topology changes. Using the real physical parameters of water in the simulation further demonstrates the robustness of our method in coping with spurious currents.

## 5. MULTIPHASE FLOW WITH INTERFACE TOPOLOGY CHANGES

---

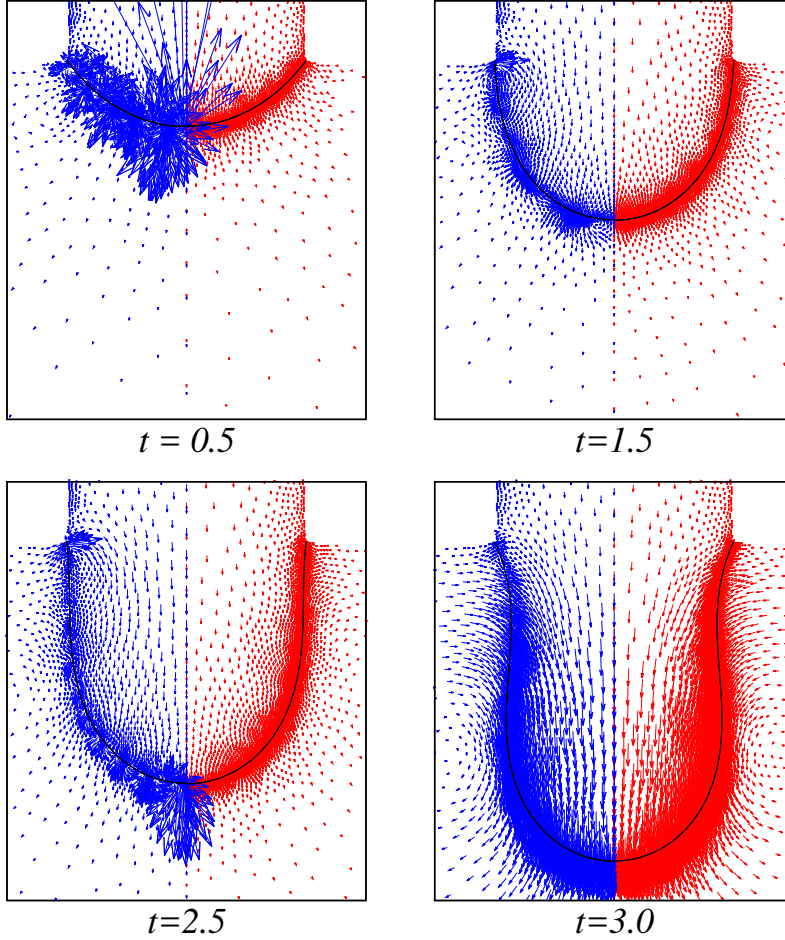


Figure 5.15: The velocity field at four instants before breakup are plotted. The red and blue vector arrows are from the simulation using a mesh with parameters  $\alpha = l_{interface} = 0.01$  and  $\alpha = l_{interface} = 0.02$  respectively.

### 5.3 Droplet head-on collision

Droplet collision occurs frequently in many natural and industrial processes, for example, the formation of raindrops, spray and atomization. The head-on collision of two droplets of the same size, is typically characterized by the *Weber* number,  $We = \rho_l V^2 D / \sigma$ , in which  $\rho_l$  is the liquid density,  $V$  is the relative velocity of the drops,  $D$  is the droplet diameter, and  $\sigma$  is the interfacial tension.

### 5.3 Droplet head-on collision

---

Experimental studies (Ashgriz and Poo, 1990; Bradley and Stow, 1978; Jiang et al., 1992) have identified four distinct outcomes with increasing values of  $We$ : (1) coalescence after minor deformation, (2) bouncing, (3) coalescence after large deformation, and (4) coalescence followed by separation with the generation of secondary droplets.

Further experimental investigation by Qian and Law (1997) revealed that the bouncing regime of tetradecane head-on collision disappeared when the pressure of the ambient gas was reduced from 1 atm to 0.6 atm, while the bouncing regime appeared for water droplet head-on collisions when the ambient pressure was increased from 1 atm to 2.7 atm. These observations suggest that the inter-droplet gas film plays an important role in determining the collision outcome. In a coalescence example, the flow in the intervening gas experiences a wide range of flow regimes, from continuum flow, to rarefied flow, and finally to molecular flow. Zhang and Law (2011) developed the first comprehensive theory for flow in the intervening gas film. Li (2016) incorporated the macroscopic theory into the moving mesh methods and successfully predicted the threshold  $We$  for coalescence-bouncing transitions. The simulated results of a bouncing example were in excellent agreement with the experimental photographs.

The interface topology change in droplet collision is different from the dripping example in the previous section. The break-up of a fluid thread is driven by interfacial tension and a universal macroscopic solution based on continuum mechanics has been found by Eggers (1997). Therefore the choice of  $l_{breakup}$  does not affect the outcome of drop formation as the breakup is predicted to take place in finite time. Whereas in the example of droplet collision, the final stage before gas film rupture involves molecular van der Waals forces. If the controlling breakup length scale  $l_{breakup}$  is set much larger than the length scale for which van der Waals forces are effective, the simulation could predict the wrong collision outcome or the wrong coalescence instant.

In this section, our method is applied to simulate the head-on collision of two droplets of the same size with a coalescence outcome. This example is used to validate our numerical implementation of interface topology change. To start with, the implementation<sup>1</sup> of the macroscopic theory is introduced, followed by

---

<sup>1</sup>This part of code was accomplished by Dr. Jie Li

## 5. MULTIPHASE FLOW WITH INTERFACE TOPOLOGY CHANGES

---

the simulation results and discussions on droplet collision.

### 5.3.1 Modelling the inter-drop gas film

When the two droplets approach each other, gas between the droplets is drained out and the inter-droplet gas film becomes so thin that it can be modelled as a disk with radius  $a$  and height  $h$  ( $h/a \ll 1$ ) as shown in Figure 5.16. We use the dimensionless *Knudsen* number  $Kn = \lambda/h$  to represent the ratio between the mean free path  $\lambda$  of the gas and the thickness of the thin film  $h$ . When  $Kn$  is close to or greater than 1, the continuum assumption fails and the film flow is governed by the Boltzmann equation, rather than by the Navier-Stokes equations.

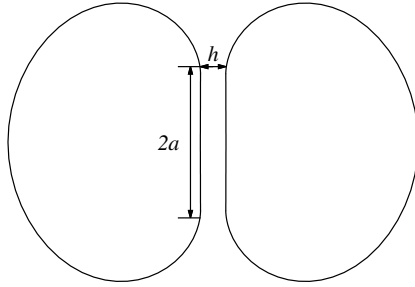


Figure 5.16: The inter-droplet gas film has been squeezed into a disk with height  $h$  and radius  $a$  ( $h \ll a$ ).

Zhang and Law (2011) introduced a comprehensive analysis of the flow in the gas film using the lubrication theory for the continuum regime and Boltzmann equations for the rarefied regime. They found that the rarefied solution for the lubrication layer only differs from the solution for continuum flow by a correction factor. A unified form of the lubrication pressure is written as:

$$p_g(r) = \frac{3\mu_g}{\Delta h^3} (r^2 - a^2) \left( \frac{dh}{dt} + 2\kappa h \right) \quad (5.7)$$

in which  $\Delta$  is a function of the *Knudsen* number  $Kn$ :

$$\Delta(Kn) = \begin{cases} 1 + 6.0966Kn + 0.9650Kn^2 + 0.6967Kn^3 & , Kn < 1 \\ 8.7583Kn^{1.1551} & , Kn \geq 1 \end{cases} \quad (5.8)$$



### 5.3 Droplet head-on collision

Our numerical method is based on the Navier-Stokes equations. To incorporate the rarefied gas effect into our method, we adopt the following form for an effective viscosity in the lubrication layer:

$$\mu = \frac{\mu_g}{\Delta(Kn)}. \quad (5.9)$$

This effective viscosity is about one tenth of the macroscopic viscosity  $\mu_g$  at  $Kn = 1$ , and decreases as  $h^{1.1551}$  with the film thickness for  $Kn \geq 1$ . The rarefied effect reduces the lubrication resistance and therefore promotes droplet coalescence. With the viscosity correction, continuum and rarefied flows are unified in a single set of Navier-Stokes equations. The transition between the two flow regimes is also achieved smoothly as the correction factor  $\Delta(Kn)$  is continuous.

In our numerical method, the thin gas film is represented by one layer of triangular elements, for example, the triangles between the interface (depicted as a thick line) and the symmetry plane (the bottom boundary  $z = 0$ ) in Figure 5.17. For simplicity, the viscosity is taken as a constant in each triangle and the value depends on the local  $Kn$  number. For triangles with one vertex on the interface, for example  $\triangle ABC$  in Figure 5.17, the height of vertex  $A$  is used to calculate  $Kn$ . For triangles with two vertices on the interface, for instance  $\triangle DEF$  in Figure 5.17, the height of the midpoint of edge  $DF$  is used.

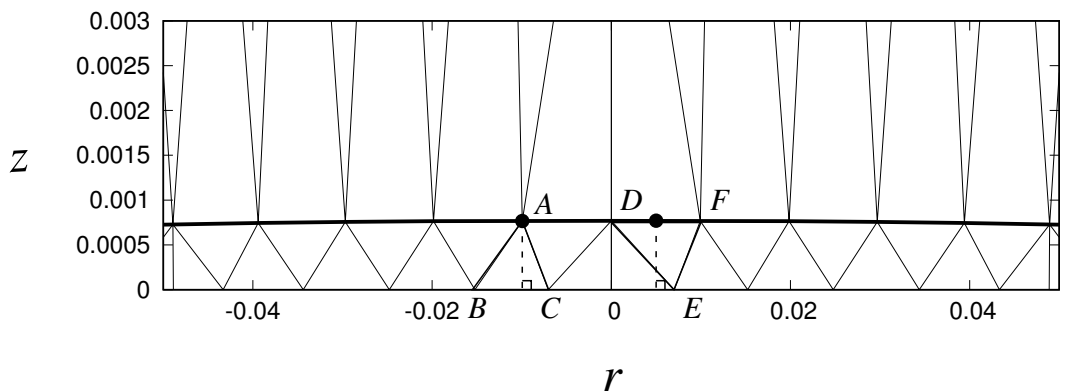


Figure 5.17: The thick line represents the interface and  $z = 0$  is the symmetry plane. In this plot, the radial scale is 10 times as large as the axial scale as otherwise it is impossible to view the triangles in the thin region.

## 5. MULTIPHASE FLOW WITH INTERFACE TOPOLOGY CHANGES

---

The final stage before droplet coalescence is dominated by the attractive van der Waals force. It can be implemented by employing a body force calculated as the negative gradient of the van der Waals potential or by adding a disjoining pressure on the interface (Israelachvili, 2011; Nir and Vassilieff, 1988). Jiang and James (2007) examined the two approaches and concluded that the calculated van der Waals forces through both methods have qualitatively similar effects. Here the van der Waals forces are attractive forces and are approximated by the disjoining pressure model:

$$p = -\frac{A_H}{6\pi h^3(\mathbf{x})} \quad (5.10)$$

where  $A_H$  is the Hamaker constant and  $h(\mathbf{x})$  is the minimum distance from  $\mathbf{x}$  to the other interface. Hence the force balance equation (4.6) turns into:

$$[\mathbf{T} \cdot \mathbf{n}]_-^+ = \left( \sigma \kappa - \frac{A_H}{6\pi h^3(\mathbf{x})} \right) \mathbf{n}. \quad (5.11)$$

In the numerical calculation of this term,  $h$  is considered linear in each interface segment as the interface is represented as a series of linear segments.

Though the van der Waals force is inversely proportional to the cubic power of the decreasing  $h$ , the magnitude of the Hamaker constant is considerably small, generally between  $O(10^{-21})$  J and  $O(10^{-18})$  J. Therefore the force only becomes effective when the gap length is very small, to the order of 10 nm. In order to precisely describe all the flow regimes in the process of droplet collision, it is required that the numerical method resolve length scales ranging from the length scale larger than the droplet diameter ( $O(10^{-4}) \sim O(10^{-2})$  m) down to 10 nm, which is a demanding task for a numerical method.

### 5.3.2 Simulation results

We apply our method to simulate the head-on collision of two tetradecane droplets of equal size. The real physical properties are used in our simulation, as listed in Table 5.3. Using the symmetry condition, we only simulate half of one droplet. The length is scaled by the droplet diameter  $D$ . The computing domain is  $[0, 40] \times [0, 40]$  and initially the droplet is centered at  $(0, 5)$ .

### 5.3 Droplet head-on collision

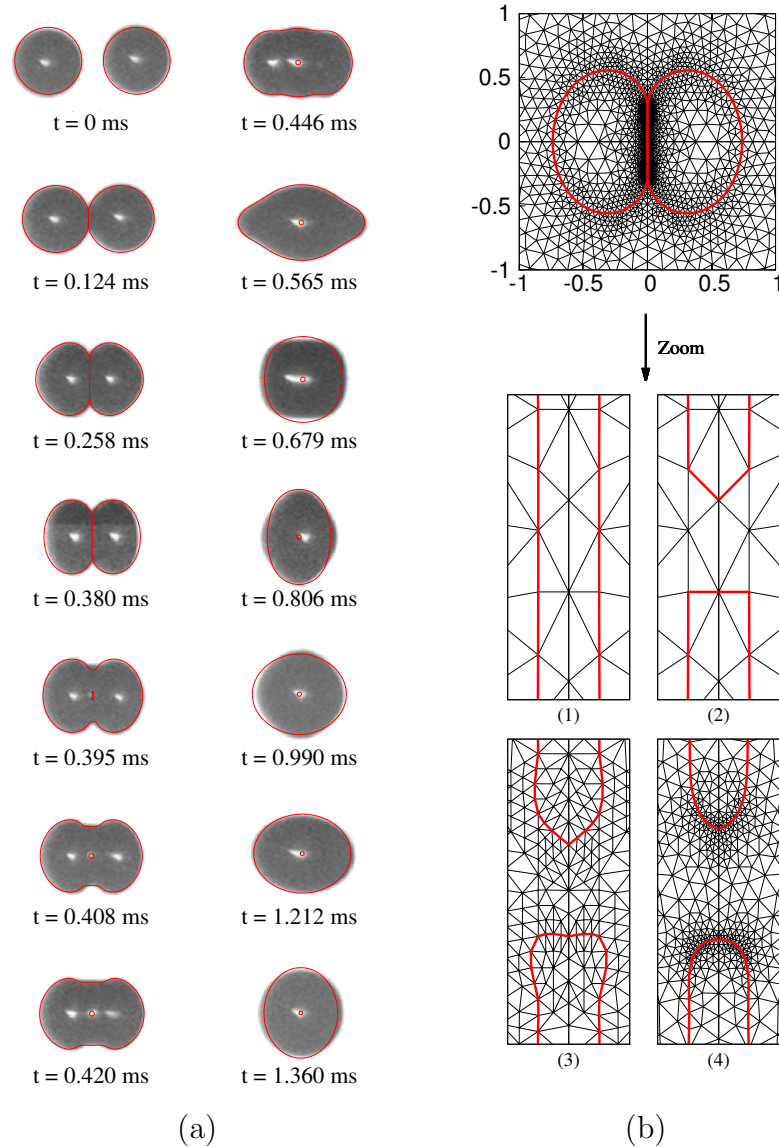


Figure 5.18: (a) Simulated sequences (in red) of the head-on collision of binary tetradecane in air at atmospheric pressure superposed onto the experimental results by Pan et al. (2008). The diameter  $D = 214.4 \mu\text{m}$ , the relative impact velocity is  $V = 0.604 \text{ m/s}$  and  $We = 2.25$ . (b) shows the mesh configuration close to the coalescence instant (the length is scaled by diameter). The zoomed region is  $[-2 \times 10^{-5}, 2 \times 10^{-5}] \times [0.276, 0.277]$ . (1 – 4) illustrate the process of droplet merging, in which the red lines represent the interface: (1) one time step before topology change; (2) the instant of the topology change; (3) 5 time steps after coalescence; (4) 50 time steps after coalescence.

## 5. MULTIPHASE FLOW WITH INTERFACE TOPOLOGY CHANGES

---

Table 5.3: Physical parameters used in the simulation

Air density	$1.225 \text{ kg} \cdot \text{m}^{-3}$
Air viscosity	$1.827 \times 10^{-5} \text{ N} \cdot \text{s} \cdot \text{m}^{-2}$
Air mean free path	$6.9 \times 10^{-8} \text{ m}$
Nitrogen density	$1.138 \text{ kg} \cdot \text{m}^{-3}$
Nitrogen viscosity	$1.787 \times 10^{-5} \text{ N} \cdot \text{s} \cdot \text{m}^{-2}$
Nitrogen mean free path	$5.88 \times 10^{-8} \text{ m}$
Tetrahedron density	$762.0 \text{ kg} \cdot \text{m}^{-3}$
Tetradecane viscosity	$2.128 \times 10^{-3} \text{ N} \cdot \text{s} \cdot \text{m}^{-2}$
Tetradecane-air interfacial tension	$2.65 \times 10^{-2} \text{ N} \cdot \text{m}^{-2}$
Tetradecane-Nitrogen interfacial tension	$2.65 \times 10^{-2} \text{ N} \cdot \text{m}^{-2}$
Tetradecane Hamaker constant	$5.0 \times 10^{-20} \text{ J}$

The first example we present is the head-on collision of two tetradecane droplets with diameter  $D = 214.4 \mu\text{m}$  in atmospheric air. The governing  $We$  number is 2.25. According to the experiment by Pan et al. (2008), this example has an outcome of coalescence. In the simulation, the breakup length scale is set to be  $10^{-5}$  of the droplet diameter. As we use the symmetry condition, this is equivalent to merging the droplets once the minimum thickness of the gas film reaches 4.29 nm, which equals  $2 \times 10^{-5}$  of the droplet diameter.

We superpose the sequence of the simulated interface shape on the experimental sequence in Figure 5.18(a). The time is calibrated by finding the instant at which the simulated interface shape matches the experimental photograph at  $t = 0$  ms. We find that in the simulation, droplet coalescence takes place at the instant  $t = 0.38576$  ms. The droplet merge instant solely depends on when the minimum gas film thickness falls below the set length scale, rather than by using an empirical instant or model. The good agreement with the experimental observations, especially with the post-coalescence oscillation, shows that our method successfully predicts the merge instant and resolved the various flow regimes of the gas film before coalescence. Although there are some discrepancies, they are acceptable since the experiment may not be exactly head-on. Furthermore, extra inaccuracy may be generated when we calibrate time.

### 5.3 Droplet head-on collision

---

Figure 5.18(b) illustrates how our adaptive mesh algorithm handles the topology change. In the simulation, the mesh related parameters are  $\alpha = 0.05$ ,  $\beta = 1.0$ ,  $G = 0.15$  and  $l_{min} = 5 \times 10^{-7}$ . The zoomed region in Figure 5.18(b) is  $[-2 \times 10^{-5}, 2 \times 10^5] \times [0.276, 0.277]$ . The newly formed interface is not smooth at the merge instant and after several time steps. Through constant remeshing, a high-quality triangulation and a much smoother interface are eventually obtained after 50 time steps. In this case, our method resolves length scales ranging from larger than  $D$  to  $10^{-5}D$ . The computing costs are not extremely high: after 50 time steps from the merge instant, the total number of vertices is 3836 and 435 vertices are on the interface. After coalescence, a thin gas disk is trapped in the droplet and will break up into many tiny bubbles. To precisely simulate the evolution of the thin gas sheet, excessive mesh topology changes are needed. The dynamics of the gas sheet after coalescence does not affect the oscillation of the merged droplet. Since our focus is the collision outcome, we then disable the rarefied effects and the van der Waals forces in our code to prohibit unnecessary topology changes.

We also simulate an example with a bounce outcome. The droplet diameter is  $341.2 \mu\text{m}$  and  $We = 2.27$ . Comparisons with the experimental results are displayed in Figure 5.19. The two droplets experience a minor deformation before bouncing apart, and the simulation effectively captures the temporal evolution of this process. This numerical simulation is also in good agreement with the experimental result. The success in simulating the two examples demonstrates that our method has accurately resolved the flow in the inter-drop gas film. Particularly, the agreement with the post-coalescence oscillation in the experiment shows that our method predicts the merge instant with high precision. Though no previous experimental studies have suggested this, it is worthwhile to mention that droplet size may have an influence on the final outcome of droplet collision. For the binary tetradecane droplet collision in 1 atm air, Li (2016) pointed out that the coalescence-bounce transition occurs at  $We = 2.3 - 2.4$  when  $D = 214.4 \mu\text{m}$ , while it takes place at  $We = 1.0 - 1.1$  when  $D = 341.2 \mu\text{m}$ .

## 5. MULTIPHASE FLOW WITH INTERFACE TOPOLOGY CHANGES

---

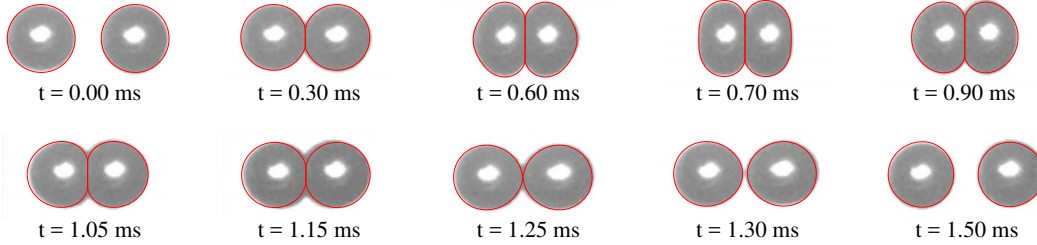


Figure 5.19: The simulated interface is drawn in red solid lines and is superposed on the experimental results by Pan et al. (2008). In this example, the ambient gas is air at atmospheric pressure, the diameter is  $D = 341.2 \mu\text{m}$ , the relative impact velocity  $V = 0.229 \text{ m/s}$  and  $We = 2.27$ .

### 5.3.3 Discussion on droplet collision

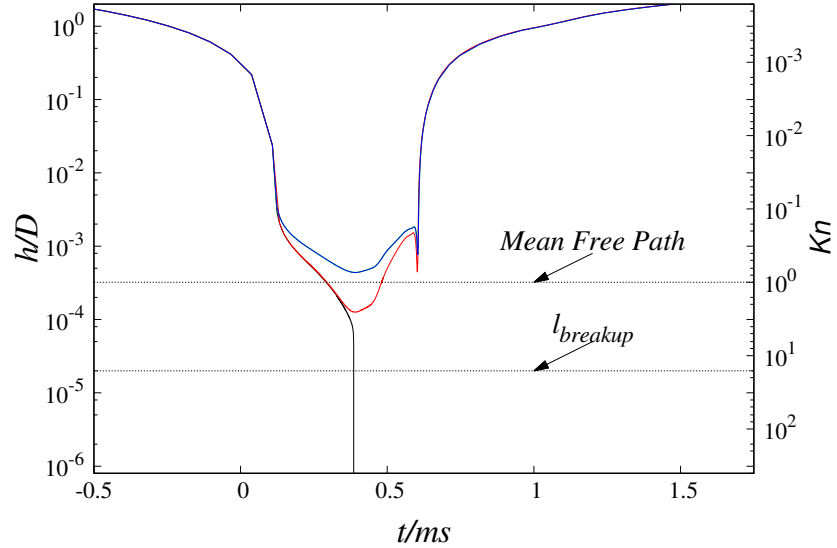
In this part, we discuss some numerical and physical issues in our simulation, including the influence of the rarefied effect and the van der Waals forces, the incompressible assumption, and comparisons with interface non-conforming methods related to this problem.

#### 5.3.3.1 Rarefied effects and van der Waals forces

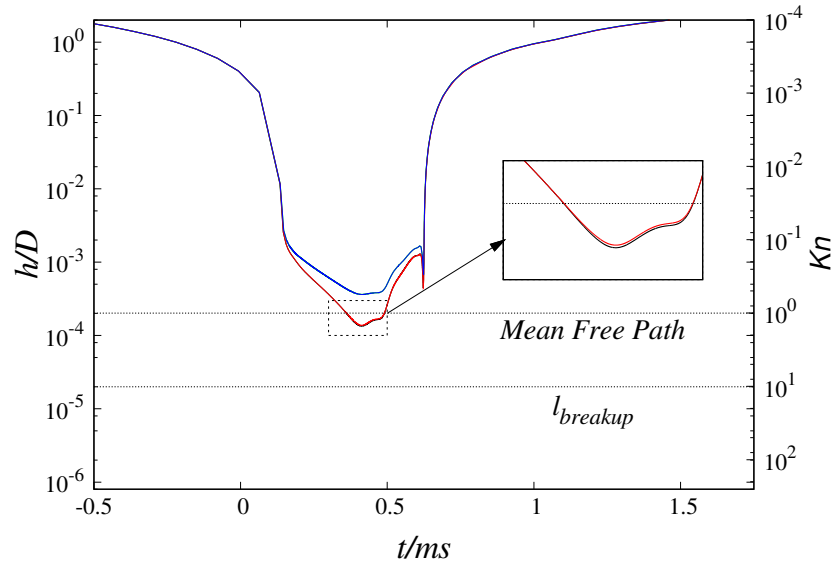
In order to investigate the effect of the rarefied gas and the van der Waals force, we simulate the droplet collision problems using only the rarefied correction, only the van der Waals force, or neither. In Figure 5.20, we plot the temporal evolution of the minimum gas film thickness  $h$  (scaled by  $D$ ) from these simulations. The black solid line is from the simulation with both effects. The red solid line presents the result from the simulation with only the rarefied gas effect. The blue solid line represents the simulation with only the van der Waals force, and the green solid line is from the simulation with no modifications.

In both Figure 5.20(a) and (b), the red or black line (with rarefied correction) are lower than the blue or green lines (without rarefied correction) when the  $Kn$  number is larger than  $10^{-1}$ . According to equations (5.8) and (5.9), the rarefied gas pressure is smaller than the gas pressure without the viscosity correction. The difference between viscosities before/after rarefied correction is small when  $Kn \ll 1$ . For instance, the difference is only 0.6% when  $Kn = 10^{-3}$ . As  $Kn$

### 5.3 Droplet head-on collision



(a)  $We = 2.25$ ,  $D = 214.4 \mu\text{m}$ .



(b)  $We = 2.27$ ,  $D = 341.1 \mu\text{m}$ .

Figure 5.20: The dimensionless minimum thickness  $h/D$  of the thin gas film between the two droplets is plotted against time. (a) presents the simulation for  $We = 2.25$  and  $D = 214.4 \mu\text{m}$  and (b) presents the result from  $We = 2.27$  and  $D = 341.1 \mu\text{m}$ . The time in the two figures is calibrated according to Figure 5.18 and Figure 5.19, respectively. Four cases are simulated for the two problems and are drawn in different colours: with both rarefied effects and van der Waals force (black), only rarefied effects (red), only van der Waals force (blue), and with no modification (green).

## 5. MULTIPHASE FLOW WITH INTERFACE TOPOLOGY CHANGES

---

increases, the effective viscosity decreases. For  $Kn = 0.1$ , the effective viscosity is around 60% of the macroscopic viscosity, and for  $Kn = 1$ , it is reduced to around one tenth of the viscosity with no correction. As a result the lubrication resistance of the rarefied gas film is reduced substantially, and this facilitates the two droplets to approach to each other.

The attractive van der Waals force is included into our method by a disjoint pressure model. As described before, it only becomes effective when  $h$  is of the order of 10 nm, e.g. the  $Kn$  number is around 1. For simulations without the rarefied correction, the film thickness is larger than the mean free path over the entire course of collision. As a result, the blue (with only van der Waals force) and the green (with no modifications) lines are identical in both figures. When the rarefied effect is present, the film thickness is able to reach below the mean free path. The effect of the van der Waals force is reflected through the difference between the red (with only rarefied effect) and the black (with both effects) lines. In Figure 5.20(a), the black line starts to deviate from the red line once  $Kn$  is larger than 1. When  $Kn$  increases to 5, the gas film thickness decreases rapidly, indicating that the van der Waals force prevails. According to equation (5.11), the attractive van der Waals force is proportional to the inverse of the cubic power of the film thickness  $h^3$ . As  $h$  decreases, the attractive force is further enhanced and drop coalescence is inevitable. In contrast, the simulation with only the rarefied effect ends with a bouncing outcome. We notice that the difference between the red and the black lines is tiny in Figure 5.20(b) as the actual outcome is bouncing.

For  $We = 2.25$  and  $D = 214.4 \mu\text{m}$ , the collision outcome is coalescence as confirmed in the experimental study of Pan et al. (2008). The experimental sequences are well reproduced by our simulation as presented in the previous section. By contrast, the simulated collision has a different outcome if the rarefied effects or the van der Waals force are not incorporated. This demonstrates the importance of the rarefied gas effect and the van der Waals force in droplet collision. A numerical method may predict a wrong collision outcome if either of the two effects is not included.

In this example, the interface topology change is performed only when  $h/D$  falls below  $2 \times 10^{-5}$ . In the two cases, the  $Kn$  number is around 10 if  $h/D < 2 \times 10^{-5}$ . At this length range, the outcome of the collision is clear: coalescence



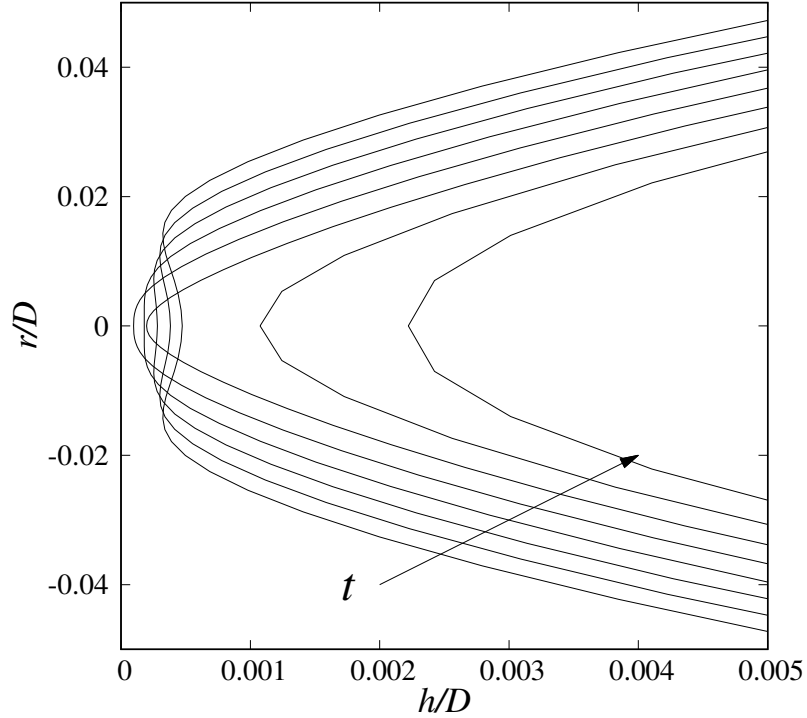


Figure 5.21: Temporal evolution of the interface shape near the second thickness minimum for tetradecane droplets collision in air with  $We = 2.27$  and  $D = 214.4 \mu\text{m}$ . The radial scale is 20 times as much as the axial scale.  $h/D = 0$  is the symmetry boundary.

is inevitable. If the breakup length scale  $l_{breakup}$  is set to be  $10^{-3}$  or  $10^{-4}$  of the droplet diameter, the collision outcome may be wrongly predicted (in the case with  $We = 2.27$  and  $D = 341.1 \mu\text{m}$ ) or the coalescence time is wrongly determined (in the case with  $We = 2.25$  and  $D = 214.4 \mu\text{m}$ ). Our choice of  $l_{breakup} = 2 \times 10^{-5} D$  is necessary in the drop collision simulation. In the two examples, there is no need to further refine  $l_{breakup}$ . In the case of bounce outcome, the  $h$  would never reach  $l_{breakup} = 2 \times 10^{-5} D$ . In the example of droplet coalescence, the *van der Waals* force has already become dominant before  $h$  reaches  $l_{breakup}$ . As shown in Figure 5.20(a), the black solid line is nearly perpendicular to the time axis before  $h$  reaches  $l_{breakup}$ . In fact, we have run the same simulation without interface topology change and the difference between the instant when  $h$  reaches  $10^{-14} D$  and the instant when  $h$  reaches  $3 \times 10^{-5} D$  is only  $5 \times 10^{-5}$

## 5. MULTIPHASE FLOW WITH INTERFACE TOPOLOGY CHANGES

---

ms. In such a short time, the bulk fluid barely moves (the velocity is of the order of 0.1 m/s). Hence further refining  $l_{breakup}$  will not improve the accuracy in the global dynamics of the two droplets, and hence setting  $l_{breakup} = 2 \times 10^{-5} D$  is sufficient enough in this example.

In the bounce example, there is a second minimum in the evolution of  $h$ . The evolution of the interface shape near the second minimum of  $h$  in the simulation for  $We = 2.27$  and  $D = 341.1 \mu\text{m}$  is depicted in Figure 5.21. This rapid decrease of  $h$  is a consequence of the interface shape change from indented to unindented.

### 5.3.3.2 Compressibility of the inter-droplet gas

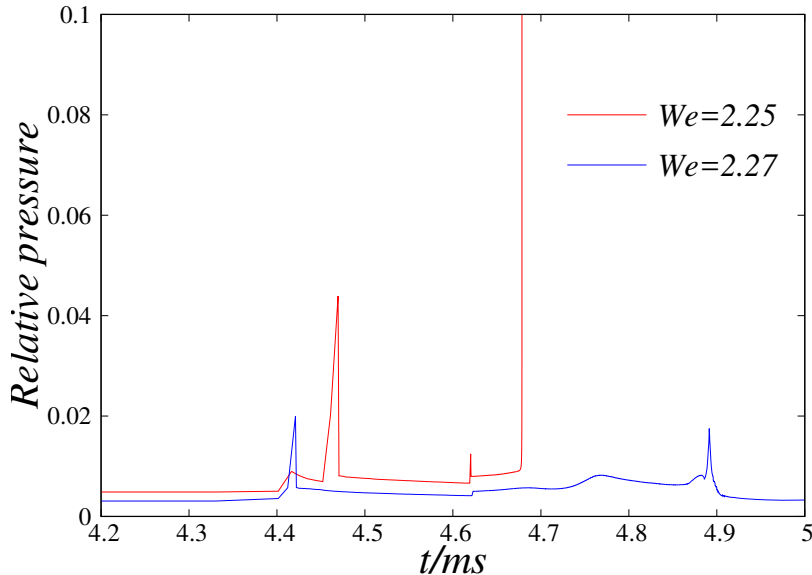


Figure 5.22: Temporal evolution of the maximum relative pressure in the droplet collision simulation for  $We = 2.25$  (in red) and  $We = 2.27$  (in blue). The time 0 is the start of the simulation.

Our method is based on the incompressible assumption. In real droplet collision, the compressibility of the gas film may come into play. To investigate this effect, we consider the two simulations in Section 5.3.2. In the example of  $We = 2.25$  and  $D = 214.4 \mu\text{m}$ , the droplet speed is  $V = 0.3 \text{ m/s}$  and the ambient pressure is  $p_0 = 1 \text{ atm} = 1.013 \times 10^5 \text{ Pa}$ . Hence the dynamic pressure is

$\rho(2V)^2/p_0 = 0.273\%$  of the ambient pressure. In Figure 5.22, the maximum relative pressure is plotted against time for the two collision problems: the red and blue solid lines represent the result from the cases for  $We = 2.25$  and  $We = 2.27$ , respectively. The relative pressure stays a small level apart from a pressure singularity. The occurrence of this pressure singularity is due to the interface topology change. When the van der Waals force prevails, the outcome of droplet collision is determined. Hence the incompressible assumption still yields the correct outcome of droplet collision.

#### 5.3.3.3 Comparison with interface non-conforming methods

It is worthwhile to compare our method to interface non-conforming methods in simulating droplet collision. In interface non-conforming methods, the interface is implicitly captured. The interface topology changes are handled automatically when two interfaces are close enough to each other, typically at a distance of the length scale of a mesh cell. However, if the size of the mesh cell is not small enough, this numerical coalescence may take place much earlier than the actual coalescence instant, or it may take place even when the actual collision outcome is bouncing. In non-conforming methods, it is still challenging to resolve all length scales involved in droplet collision, which span more than 5 orders of magnitude. Once there are cells crossed by two interfaces, an empirical model or parameter is usually necessary to determine whether and when coalescence occurs. For example, Pan et al. (2008) avoided the numerical coalescence by using a front-tracking method and the coalescence instant was based on the experimental results. In their simulation, the minimum gap thickness was about  $0.2 \mu\text{m}$ , which is still an order of magnitude larger than the mean free path. An adjusted Hamaker constant was used which is about  $10^5$  times larger than the real value. In this way, the van der Waals force could be dominant at a larger length scale in their simulation. Kwakkel et al. (2013) prohibited the automatic topology changes by using two marker functions (LS and VOF) and described the flow within the intervening gas film using a film drainage model based on the theory by Zhang and Law (2011). The temporal evolution of the minimum film thickness  $h$  in their simulation was rather smooth and the second minimum of  $h$

## 5. MULTIPHASE FLOW WITH INTERFACE TOPOLOGY CHANGES

---

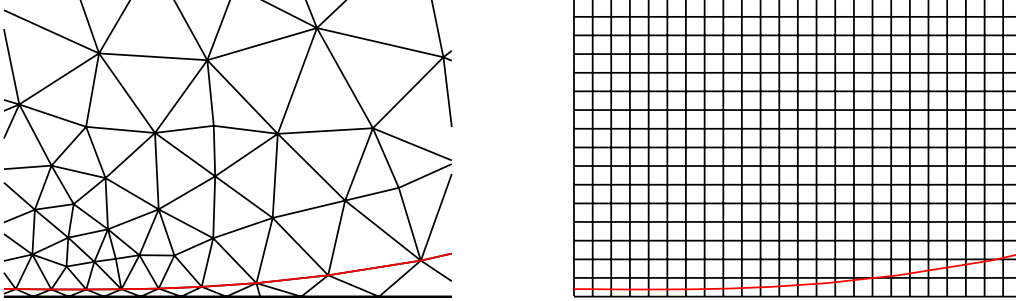


Figure 5.23: The interface represented by the red solid line coincides with mesh lines in our method (left panel). In contrast it intersects cells in non-conforming method (right panel).

did not occur. This indicates that their simulation failed to capture the shape transition from an indented interface to an unindented one.

By contrast, in our method, the adaptive mesh algorithm is able to improve the mesh resolution at the interface region while keeping the total number of vertices at a reasonable number. The rarefied gas effects and the van der Waals force have been correctly incorporated and our method is governed solely by the Navier-Stokes equations with an effective viscosity. All length scales involved in droplet collision are resolved, and the real physical parameters are used. Though the interface topology change requires an explicit treatment, the minimum distance between the two droplets is the only factor that determines whether and when the simulation proceeds to coalescence. As shown in Section 5.3.3.1, the choice of the breakup scale  $l_{breakup}$  ensures that the topology change is only performed once droplet coalescence is certain. Unlike the non-conforming methods, our method does not rely on an empirical model or on adjusted parameters to determine the collision outcome.

Another advantage of our method is that each element only contains one phase, and the viscosity does not need approximation. In contrast, interfacial cells contain a mixture of two phases in non-conforming methods. A comparison between the two interface representation is depicted in Figure 5.23. The viscosity

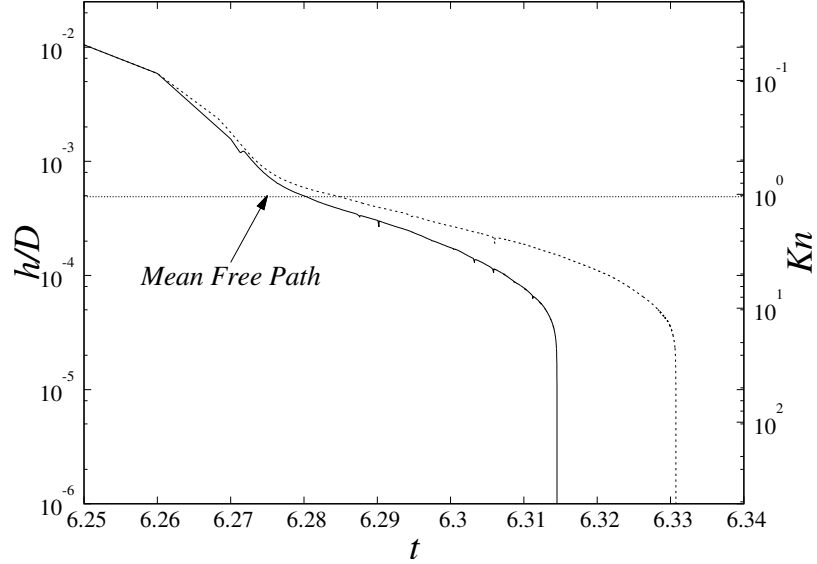


Figure 5.24: Temporal evolution of the minimum thickness of the inter-drop gas film in the  $We = 0.2$  tetradecane droplet collision with the size of  $D = 240 \mu\text{m}$ . The solid/dashed lines depict the cases with/without rarefied viscosity correction, respectively.

in non-conforming method is usually calculated as a weighted mean:

$$\mu = \mu_l C + \mu_g(1 - C) \quad (5.12)$$

where  $\mu_l$  and  $\mu_g$  denote the viscosity of the liquid and gas, and  $C$  is the volume fraction of the liquid phase in the cell. When the viscosity ratio is high, this approximation may inaccurately describe the dynamics of the gas phase. For instance, if  $\mu_l/\mu_g = 100$ , the approximated viscosity is 50 times larger than the gas viscosity if  $C = 0.5$ . The approximation over-estimates the viscosity in the cell intersected by the interface, and hence, the lubrication pressure which is proportional to the viscosity. An exaggerated lubrication pressure may lead to a delay in the coalescence instant or may even shift the outcome from coalescence to rebound as it can prevent the gas film thickness from reaching the intermolecular length scale. For instance, a numerical experiment by Pan and Suga (2005) using the LS method predicted the outcome of the tetradecane droplet collision in nitrogen at  $We = 0.2$  to be bouncing. According to the phase diagram depicting

## 5. MULTIPHASE FLOW WITH INTERFACE TOPOLOGY CHANGES

---

the regime of tetradecane droplet collision (Qian and Law, 1997), the outcome should be coalescence. In their simulation, numerical coalescence is not prohibited and the cell size is  $1/80$  of the droplet diameter ( $D = 240 \mu\text{m}$ ). The cell size is roughly two orders of magnitude larger than the scale at which the van der Waals force dominates. Even though their method has not incorporated the van der Waals force, the outcome is still coalescence as long as the minimum thickness of the inter-drop gas film reaches the same order of the magnitude as the cell size. The bouncing result indicates that the lubrication pressure of the gas film is so strong that the gas film can not be further squeezed. We conducted the same numerical experiment using the same parameters. The physical parameters of nitrogen gas are listed in Table 5.3. The temporal evolution of the minimum gas thickness is plotted in Figure 5.24 for both cases with (solid line) and without (dashed line) the rarefied viscosity corrections. Although the two cases have different coalescence instants, the outcome is clearly coalescence, which is in accord with the phase diagram by Qian and Law (1997).

To summarise, our method is capable of resolving all length scales involved in droplet head-on collisions at a feasible computing cost. No extra empirical/adjusted parameters or coalescence/bounce models are needed. The topology change is decided solely by whether the minimum gas film thickness reaches the scale at which the intermolecular force is dominant. The accurate description of the flow within the inter-drop gas film across different flow regimes enables the method accurately to predict the outcome of droplet collision.

# Chapter 6

## FEM applied to non-isothermal multiphase flows

This chapter is dedicated to non-isothermal multiphase flows. The effect of temperature variation on the flow is through the temperature dependence of important fluid properties, including density and interfacial tension. The induced density non-uniformity leads to buoyancy force. The non-uniform interfacial tension results in a fluid motion along the interface, and eventually flow in the bulk fluid. This flow is often called thermocapillary flow, and is common in many technical processes such as crystal growth and welding. Motivated by its application, we decide to extend our numerical method to include non-isothermal effects. This chapter starts with the governing equations for non-isothermal multiphase flows, followed by numerical implementation of thermal-induced buoyancy and thermocapillarity. The implementation is validated using three benchmark examples. At the end of this chapter, we apply our method to study the effect of thermocapillary flow in the break-up of a liquid bridge.

### 6.1 Mathematical formulation for thermocapillary flow

We consider non-isothermal flow with two incompressible immiscible Newtonian fluids. Their physical properties are density  $\rho_i$ , viscosity  $\mu_i$ , thermal con-

## 6. FEM APPLIED TO NON-ISOTHERMAL MULTIPHASE FLOWS

---

ductivity  $k_i$  and specific heat capacity  $c_{p,i}$  ( $i = 1, 2$ ). The thermal diffusivity is expressed as:

$$\alpha = \frac{k}{\rho c_p}. \quad (6.1)$$

In addition to  $\eta$  and  $\lambda$  in equation (4.1), we define  $\chi$  as the thermal conductivity ratio:

$$\chi = \frac{k_2}{k_1}, \quad (6.2)$$

and  $\gamma$  as the heat capacity ratio:

$$\gamma = \frac{c_{p,2}}{c_{p,1}}. \quad (6.3)$$

We consider a linear relationship between density and temperature:

$$\rho_i = \rho_{i,0}[1 - \beta_i(T - T_0)], \quad (6.4)$$

where  $\beta_i$  is the isobaric thermal expansion coefficient<sup>1</sup> and the subscript 0 indicates a reference condition (Reddy and Gartling, 2010).

For simplicity, the interfacial tension is approximated as a linear function of the temperature:

$$\sigma = \sigma_0 + \frac{d\sigma}{dT}(T - T_0), \quad (6.5)$$

where  $\sigma_0$  is the value of interfacial tension at reference temperature  $T_0$ , and  $d\sigma/dT$  is a negative constant.

The governing equations for non-isothermal multiphase flows include the continuity equation, the momentum equation, and the convection diffusion equation for temperature. They are expressed in vector form as follows:

$$\nabla \cdot \mathbf{u} = 0, \quad (6.6a)$$

$$\rho_{i,0} \frac{d\mathbf{u}}{dt} = \nabla \mathbf{T} + \rho_{i,0}(1 - \beta_i(T - T_0))\mathbf{g}, \quad (6.6b)$$

$$\rho_{i,0} c_{p,i} \frac{dT}{dt} = \nabla \cdot (k_i \nabla T), \quad (6.6c)$$

---

<sup>1</sup> The general equation of state is written as  $\delta\rho/\rho_0 = -\beta_p\delta T + \kappa_T\delta p$  where  $\beta_p$  is the isobaric thermal expansion and  $\kappa_T$  is the isothermal compressibility (Charru, 2011). Here we consider incompressible flow and drop the  $\kappa_T\delta p$  term.



## 6.1 Mathematical formulation for thermocapillary flow

---

where  $\mathbf{u}$  and  $T$  denote velocity and temperature, respectively, the stress tensor is  $\mathbf{T} = -p\mathbf{I} + \mu_i (\nabla\mathbf{u} + \nabla\mathbf{u}^T)$ , and we use the material derivatives in the above equations. We adopt the Boussinesq approximation, which only considers the density variation in the gravity term. This approximation is restricted to flows with small density differences ( $\Delta\rho/\rho_0 \ll 1$ ) such that we can ignore the non-uniform density in the inertial term and the continuity equation (Reddy and Gartling, 2010).

On the interface, the force balance condition reads:

$$[\mathbf{T} \cdot \mathbf{n}]_{-}^{+} = \sigma\kappa\mathbf{n} + \frac{d\sigma}{ds}\mathbf{t}, \quad (6.7)$$

in which  $s$  represents the arc-length, and  $\mathbf{n}$  and  $\mathbf{t}$  are the unit normal and tangent vector, respectively.

Another condition on the interface is the balance between heat flux:

$$[-k_i \nabla T \cdot \mathbf{n}]_{-}^{+} = 0. \quad (6.8)$$

In addition to the ratio of physical properties and the dimensionless numbers introduced in Section 4.1, more dimensionless numbers are required to define a non-isothermal multiphase flow. Compared to the isothermal two-phase system, there are five more physical variables, namely  $k$ ,  $c_p$ ,  $\beta$ ,  $d\sigma/dT$ , and  $\Delta T$  (the temperature scale), and one more dimension, e.g. temperature, in a non-isothermal system. Hence, we need four more dimensionless numbers.

We first introduce the *Péclet* number for heat transfer:

$$Pe = \frac{LU}{\alpha}, \quad (6.9)$$

which characterises the relative importance of heat advection to heat diffusion.  $Pe$  and  $Re$  are related through the *Prandtl* number:

$$Pe = Re \times Pr, \quad Pr = \frac{\nu}{\alpha} = \frac{\mu/\rho}{k/(\rho c_p)} = \frac{c_p \mu}{k}, \quad (6.10)$$

where  $Pr$  measures the ratio between the viscous diffusion rate and the thermal diffusion rate. Typically, for liquid metal  $Pr \ll 1.0$ , for gases,  $Pr \approx 1.0$  and for very viscous liquid  $Pr \gg 1.0$ .

## 6. FEM APPLIED TO NON-ISOTHERMAL MULTIPHASE FLOWS

---

The second dimensionless number, the *Rayleigh* number, is defined as:

$$Ra = \frac{g\beta\Delta TL^3}{\nu\alpha}, \quad (6.11)$$

which characterises the ratio between the thermal-driven buoyancy force and the viscous force. The *Ra* number is an analogy to the *Pe* number if we use the velocity scale  $U_\beta = \beta g L^2 \Delta T / \nu$  in equation (6.9). This velocity scale can be obtained from the balance between viscous stress and pressure difference due to buoyancy:  $\mu U / L \sim \Delta \rho g L$  yields  $U \sim U_\beta$ .

The third is the *Marangoni* number defined as :

$$Ma = \frac{\Delta\sigma L}{\mu\alpha} = \left| \frac{d\sigma}{dT} \right| \frac{\Delta T L}{\mu\alpha}, \quad (6.12)$$

which is regarded as the ratio between thermal-induced interfacial tension gradient to viscous force. The *Ma* number is also analogous to *Pe* with  $U_{\Delta\sigma} = |d\sigma/dT|\Delta T/\mu$  substituted into equation (6.9). We can obtain this velocity scale from the balance between the Marangoni stress and the viscous stress:  $\Delta\sigma/L \sim \mu U/L$  yields  $U \sim U_{\Delta\sigma}$ .

Last, we define the *Capillary* number:

$$Ca = \frac{\mu U_{\Delta\sigma}}{\sigma_0} = \left| \frac{d\sigma}{dT} \right| \frac{\Delta T}{\sigma_0} = \frac{\Delta\sigma}{\sigma_0}, \quad (6.13)$$

as a measure of interface deformation due to thermocapillarity. When  $Ca \rightarrow 0$ , the interface is considered nondeformable.

### 6.2 Numerical implementation

To include the temperature effect, we first develop an FEM solver for the convection-diffusion equation of the temperature. The thermal-induced buoyancy terms and thermocapillarity are then added into the existing NS solver. Details of numerical implementation are presented in this section.

### 6.2.1 An FEM solver for temperature equation

The formulation of equation (6.6c) in two-dimensional geometry is expressed as (the subscript  $i$  is dropped for convenience):

$$\rho_0 c_p \frac{dT}{dt} = \frac{\partial}{\partial x} \left( k \frac{\partial T}{\partial x} \right) + \frac{\partial}{\partial z} \left( k \frac{\partial T}{\partial z} \right). \quad (6.14)$$

Following standard FEM procedure, we multiply the above equation by the test function  $\phi$  and integrate it over the whole domain to obtain the weak formulation:

$$\int_{\Omega} \rho_0 c_p \phi \frac{dT}{dt} dx dz + \int_{\Omega} k \left( \frac{\partial T}{\partial x} \frac{\partial \phi}{\partial x} + \frac{\partial T}{\partial z} \frac{\partial \phi}{\partial z} \right) dx dz = \int_{\partial\Omega} k \nabla T \cdot \mathbf{n} \phi dl. \quad (6.15)$$

In most cases, the Dirichlet boundary condition for temperature is imposed on the domain boundaries. We set  $\phi = 0$  there, and the boundary integral term vanishes. Due to the boundary condition (6.8), the integral on the interface  $\Gamma$  is:

$$\int_{\Gamma} [k_i \nabla T \cdot \mathbf{n}]_+^- \phi dl = 0, \quad (6.16)$$

The computational domain is discretised using the same triangulation with which we solve the incompressible Navier-Stokes equation. We approximate temperature using P2 finite element space:

$$T = \sum_{i=1}^{N_{P2}} T_i \phi_i, \quad (6.17)$$

where  $T_i$  is the approximate temperature on node  $\mathbf{x}_i$ ,  $\phi_i$  is the P2 basis function defined on node  $\mathbf{x}_i$  and  $N_{P2}$  is the total number of temperature nodes. According to Galerkin finite element method, we choose the P2 basis function  $\phi_j$ ,  $j = 1, 2, \dots, N_{P2}$  as the test function and the discretised weak formulation is written as:

$$\mathbf{M}^T \frac{d\mathbf{T}}{dt} + \mathbf{K}^T \mathbf{T} = \mathbf{0}, \quad (6.18)$$

in which:

$$M_{ij}^T = \int_{\Omega} \rho_0 c_p \phi_i \phi_j dx dz, \quad K_{ij}^T = \int_{\Omega} k \left( \frac{\partial \phi_i}{\partial x} \frac{\partial \phi_j}{\partial x} + \frac{\partial \phi_i}{\partial z} \frac{\partial \phi_j}{\partial z} \right) dx dz, \quad (6.19)$$

and  $\mathbf{T} = (T_1, T_2, \dots, T_{N_{P2}})^T$ .

## 6. FEM APPLIED TO NON-ISOTHERMAL MULTIPHASE FLOWS

---

The temperature equation is also solved on a moving mesh using a semi-implicit method. The material derivative is approximated as below:

$$\left(\frac{d\mathbf{T}}{dt}\right)^{n+1} \approx \frac{\mathbf{T}^{n+1} - \tilde{\mathbf{T}}^n}{\Delta t}. \quad (6.20)$$

where  $\tilde{\mathbf{T}}^n$  is obtained using the method of characteristics in the ALE framework. Equation (6.19) is turned into linear equations:

$$\left(\frac{\mathbf{M}^T}{\Delta t} + \mathbf{K}^T\right) \mathbf{T}^{n+1} = \frac{\mathbf{M}^T}{\Delta t} \tilde{\mathbf{T}}^n. \quad (6.21)$$

which can be solved using the SPOOLES (Ashcraft et al., 2002).

The temperature equation in the axisymmetric case is:

$$\rho_0 c_p \frac{dT}{dt} = \frac{1}{r} \frac{\partial}{\partial r} \left( k r \frac{\partial T}{\partial r} \right) + \frac{\partial}{\partial z} \left( k \frac{\partial T}{\partial z} \right). \quad (6.22)$$

It is solved in a similar way as in the two-dimensional case and its weak formulation is presented in Appendix C.

### 6.2.2 Coupling the temperature solver with the NS solver

In non-isothermal multiphase flow, the force balance condition on the interface has to account for the interfacial tension gradient in equation (6.7). In the weak formulation of the momentum equation, the boundary integral on the interface needs to be modified accordingly. The thermal-induced buoyancy force is added as a source term. The new weak formulations are as follows:

$$\begin{aligned} \int_{\Omega} \left( \rho_0 \phi \frac{du}{dt} + 2\mu \frac{\partial \phi}{\partial x} \frac{\partial u}{\partial x} + \mu \frac{\partial \phi}{\partial z} \frac{\partial u}{\partial z} + \mu \frac{\partial \phi}{\partial z} \frac{\partial v}{\partial x} - p \frac{\partial \phi}{\partial x} \right) dx dz \\ = \int_{\Gamma} \phi \left( \sigma \kappa n_x + \frac{d\sigma}{dl} t_x \right) dl, \end{aligned} \quad (6.23a)$$

$$\begin{aligned} \int_{\Omega} \left( \rho_0 \phi \frac{dv}{dt} + \mu \frac{\partial \phi}{\partial x} \frac{\partial u}{\partial z} + \mu \frac{\partial \phi}{\partial x} \frac{\partial v}{\partial x} + 2\mu \frac{\partial \phi}{\partial x} \frac{\partial v}{\partial z} - p \frac{\partial \phi}{\partial z} \right) dx dz \\ = \int_{\Gamma} \phi \left( \sigma \kappa n_z + \frac{d\sigma}{dl} t_z \right) dl - \int_{\Omega} (\rho_0 \beta g (T - T_0)) \phi dx dz. \end{aligned} \quad (6.23b)$$

Unlike the isothermal situation, we need to evaluate  $d\sigma/ds$  and  $\mathbf{t}$  numerically. Similar to the evaluation of  $\mathbf{n}$ , the unit tangent vector  $\mathbf{t}$  on an interface edge is calculated directly and is constant along this edge. The interfacial tension depends on the temperature, which is defined at the two vertices and one midpoint in each interface edge. Hence we consider  $\sigma$  quadratic on the segment and calculate  $d\sigma/ds$  according to its local representation. This numerical evaluation is of second order convergence, as shown in later text.

We adopt a straightforward approach to address the coupling between the temperature equation and the momentum equation. The computational order from time level  $n$  to  $n + 1$  is as follows:

- (1) Update the triangulation from  $T_h^n$  to  $T_h^{n+1}$  and calculate mesh velocity  $\mathbf{a}$ ;
- (2) Use the method of characteristics to find the characteristic foot and use interpolation to determine  $\tilde{\mathbf{U}}_n$  and  $\tilde{\mathbf{T}}_n$ ;
- (3) Solve the temperature equation on  $T_h^{n+1}$  and update the temperature field for time level  $n + 1$ ;
- (4) Calculate the non-isothermal source terms using the updated temperature, solve the Navier-Stokes equations using the *uzawa* method and update the velocity field for time level  $n + 1$ .

## 6.3 Validation tests

In this section, our implementation of non-isothermal effects are validated through three benchmark tests: (1) natural convection in a square cavity; (2) thermocapillary convection in two superimposed layers; and (3) droplet migration under a temperature gradient.

### 6.3.1 Natural convection in a square cavity

Natural convection problems are characterised by the fluid motion produced by temperature-induced buoyancy forces. In general the fluid density decreases when the temperature increases. Fluid close to a heat source becomes warmer and lighter than its surroundings. The warmer fluid rises due to buoyancy and the surrounding cooler fluid moves to replace it. The cooler fluid is then heated and

## 6. FEM APPLIED TO NON-ISOTHERMAL MULTIPHASE FLOWS

---

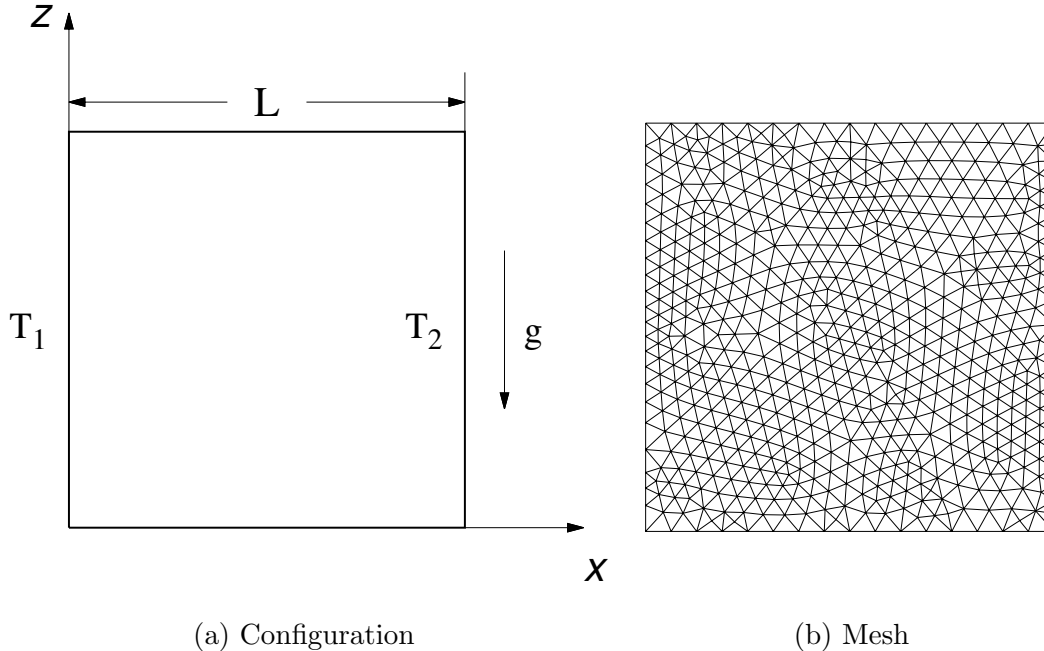


Figure 6.1: Configuration of natural convection in a square cavity of side  $L$  and the computational mesh.

this process continues, forming a convection current. Natural convection appears in many practical problems, including reactor insulation, the ventilation of rooms, solar energy collection, etc. It has also been widely used as a benchmark test to assess the accuracy of a numerical method to solve heat transfer equations. In this section, we consider the natural convection in a square cavity with two vertical walls heated differently and compare our results with the benchmark results of De Vahl Davis (1983).

The set-up of this benchmark test is illustrated in Figure 6.1(a): a two-dimensional square cavity with side length equal to  $L$ . We only consider one phase flow in this example. The top and bottom walls are insulated and the temperatures of the two vertical sides are  $T_1$  and  $T_2$ , respectively ( $T_1 > T_2$ ). No-slip boundary conditions are applied to all walls of the cavity. Two non-dimensional numbers governing this problem are the *Prandtl* number and the *Rayleigh* num-

ber, expressed as:

$$Pr = \frac{\nu}{\alpha}, \quad (6.24a)$$

$$Ra = \frac{\beta g \Delta T L^3}{\alpha \nu} = \frac{\beta g (T_1 - T_2) L^3}{\alpha \nu}. \quad (6.24b)$$

In accordance with the benchmark results, we set  $Pr = 0.71123$  and consider a range of values for  $Ra$  ( $= 10^3, 10^4, 10^5, 10^6$ ). We employ a mesh with uniform mesh size density (mesh size gradient  $G = 0$  and mesh size density  $l_s = l_{max} = 0.025$ ), as shown in Figure 6.1(b). There are approximately 20 nodes on each side of the cavity. The benchmark results are presented in dimensionless form, denoted with a tilde on the top:  $\tilde{T} = (T - T_2)/(T_1 - T_2)$ ,  $\tilde{u} = uL/\alpha$ ,  $\tilde{v} = vL/\alpha$ ,  $\tilde{x} = x/L$  and  $\tilde{z} = z/L$ . The following quantities are examined and compared with the benchmark test:

1. the maximum and minimum vertical velocity ( $\tilde{v}_{max}$  and  $\tilde{v}_{min}$ ) on the horizontal mid-plane ( $\tilde{x} = 0.5$ ) and their location;
2. the maximum and minimum horizontal velocity ( $\tilde{u}_{max}$  and  $\tilde{u}_{min}$ ) on the vertical mid-plane ( $\tilde{z} = 0.5$ ) and their location;
3. the average *Nusselt* number defined by De Vahl Davis (1983),  $\overline{Nu} = \int_{\Omega} (\tilde{u}\tilde{T} - \frac{\partial \tilde{T}}{\partial \tilde{x}}) d\Omega$ . The *Nusselt* number measures the ratio between convective heat transfer and conductive heat transfer. A large value for  $Nu$  indicates that convection is dominant, and a small value for  $Nu$  indicates that conduction dominates;
4. the average *Nusselt* number on the horizontal mid-plane  $Nu_{\frac{1}{2}}$  and the left wall boundary  $Nu_0$ ;
5. the maximum and minimum local *Nusselt* numbers  $Nu_{max}$  and  $Nu_{min}$  on the hot wall.

The fluid is at rest initially, and the initial temperature is set at  $T_2$  everywhere inside the cavity. We run the simulation until the examined values we examine converges, meaning that the flow reaches the steady stage. For example, the relative error of  $\tilde{u}_{max}$  compared to the benchmark value is plotted against the dimensionless time  $t\alpha/L^2$  in Figure 6.2, and it converges at  $t\alpha/L^2 = 40000$  for the four  $Ra$  cases. The eight examined quantities from our simulation and the benchmark results are listed in Table 6.1. For most examined values, the relative

## 6. FEM APPLIED TO NON-ISOTHERMAL MULTIPHASE FLOWS

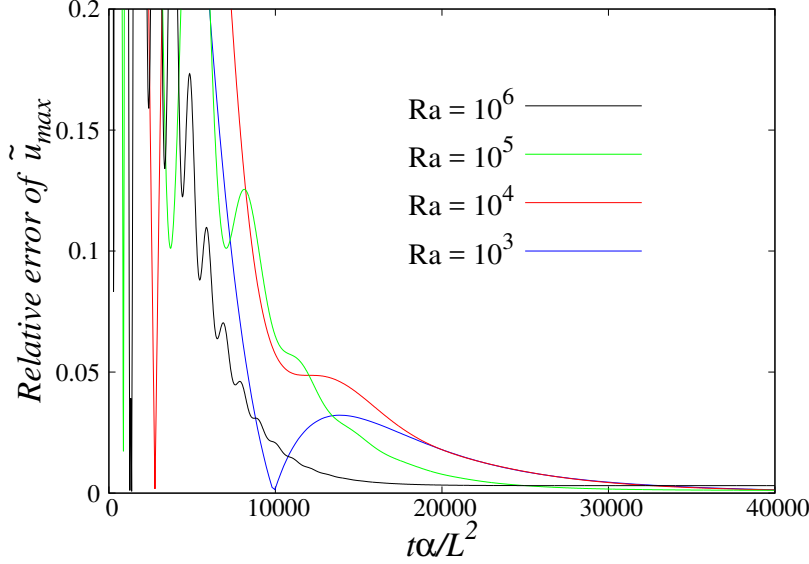


Figure 6.2: The temporal evolution of the relative error  $\tilde{u}_{max}$  compared to the benchmark value.

Table 6.1: Comparison with benchmark solution in De Vahl Davis (1983)

	<i>Ra</i>							
	Benchmark solution				Present work			
	$10^3$	$10^4$	$10^5$	$10^6$	$10^3$	$10^4$	$10^5$	$10^6$
$\tilde{u}_{max}$	3.649	16.178	34.730	64.630	3.6488	16.189	34.769	64.839
$\tilde{z}_{\tilde{u}_{max}}$	0.813	0.823	0.855	0.850	0.823	0.824	0.856	0.848
$\tilde{v}_{max}$	3.697	19.617	68.590	219.36	3.698	19.630	68.612	222.07
$\tilde{x}_{\tilde{w}_{max}}$	0.178	0.119	0.066	0.0379	0.178	0.120	0.065	0.0380
$\overline{Nu}$	1.118	2.243	4.519	8.800	1.118	2.244	4.525	8.927
$Nu_{\frac{1}{2}}$	1.118	2.243	4.519	8.799	1.112	2.245	4.526	8.934
$Nu_0$	1.117	2.238	4.509	8.817	1.126	2.270	4.527	8.292
$Nu_{max}$	1.505	3.528	7.717	17.925	1.507	3.537	7.765	18.228
$Nu_{min}$	0.692	0.586	0.729	0.989	0.691	0.582	0.716	0.958

error compared to the benchmark value is less than 2%. The relative error of  $Nu_{min}$  in the  $Ra = 10^6$  case is around 3%. De Vahl Davis (1983) performed simulations using finite difference with varied mesh sizes (structured mesh from



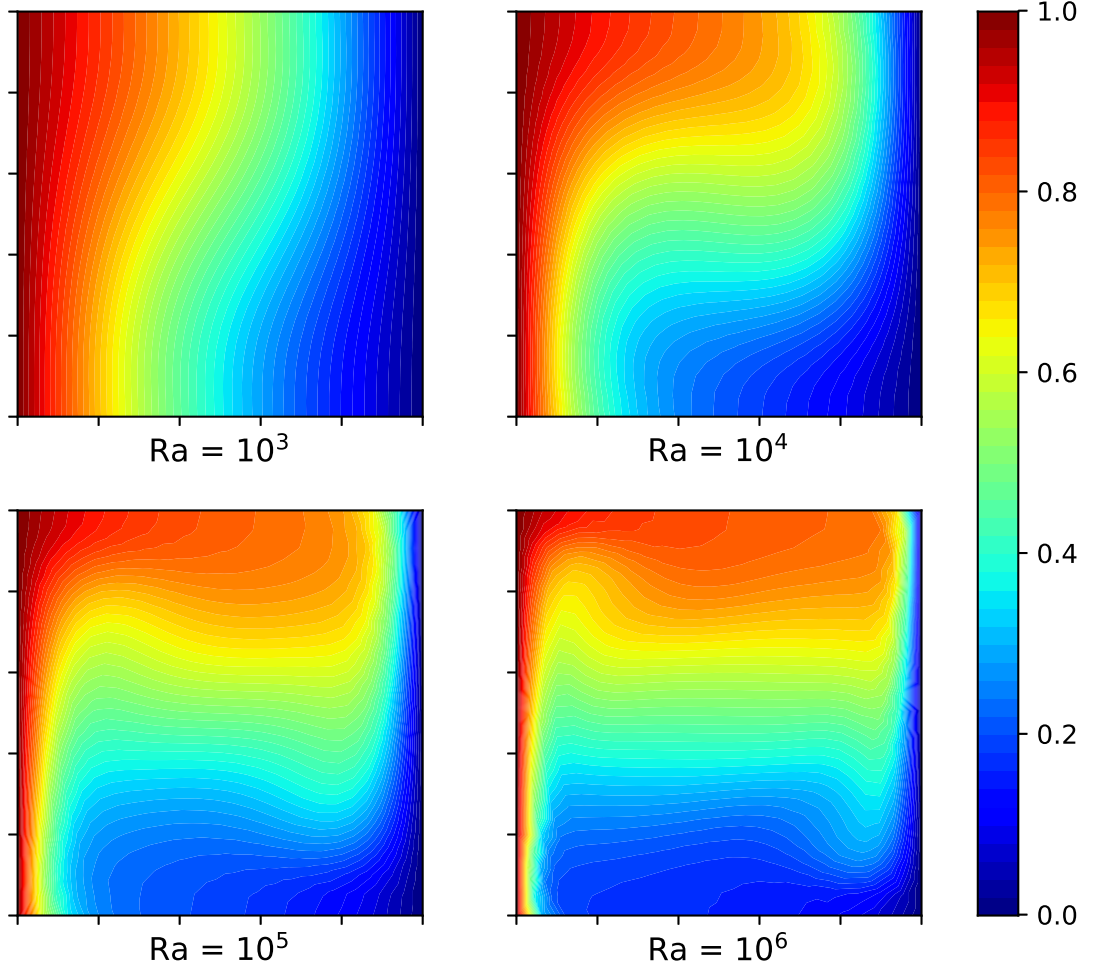


Figure 6.3: Temperature field of the steady-state natural convection in a square cavity for  $Ra = 10^3, 10^4, 10^5$  and  $10^6$  while  $Pr = 0.71$ . The value of the dimensionless temperature is represented by colour.

$10 \times 10$  to  $80 \times 80$ ), and then used extrapolation to obtain the benchmark solution. In their simulation of  $Ra = 10^6$  with mesh  $40 \times 40$ , the relative error of  $Nu_{min}$  (equal to 1.02 in the simulation) is also around 3%. From the good quantitative agreement with the benchmark results, we conclude that the FEM solver for temperature and the thermal-induced buoyancy are implemented correctly and accurately.

The steady-state temperature and velocity fields from our simulation for  $Ra = 10^3, 10^4, 10^5$  and  $10^6$  with  $Pr$  fixed at 0.71 are shown in Figure 6.3 and Fig-

## 6. FEM APPLIED TO NON-ISOTHERMAL MULTIPHASE FLOWS

---

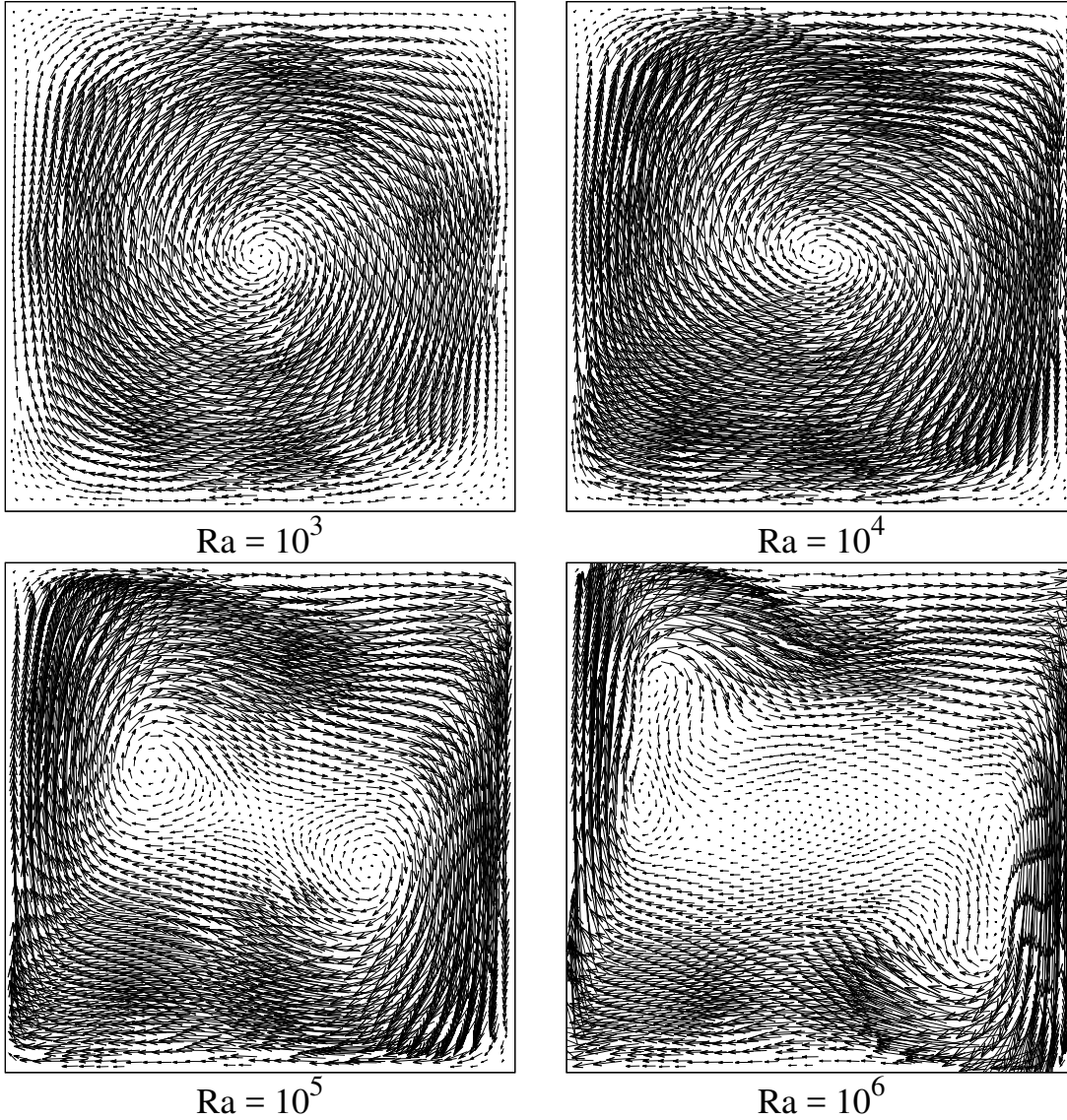


Figure 6.4: Velocity field of the steady-state natural convection in a square cavity for  $Ra = 10^3, 10^4, 10^5$  and  $10^6$  while  $Pr = 0.71$ . The size of the vector is adjusted for the clarity of visualisation: it is multiplied by 0.03, 0.01, 0.003 and 0.001 for  $Ra = 10^3, 10^4, 10^5$  and  $10^6$ , respectively. The velocity is scaled by  $\alpha/L$ .

ure 6.4, respectively. The value of the dimensionless temperature is represented by the colour. The size of the velocity vector is also adjusted for the clarity of visualisation. At a smaller  $Ra$  number, the flow is relatively weak and the tem-

perature field is slightly perturbed from a conduction solution. For  $Ra = 10^3$  and  $10^4$ , the flow shows a single clockwise cell in the cavity. As  $Ra$  increases, the convection strengthens as reflected by the increase in  $\overline{Nu}$  in Table 6.1. At larger  $Ra$  numbers, the temperature field in the centre of the cavity becomes more vertically stratified. The flow structure is different from the cases with smaller  $Ra$  number: there are two vortices in the case for  $Ra = 10^5$  and perhaps more in  $Ra = 10^6$ . The flow close to the two vertical boundaries is significantly stronger than that in the centre of the cavity. This is due to the larger buoyancy forces induced by the larger local temperature gradient.

### 6.3.2 Thermocapillary convection of two superimposed fluids

To verify our implementation of thermocapillarity, we consider the thermocapillary driven convection of two superimposed planar fluids (Pendse and Esmaeeli, 2010). The set-up of the problem is shown in Figure 6.5. The heights of the upper fluid  $A$  and the lower fluid  $B$  are  $a$  and  $b$ , respectively. In the horizontal direction, the fluids extend to infinity. We impose a uniform temperature on the top wall:

$$T_a(x, a) = T_c, \quad (6.25)$$

and a sinusoidal temperature on the bottom wall:

$$T_b(x, -b) = T_h + T_0 \cos(\omega x), \quad (6.26)$$

in which  $T_h > T_c > T_0$  and  $\omega = 2\pi/l$  is the wave number.

The above boundary conditions establish a periodic temperature field in the horizontal direction with a period length of  $l$ . It is sufficient to consider the solution in one period domain with  $-l/2 \leq x \leq l/2$ . The characteristic length, temperature and velocity scales are as follows:

$$L = b, \quad \Delta T = T_0, \quad U_{\Delta\sigma} = \left| \frac{d\sigma}{dT} \right| \frac{T_0}{\mu_B}. \quad (6.27)$$

The three governing dimensionless numbers are defined as:

$$Re = \frac{U_{\Delta\sigma} b}{\nu_B}, \quad Ma = \frac{U_{\Delta\sigma} b}{\alpha_B}, \quad Ca = \frac{\mu_B U_{\Delta\sigma}}{\sigma_0} \quad (6.28)$$

## 6. FEM APPLIED TO NON-ISOTHERMAL MULTIPHASE FLOWS

---

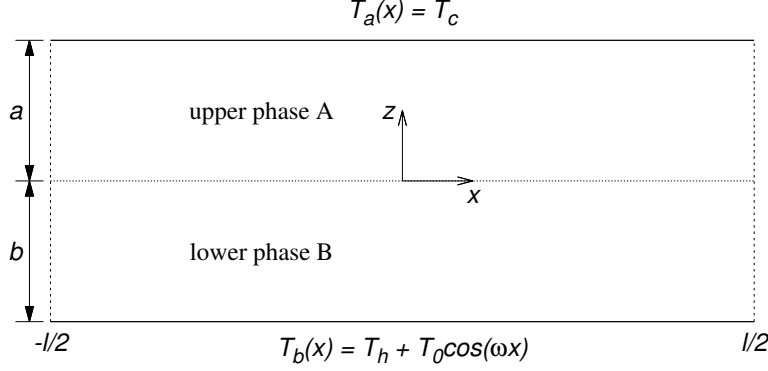


Figure 6.5: Fluids  $A$  and  $B$  are separated by the interface depicted in the dotted line. They are confined by the top and bottom walls, but extend to infinity in the horizontal direction. Uniform temperature is imposed on the top wall while a sinusoidal temperature is imposed on the bottom wall.

and we denote the ratio of viscosity and thermal conductivity as below:

$$\lambda = \frac{\mu_A}{\mu_B}, \quad \chi = \frac{k_A}{k_B}. \quad (6.29)$$

An analytical solution for the thermocapillary driven convection of superimposed fluids when  $Ma \ll 1$ ,  $Re \ll 1$  and  $Ca \ll 1$  was given by Pendse and Esmareli (2010). They solved the Stokes equation for velocity and the Laplace equation for temperature. The analytical solution is as below:

$$T^A(x, z) = T_0 f(\tilde{a}, \tilde{b}, \chi) \sinh(\tilde{a} - \omega z) \cos(\omega x) + \frac{(T_c - T_h)z + \chi T_c b + T_h a}{a + \chi b}, \quad (6.30a)$$

$$u^A(x, z) = U \left\{ [C_1^A + \omega(C_2^A + C_3^A z)] \cosh(\omega z) + (C_3^A + \omega C_1^A z) \sinh(\omega z) \right\} \sin(\omega x), \quad (6.30b)$$

$$v^A(x, z) = -\chi U [C_1^A \cosh(\omega z) + (C_2^A + \omega C_3^A z) \sinh(\omega z)] \cos(\omega x) \quad (6.30c)$$

in the upper layer and,

$$T^B(x, z) = T_0 f(\tilde{a}, \tilde{b}, \chi) [\sinh(\tilde{a}) \cosh(\omega z) - \chi \sinh(\omega z) \cosh(\tilde{a})] \cos(\omega x) + \frac{\chi(T_c - T_h)z + \chi T_c b + T_h a}{a + \chi b} \quad (6.31a)$$

$$u^B(x, z) = U \left\{ [C_1^B + \omega(C_2^B + C_3^B z)] \cosh(\omega z) + (C_3^B + \omega C_1^B z) \sinh(\omega z) \right\} \sin(\omega x), \quad (6.31b)$$

$$v^B(x, z) = -\chi U [C_1^B z \cosh(\omega z) + (C_2^B + C_3^B z) \sinh(\omega z)] \cos(\omega x), \quad (6.31c)$$

in the lower layer. In the above equations, the constants are expressed as:

$$\tilde{a} = a\omega, \quad \tilde{b} = b\omega. \quad (6.32a)$$

$$f(\tilde{a}, \tilde{b}, \chi) = \frac{1}{\chi \sinh(\tilde{b}) \cosh(\tilde{a}) + \sinh(\tilde{a}) \cosh(\tilde{b})}, \quad (6.32b)$$

$$C_1^A = \frac{\sinh^2(\tilde{a})}{\sinh^2(\tilde{a}) - \tilde{a}^2}, \quad C_2^A = \frac{-a\tilde{a}}{\sinh^2(\tilde{a}) - \tilde{a}^2}, \quad C_3^A = \frac{2\tilde{a} - \sinh^2(2\tilde{a})}{2[\sinh^2(\tilde{a}) - \tilde{a}^2]}, \quad (6.32c)$$

$$C_1^B = \frac{\sinh^2(\tilde{b})}{\sinh^2(\tilde{b}) - \tilde{b}^2}, \quad C_2^B = \frac{-b\tilde{b}}{\sinh^2(\tilde{b}) - \tilde{b}^2}, \quad C_3^B = \frac{\sinh(2\tilde{b}) - 2\tilde{b}}{2[\sinh^2(\tilde{b}) - \tilde{b}^2]}. \quad (6.32d)$$

and,

$$U = \left| \frac{d\sigma}{dT} \right| \frac{T_0}{\mu_B} g(\tilde{a}, \tilde{b}, \chi) h(\tilde{a}, \tilde{b}, \lambda), \quad (6.33)$$

in which,

$$g(\tilde{a}, \tilde{b}, \chi) = \sinh(\tilde{a}) f(\tilde{a}, \tilde{b}, \chi), \quad (6.34a)$$

$$h(\tilde{a}, \tilde{b}, \lambda) = \frac{(\sinh^2(\tilde{a}) - \tilde{a}^2)(\sinh^2(\tilde{b}) - \tilde{b}^2)}{\lambda(\sinh^2(\tilde{b}) - \tilde{b}^2)(\sinh(2\tilde{a}) - 2\tilde{a}) + (\sinh^2(\tilde{a}) - \tilde{a}^2)(\sinh(2\tilde{b}) - 2\tilde{b})}. \quad (6.34b)$$

In our simulation, we set  $a = b = l/4 = 1$ ,  $\rho_B = 1.0$ ,  $\nu_B = 1.0$ ,  $\alpha_B = 1.0$ ,  $d\sigma/dT = -10^{-4}$ ,  $\sigma_0 = 1.0$ ,  $T_c = 1.0$ ,  $T_h = 3.0$ , and  $T_0 = 1.0$ . The three non-dimensional numbers are  $Re = Ma = Ca = 10^{-4} \ll 1.0$ . We vary the thermal conductivity ratio  $\chi$  while the other ratios are fixed. The computational mesh is a uniform mesh with  $l_{max} = 0.1$  and it has 313 vertices. Figure 6.6 shows the contour map of temperature for the thermal conductivity ratios:  $\chi = 0.2$ , 1.0, and 5.0. The blue dashed isothermal line represents the simulation results, and the red solid isothermal line represents the analytical solution. The maximum relative errors for the temperature solution are documented in Table 6.2. The simulated

Table 6.2: Maximum relative error of temperature compared to the analytical solution

$\chi$	0.2	1.0	5.0
relative error	$9.87 \times 10^{-6}$	$1.0 \times 10^{-5}$	$1.32 \times 10^{-5}$

## 6. FEM APPLIED TO NON-ISOTHERMAL MULTIPHASE FLOWS

---

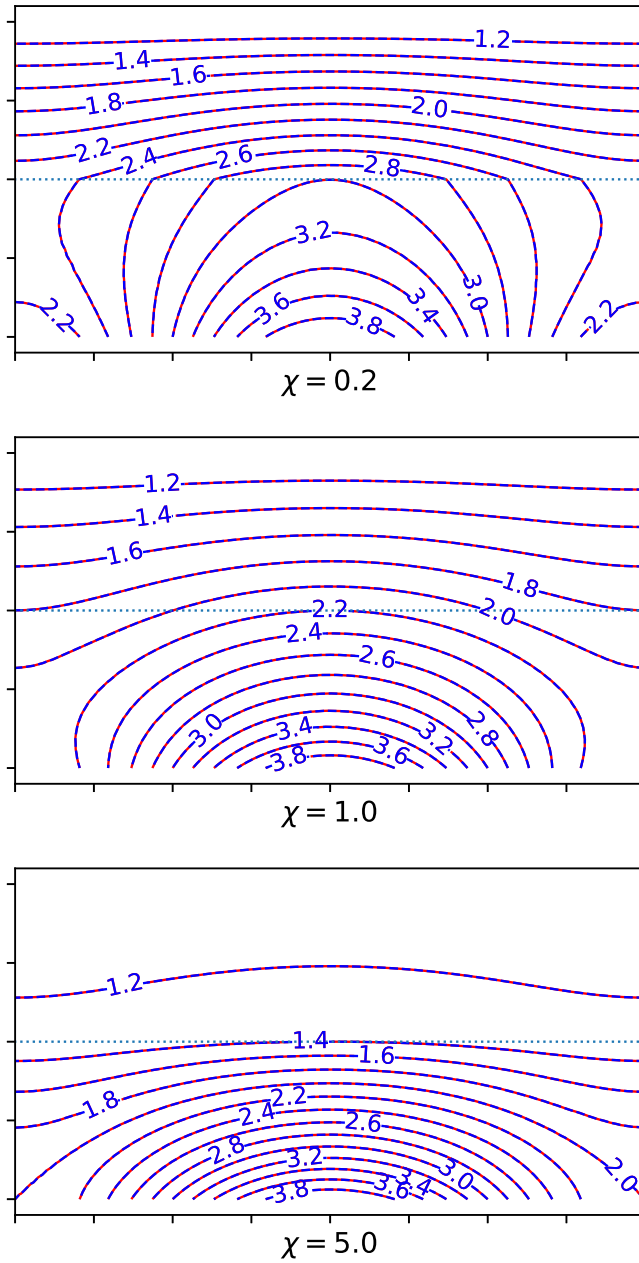


Figure 6.6: The contour map of temperature is presented for thermal conductivity ratios  $\chi = 0.2$ , 1.0 and 5.0. All other physical property ratios are fixed at 1.0. The simulated results and the analytical solutions are represented by blue dashed and red solid lines respectively, labelled with the temperature value. The interface is drawn as a blue dotted line.

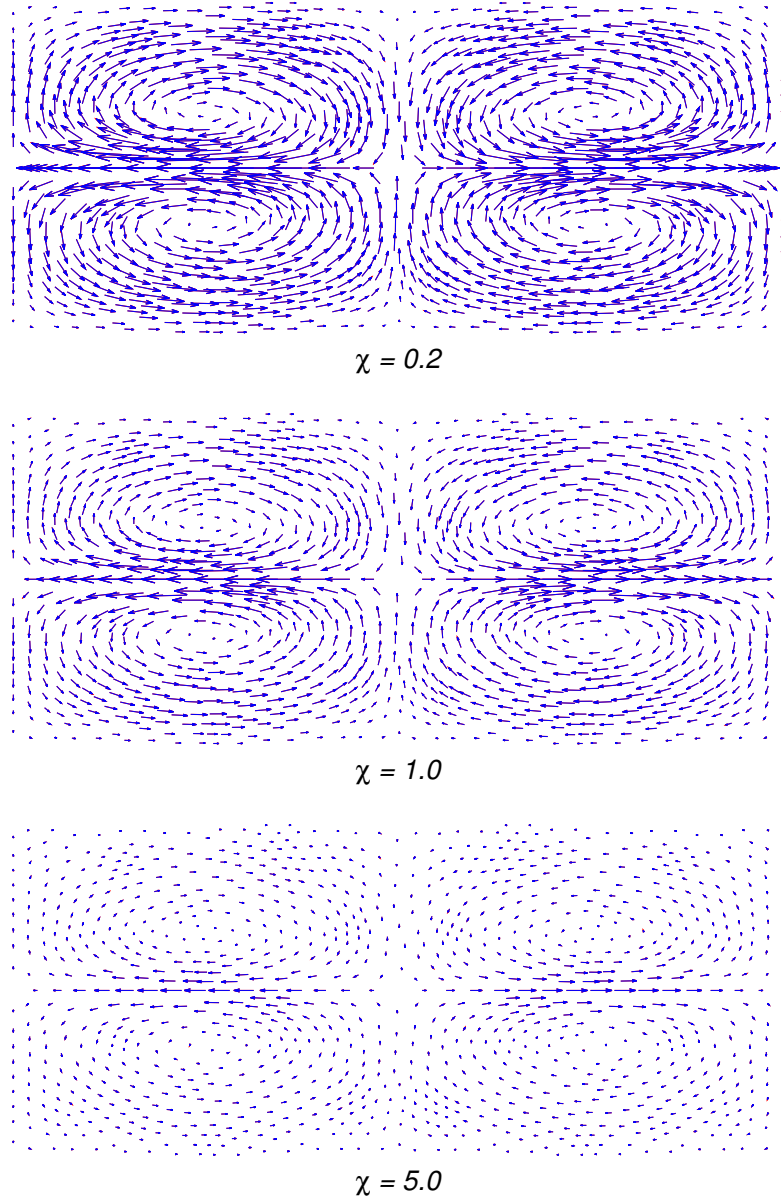


Figure 6.7: The velocity vectors are plotted for thermal conductivity ratios  $\chi = 0.2$ ,  $1.0$  and  $5.0$ . The blue and red arrows represent velocity vectors from our simulation and the analytical solution, respectively. For the clarity of visualisation, we multiply the magnitude of the vectors by  $10^5$ .

## 6. FEM APPLIED TO NON-ISOTHERMAL MULTIPHASE FLOWS

---

results are in good quantitative agreement with the analytical solutions given by equations (6.30) and (6.31). The maximum relative error is of the order of  $10^{-5}$  and the simulated contour map is nearly identical to the analytical solution. We observe that with a decreasing values of  $\chi$ , the isothermal lines in the upper layer become denser and the temperature gradient along the interface is larger.

The velocity field is plotted in Figure 6.7. The blue arrows represent the simulation results and the red arrows are from the analytical solution. The magnitude of the vectors are all multiplied by  $10^5$  such that they are visible. It can be clearly seen that the velocity solution from the simulation agrees very well with the analytical solution. We observe that the magnitude of the velocity vector increases with the decreasing thermal conductivity ratio  $\chi$ . The strengthened convection is due to the larger temperature gradient along the interface and hence the stronger Marangoni stresses.

### 6.3.3 Thermocapillary migration of a spherical droplet

In this section, we examine the accuracy of our method with another benchmark example: the migration of a spherical droplet under a constant temperature gradient.

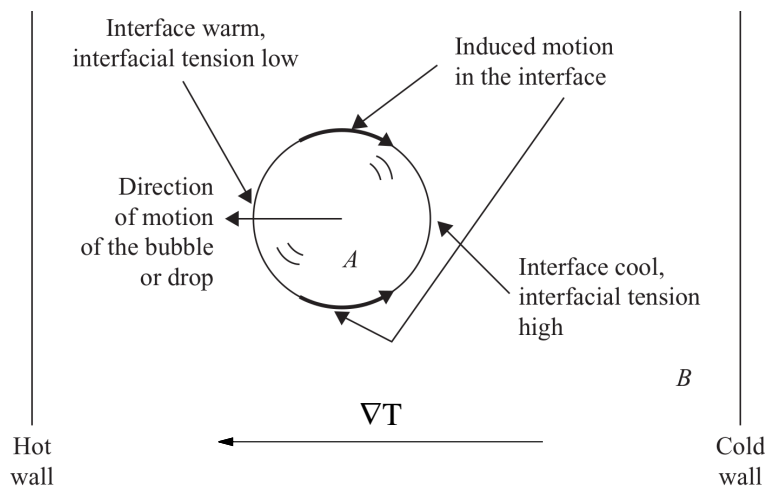


Figure 6.8: A droplet migrates towards the warmer side when a temperature gradient is imposed. This figure is adapted from Figure 2-19 in Leal (2007).



The configuration of this problem is sketched in Figure 6.8. A droplet of fluid  $A$  is surrounded by fluid  $B$  which is heated on one side and cooled at the other. The imposed temperature gradient establishes a gradient in the interfacial tension along the drop interface. As the interfacial tension is reduced on the warm side, the interface is pulled from the warm to the cool side of the droplet. The fluid in the vicinity of the interface is dragged towards the cooler end of the droplet. This motion causes higher pressure to develop just beyond the cooler end relative to the warmer end. As a result of the pressure difference, the droplet migrates towards the warm side. Young et al. (1959) were the first to investigate the steady thermocapillary migration of a droplet. In the limit of Stokes flow, negligible heat convection and a nondeformable interface ( $Re, Ma, Ca \rightarrow 0$ ), the droplet maintains a spherical shape and migrates with a constant velocity towards the warm end. In the absence of gravity, the analytical solution of the terminal velocity of a droplet of radius  $R$  under a constant temperature gradient  $\nabla T_\infty$  is :

$$U_{YGB} = \frac{2U}{(2 + 3\lambda)(2 + \chi)} \quad (6.35)$$

where  $U = |d\sigma/dT\nabla T_\infty|R/\mu_B$  is the characteristic velocity,  $\lambda = \mu_A/\mu_B$  is the viscosity ratio, and  $\chi = k_A/k_B$  is the thermal conductivity ratio. Using  $R$  as the characteristic length, we define three dimensionless numbers:

$$Re = \frac{UR}{\nu_B}, \quad Ma = \frac{UR}{\alpha_B}, \quad Ca = \frac{\mu_B U}{\sigma_0}. \quad (6.36)$$

In the following sections, we carry out simulations for a limiting case and a case with finite  $Re, Ma, Ca$ .

### 6.3.3.1 Solution for a limiting case: $Re, Ma, Ca \ll 1.0$

The assumptions for the analytical solution are  $Re, Ma, Ca \rightarrow 0$ , an infinite domain, and the absence of gravity. In our numerical simulation, we only simulate half of the configuration due to symmetry. The domain size in our numerical simulation is  $100R \times 200R$  and initially the droplet is placed at  $(0, 0)$ . We apply a symmetry boundary to  $r = 0$  and no-slip boundary conditions to other boundaries. A linear temperature field is imposed in the vertical direction, with  $T = 100$  on the top wall and  $T = -100$  on the bottom wall. The temperature

## 6. FEM APPLIED TO NON-ISOTHERMAL MULTIPHASE FLOWS

---

gradient is a constant  $\nabla T_\infty = 1.0$  and the reference temperature is  $T_0 = 0$ . For simplicity, the same physical properties are used for fluids  $A$  and  $B$ . The physical parameters are set as below:

$$R = 1.0, \rho = 1.0, k = 1.0, \mu = 1.0, c_m = 1.0, d\sigma/dT = -10^{-4}, \sigma_0 = 0.1. \quad (6.37)$$

Under this numerical set-up, the values of the dimensionless numbers are  $Re = Ma = 10^{-4}$ , and  $Ca = 10^{-3}$ . The analytical terminal velocity is  $U_{YGB} = 1.3333 \times 10^{-5}$ .

Table 6.3: Numerical results for different mesh resolutions

$\alpha$	$N$	$N_{total}$	$U_m$	relative error (%)
0.2	8	236	$1.2368 \times 10^{-5}$	7.24
0.1	16	284	$1.3094 \times 10^{-5}$	1.79
0.05	32	411	$1.3273 \times 10^{-5}$	0.45
0.025	64	643	$1.3316 \times 10^{-5}$	0.14
0.0125	128	1100	$1.3325 \times 10^{-5}$	0.07
0.00625	256	2058	$1.3335 \times 10^{-5}$	0.01

Fixing the mesh size gradient at  $G = 0.15$ , we vary the mesh size scale  $\alpha$  to change the mesh resolution. In general, the total number of mesh vertices grows linearly with the inverse of the mesh size scale. The migration velocity of the droplet  $U_m$  is calculated as:

$$U_m = \frac{\int_{\Omega_d} v r dr dz}{\int_{\Omega_d} r dr dz}. \quad (6.38)$$

where  $\Omega_d$  denotes the droplet domain.

The numerical results for different mesh resolutions are summarised in Table 6.3 where  $N$  is the number of vertices on the interface and  $N_{total}$  is the total number of mesh vertices. The relative error for  $U_m$  is plotted against the mesh size scale  $\alpha$  in Figure 6.9(a). The relative error converges to zero almost following  $2\alpha^2$  as  $\alpha$  decreases. This example demonstrates the second order convergence of our method. The evolution of the migration velocity is illustrated in Figure 6.9(b). Since the values of  $Re$  and  $Ma$  are very small, the flow converges to the

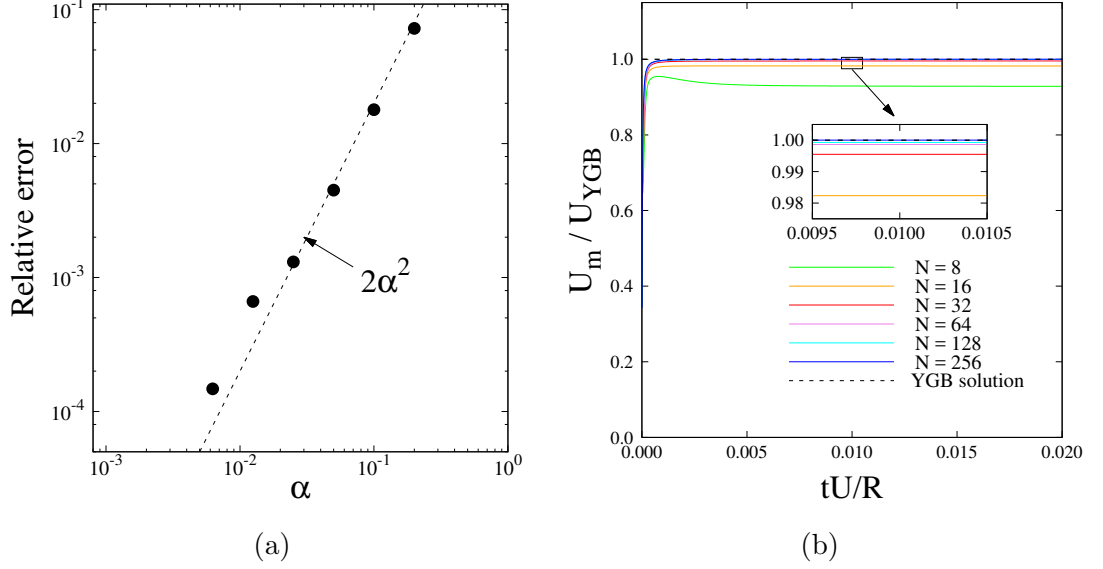


Figure 6.9: (a) The relative error vanishes with a decreasing mesh size scale  $\alpha$  at a second-order convergence rate; (b) At very small values of  $Ma$  and  $Re$ , the migration velocity converges very quickly and the relative error is less than 1% when the number of interface nodes exceeds 32.

steady solution very quickly. The final steady migration velocity converges to the analytical solution with a relative error of less than 0.5% when  $N$  is greater than 32.

### 6.3.3.2 Solution for finite $Re$ , $Ma$ and $Ca$

Our numerical method is capable of simulating the thermocapillary migration of a droplet at finite values of  $Ma$  and  $Re$ . Though no analytical solution is available for this problem, a few numerical tests are documented in the literature. In our numerical simulation, we fix  $Re$  and  $Ca$  while varying  $Ma$  by adjusting the thermal conductivity  $k$ . The physical parameters are still kept the same for the fluid both inside and outside the droplet ( $\eta = \chi = \eta = \lambda = 1.0$ ).

We set  $R = 1.0$ ,  $\rho = 1.0$ ,  $\sigma = 10^{-4}$ ,  $d\sigma/dT = -10^{-5}$ ,  $\mu = 0.01$ ,  $c_m = 1.0$ , and  $\nabla T_\infty = 1.0$  to fix  $Re = 1.0$  and  $Ca = 0.1$ . The thermal conductivity  $k$  is set at 0.01, 0.001, and 0.0001 such that  $Ma = 1.0$ , 10.0, and 100.0. The size

## 6. FEM APPLIED TO NON-ISOTHERMAL MULTIPHASE FLOWS

---

of the computing domain is  $[0, 5R] \times [-7.5R, 7.5R]$ , and initially the droplet is centered at  $(0, 0)$ . The mesh parameters are set at  $\alpha = 0.025$  (64 nodes on the interface),  $G = 0.15$ , and  $l_{max} = 2.0$ . Under the influence of thermocapillarity, the droplet starts migrating towards the warmer region (upwards in our simulation) and finally reaches a steady migration velocity. The normalised migration velocity  $U_m/U_{YGB}$  is plotted against dimensionless time  $tU/R$  ( $U = |d\sigma/dT\nabla T_\infty|T/\mu_B$ ) in Figure 6.10. Our simulated results are drawn in dots and is compared to the numerical results of Liu et al. (2012) using the lattice Boltzmann method (LBM), which is depicted with solid lines.

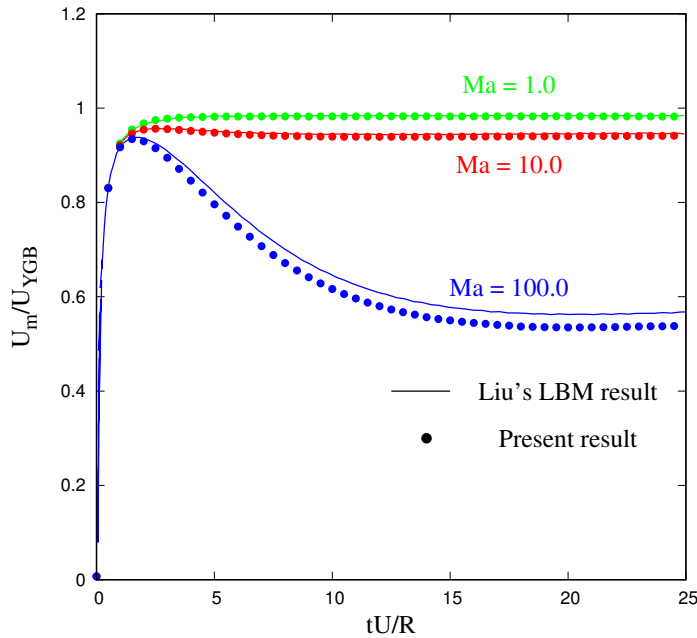


Figure 6.10: In the simulation,  $Ca$  is kept at 0.1 and  $Re$  is fixed at 1.0.  $Ma$  is varied from 1.0 (green), 10.0 (red) to 100.0 (blue). The dots presents the numerical result from our simulation while the solid line presents numerical results from the Lattice Boltzmann simulation from Liu et al. (2012)

From Figure 6.10 we observe that for small values of  $Ma$ , the evolution of the migration velocity consists of two stages: the initial acceleration and the steady migration. For relatively large values of  $Ma$ , after the initial acceleration, the migration velocity decreases and then reaches the steady migration velocity which

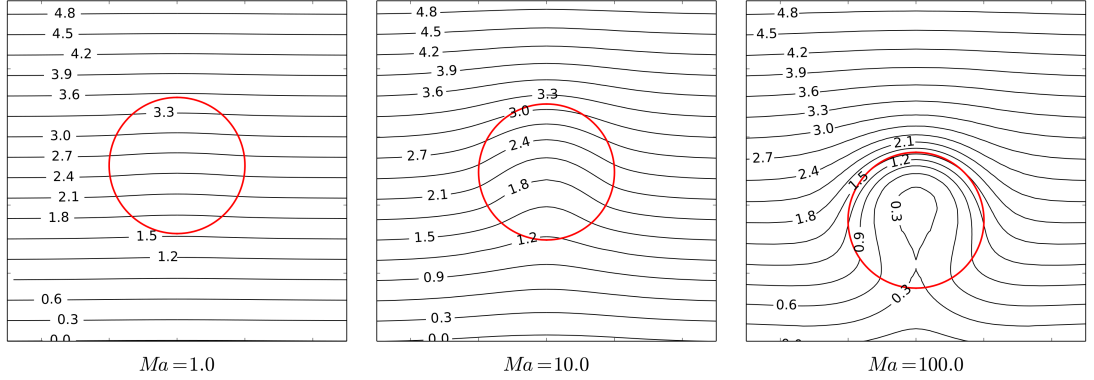


Figure 6.11: The temperature field around the droplet in case of  $Ma = 1.0$ ,  $10.0$  and  $100.0$  when  $tU/R = 20.0$ .

is much smaller than  $U_{YGB}$ . It is evident that the terminal migration velocity decreases with an increase in the  $Ma$  number. This is consistent with the previous theoretical and numerical investigations in the case of non-deformable droplets or bubbles (Shankar and Subramanian, 1988; Yin et al., 2008). The dependence of the final migration velocity on the  $Ma$  number can be explained through the contour map of the temperature. We plot the contour map of temperature from the three simulations in Figure 6.11. The droplet interface is drawn in red solid lines and the value of the temperature is labelled on each contour. The dimensionless time is  $tU/R = 20.0$ . The temperature field in the case for  $Ma = 1.0$  is close to the conduction solution. In contrast, the background linear temperature field is disturbed by the migrating droplet in the case of  $Ma = 100.0$ . In this problem, the  $Ma$  number is analogous to the  $Pe$  number. As the  $Ma$  number increases, the convective transport is enhanced, resulting in wrapping of the isotherm lines near the front of the migrating droplet. In the contour map for  $Ma = 100.0$ , the isotherm line labelled  $1.5$  almost coincides with the front of the droplet interface. This indicates a significant reduction in the temperature gradient along the interface, and hence, a reduction in the driving force for droplet migration.

Though good agreement has been achieved with the simulation results of Liu et al. (2012) for small values of  $Ma$ , there exist some discrepancies for  $Ma = 100.0$ . The relative error of the steady migration velocity is around 5%

## 6. FEM APPLIED TO NON-ISOTHERMAL MULTIPHASE FLOWS

---

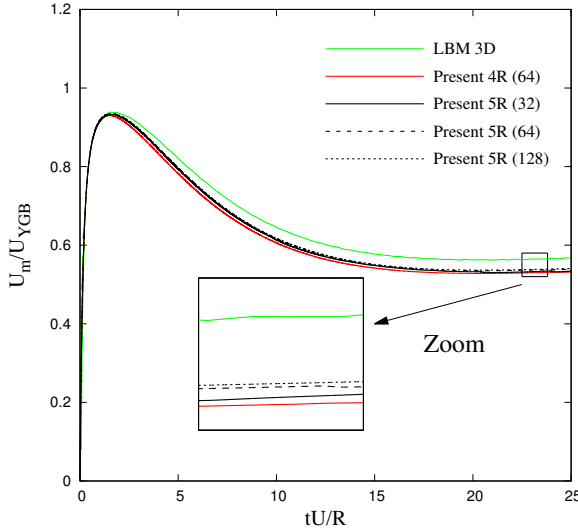


Figure 6.12: The temporal evolution of migration velocity at  $Re = 1.0$ ,  $Ma = 100.0$  and  $Ca = 0.1$ , from 3D LBM and our axisymmetric simulation with different mesh resolutions and mesh domains.

compared to the LBM simulation. We note that our simulation is axisymmetric, while Liu et al. (2012) performed the three-dimensional simulation with a cuboid computing domain of  $7.5R \times 7.5R \times 15R$ . We have checked the convergence of our method using different mesh sizes (32, 64 and 128 vertices on the interface). Another axisymmetric simulation has been carried out with a "narrower" domain ( $[0, 4R] \times [-7.5R, 7.5R]$ ). Comparisons with the result from Liu et al. (2012) are plotted in Figure 6.12. Our simulation converges to a value lower than the 3D simulation, as illustrated in the zoomed image. The difference from the simulation of a "narrower" domain is not significant. The three-dimensional effects may contribute to the discrepancy between our axisymmetric simulation and the 3D LBM simulation.

### 6.4 Liquid bridge with thermocapillarity

In this section, we apply our numerical method to study liquid bridge breakup with the thermocapillary effect. A non-isothermal liquid bridge can be regarded

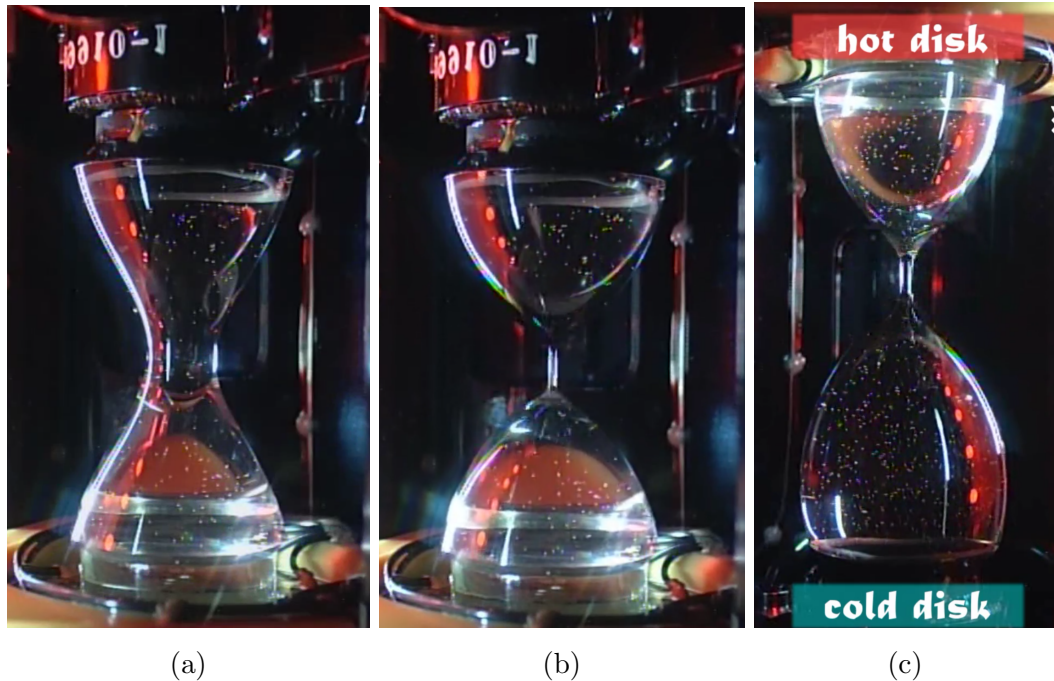


Figure 6.13: Experimental pictures from the space experiment by Ueno et al. (2012): (a) a perturbed liquid bridge shape; (b) the isothermal breakup shape; (c) the non-isothermal breakup shape.

as the simplest idealisation of the configuration in the floating zone crystal growth process. In this process, the molten material passes through a heated ring, melts, and re-solidifies into a single crystal. The quality of the formed crystal is affected by the thermocapillary motion in the molten zone, which motivated the studies on the thermocapillary stabilities within the bridge (Davis, 1987; Schatz and Neitzel, 2001). The breakup of a non-isothermal liquid bridge has been received little attention. Recently Ueno et al. (2012) reported the experimental study of a liquid bridge break-up under the thermocapillary effect. This experiment was conducted on the International Space Station in a micro-gravity environment. The fluid used was the 10 *cSt* silicon oil and the bridge diameter was 30 mm. The liquid bridge was stretched to a perturbed shape so that it was no longer possible for the bridge to return to a static state, as shown in Figure 6.13(a). Figure 6.13 (b) and (c) display the isothermal and non-isothermal breakup shapes. In both

## 6. FEM APPLIED TO NON-ISOTHERMAL MULTIPHASE FLOWS

---

figures, a thin thread forms in the centre of the bridge. The difference is that the up-and-down symmetry of the bridge is broken due to the thermocapillary motion in the non-isothermal case. In this section, we numerically investigate this problem to better understand the role played by the thermocapillary effect.

### 6.4.1 Configuration and numerical set-up

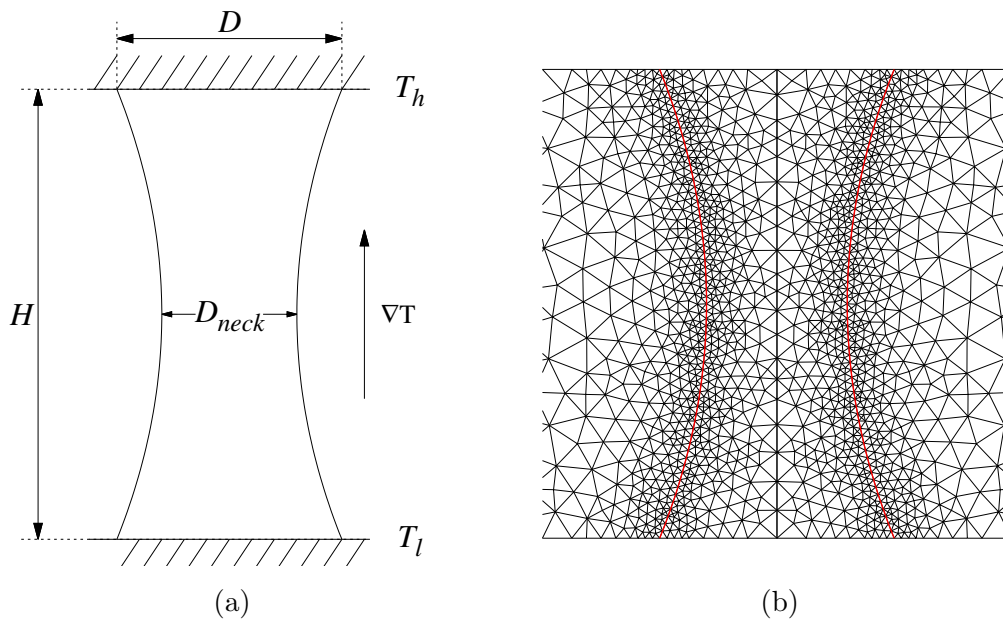


Figure 6.14: Configuration (a) and mesh (b) for our study of liquid bridge.

As illustrated in Figure 6.14(a), we consider a liquid bridge of height  $H$  held captive by two coaxial disk with a diameter  $D$ . The contact points of the interface with the walls are kept fixed, i.e. the moving contact line is not considered in our study. Since we are only interested in the break-up behaviour rather than the dynamics of stretching a liquid bridge, we start the simulation with a perturbed interface shape. The initial interface shown in Figure 6.14(a) is fitted to a parabola. The diameter at the neck of the bridge is  $D_{neck}$ . This shape is similar to the interface shape in Figure 6.13(a). In our simulation, the aspect ratio  $H/D$  is kept at 2 and the ratio between the neck diameter and the end diameter



## 6.4 Liquid bridge with thermocapillarity

---

$D_{neck}/D$  is fixed at 0.6. The two ratios are chosen such that the perturbed shape can lead to break-up.

We perform two-phase simulations on this problem. The bridge fluid is denoted as fluid 2 and the surrounding fluid is denoted as fluid 1. In non-isothermal cases, the top and bottom walls are heated to different temperatures  $T_h$  and  $T_l$  ( $T_h > T_l$ ), respectively. Initially the temperature is linearly distributed and the temperature gradient is a constant noted as  $\nabla T$ . The characteristic length scale is  $D$  and the characteristic scale for temperature variation is  $\nabla T D$ . In this section, both isothermal and non-isothermal simulations are performed. For the convenience of comparison, we choose  $Oh$ ,  $Pr$ , and  $Ca$  as the dimensionless number set, written as:

$$Oh = \frac{\mu}{\sqrt{\rho\sigma_0 D}}, \quad Pr = \frac{c_p \mu}{k}, \quad Ca = \left| \frac{d\sigma}{dT} \right| \frac{\nabla T D}{\sigma_0}. \quad (6.39)$$

The focus of this section is the role played by the above three dimensionless numbers. Ratios of the physical properties are kept fixed. We consider a liquid-gas system and set the density ratio  $\eta$ , the viscosity ratio  $\lambda$ , the thermal conductivity ratio  $\chi$ , and the heat capacity ratio  $\gamma$ , as below:

$$\eta = 500.0, \quad \lambda = 50.0, \quad \chi = 50.0, \quad \gamma = 1.0. \quad (6.40)$$

For comparison, a water-air system has the ratios:  $\eta \approx 840$ ,  $\lambda \approx 50.0$ ,  $\chi \approx 30.0$  and  $\gamma \approx 4.2$ .

The computational mesh used in our simulation is shown in Figure 6.14(b), where the mesh lines are drawn in black and the interface is in red. The mesh scale  $\alpha$  is set to be 0.025 and the mesh gradient  $G$  is set at 0.1. The maximum mesh size on the interface and two walls are set at  $l_{interface} = l_{wall} = 0.025$ . The global minimum length scale  $l_{min} = 0.002$ . In our simulation, pinchoff takes place once the minimum neck diameter falls below  $0.01D$ . We consider the axisymmetric case and only simulate half of the configuration. The size of the computational mesh is  $[0, 5D] \times [0, H]$ . At  $r = 5D$ , a Dirichlet boundary condition for temperature is imposed so that temperature varies linearly from  $T_l$  to  $T_h$ . Simulation results are presented in the following sections.

## 6. FEM APPLIED TO NON-ISOTHERMAL MULTIPHASE FLOWS

---

### 6.4.2 Mesh convergence

Before we carry out the parameter study, a mesh convergence-check is conducted. We consider a liquid bridge with  $Oh = 0.01$  and both isothermal and non-isothermal convergence tests are performed. In the non-isothermal simulation, the two other dimensionless numbers are  $Pr = 5$  and  $Ca = 0.2$ . We use meshes with 32, 64 and 128 nodes on the interface and plot the temporal evolution of the minimum neck diameter  $D_{neck}/D$  in Figure 6.15.

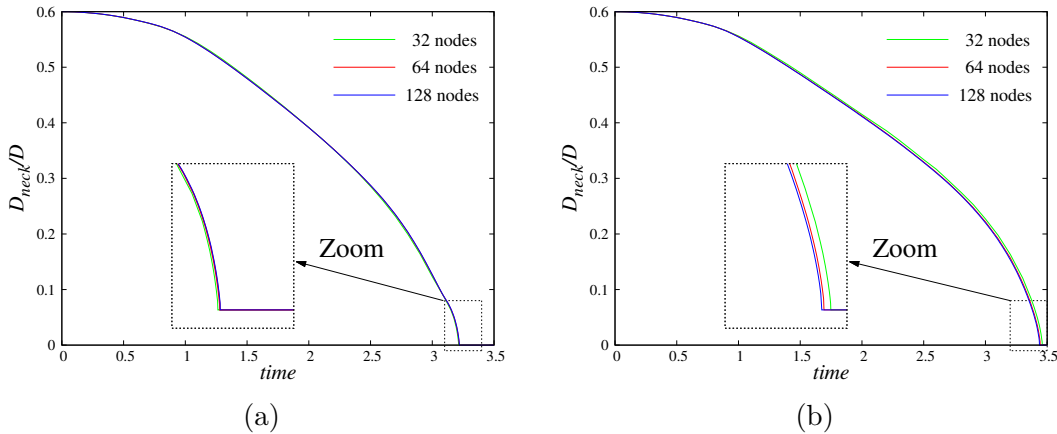


Figure 6.15: The temporal evolution of the minimum neck diameter is plotted for simulation with 32 (green), 64 (red) and 128 (blue) nodes on the interface. (a) shows an isothermal simulation with  $Oh = 0.01$ , and (b) shows a non-isothermal simulation with  $Oh = 0.01$ ,  $Pr = 5$ , and  $Ca = 0.2$ . From the close-up, the evolution using 64 nodes on the interface overlays with that using 128 nodes.

Figure 6.15(a) and (b) show the isothermal and non-isothermal simulations, respectively. The temporal evolution of  $D_{neck}/D$  using 64 nodes (red solid line) on the interface is almost identical to that of the simulation with 128 nodes (in blue solid line) on the interface. We conclude that our numerical simulation converges and the mesh with 64 nodes on the interface is sufficient for this problem.

### 6.4.3 Isothermal simulation: effect of $Oh$

We first carry out a series of isothermal numerical simulations with values of  $Oh$  ranging from 0.005 to 1.0. According to the pinchoff shape, two regimes are

## 6.4 Liquid bridge with thermocapillarity

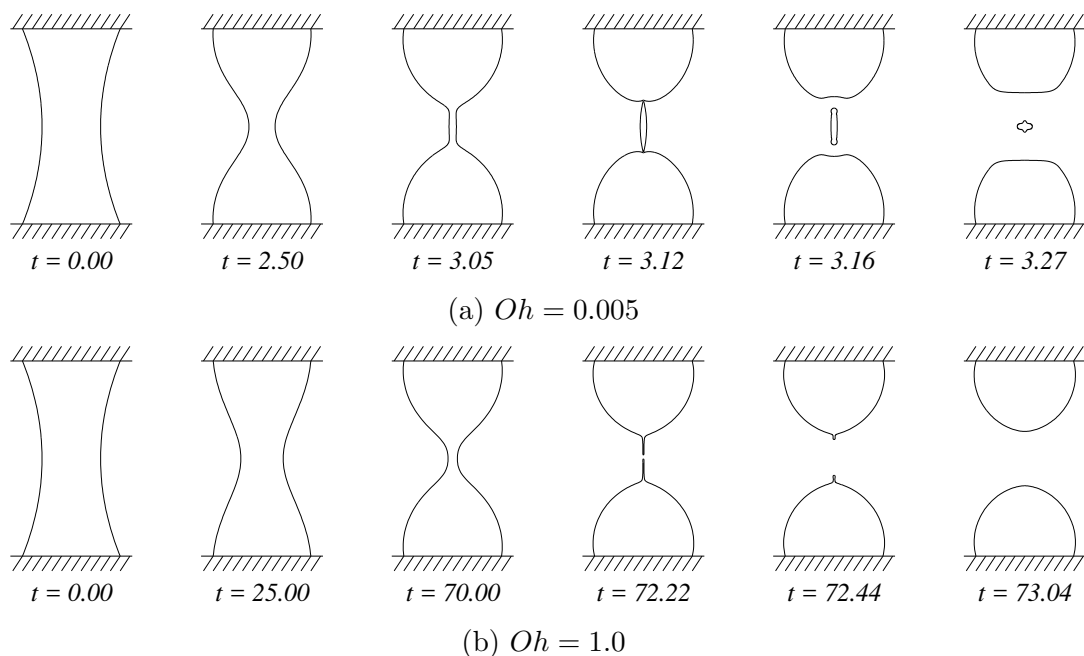


Figure 6.16: The temporal evolution of the interface shapes in the two break-up regimes are illustrated. (a) the distinct feature of the inertial regime is the overturning at the necks ( $t = 3.12$ ) and the formed satellite droplet; (b) the viscous regime does not exhibit overturning and the break-up takes place at the middle of the bridge, thus leaving no satellite droplet.

identified: the viscous regimes for high  $Oh$  number, and the inertial regime for low  $Oh$  number. The temporal evolution of the interface shapes from the two regimes are displayed in Figure 6.16: (a) is from the simulation with  $Oh = 0.005$  while (b) is from the simulation with  $Oh = 1.0$ .

In the inertial regime, the inertial and the capillary force are in balance (Eggers, 1997). The distinct feature of the inertial regime breakup is the overturning near the necks as shown at  $t = 3.12$  in Figure 6.16(a). The thread between the two necks forms a satellite droplet after breakup. The diameter of the satellite droplet  $D_{satellite}$  and the pinchoff instance  $T_{breakup}$  is recorded in Table 6.4. As the  $Oh$  number increases, the satellite droplet becomes smaller and the breakup is delayed.

In the viscous regime, the viscous and the capillary force are in balance (Pa-

## 6. FEM APPLIED TO NON-ISOTHERMAL MULTIPHASE FLOWS

---

Table 6.4: Size of the satellite droplet and time to breakup in isothermal simulations with different values of  $Oh$

$Oh$	$D_{satellite}/D$	$T_{breakup}$
0.005	0.1	3.12
0.01	0.094	3.22
0.05	0.062	4.33
0.1	0.05	7.12
0.5	0.023	36.71
1.0	0.0	72.22

pageorgiou, 1995). As illustrated in Figure 6.16(b), overturning does not occur and the thread in the middle is very thin. In the example of  $Oh = 1.0$ , breakup takes place in the middle of the bridge. The two long ligaments retract back but no subsequent breakup occurs due to the strong viscous force. As a result, there is no droplet generated during this process. If the breakup length scale  $l_{breakup}$  is set smaller, we can resolve a smaller daughter droplet. For instance, the numerical investigation of Li and Sprittles (2016) on a capillary bridge did not stop until the neck diameter reached  $10^{-4}D$  and a tiny daughter droplet was formed. They also identified another transition regime, which is beyond the scope of this thesis. We note that in all isothermal simulations, the up-and-down symmetry is retained as expected.

### 6.4.4 Non-isothermal simulation: effect of $Ca$

In this section, we investigate the effect of  $Ca$  in the break-up of a liquid bridge. The value of  $Pr$  is fixed at 5.0 in all simulations (for comparison, the  $Pr$  number of water is 7.56). The initial temperature field in the liquid bridge is linear and the average temperature of the interface is equivalent to the reference temperature. Under this configuration, the average surface tension on the interface is equal to the surface tension in the isothermal simulation. The length is

## 6.4 Liquid bridge with thermocapillarity

scaled by the bridge diameter  $D$  and temperature is scaled as below:

$$\tilde{T} = \frac{T - T_l}{T_h - T_l}. \quad (6.41)$$

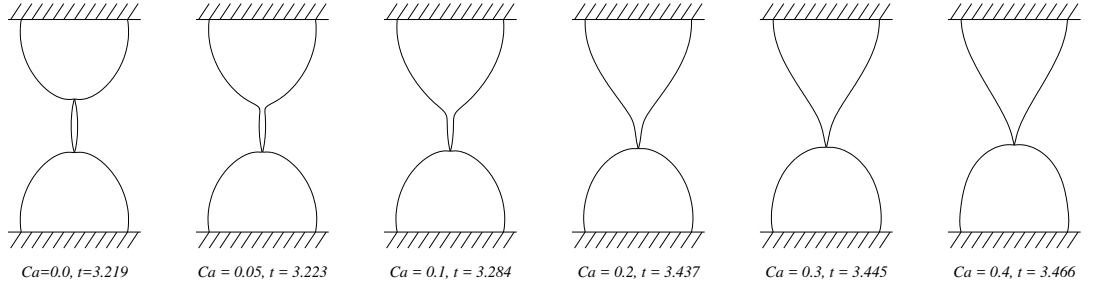


Figure 6.17: Break-up shape and instant for  $Oh = 0.01$  and varied values of  $Ca$ .

We first consider a liquid bridge with  $Oh = 0.01$ , whose isothermal counterpart falls into the inertial regime. The break-up shapes from simulations with a range of values of  $Ca$  are illustrated in Figure 6.17. The up-and-down symmetry is broken by the imposed temperature variation and such asymmetry is more severe with a larger value of  $Ca$ . For example, the breakup shape in the case for  $Ca = 0.05$  has two necks (local minima of the distance from the interface to the axis), but for  $Ca = 0.1$ , the upper neck is not as obvious and disappears for  $Ca > 0.1$ . The subsequent evolution of the interface after break-up also differs with different values of  $Ca$ . The temporal evolution of the interface shape and the temperature field for the simulations of  $Ca = 0.05$  and  $Ca = 0.2$  are shown in Figure 6.18 and Figure 6.19, respectively. The interface is represented by black solid lines and the colour represents the dimensionless temperature. In the case for  $Ca = 0.05$ , the post-pinchoff evolution of the interface is similar to what we have observed in the simulation of a dripping faucet (see Figure 5.8): following the first breakup, the liquid ligament attached to the upper part of the bridge retracts, resulting in a secondary breakup (at  $t = 3.26$ ) and generating a small satellite droplet. By contrast, in the case for  $Ca = 0.2$ , the ligament attached to the upper part is not as thin or as long as in  $Ca = 0.05$ . The retraction of the interface due to capillarity is not as strong and thus there is no satellites droplets formed during this process. Thermocapillary motion in this example separates fluid in the bridge

## 6. FEM APPLIED TO NON-ISOTHERMAL MULTIPHASE FLOWS

---

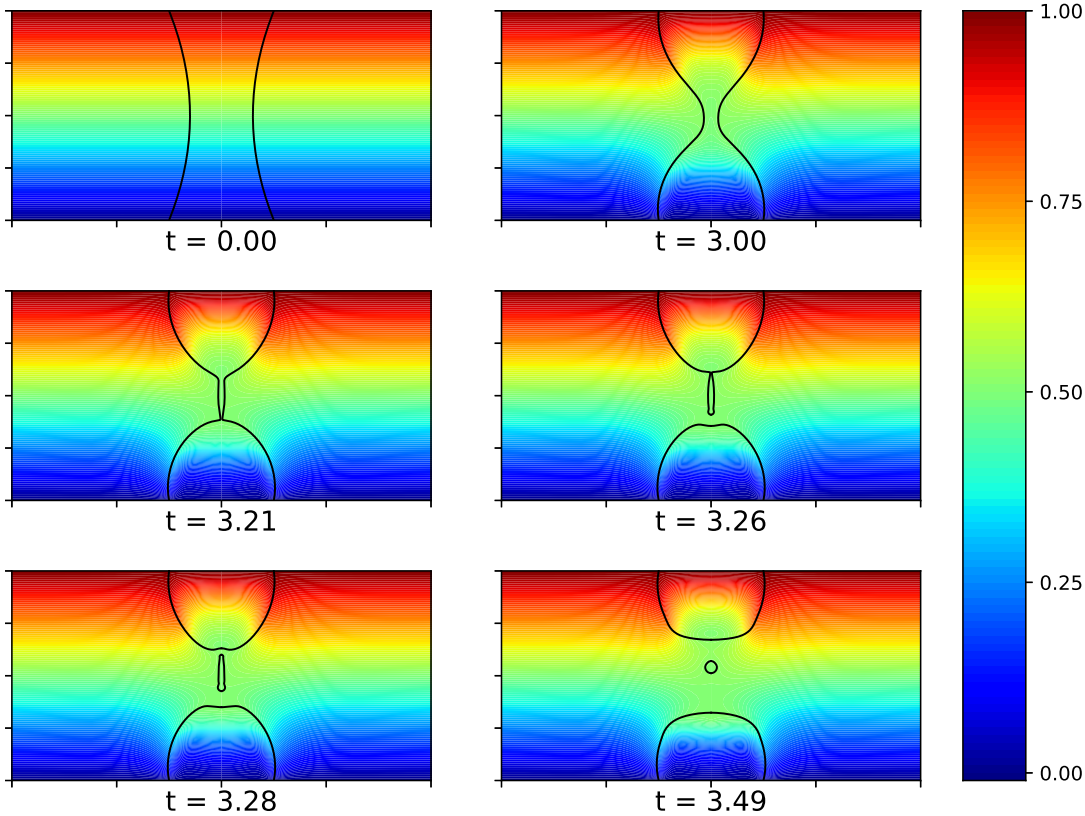


Figure 6.18: Temporal evolution of the interface shape and the thermal field in the simulation with  $Oh = 0.01$ ,  $Ca = 0.05$  and  $Pr = 5$ .

into two parts without loss such as satellites droplets. This phenomenon can be beneficial for some printing processes where satellite droplets should be avoided.

From Figure 6.17 we also observe that time to break-up increases slightly with an increasing value of  $Ca$ . This is due to the interfacial flow driven by the interfacial tension gradient. The velocity fields at time  $t = 2.0$  from two simulations ( $Ca = 0.0$  and  $0.2$ ) are drawn in Figure 6.20, where the left half is from the isothermal simulation while the right half is from the simulation with  $Ca = 0.2$ . The interfaces are drawn in black solid lines. As set initially, the bottom end is cold and the interfacial tension close to this end is larger. The direction of the thermocapillarity-driven Marangoni flow is downwards near the interface. Due to mass conservation, the bulk fluid moves upwards. In contrast,

## 6.4 Liquid bridge with thermocapillarity

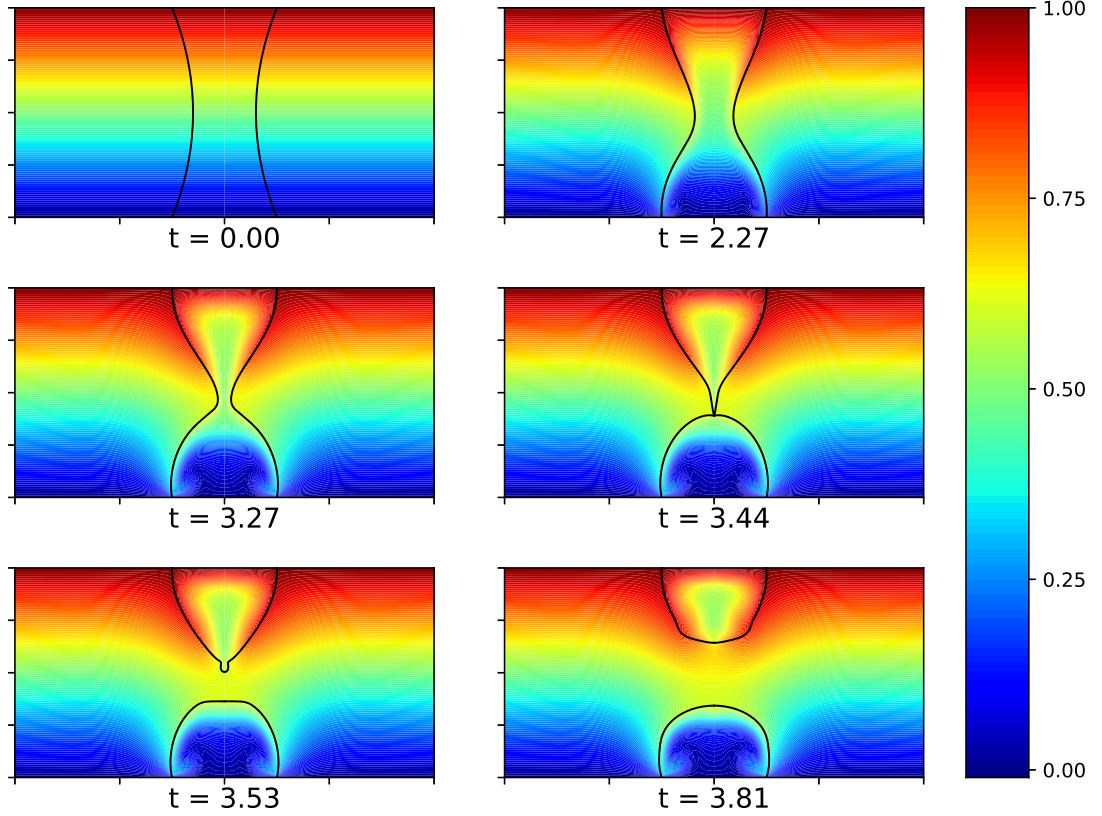


Figure 6.19: Temporal evolution of the interface shape and the thermal field in the simulation with  $Oh = 0.01$ ,  $Ca = 0.2$  and  $Pr = 5$ .

the isothermal flow is upwards in the upper half and downwards in the lower half. The fluid near the neck all flows outwards from the neck region, indicating that the neck is thinning. The non-isothermal interfacial flow is a composite of the Marangoni flow in the tangential direction and the capillary squeezing in the normal direction. When the thermocapillary flow is rather strong such as  $Ca = 0.2$ , the interfacial flow is still sustained towards the cold side and the flow in the neck region is not all outwards. Thinning of the neck is delayed and hence the pinchoff instant is also delayed. This can also explain the disappearance of the upper neck. Since the thermal-driven interfacial flow near the upper neck has the opposite direction to the capillary-driven interfacial flow, the thinning of the upper neck is significantly slowed. In the two non-isothermal examples,

## 6. FEM APPLIED TO NON-ISOTHERMAL MULTIPHASE FLOWS

---

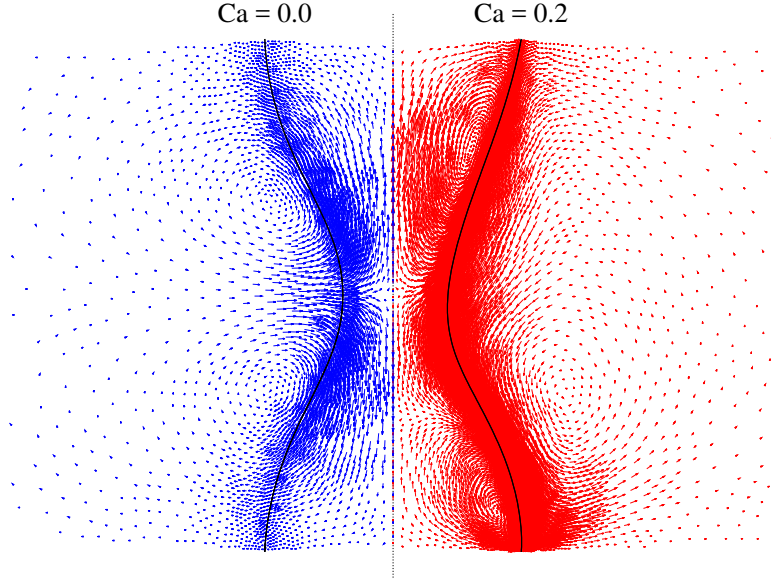


Figure 6.20: Velocity field ( $t = 2.0$ ) for  $Oh = 0.01$ ,  $Ca = 0.0$  (blue) and  $0.2$  (red).

the initial linear temperature field within the bridge is substantially disturbed by convection. If we characterise velocity with  $U_{\Delta\sigma} = |d\sigma/dT|\Delta TD/\nu$ , the  $Pe$  number (in the same form as the  $Ma$  number) is 625 in the case for  $Ca = 0.05$  and is 2500 in the case for  $Ca = 0.2$ . The return flow near the axis transports colder fluid upwards and, as shown in Figure 6.18 and Figure 6.19, the temperature of the interface fluid is in general higher than that of the bulk fluid at the same height.

Next, we consider the non-isothermal flow in a liquid bridge with  $Oh = 1.0$ , whose isothermal counterpart falls into the viscous break-up regime. The interface profile at the pinchoff instant for a range of values of  $Ca$  ( $= 0.0, 0.05, 0.1, 0.2, 0.3$  and  $0.4$ ) are shown in Figure 6.21. The non-isothermal break-up becomes asymmetric: after break-up, the upper part has less volume. With a larger value of  $Ca$ , such asymmetry is more obvious. The volume ratio between the upper fraction and the lower fraction of the liquid bridge  $R_V$  is plotted against  $Ca$  in Figure 6.22(a) in which  $R_V$  decreases with an increasing  $Ca$ .

The pinchoff instant is plotted against  $Ca$  in Figure 6.22(b). The process is accelerated by thermocapillary motion and the time to breakup is reduced by



## 6.4 Liquid bridge with thermocapillarity

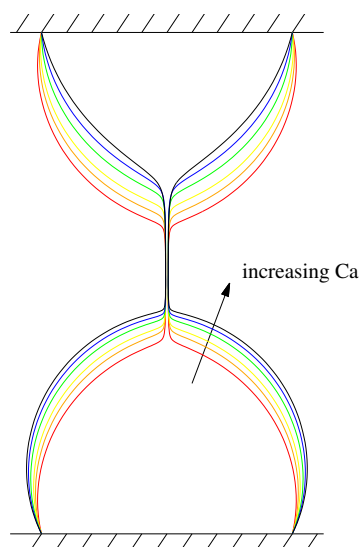


Figure 6.21: Interface profiles at the pinchoff instant for different values of  $Ca$  are drawn in colours: 0.0 (red), 0.05 (orange), 0.1 (yellow), 0.2 (green), 0.3 (dark blue) and 0.4 (black). In all cases,  $Oh = 1.0$ .

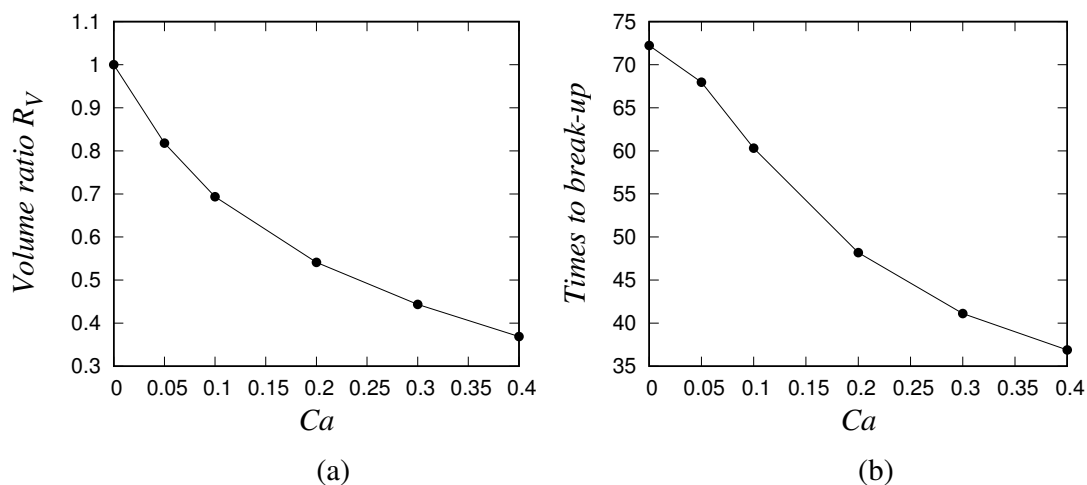


Figure 6.22: Volume ratio between the upper and lower fractions of the liquid bridge  $R_V$  (a) and time to pinchoff (b) are plotted against  $Ca$ .

almost half when  $Ca = 0.4$ . The velocity field at  $t = 20.0$  from the isothermal simulation and simulation with  $Ca = 0.2$  is shown in Figure 6.23. The blue

## 6. FEM APPLIED TO NON-ISOTHERMAL MULTIPHASE FLOWS

---

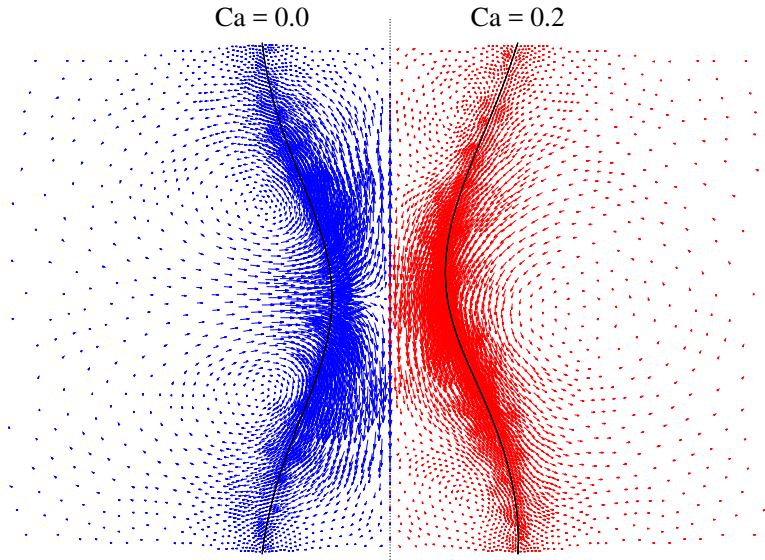


Figure 6.23: Arrows in blue represents the velocity field from the isothermal simulation while the red arrows the velocity field from the non-isothermal simulation with  $Ca = 0.2$ . The magnitude of the isothermal velocity is amplified five times so that it is comparable to the non-isothermal velocity.

arrows representing the isothermal flow field have their magnitude multiplied by five times such that they are visually comparable to the non-isothermal case drawn as red arrows. This indicates that the neck thins much faster in the non-isothermal cases. It can also be observed from the non-isothermal velocity field that the bulk fluid of the bridge is transported towards to the bottom end. This leads to the upper part having less volume at the pinchoff instant.

Compared to the inertial regime, due to strong viscous dissipation, the velocity is much lower and so is the heat convection. The heat transfer is dominated by conduction. For example, the  $Pe$  number is 0.25 in the case for  $Oh = 1.0$  and  $Ca = 0.2$ . As a result the initial linear temperature field is less perturbed by the evolution of the bridge. Figure 6.24 displays the temporal evolution of the interface shape and the temperature field. It is evident that the temperature field does not exhibits large changes in spite that the interface experiences a topology change.

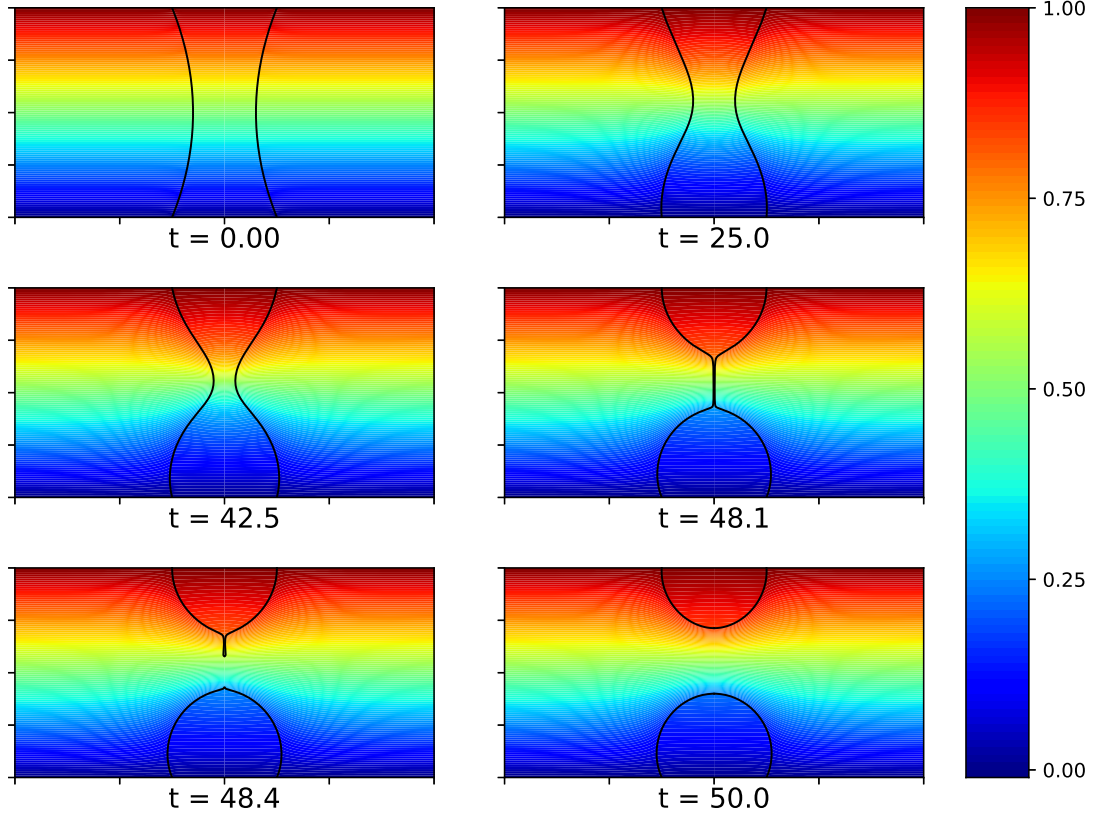


Figure 6.24: Temporal evolution of the temperature field inside the liquid bridge from the non-isothermal simulation with  $Oh = 1.0$  and  $Ca = 0.2$ .

### 6.4.5 Conclusion

In this section we have conducted a parameter study on two-phase liquid bridge with an initially linear temperature distribution. The initial interface shape is fitted to a parabola. A series of isothermal simulations are conducted with a range of values of  $Oh$ . The inertial and viscous regimes are identified for liquid bridge breakup. We then fix the  $Oh$  number and vary the  $Ca$  number to investigate the effect of thermocapillarity on liquid bridge breakup.

The  $Ca$  number measures the relative importance of the Marangoni flow in the tangential direction and the capillary squeeze in the normal direction. The non-isothermal flow in the liquid bridge is a composite of the two. When  $Ca > 0$ , the flow in liquid bridge is asymmetric, and the asymmetry is enhanced as

## 6. FEM APPLIED TO NON-ISOTHERMAL MULTIPHASE FLOWS

---

$Ca$  increases. For the viscous regime (large  $Oh$  number), the Marangoni flow accelerates the break-up process. By contrast, for the inertial regime (small  $Oh$  number), it delays breakup slightly. The thermocapillary motion slows the thinning at the upper neck of the bridge and may lead to the disappearance of the satellite droplet.

# Chapter 7

## Conclusions and future works

The objective of this thesis is to develop a numerical tool for simulating non-isothermal multiphase flows, and to apply the method to study the non-isothermal break-up of liquid bridge. In this chapter, the main conclusions are presented first, followed by recommendations for future work.

Our numerical method is based on the numerical method developed by Li (2013) for simulating multiphase flows: the computational domain is divided into unstructured triangular mesh; the interface is represented explicitly by mesh lines (interface-conforming); the mesh is adapted to follow the moving interface; the governing equations are discretised using the  $P2 - P1d$  finite element method (FEM) and are solved with *uzawa* iterations.

Two major modifications have been made to the original method:

(1). For the study of non-isothermal flows, an FEM solver for the advection diffusion equation of temperature has been implemented. The numerical representation of the force balance condition has been extended to account for non-uniform interfacial tension. The thermal-induced buoyancy has also been included into the previous Navier-Stokes solver.

(2). Interface topology changes are involved in many multiphase flow problems, while our previous numerical method lacks of related treatment. Using rules in the adaptive mesh generator, we achieve one layer of elements in the thin regions prior to interface topology changes. The interface can then be split and re-connected easily. This treatment has been incorporated into our numerical method.

## 7. CONCLUSIONS AND FUTURE WORKS

---

The success of a numerical study lies on the accuracy and robustness of the numerical method. For this purpose, we have thoroughly examined the accuracy of our numerical methods through a number of benchmark tests with focus on the interface force balance condition, the topology changes and non-isothermal effects:

### 1. interface force balance condition

For the example of a circular/spherical droplet, we prove that our numerical method achieves the balance between interfacial tension and the associated pressure jump at a discrete level. As a result, the static Laplace solution for a circular/spherical droplet exists. The numerical stability of this solution is further examined. We have found that for  $Oh \geq 10^{-3}$ , the magnitude of the dimensionless spurious current is reduced to machine error, around  $10^{-15}$ , even after a long period. This indicates that the solution is numerically stable.

Another benchmark test, the axisymmetric oscillation of a freesurface droplet and bubble, is performed to validate the temporal and spatial accuracy of our method. The simulated results are in excellent agreement with the analytical solution by Prosperetti (1980), including the example with a weak viscous damping  $Oh = 10^{-3}$ . Droplet/bubble oscillation with  $Oh \sim 10^{-3}$  is rarely seen in the literature since the weak viscous damping is not able to suppress spurious currents in some methods. The success of this benchmark test demonstrates the capability of our method in coping with the spurious currents.

### 2. interface topology changes

In contrast to interface non-conforming methods, interface topology changes are not dealt with automatically in our method. A mesh parameter  $l_{breakup}$  is required to determine whether the topology changes should occur. We have used two different benchmark examples for validation: dripping from a faucet and binary droplet collision. The choice of  $l_{breakup}$  has little effects in the former, while it may alter the simulation outcome in the latter.

In the dripping faucet simulation, the physical parameters are set in accord with the dripping experiment by Peregrine et al. (1990). We start with simulating the equilibrium shape of a pendant droplet given a certain volume. The simulation results are in good agreement with the analytical solution, and a second order convergence rate is demonstrated through a convergence study. All stages of

---

the dripping experiment are well reproduced in our simulation, despite the weak viscous damping,  $Oh \sim 10^{-3}$ . This benchmark test validates our treatment in topology changes, and also shows the ability of our method in retaining the numerical force balance on the interface.

The simulation of binary droplet collision requires the method to not only include the rarefied gas effect and the intermolecular force, but also to resolve a disparity in length scales from  $10^{-4}$  m to  $10^{-9}$  m. Inaccuracy in modelling the inter-droplet flow and a mischosen  $l_{breakup}$  may lead to a wrong prediction of the collision outcome. Previous VOF or LS simulations rely on an empirical model or parameter in deciding whether and when the thin gas film ruptures. In contrast, we resolve the flow until the inevitability of the interface topology change, e.g. the intermolecular van der Waals force dominates. Remarkable agreement has been obtained with the experimental results of a coalescence example in Pan et al. (2008). We not only predict the correct outcome of the collision, but also the precise instant of film rupture. This shows the accuracy of our method in modelling the inter-drop gas film. The robustness of our method is also demonstrated through the fact that the method resolves an extreme range of length scales.

### **3. thermocapillarity**

For the application in non-isothermal multiphase flows, we first validate the FEM solver for temperature. The relative error compared to the benchmark results of the natural convection in a square cavity are all within 3%. The numerical treatment of non-uniform interfacial tension due to the temperature inhomogeneity are examined using two examples: the thermocapillary convection in two superimposed layers and the migration of a spherical droplet subject to a constant temperature gradient. We have found that our simulation are in good agreement with the corresponding analytical solution. The convergence study in droplet migration shows a second order convergence rate. The droplet migration with a finite  $Re$ ,  $Ma$  and  $Ca$  is also simulated. Our axisymmetric simulation agrees well with Liu et al. (2012) in low  $Ma$  examples. The 5% discrepancy in the  $Ma = 100$  example is believed to due to the difference from three-dimensional simulation.

## 7. CONCLUSIONS AND FUTURE WORKS

---

Having validated our numerical method for non-isothermal multiphase flow, we conduct a two-phase numerical investigation on the break-up of a liquid bridge with an initially linear temperature field. This configuration occurs in many technical applications such as crystal growth and welding. Keeping all other dimensionless numbers fixed, we focus on the influence of  $Oh$  and  $Ca$ . A series of isothermal simulations are conducted, and two breakup regimes are identified, namely the inertial regime (small  $Oh$ ) and the viscous regime (large  $Oh$ ). In non-isothermal situation, the flow on the interface is a composition of the two flows: the Marangoni flow in the tangential direction and the capillary squeeze in the normal direction. The ratio between the two is measured by the  $Ca$  number. The influence of  $Ca$  has been investigated for two examples:  $Oh = 0.01$  for inertial breakup and  $Oh = 1.0$  for viscous breakup. The up-and-down symmetry in non-isothermal flow is broken and the symmetry is enhanced as  $Ca$  increases. In the case where  $Oh = 0.01$ , for some large  $Ca$  number ( $\geq 0.2$  in our simulation), the asymmetric breakup leaves no formation of satellite droplets, unlike the isothermal simulation. Due to the thermocapillary motion, the breakup is slightly delayed. In contrast, the breakup is accelerated with an increase in the values of  $Ca$  when  $Oh = 1.0$ .

During our work, we have identified many possibilities for future work, which are listed below:

### **thermocapillary motion within a long confined thread**

In developing a microfluidic flow focusing device, De Saint Vincent et al. (2015) induced a temperature fluctuation along the interface by applying a laser beam. Without thermocapillarity, the long thread is rather stable due to the geometric confinement (Humphry et al., 2009). For a comprehensive understanding of the problem, it is worthwhile to carry out a numerical study to investigate the role of thermocapillary motion. This can be of benefit for the droplet generation in a long and confined micro-tube.

### **isoparametric moving mesh:**

Currently the edge midpoints on interface edges are not moving in a Lagrangian way. If they can be put on the moving interface, the interface will be represented by piecewisely quadratic segments. Since more nodes are on the interface with the same number of interface edges, it is expected that such treatment



---

is more efficient compared to the straight edge method with similar accuracy. However, a great deal of work is required to verify whether the current curvature estimation, mesh movement, mesh refinement etc., are still valid under the framework of an isoparametric representation of the interface.

**moving contact line modelling:**

Many microfluidic applications involve a droplet attached to a wall boundary. With moving contact line modelling incorporated, the method can be applied to the study of the thermocapillary motion of a droplet attached to a plate or a tube. Numerical investigations by Sui (2014) and Fath and Bothe (2015) have shown that adding moving contact motion may yield new migration phenomena: the droplet can also migrate to the cold side with a large contact angle. Furthermore, with a valid implementation of moving contact lines, the applicable range of our method will be further extended.

**generalising the interface topology changes:**

Our numerical treatment of interface topology changes have been used to break-up the thin region between an interface and a symmetry boundary. It is worthwhile to generalise this treatment to break-up between two interfaces with arbitrary shapes and locations. This can be useful in problems such as the collision of droplets with different size, droplet splashing or a bubble crossing a water-oil interface.

**three dimensional configuration:**

We have seen that our adaptive moving mesh generator has reduced a great amount of computational costs compared to structured uniform mesh. This makes us wonder how much computational costs can be reduced with a similar mesh generator in three-dimensional configuration. Additionally, a three-dimensional method is more general than our current method for two-dimensional and axisymmetric flows.

## 7. CONCLUSIONS AND FUTURE WORKS

---

# Appendix A

## Numerical implementation of FEM

In this section, we introduce some technical details in the numerical implementation of FEM: the mesh data structure, the storage for a sparse matrix and the numerical technique to calculate integrals over a triangle.

### A.1 Mesh data structure

Our method uses an unstructured triangular mesh, which requires the connectivity information between elements to be explicitly stored. To define a triangulation of a region  $\Omega$ , we need to know the total number of nodes (`NUMBEROFNODES`), the total number of triangles (`NUMBEROFTRIANGLES`), and the total number of edges (`NUMBEROFEDGES`).

The coordinates of the nodes are stored in a list `LISTOFNODES` with the size being `NUMBEROFNODES` (see Table A.1). The list of triangles is also called the connectivity of the triangulation. It is defined as `LISTOFTRIANGLES` with the size `NUMBEROFTRIANGLES` (see Table A.2). The  $i$ -th element in `LISTOFTRIANGLES` contains the numbers of three vertices of the  $i$ -th triangle. The edge information is stored explicitly using the `LISTOFEDGES` whose size is `NUMBEROFEDGES` (see Table A.3).

It is often useful to give further information between neighbouring nodes and edges, between neighbouring edges and triangles, and between triangles

## A. NUMERICAL IMPLEMENTATION OF FEM

---

<i>x</i> -Coordinate	<i>y</i> -Coordinate
$x_0$	$y_0$
$x_1$	$y_1$
...	...
$x_{\text{NumberOfNodes}-1}$	$y_{\text{NumberOfNodes}-1}$

Table A.1: LISTOFNODES[NUMBEROFNODES]

Number of 1st node	Number of 2nd node	Number of 3rd node
$n_{0,0}$	$n_{0,1}$	$n_{0,2}$
$n_{1,0}$	$n_{1,1}$	$n_{1,2}$
...	...	...
$n_{\text{NumberOfTriangles}-1,0}$	$n_{\text{NumberOfTriangles}-1,1}$	$n_{\text{NumberOfTriangles}-1,2}$

Table A.2: LISTOFTRIANGLES[NUMBEROFTRIANGLES]

Number of 1st node	Number of 2nd node
$n_{0,0}$	$n_{0,1}$
$n_{1,0}$	$n_{1,1}$
...	...
$n_{\text{NumberOfEdges}-1,0}$	$n_{\text{NumberOfEdges}-1,1}$

Table A.3: LISTOFEDGES[NUMBEROFEDGES]

and nodes. For example, LISTOFTRIANGLES provides the three nodes in one triangle, from which we can find the list of triangles that contains each node: NODES\_TRIANGLES. As the number of triangles that includes one node varies from node to node, we need to keep track this number by a list NUMBEROF-

`TRIANGLESATNODES` whose size is `NUMBEROFNODES`. Similarly, from the `LISTOFEDGES` we can find the list of edges that includes each node `NODES_EDGES`. Again, the number of edges that contains one node varies from node to node, we need keep track this number by a list `NUMBEROFEDGESATNODES`. Finally, from `NODES_TRIANGLES` and `NODES_EDGES` we find the list of edges included in each triangle: `TRIANGLES_EDGES`, and the list of triangle which include one edge: `EDGES_TRIANGLES`. The size of the list `TRIANGLES_EDGES` is `NUMBEROFTRIANGLES×3`, while the size of `EDGES_TRIANGLES` is more complicate because an interior edge is included in two triangles while a boundary edge is include in one triangle only. We need an additional list `NUMBEROFTRIANGLESATEDGES[NUMBEROFEDGES]`.

The boundary information is stored explicitly for the convenience in applying boundary conditions. Assuming there are `NUMBEROFBOUNDARIES` boundaries, we define `LISTOFNODESATBOUNDARIES` and `LISTOFEDGESATBOUNDARIES`, which store the nodes and edges on this boundaries, respectively. The name and condition for boundaries are stored in the string list, `BOUNDARYNAMES` and `BOUNDARYCONDS`, respectively. As the number of edges/nodes may be different from boundary to boundary, these numbers are stored by the list `NUMBEROFEDGESATBOUNDARIES` and `NUMBEROFNODESATBOUNDARIES`, respectively. To differ nodes/edges on the boundaries from interior nodes/edges, the status of each node/edge is stored in the list `NDTYPE` and `EDTYPE`, the value of the element in which equals the number of the boundary.

As the method is applied to fluid flows with two or more phases, we use the `NUMBEROFDOMAINS` to denote the number of phases. Triangles in each phase are stored in the `LISTOFTRIANGLESATDOMAINS`. To differ triangles in one phase from those in another phase, the list `TRTYPE` is used. The value of elements in this list represents the number of the domain.

## **A.2 Storage for a sparse matrix**

An important observation is that the matrix obtained in the finite element method is sparse. For example,  $A_{ij}$  in equation (3.12) is nonzero only when node  $i$  is one of the nodes of a triangle that is adjacent to node  $j$ . When a sparse

## A. NUMERICAL IMPLEMENTATION OF FEM

---

matrix of dimension  $N \times N$  contains only a few times of  $N$  nonzero elements (a typical case in the finite element method), it is surely inefficient – and often physically impossible – to allocate storage for all  $N^2$  elements. Even if one did allocate such storage, it would be inefficient or prohibitive in machine time to loop over all of it in search of nonzero elements.

Obviously we require a kind of indexed storage scheme, which stores only nonzero matrix elements, along with sufficient auxiliary information to determine where an element logically belongs and how the various elements can be looped over in common matrix operations. Our method uses the compressed sparse row matrix (CSR) format, which requires storage of less than three times the number of nonzero matrix element (Press et al., 1996). To represent a matrix  $\mathbf{A}$  of dimension  $N \times N$ , the CSR scheme sets up two integer arrays  $ia$  and  $ja$ , and one double array  $a$ . The size of these arrays are defined by three integer  $nrow$  (number of rows),  $ncol$  (number of columns), and  $nnz$  (number of nonzero matrix element). The storage rules are:

- The nonzero elements are saved in the variable  $a[nnz]$  ordered by row and, within each row, ordered by columns.
- The variable  $ia[i]$  is the location of first nonzero element of row  $i + 1$  in the array  $ja$ .  $ia[i + 1] - ia[i]$  is the number of the nonzero elements in row  $i + 1$ . The size of  $ia$  is  $nrow + 1$ .
- The variable  $ja[nnz]$  is the column index of the corresponding nonzero elements.

As an example, consider the matrix

$$\begin{pmatrix} 3. & 0. & 1. & 0. & 0. \\ 0. & 4. & 0. & 0. & 0. \\ 0. & 7. & 5. & 9. & 0. \\ 0. & 0. & 0. & 0. & 2. \\ 0. & 0. & 0. & 6. & 5. \end{pmatrix} \quad (\text{A.1})$$

In CSR format, matrix (A.1) is represented by one array  $ia$  of length 5 and two arrays  $ja$  and  $a$  of lengths 8, as follows:

index $i$	0	1	2	3	4	5			
ia[ $i$ ]	1	3	4	7	8	10			
ja[ $i$ ]	1	3	2	2	3	4	5	4	5
a[ $i$ ]	3.	1.	4.	7.	5.	9.	2.	6.	5.

Table A.4: CSR representation of matrix (A.1).

### A.3 Hammer integration formulas

The Hammer formulas are used to numerically calculate the integration over the reference element (Dhatt et al., 2012). For example, we consider an integrand  $f(\xi, \eta)$  and the integration is approximated as below:

$$\int_0^1 \int_0^{1-\eta} f(\xi, \eta) d\xi d\eta \approx \sum_{i=1}^r w_i f(s_i, t_i). \quad (\text{A.2})$$

These integration formulas are exact for polynomial of order  $m$  ( $\xi^i \eta^j$  with  $i + j \leq m$ ) and they are provided in Figure A.1 and A.2.

## A. NUMERICAL IMPLEMENTATION OF FEM

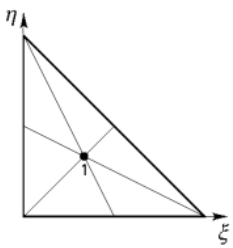
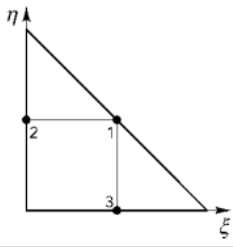
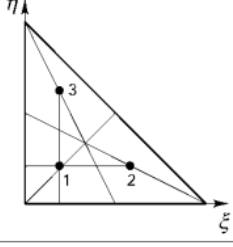
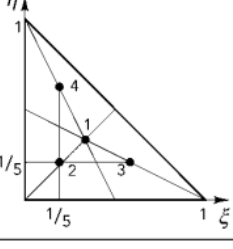
	Order $m$	Number of points $r$	Coordinates		Weight $w_i$
			$\xi_i$	$\eta_i$	
	1	1	1/3	1/3	1/2
	2	3	1/2 0 1/2	1/2 1/2 0	1/6
	2	3	1/6 2/3 1/6	1/6 1/6 2/3	1/6
	3	4	1/3 1/5 3/5 1/5	1/3 1/5 1/5 3/5	-27/96 25/96

Figure A.1: Direct formulas for Hammer integration over a reference triangle (part 1). The image is from Dhatt et al. (2012).



### A.3 Hammer integration formulas

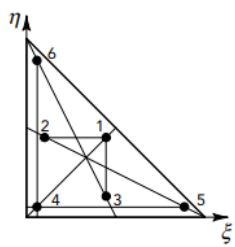
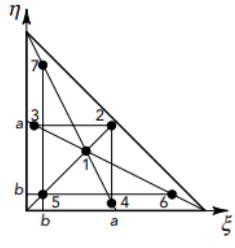
	Order $m$	Number of points $r$	Coordinates		Weight $w_i$
			$\xi_i$	$\eta_i$	
	4	6	$a$ $1 - 2a$ $a$ $b$ $1 - 2b$ $b$	$a$ $a$ $1 - 2a$ $b$ $b$ $1 - 2b$	$\left. \begin{array}{l} 0.111690794839005 \\ \\ \\ \end{array} \right\}$ $\left. \begin{array}{l} \\ \\ 0.054975871827661 \end{array} \right\}$
	5	7	$1/3$ $a$ $1 - 2a$ $a$ $b$ $1 - 2b$ $b$	$1/3$ $a$ $a$ $1 - 2a$ $b$ $b$ $1 - 2b$	$\left. \begin{array}{l} 9/80 \\ A = \frac{155 + \sqrt{15}}{2400} \\ = 0.0661970763942530 \end{array} \right\}$ $\left. \begin{array}{l} \frac{31}{240} - A = \\ = 0.0629695902724135 \end{array} \right\}$
	6	12	$a$ $1 - 2a$ $a$ $b$ $1 - 2b$ $b$ $c$ $d$ $1 - (c + d)$ $1 - (c + d)$ $c$ $d$	$a$ $a$ $1 - 2a$ $b$ $b$ $1 - 2b$ $d$ $c$ $c$ $c$ $1 - (c + d)$ $1 - (c + d)$	$\left. \begin{array}{l} 0.025422453185103 \\ \\ \\ \end{array} \right\}$ $\left. \begin{array}{l} \\ \\ 0.058393137863189 \end{array} \right\}$ $\left. \begin{array}{l} \\ \\ 0.041425537809187 \end{array} \right\}$

Figure A.2: Direct formulas for Hammer integration over a reference triangle (part 2). The image is from Dhatt et al. (2012).

## A. NUMERICAL IMPLEMENTATION OF FEM

---

# Appendix B

## The force balance on the interface

In this part, the dynamic boundary condition on the interface is derived. We start with the two-dimensional case (on the  $x - z$  plane). The parametric representation of the interface shape is as below:

$$\begin{cases} x = x(s), \\ z = z(s). \end{cases} \quad (\text{B.1})$$

We use  $l$  to denote the arc-length and  $dl = \sqrt{x'^2 + z'^2} ds$ . Note that in the section, the dash  $'$  denotes the derivative with respect to  $s$ . A very small piece of interface with length  $\Delta l$  ( $\Delta l \rightarrow 0$ ) is considered, as illustrated in the left panel of Figure B.1. This piece of interface is subject to the force applied by the bulk fluid of both phase 1 and 2 and the surface tension force along the tangent direction. The force balance equation reads:

$$(\mathbf{T}_2 \cdot \mathbf{n} - \mathbf{T}_1 \cdot \mathbf{n})\Delta l + \sigma(s + \Delta s)\mathbf{t}(s + \Delta s) - \sigma(s)\mathbf{t}(s) = \mathbf{0}, \quad (\text{B.2})$$

where  $\mathbf{T}$  is the stress tensor in equation (4.4),  $\sigma$  is the interfacial tension,  $\mathbf{n}$  is the unit normal vector and  $\mathbf{t}$  is the unit tangent vector:

$$\begin{cases} \mathbf{n} = \frac{z'}{\sqrt{x'^2 + z'^2}}\vec{e}_x - \frac{x'}{\sqrt{x'^2 + z'^2}}\vec{e}_z, \\ \mathbf{t} = \frac{x'}{\sqrt{x'^2 + z'^2}}\vec{e}_x + \frac{z'}{\sqrt{x'^2 + z'^2}}\vec{e}_z, \end{cases} \quad (\text{B.3})$$

## B. THE FORCE BALANCE ON THE INTERFACE

---

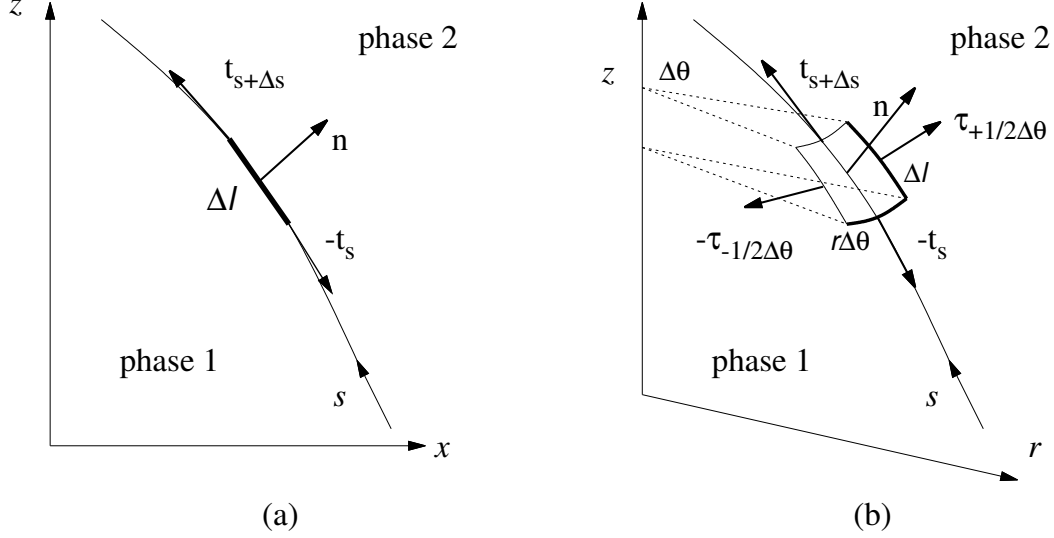


Figure B.1: The interface piece is represented by (a)  $\Delta l$  in two-dimensional  $x - z$  plane, and (b)  $\Delta l \times r\Delta\theta$  in axisymmetric  $r - z$  plane.

in which  $\vec{e}_x$  and  $\vec{e}_z$  are the unit vectors in the direction of the  $x$  and  $z$  axes, respectively. Let  $\Delta l \rightarrow 0$  and we obtain:

$$(\mathbf{T}_1 - \mathbf{T}_2) \cdot \mathbf{n} = \frac{d(\sigma\mathbf{t})}{dl} = \frac{d\sigma}{dl}\mathbf{t} + \frac{d\mathbf{t}}{dl}\sigma = \frac{d\sigma}{dl}\mathbf{t} + \sigma\kappa\mathbf{n}, \quad (\text{B.4})$$

where  $\kappa$  is the curvature. When  $\sigma$  is a constant, the term  $d\sigma/dl\mathbf{t}$  on the right hand side vanishes.

In the above equation, the last equality is due to the Frenet–Serret formula (Aris, 2012):

$$\frac{d\mathbf{t}}{dl} = \kappa\mathbf{n}. \quad (\text{B.5})$$

The curvature  $\kappa$  in two-dimensional configuration has the form as below:

$$\kappa = \frac{x''z' - z''x'}{(x'^2 + z'^2)^{3/2}}. \quad (\text{B.6})$$

Similarly we can obtain the force balance condition in the axisymmetric configuration (on the  $r - z$  plane). Consider a small interface quadrilateral element in the right panel of Figure B.1. The element is small enough such that we can make

---

the approximations: (1) the surface area is  $\Delta l \times r \Delta \theta$ ; (2) the normal vector is constant on this surface element. The force balance equation of this small element reads:

$$\begin{aligned}
(\mathbf{T}_1 - \mathbf{T}_2) \cdot \mathbf{n} r \Delta \theta \Delta l + \sigma(s + \Delta s) \mathbf{t}(s + \Delta s) r(s + \Delta s) \Delta \theta - \sigma(s) \mathbf{t}(s) r(s) \Delta \theta \\
+ \sigma(s + 1/2 \Delta s) \boldsymbol{\tau}(+1/2 \Delta \theta) \Delta l - \sigma(s + 1/2 \Delta s) \boldsymbol{\tau}(-1/2 \Delta \theta) \Delta l = \mathbf{0}
\end{aligned} \tag{B.7}$$

in which  $\mathbf{n}$  and  $\mathbf{t}$  are the unit normal and tangent vectors in the  $r - z$  plane and  $\boldsymbol{\tau}$  represents the unit vector in the azimuthal direction which is perpendicular to the  $r - z$  plane, as illustrated in the schematic in the right panel of Figure B.1. We let  $\Delta \theta \rightarrow 0$  and  $\Delta l \rightarrow 0$  and achieve:

$$(\mathbf{T}_1 - \mathbf{T}_2) \cdot \mathbf{n} = \frac{1}{r} \frac{d(\sigma r \mathbf{t})}{dl} + \sigma \frac{1}{r} \frac{d\boldsymbol{\tau}}{d\theta}. \tag{B.8}$$

Here we have used the fact that  $\partial \sigma / \partial \theta = 0$  in the axisymmetric configuration although  $\sigma$  is non-uniform.

In the  $r - z$  plane, the interface has the parametric representation  $r = r(s)$ ,  $z = z(s)$ . The normal and tangent vectors have similar formulation to equation (B.3). We can use the previous result to simplify the first term on the right hand side of equation (B.8):

$$\begin{aligned}
\frac{1}{r} \frac{d(\sigma r \mathbf{t})}{dl} &= \frac{d\sigma}{dl} \mathbf{t} + \frac{\sigma}{r} \frac{dr}{dl} \mathbf{t} + \sigma \frac{d\mathbf{t}}{dl} \\
&= \frac{d\sigma}{ds} \mathbf{t} + \frac{\sigma}{r} \frac{r'}{\sqrt{r'^2 + z'^2}} \mathbf{t} + \sigma \frac{r'' z' - z'' r'}{(r'^2 + z'^2)^{3/2}} \mathbf{n}.
\end{aligned} \tag{B.9}$$

For the second term on the right hand side of equation (B.8),

$$\frac{\sigma}{r} \frac{d\boldsymbol{\tau}}{d\theta} = -\frac{\sigma}{r} \left( \frac{r'}{\sqrt{r'^2 + z'^2}} \mathbf{t} + \frac{z'}{\sqrt{r'^2 + z'^2}} \mathbf{n} \right). \tag{B.10}$$

With the above two equations, we conclude that the force balance condition in axisymmetric configuration reads:

$$\begin{aligned}
(\mathbf{T}_1 - \mathbf{T}_2) \cdot \mathbf{n} &= \frac{d\sigma}{dl} \mathbf{t} + \sigma \left( \frac{r'' z' - z'' r'}{(r'^2 + z'^2)^{3/2}} - \frac{z'}{r \sqrt{r'^2 + z'^2}} \right) \mathbf{n} \\
&= \frac{d\sigma}{dl} \mathbf{t} + \sigma \kappa \mathbf{n}
\end{aligned} \tag{B.11}$$

## B. THE FORCE BALANCE ON THE INTERFACE

---

in which  $\kappa$  is the curvature in axisymmetric configuration. Note that the formulation of  $\kappa$  is affected by the defined orientation of the interface. In this thesis, we always consider the anti-clockwise direction as the orientation of the interface in  $x - z$  or  $r - z$  plane. For free-surface problem, the outer-side fluid is considered passive:  $\mathbf{T}_2 = -p_0\mathbf{I}$  where  $p_0$  is a constant, usually set at 0.

# Appendix C

## Weak formulation in axisymmetric geometry

We multiply  $\psi$  on both side of equation (4.8a) to obtain the weak form of the continuity equation and integrate over the whole domain:

$$\int_{\Omega} \left( \frac{\partial u}{\partial r} + \frac{u}{r} + \frac{\partial v}{\partial z} \right) \psi r dr dz = 0. \quad (\text{C.1})$$

The momentum equation and heat transfer equation (4.8b), (4.8c), and (6.22) are multiplied with  $\phi$  on both sides. Following the similar procedure in 4.2.1, we obtain the weak formulations:

$$\begin{aligned} \int_{\Omega} \left( \rho \phi \frac{du}{dt} + 2\mu \frac{\partial \phi}{\partial r} \frac{\partial u}{\partial r} + 2\phi \mu \frac{u}{r^2} + \mu \frac{\partial \phi}{\partial z} \frac{\partial u}{\partial z} + \mu \frac{\partial \phi}{\partial z} \frac{\partial v}{\partial r} - p \left( \frac{\phi}{r} + \frac{\partial \phi}{\partial r} \right) \right) r dr dz \\ = \int_{\Gamma} \left( \sigma \kappa n_r + \frac{d\sigma}{ds} t_r \right) r \phi dl + \int_{\Omega} f_r \phi r dr dz, \end{aligned} \quad (\text{C.2a})$$

$$\begin{aligned} \int_{\Omega} \left( \rho \phi \frac{dv}{dt} + \mu \frac{\partial \phi}{\partial r} \frac{\partial v}{\partial z} + \mu \frac{\partial \phi}{\partial r} \frac{\partial v}{\partial r} + 2\mu \frac{\partial \phi}{\partial z} \frac{\partial v}{\partial z} - p \frac{\partial \phi}{\partial z} \right) r dr dz \\ = \int_{\Gamma} \left( \sigma \kappa n_z + \frac{d\sigma}{ds} t_z \right) r \phi dl + \int_{\Omega} f_z \phi r dr dz, \end{aligned} \quad (\text{C.2b})$$

$$\int_{\Omega} \left( \rho c_p \frac{dT}{dt} + k \frac{\partial T}{\partial r} \frac{\partial \phi}{\partial r} + k \frac{\partial T}{\partial z} \frac{\partial \phi}{\partial z} \right) r dr dz = 0. \quad (\text{C.2c})$$

in which  $\mathbf{n} = (n_r, n_z)$  and  $\mathbf{t} = (t_r, t_z)$  are the normal and tangent vectors on the interface  $\Gamma$ . Note that the force balance conditions on the interface are in

## **C. WEAK FORMULATION IN AXISYMMETRIC GEOMETRY**

---

different form in isothermal and non-isothermal cases (see equation (4.6) and equation (6.7)). In isothermal cases, the  $d\sigma/ds$  term in equation (C.2) vanishes.



# Appendix D

## Computing information

Simulations in this thesis were all performed using the computers of the BP Institute, Cambridge. The detailed information about the machine is presented in the Table D.1. Note that all simulations are run on a single core.

Though this thesis mainly focuses on the accuracy and the capability of the numerical method, rather than the efficiency, it is worthwhile to provide some information regarding the computing cost for the reader, and for future users of the method. An estimated computational time for some simulations carried out in the thesis are presented in Table D.2. Since the mesh is adaptive, there is no fixed number of vertices for each simulation and the number of vertices of the initial mesh is used. In some cases, the initial mesh is coarse, but it will be refined during the computation. For example, the initial number of vertices in the droplet collision simulation is 304, but the number of vertices is 3836 when break-up takes place.

Table D.1: CPU information

CPU model name	Intel(R) Xeon(R) CPU E5-2680 0@2.70GHz
CPU cache size	20480 KB
CPU cores	8
Number of logical cores	16
Total memory	128 GB

## D. COMPUTING INFORMATION

---

Table D.2: Computing time

Simulation	# of vertices	# of time steps	Time
Laplace solution $Oh = 10^{-3}$	1573	400000	5 days
Drop Oscillation $Oh = 10^{-2}$	591	2000	11 minutes
Dripping	1017	434500	12 days
Droplet collision ( $We = 2.25$ )	394	625000	23 days
Liquid bridge ( $Oh = 0.01, Ca = 0.2$ )	827	20000	2 days

# Bibliography

- T. Abadie, J. Aubin, and D. Legendre. On the combined effects of surface tension force calculation and interface advection on spurious currents within volume of fluid and level set frameworks. *Journal of Computational Physics*, 297:611–636, 2015. 12
- A. Anilkumar, R. Grugel, X. Shen, C. Lee, and T. Wang. Control of thermocapillary convection in a liquid bridge by vibration. *Journal of Applied Physics*, 73(9):4165–4170, 1993. 7
- Rutherford Aris. *Vectors, tensors and the basic equations of fluid mechanics*. Courier Corporation, 2012. 160
- C. Ashcraft, R. Grimes, D. Pierce, and D. Wah. Solving linear systems using spooles 2.2. *Boeing Phantom Works*, 2002. 52, 112
- N. Ashgriz and Y. Poo. Coalescence and separation in binary collisions of liquid drops. *Journal of Fluid Mechanics*, 221:183–204, 1990. 91
- B. Bejanov, J. Guermond, and P. Minev. A grid-alignment finite element technique for incompressible multicomponent flows. *Journal of Computational Physics*, 227(13):6473–6489, 2008. 10
- H. Bénard. Les tourbillons cellulaires dans une nappe liquide.-méthodes optiques d’observation et d’enregistrement. *Journal de Physique Théorique et Appliquée*, 10(1):254–266, 1901. 5
- M. Bern and P. Plassmann. Mesh generation. *Handbook of Computational Geometry*, 6, 1999. 20

## BIBLIOGRAPHY

---

- W. Bond. The surface tension of a moving water sheet. *Proceedings of the Physical Society*, 47(4):549, 1935. 45
- M. Bowen and B. Tilley. Thermally induced van der waals rupture of thin viscous fluid sheets. *Physics of Fluids*, 24(3):032106, 2012. 8
- M. Bowen and B. Tilley. On self-similar thermal rupture of thin liquid sheets. *Physics of Fluids*, 25(10):102105, 2013. 8
- J. Brackbill, D. Kothe, and C. Zemach. A continuum method for modeling surface tension. *Journal of Computational Physics*, 100(2):335–354, 1992. 11
- S. Bradley and C. Stow. Collisions between liquid-drops. *Philosophical Transactions of the Royal Society A*, 287:635, 1978. 91
- F. Charru. Hydrodynamic instabilities (cambridge texts in applied mathematics vol 37), 2011. 5, 108
- X. Chen, D. Ma, V. Yang, and S. Popinet. High-fidelity simulations of impinging jet atomization. *Atomization and Sprays*, 23(12), 2013. 9
- A. Clout and G. Lebon. A nonlinear stability analysis of the b enard–marangoni problem. *Journal of Fluid Mechanics*, 145:447–469, 1984. 5
- V. Cristini, J. Bławdziewicz, and M. Loewenberg. An adaptive mesh algorithm for evolving surfaces: simulations of drop breakup and coalescence. *Journal of Computational Physics*, 168(2):445–463, 2001. 10
- A. Darhuber and S. Troian. Principles of microfluidic actuation by modulation of surface stresses. *Annual Review of Fluid Mechanics*, 37:425–455, 2005. 2
- S. Davis. Rupture of thin liquid films. *Waves on fluid interfaces*, pages 291–302, 1983. 5
- S. Davis. Thermocapillary instabilities. *Annual Review of Fluid Mechanics*, 19(1):403–435, 1987. 1, 5, 7, 131
- S. Davis. Interfacial fluid dynamics. *Perspectives in fluid dynamics*, pages 1–51, 2002. 1

- S. Davis and G. Homsy. Energy stability theory for free-surface problems—buoyancy-thermocapillary layers. *Journal of Fluid Mechanics*, 98(3):527–553, 1980. 5
- P. De Gennes, F. Brochard-Wyart, and D. Quéré. Capillarity and gravity. In *Capillarity and Wetting Phenomena*, pages 33–67. Springer, 2004. xiii, 3
- M. De Saint Vincent, H. Chraïbi, and J. Delville. Optical flow focusing: Light-induced destabilization of stable liquid threads. *Physical Review Applied*, 4(4):044005, 2015. 8, 148
- G. De Vahl Davis. Natural convection of air in a square cavity: a bench mark numerical solution. *International Journal for Numerical Methods in Fluids*, 3(3):249–264, 1983. xvii, 114, 115, 116
- O. Desjardins, V. Moureau, and H. Pitsch. An accurate conservative level set/ghost fluid method for simulating turbulent atomization. *Journal of Computational Physics*, 227(18):8395–8416, 2008. 9
- G. Dhatt, E. Lefrançois, G. Touzot, et al. *Finite element method*. John Wiley & Sons, 2012. xvi, 155, 156, 157
- H. Dijkstra and P. Steen. Thermocapillary stabilization of the capillary breakup of an annular film of liquid. *Journal of Fluid Mechanics*, 229:205–228, 1991. 7
- H. Ding, P. Speltz, and C. Shu. Diffuse interface model for incompressible two-phase flows with large density ratios. *Journal of Computational Physics*, 226(2):2078–2095, 2007. 9
- D. Dritschel. Contour surgery: a topological reconnection scheme for extended integrations using contour dynamics. *Journal of Computational Physics*, 77(1):240–266, 1988. 20, 55
- F. Durbin. Numerical inversion of laplace transforms: an efficient improvement to dubner and abate’s method. *The Computer Journal*, 17(4):371–376, 1974. 65

## BIBLIOGRAPHY

---

- J. Eggers. Nonlinear dynamics and breakup of free-surface flows. *Reviews of Modern Physics*, 69(3):865, 1997. 76, 86, 91, 135
- J. Eggers and T. Dupont. Drop deformation in a one-dimensional approximation of the navier-stokes equation. *Journal of Fluid Mechanics*, 262:205, 1994. 76, 87
- R. Eötvös. Ueber den zusammenhang der oberflächenspannung der flüssigkeiten mit ihrem molecularvolumen. *Annalen der Physik*, 263(3):448–459, 1886. 4
- J. Étienne, E. Hinch, and J. Li. A lagrangian–eulerian approach for the numerical simulation of free-surface flow of a viscoelastic material. *Journal of Non-newtonian Fluid Mechanics*, 136(2):157–166, 2006. 13, 14, 51
- A. Eyer and H. Leiste. Striation-free silicon crystals by float-zoning with surface-coated melt. *Journal of Crystal Growth*, 71(1):249–252, 1985. 7
- A. Fath and D. Bothe. Direct numerical simulations of thermocapillary migration of a droplet attached to a solid wall. *International Journal of Multiphase Flow*, 77:209–221, 2015. 149
- M. Francois, S. Cummins, E. Dendy, D. Kothe, J. Sicilian, and M. Williams. A balanced-force algorithm for continuous and sharp interfacial surface tension models within a volume tracking framework. *Journal of Computational Physics*, 213(1):141–173, 2006. 12
- L. Freitag and C. Ollivier-Gooch. Tetrahedral mesh improvement using swapping and smoothing. *International Journal for Numerical Methods in Engineering*, 40:3979–4002, 1997. 20
- N. Fuchikami, S. Ishioka, and K. Kiyono. Simulation of a dripping faucet. *Journal of the Physical Society of Japan*, 68(4):1185–1196, 1999. 76, 80, 87
- E. Furlani and M. Hanchak. Nonlinear analysis of the deformation and breakup of viscous microjets using the method of lines. *International Journal for Numerical Methods in Fluids*, 65(5):563–577, 2011. 8

- C. Geuzaine and J. Remacle. Gmsh: A 3-d finite element mesh generator with built-in pre-and post-processing facilities. *International Journal for Numerical Methods in Engineering*, 79(11):1309–1331, 2009. 17
- R. Glowinski and P. Le Tallec. *Augmented Lagrangian and operator-splitting methods in nonlinear mechanics*, volume 9. SIAM, 1989. 15
- M. Gockenbach. *Understanding and implementing the finite element method*. Siam, 2006. 29
- D. Gueyffier, J. Li, A. Nadim, R. Scardovelli, and S. Zaleski. Volume-of-fluid interface tracking with smoothed surface stress methods for three-dimensional flows. *Journal of Computational Physics*, 152(2):423–456, 1999. 76
- E. Guggenheim. The principle of corresponding states. *The Journal of Chemical Physics*, 13(7):253–261, 1945. 4
- M. Gunzburger. *Finite Element Methods for Viscous Incompressible Flows: A guide to theory, practice, and algorithms*. Elsevier, 2012. 50
- F. Hecht. Bamg: bidimensional anisotropic mesh generator. *User Guide. INRIA, Rocquencourt*, 1998. 17
- M. Herrmann. A balanced force refined level set grid method for two-phase flows on unstructured flow solver grids. *Journal of Computational Physics*, 227(4): 2674–2706, 2008. 12
- K. Humphry, A. Ajdari, A. Fernández-Nieves, H. Stone, and D. Weitz. Suppression of instabilities in multiphase flow by geometric confinement. *Physical Review E*, 79(5):056310, 2009. 148
- J. Israelachvili. *Intermolecular and surface forces: revised third edition*. Academic press, 2011. 94
- X. Jiang and A. James. Numerical simulation of the head-on collision of two equal-sized drops with van der waals forces. *Journal of Engineering Mathematics*, 59(1):99–121, 2007. 94

## BIBLIOGRAPHY

---

- Y. Jiang, A. Umemura, and C. Law. An experimental investigation on the collision behaviour of hydrocarbon droplets. *Journal of Fluid Mechanics*, 234:171, 1992. 91
- A. Karbalaei, R. Kumar, and H. Cho. Thermocapillarity in microfluidics—a review. *Micromachines*, 7(1):13, 2016. 4
- H. Kawamura, K. Nishino, S. Matsumoto, and I. Ueno. Report on microgravity experiments of marangoni convection aboard international space station. *Journal of Heat Transfer*, 134(3):031005, 2012. xiii, 7
- H. Kuhlmann and H. Rath. Hydrodynamic instabilities in cylindrical thermocapillary liquid bridges. *Journal of Fluid Mechanics*, 247:247–274, 1993. 7
- M. Kwakkel, W. Breugem, and B. Boersma. Extension of a CLSVOF method for droplet-laden flows with a coalescence/breakup model. *Journal of Computational Physics*, 253:166–188, 2013. 13, 103
- B. Lafaurie, C. Nardone, R. Scardovelli, S. Zaleski, and G. Zanetti. Modelling merging and fragmentation in multiphase flows with SURFER. *Journal of Computational Physics*, 113:134–147, 1994. 9
- L. Leal. *Advanced transport phenomena: fluid mechanics and convective transport processes*, volume 7. Cambridge University Press, 2007. 124
- J. Li. An arbitrary lagrangian eulerian method for three-phase flows with triple junction points. *Journal of Computational Physics*, 251:1–16, 2013. vii, 9, 10, 11, 13, 14, 17, 49, 145
- J. Li. Macroscopic model for head-on binary droplet collisions in a gaseous medium. *Physical Review Letters*, 117(21):214502, 2016. 11, 13, 91, 97
- J. Li and G. Wells. Cued 3d7, lecture notes, finite element methods. url: <http://www2.eng.cam.ac.uk/~j1305/3D7/unFill.pdf>. 33
- J. Li, M. Hesse, J. Ziegler, and A. Woods. An arbitrary Lagrangian Eulerian method for moving-boundary problems and its application to jumping over water. *Journal of Computational Physics*, 208:289–314, 2005. 11, 66, 68



- Y. Li and J. Sprittles. Capillary breakup of a liquid bridge: identifying regimes and transitions. *Journal of Fluid Mechanics*, 797:29–59, 2016. 136
- H. Liu, Y. Zhang, and A. Valocchi. Modeling and simulation of thermocapillary flows using lattice boltzmann method. *Journal of Computational Physics*, 231(12):4433–4453, 2012. 128, 129, 130, 147
- F. Mashayek and N. Ashgriz. Nonlinear instability of liquid jets with thermocapillarity. *Journal of Fluid Mechanics*, 283:97–123, 1995. 8
- G. McKinley and M. Renardy. Wolfgang von ohnesorge. *Physics of Fluids*, 23(12):127101, 2011. 45
- S. Middleman. *Modeling axisymmetric flows: dynamics of films, jets, and drops*. Academic Press, 1995. 45
- B. Munson, T. Okiishi, A. Rothmayer, and W. Huebsch. *Fundamentals of fluid mechanics*. John Wiley & Sons, 2014. 44
- N. Nahas and R. Panton. Control of surface tension flows: instability of a liquid jet. *Journal of Fluids Engineering*, 112(3):296–301, 1990. 7
- S. Nakamura, T. Hibiya, K. Kakimoto, N. Imaishi, S. Nishizawa, A. Hirata, K. Mukai, S. Yoda, and T. Morita. Temperature fluctuations of the marangoni flow in a liquid bridge of molten silicon under microgravity on board the tr-ia-4 rocket. *Journal of Crystal Growth*, 186(1-2):85–94, 1998. 7
- S. Nir and C. Vassiliev. *Van der Waals interactions in thin films*. Marcel Dekker, New York, 1988. 94
- W. Ohnesorge. Die bildung von tropfen an düsen und die auflösung flüssiger strahlen. *ZAMM-Journal of Applied Mathematics and Mechanics/Zeitschrift für Angewandte Mathematik und Mechanik*, 16(6):355–358, 1936. 44
- C. Ollivier-Gooch. Grummp version 0.5. 0 user’s guide. *University of British Columbia*, 2010. 17

## BIBLIOGRAPHY

---

- J. Padday and A. Pitt. The stability of axisymmetric menisci. *Philosophical Transactions of the Royal Society A*, 275(1253):489–528, 1973. 81
- K. Pan, C. Law, and B. Zhou. Experimental and mechanistic description of merging and bouncing in head-on binary droplet collision. *Journal of Applied Physics*, 103(6):064901, 2008. 13, 95, 96, 98, 100, 103, 147
- Y. Pan and K. Suga. Numerical simulation of binary liquid droplet collision. *Physics of Fluids (1994-present)*, 17(8):082105, 2005. 105
- D. Papageorgiou. On the breakup of viscous-liquid threads. *Physics of Fluids*, 7(7):1529–1544, 1995. 135
- J. Pearson. On convection cells induced by surface tension. *Journal of fluid mechanics*, 4(5):489–500, 1958. 5
- B. Pendse and A. Esmaeeli. An analytical solution for thermocapillary-driven convection of superimposed fluids at zero reynolds and marangoni numbers. *International Journal of Thermal Sciences*, 49(7):1147–1155, 2010. 119, 120
- D. Peregrine, G. Shoker, and A. Symon. The bifurcation of liquid bridges. *Journal of Fluid Mechanics*, 212:25–39, 1990. xiv, 76, 77, 86, 89, 146
- S. Popinet. Gerris: a tree-based adaptive solver for the incompressible euler equations in complex geometries. *Journal of Computational Physics*, 190(2):572–600, 2003. 10
- S. Popinet. An accurate adaptive solver for surface-tension-driven interfacial flows. *Journal of Computational Physics*, 228(16):5838–5866, 2009. 12, 62
- S. Popinet. Numerical models of surface tension. *Annual Review of Fluid Mechanics*, 50:1–28, 2018. 13, 45
- S. Popinet and S. Zaleski. A front-tracking algorithm for accurate representation of surface tension. *Int. J. Numer. Methods Fluids*, 30(6):775–793, 1999. 12, 57
- W. Press, S. Teukolsky, W. Vetterling, and B. Flannery. *Numerical Recipes in C*, volume 2. Cambridge University Press, 1996. 55, 154

- A. Prosperetti. Free oscillations of drops and bubbles: the initial-value problem. *Journal of Fluid Mechanics*, 100(2):333–347, 1980. 65, 146
- J. Qian and C. Law. Regimes of coalescence and separation in droplet collision. *Journal of Fluid Mechanics*, 331:59–80, 1997. 13, 91, 106
- S. Quan and D. Schmidt. A moving mesh interface tracking method for 3d incompressible two-phase flows. *Journal of Computational Physics*, 221(2):761–780, 2007. xiv, 10, 72, 73
- S. Quan, J. Lou, and D. Schmidt. Modeling merging and breakup in the moving mesh interface tracking method for multiphase flow simulations. *Journal of Computational Physics*, 228(7):2660–2675, 2009. 11
- J. Reddy and D. Gartling. *The finite element method in heat transfer and fluid dynamics*. CRC press, 2010. 29, 49, 108, 109
- Y. Renardy and M. Renardy. Prost: a parabolic reconstruction of surface tension for the volume-of-fluid method. *Journal of Computational Physics*, 183(2):400–421, 2002. 12, 57
- R. Rupp, G. Müller, and G. Neumann. Three-dimensional time dependent modelling of the marangoni convection in zone melting configurations for gaas. *Journal of Crystal growth*, 97(1):34–41, 1989. 7
- J. Scanlon and L. Segel. Finite amplitude cellular convection induced by surface tension. *Journal of Fluid Mechanics*, 30(01):149–162, 1967. 5
- R. Scardovelli and S. Zaleski. Direct numerical simulation of free-surface and interfacial flow. *Annual Review of Fluid Mechanics*, 31(1):567–603, 1999. 9, 56, 71
- M. Schatz and G. Neitzel. Experiments on thermocapillary instabilities. *Annual Review of Fluid Mechanics*, 33(1):93–127, 2001. 2, 7, 131
- L. Scriven and C. Sternling. The marangoni effects. *Nature*, 187:186 – 188, 1960. 2, 5

## BIBLIOGRAPHY

---

- J. Sethian. Evolution, implementation, and application of level set and fast marching methods for advancing fronts. *Journal of Computational Physics*, 169:503–555, 2001. 21
- N. Shankar and R. Subramanian. The stokes motion of a gas bubble due to interfacial tension gradients at low to moderate marangoni numbers. *Journal of Colloid and Interface Science*, 123(2):512–522, 1988. 129
- J. Shewchuk. Triangle: Engineering a 2d quality mesh generator and delaunay triangulator. In *Applied computational geometry towards geometric engineering*, pages 203–222. Springer, 1996. 17
- K. Smith. On convective instability induced by surface-tension gradients. *Journal of Fluid Mechanics*, 24(02):401–414, 1966. 5
- M. Smith and S. Davis. Instabilities of dynamic thermocapillary liquid layers. part 1. convective instabilities. *Journal of Fluid Mechanics*, 132:119–144, 1983a. 6
- M. Smith and S. Davis. Instabilities of dynamic thermocapillary liquid layers. part 2. surface-wave instabilities. *Journal of Fluid Mechanics*, 132:145–162, 1983b. 6
- H. Stone. Dynamics of drop deformation and breakup in viscous fluids. *Annual Review of Fluid Mechanics*, 26(1):65–102, 1994. 45
- Y. Sui. Moving towards the cold region or the hot region? thermocapillary migration of a droplet attached on a horizontal substrate. *Physics of Fluids (1994-present)*, 26(9):092102, 2014. 149
- M. Sussman, P. Smereka, and S. Osher. A level set approach for computing solutions to incompressible two-phase flow. *Journal of Computational Physics*, 114(1):146–159, 1994. 9
- B. S. Tilley and M. Bowen. Thermocapillary control of rupture in thin viscous fluid sheets. *Journal of Fluid Mechanics*, 541:399–408, 2005. 8

- G. Tryggvason, B. Bunner, A. Esmaeeli, D. Juric, N. Al-Rawahi, W. Tauber, J. Han, S. Nas, and Y. Jan. A front-tracking method for the computations of multiphase flow. *Journal of Computational Physics*, 169(2):708–759, 2001. 9
- I. Ueno, K. Nishino, M. Ohnishi, H. Kawamura, M. Sakurai, and S. Matsumoto. Liquid bridge pinch off and satellite drop formation under thermocapillary effect in japanese experiment module'kibo'aboard the international space station. *arXiv preprint arXiv:1210.4073*, 2012. xvi, 131
- S. Vanhook, M. Schatz, J. Swift, W. McCormick, and H. Swinney. Long-wavelength surface-tension-driven Bénard convection: experiment and theory. *Journal of Fluid Mechanics*, 345:45–78, 1997. 5
- M. Wanschura, V. Shevtsova, H. Kuhlmann, and H. Rath. Convective instability mechanisms in thermocapillary liquid bridges. *Physics of Fluids*, 7(5):912–925, 1995. 7
- Z. Xie, D. Pavlidis, P. Salinas, J. Percival, C. Pain, and O. Matar. A balanced-force control volume finite element method for interfacial flows with surface tension using adaptive anisotropic unstructured meshes. *Computers & Fluids*, 138:38–50, 2016. 59
- J. Xu and S. Davis. Liquid bridges with thermocapillarity. *Physics of Fluids (1958-1988)*, 26(10):2880–2886, 1983. 6
- J. Xu and S. Davis. Convective thermocapillary instabilities in liquid bridges. *Physics of Fluids (1958-1988)*, 27(5):1102–1107, 1984. 6
- J. Xu and S. Davis. Instability of capillary jets with thermocapillarity. *Journal of Fluid Mechanics*, 161:1–25, 1985. 6
- Z. Yin, P. Gao, W. Hu, and L. Chang. Thermocapillary migration of nondeformable drops. *Physics of Fluids (1994-present)*, 20(8):082101, 2008. 129
- N. Young, J. Goldstein, and M. Block. The motion of bubbles in a vertical temperature gradient. *Journal of Fluid Mechanics*, 6(03):350–356, 1959. 125

## BIBLIOGRAPHY

---

- P. Yue, C. Zhou, J. Feng, C. Ollivier-Gooch, and H. Hu. Phase-field simulations of interfacial dynamics in viscoelastic fluids using finite elements with adaptive meshing. *Journal of Computational Physics*, 219(1):47–67, 2006. 10, 20
- S. Zaleski, J. Li, and S. Succi. Two-dimensional navier-stokes simulation of deformation and breakup of liquid patches. *Physical Review Letters*, 75(2):244, 1995. 9
- P. Zhang and C. Law. An analysis of head-on droplet collision with large deformation in gaseous medium. *Physics of Fluids (1994-present)*, 23(4):042102, 2011. 25, 91, 92, 103
- X. Zheng, J. Lowengrub, A. Anderson, and V. Cristini. Adaptive unstructured volume remeshing II: Application to two- and three-dimensional level-set simulations of multiphase flow. *Journal of Computational Physics*, 208:626–650, 2005. 20